UNIVERSITY OF CALIFORNIA

Los Angeles

The Search for Optical Cycling Molecules

A dissertation submitted in partial satisfaction

of the requirements for the degree

Doctor of Philosophy in Physics

by

Guanming Lao

2024

ABSTRACT OF THE DISSERTATION

The Search for Optical Cycling Molecules

by

Guanming Lao

Doctor of Philosophy in Physics

University of California, Los Angeles, 2024

Professor Eric R. Hudson, Chair

Cold molecules represent a frontier in the field of physics. Optical cycling, a process allowing repeated absorption and emission of photons by a molecule without altering its internal state, is the key to trapping and cooling molecules, as well as to quantum manipulation. However, the search for these molecules faces challenges including identifying suitable species that exhibit the required closed transition pathways for efficient optical cycling. The complexity of molecular structures, such as the electronic, vibrational and rotational properties, presents substantial hurdles in advancing this domain. To better understand these molecular physical and chemical properties, we have been working on the optical cycling properties of many different molecules, ranging from diatomic molecular ions to large neutral molecules with mass $>$ 300 amu. The results suggest that many of these candidates could potentially be laser-cooled using just a few repumping lasers, although significant progress is still required.

This dissertation focuses on the search of optical cycling molecules by presenting comprehensive studies of a diatomic molecular ion (SiO^+) and molecules with optical cycling centers (OCCs). Through detailed analysis utilizing molecular Hamiltonian and experimental approaches such as high-resolution laser spectroscopy and dispersed laser-induced fluorescence (DLIF) spectroscopy, we studied the key mechanisms underlying these molecules. This work elucidates the electronic, vibrational, and rotational structures essential for achieving effi-

cient optical cycling, investigates how the non-Born-Oppenheimer (non-BO) effects, such as the Fermi resonance and Jahn-Teller effects, may affect the cycling properties. The findings of new molecular species, such as the large molecules like Ca/SrOPh-diadamantanes, offer new insights into the selection criteria for potential molecules. Our findings not only enriched the promising molecular systems for laser cooling and quantum state detection, but also provides a foundation for future exploration and application of these molecules in advancing quantum technologies and precision spectroscopy.

The dissertation of Guanming Lao is approved.

Wesley C. Campbell

Justin R. Caram

Paul Hamilton

Eric R. Hudson, Committee Chair

University of California, Los Angeles

2024

The supreme good is like water.

— Lao Tzu

Table of Contents

List of Figures

List of Tables

Acknowledgments

I would like to express my deepest gratitude to all those who have supported and guided me throughout the course of my dissertation. I am especially grateful to my advisors, Professor Eric Hudson and Professor Wes Campbell. Your expertise and guidance have been invaluable in shaping my research and academic growth, and I learned a lot from your curiosity and physical intuition. I would also like to thank my committee members, Professor Justin Caram and Professor Paul Hamilton, for the valuable comments and suggestions to improve this work.

Many thanks go to my lab colleagues, Dr. Guo-Zhu Zhu and Dr. Haowen Zhou, who were more than supportive in providing collaboration and technical help to make the research atmosphere bright and lively. I also thank Professor Anastassia Alexandrova, Professor Anna Krylov, Dr. Claire Dickerson, Cecilia Chang, Taras Khvorost and Paweł Wójcik for the calculation and the vibrational analysis of the molecules, which have greatly enhanced the quality of the research. In addition, thanks to Professor John Doyle, Dr. Debayan Mitra, Dr. Zack Lasner, and Professor Benjamin Augenbraun for the collaboration of the CaOPh and SrOPh projects, their insight and guidance during the meetings greatly affected us in a positive way.

Additionally, I am grateful to the entire AMO community at UCLA. Thanks to Dr. Hao Wu, Dr. Matthew Boguslawski, Dr. Christian Schneider, Dr. Elizabeth West, Dr. Anthony Ransford, Dr. Michael Mills, Dr. Conrad Roman, Dr. Changling Zhao, Dr. Andrei Tretiakov, Eddie Chang, Richard Elwell, Thomas Dellaert, Patrick McMillin, Sami Khamis, Randy Putnam, Zachary Wall, Grant Mitts, Clayton Ho, Sam Vizvary, Barry Li, Yongjia He, Michael Bareian and James Terhune for helping us setting up the experiments and the constructive discussions.

Lastly, I would like to thank my family and my friends for their support and understanding during this academic journey. Their encouragement and love have been my strength and motivation. Thanks to Professor David Weitz, Professor David Schuster, and Professor

Daomu Zhao for their invaluable advice and support. I would also like to acknowledge the financial support provided by the UCLA Physics and Astronomy department, which enabled me to conduct the experiments and analysis necessary for this study.

Curriculum Vitae

2013 – 2018	B.S. in Physics, Zhejiang University (ZJU), Hangzhou, China.
2018 – Present	Ph.D. student in Physics, University of California, Los Angeles (UCLA).

Publications

[1] Guo-Zhu Zhu, Debayan Mitra, Benjamin L. Augenbraun, Claire E. Dickerson, Michael J. Frim, Guanming Lao, Zack D. Lasner, Anastasia N. Alexandrova, Wesley C. Campbell, Justin R. Caram, John M. Doyle, and Eric R. Hudson, "Functionalizing aromatic compounds with optical cycling centers," Nat. Chem. 14, 995 (2022) .

[2] Guanming Lao, Guo-Zhu Zhu, Claire E. Dickerson, Benjamin L. Augenbraun,Anastasia N. Alexandrova, Justin R. Caram, Eric R. Hudson, and Wesley C. Campbell, "Laser spectroscopy of aromatic molecles with optical cycling centers: strontium (I) phenoxides," J. Phys. Chem. Lett. 13(47), 11029-11035 (2022) .

[3] Guo-Zhu Zhu, Guanming Lao, Clayton Ho, Wesley C. Campbell, and Eric R. Hudson, "High-resolution laser-induced fluorescence spectroscopy of $^{28}Si^{16}O^+$ and $^{29}Si^{16}O^+$ in a cryogenic buffer-gas cell," J. Mol. Spectrosc. 384, 111582 (2022) .

[4] Guo-Zhu Zhu, Guanming Lao, Claire E. Dickerson, Justin R. Caram, Wesley C. Campbell, Anastasia N. Alexandrova, and Eric R. Hudson, "Extending the large molecule limit: The role of Fermi resonance in developing a quantum functional group," J. Phys. Chem. Lett. 15(2), 590-597 (2024)

CHAPTER 1

Introduction

In the realm of quantum physics, laser cooling has emerged as a pivotal technique, enabling the precise control and manipulation of atomic motion. Initially applied to neutral atoms, this method has allowed scientists to achieve temperatures near absolute zero, unveiling new states of matter such as the Bose-Einstein condensate state [1, 2] and facilitating significant applications and studies in quantum mechanics, including quantum simulation [3, 4], atomic clocks [5], quantum computing and information processing [6, 7], investigations of fundamental quantum phenomena [8, 9], and matter-wave interferometry [10, 11]. The technique hinges on the principle of optical cycling, effectively cooling them down through the absorption and re-emission of photons.

Transitioning from atoms to molecules, the concept of laser cooling encounters both new challenges and opportunities. Molecules, with their complex energy level structures due to vibrational and rotational states, present a more intricate landscape for cooling compared to the atomic cases [12, 13]. Despite these complexities, the successful demonstration of laser cooling of molecules were achieved in 2010s [14–18], utilizing a combination of innovative techniques such as buffer-gas cooling, Sisyphus cooling, and magneto-optical trapping.

The laser cooling of molecules holds the promise of unlocking new territories in science and technology. Cooling molecules to ultra-cold temperatures could revolutionize our understanding of quantum chemistry, enabling the direct observation of chemical reactions at the quantum level, and paving the way for the development of quantum-controlled chemistry [19–21]. Moreover, the ultra-cold molecules can serve as highly sensitive probes for fundamental constants and the investigation of quantum phenomena that are elusive at higher

temperatures, and the cooling of molecules has profound implications for precision measurement [22–24] and quantum computing [25, 26]. In quantum computing, molecules cooled to near absolute zero could act as qubits with long coherence times and strong interactions, enhancing the performance and scalability of quantum computers.

For the scalability, extending the current laser cooling methods to larger and larger molecules is necessary. Although the laser cooling of multiple diatomic or polyatomic molecules has already been demonstrated, achieving efficient laser cooling of large molecules requires overcoming significant obstacles. The rich vibrational and rotational structures of these molecules require tailored laser cooling schemes that can cope with their complexity. In addition, some non-Born-Oppenheimer effects, such as the Jahn-Teller effect [27, 28], Fermi resonance [29], intramolecular vibrational energy transfer [30], spin-orbit coupling and spin-spin interaction [31], can introduce extra challenges into these laser cooling schemes.

Based on the criteria proposed by Prof. Di Rosa [32], our research identifies molecules with optical cycling centers (OCCs) as a promising avenue for exploring species amenable to laser cooling. Hence, the main focus of our research for such molecular species is the phenoxides functionalized with OCCs, a Ca-O or Sr-O unit [33]. By integrating such a functional group with an alkaline earth metal atom as the cycling center, the optical cycling transition can then be addressed between molecular orbitals localized on the metal atom. This dissertation synthesizes our work conducted during my doctoral studies, focusing on several key aspects: i) the spectra and optical cycling scheme of a diatomic molecular ion, SiO^+, ii) the dispersed laser induced fluorescence spectra of calcium and strontium phenoxides, iii) the rotational spectra of the strontium phenoxide, and iv) examining non-Born-Oppenheimer effects evidenced in the spectra, including Fermi resonance and Jahn-Teller effects. Through these focused inquiries, the dissertation aims to contribute to our understanding of laser cooling of molecules with OCCs as well as the scalability of such molecules.

CHAPTER 2

Molecular structure and transition

State preparation and measurement in molecule requires a comprehensive understanding of the structural characteristics of the target molecule; however, the complexity of this endeavor varies between cases. To equip readers with foundational knowledge for the subsequent chapters of this thesis, this chapter will provide a detailed description of the molecular structures discussed herein. Additionally, it will clarify the notations and concepts employed and delve into the underlying mathematical background. Relevant materials on these topics can be found in Ref. [13, 31, 34, 35].

2.1 Born-Oppenheimer approximation

For a given molecule, its internal energy levels are determined by the molecular Hamiltonian H_0, which typically contains the electronic, vibrational, rotational and hyperfine terms [31, 34]:

$$H_0 = H_{el} + H_{vib} + H_{rot} + H_{hf}. \tag{2.1}$$

The electronic term H_{el} acts on the space coordinates of the electrons ($\boldsymbol{r}$) and nuclei ($\boldsymbol{R}$) in the molecule:

$$H_{el}\psi(\boldsymbol{r}, \boldsymbol{R}) = E_{el}\psi(\boldsymbol{r}, \boldsymbol{R}). \tag{2.2}$$

Although it is never possible to express the actual Hamiltonian as Eq.(2.1), as these Hamiltonian operators act on different coordinate spaces, (H_{el}, H_{vib} and H_{rot} are mainly represented in the coordinates of electron $\boldsymbol{r}$, nuclei coordinates $\boldsymbol{R}$, and angular coordinates (θ, ψ), respectively), we can introduce the Born-Oppenheimer approximation to simplify the model

and calculation as follows:

Born-Oppenheimer (BO) approximation: if the coupling between electronic and vibrational states are weak, the electronic and vibrational eigen-wavefunction could be separated in the following manner:

$$\psi(\boldsymbol{r}, \boldsymbol{R}) = \psi_e(\boldsymbol{r}; \boldsymbol{R})\psi_v(\boldsymbol{R}), \tag{2.3}$$

here ψ is the wave function on the nuclear coordinates, and $\psi_e(\boldsymbol{r}; \boldsymbol{R})$ is the electronic wavefunction. The nuclei coordinates $\boldsymbol{R}$ are considered to be parametric in $\psi_e(\boldsymbol{r}; \boldsymbol{R})$ because the electronic wavefunction can be regarded as a slow-varying function of $\boldsymbol{R}$. With the BO approximation, the molecular wavefunction could be written as the product of the electronic, vibrational, rotational and hyperfine wavefunction:

$$\psi_0 = \psi_e(\boldsymbol{r}; \boldsymbol{R})\psi_v(\boldsymbol{R})\psi_{rot}\psi_{hf}. \tag{2.4}$$

By representing the total wavefunction as a product of independent terms, we can analyze the energy level structure based on the symmetry of the wavefunction and its associated quantum numbers. Mixtures of different terms, like spin-orbit and spin-rotation couplings, are treated as off-diagonal Hamiltonian matrix elements within this framework. We will delve deeper into these topics in subsequent discussions.

The BO approximation fails in some cases, such as highly symmetric molecules. For such molecules, the geometric distortion that results from certain electron configurations could lead to the breaking of the symmetry. This phenomenon could be further explained with the Jahn-Teller effect in polyatomic molecule[28] or the Renner–Teller effect in linear molecule[36]. Further details about how the symmetry affects molecular levels will be given in Chap. 6.

2.2 Electronic structure

The Born-Oppenheimer approximation separates the electronic and nuclear motions, which allows us to solve the Schrodinger equation for the motion of the electrons in the electrostatic field produced by fixed nuclear charges.

The most commonly used method of describing the molecular orbitals is the linear combination of atomic orbitals (LCAO) method. It involves consideration of the interaction of the atomic orbitals of the separated atoms to form molecular orbitals that accommodate the available electrons. Homonuclear diatomic molecule, for example, has simple structure which is straightforward for understanding of the LCAO: Figure 2.1 shows how the s and p atomic orbitals can combine to form different bonding and antibonding orbitals in molecule.

Though orbitals in larger molecules can be very complex, there are a few ways available for the description of their structure, such as the point group symmetry. Homonuclear and heteronuclear diatomic molecules, for example, have $D_{\infty h}$ or $C_{\infty v}$ symmetry, respectively; some molecules involved in this thesis such as CaOPh, CaO-Adamantane and CaOPh-3F are of C_{2v}, C_{3v} and C_s symmetry, respectively. If there is no additional factor with a different symmetry affecting the molecule (such as crossings in the curves), the electronic (and vibrational) eigen-wavefunctions should follow the molecular symmetry. Therefore, in convention, these orbitals are distinguished with the irreducible representations of the point group of the molecule, e.g., notations $\Sigma^{\pm}, \Pi, \Delta, \dots$ for the heteronuclear diatomic molecules, A_1, A_2, B_1 and B_2 for the C_{2v} type molecules, and A' and A'' for the C_s type molecules. Combined with the other notations such as $(X, A, B, C, \dots)$ for the ground and excited electronic levels and a superscript $2S + 1$ for the multiplicity of spin, the system of labeling can describe these states in a comprehensive manner.

A special case of the molecular orbitals is the ones in M-O-R type molecule. Here M is an alkaline-earth metal atom ionically bonded to oxygen (O) forming an optical cycling center (OCC), and R is a molecular ligand. In these molecules, one of the valence electron on the metal atom participates into the bonding with the oxygen, while the remaining

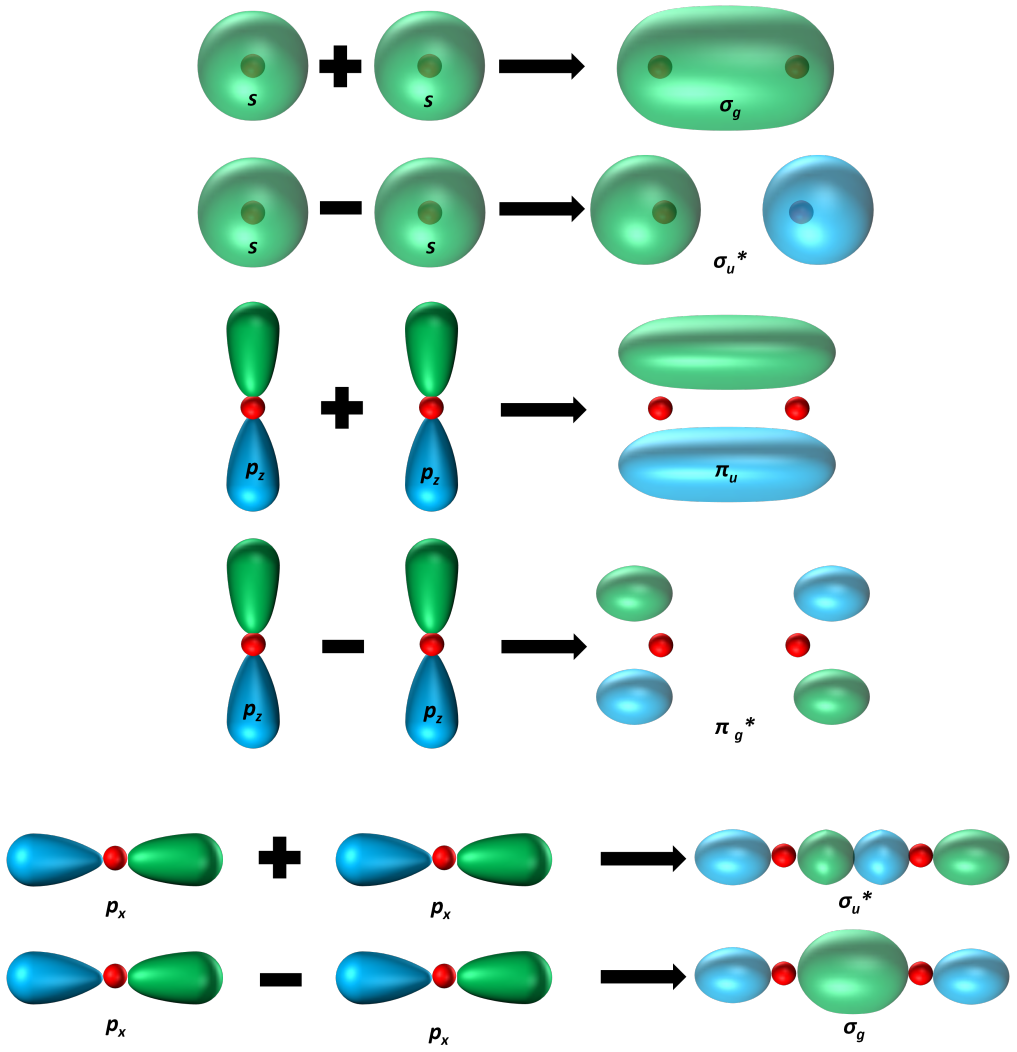

Figure 2.1: Relations of the linear combination of atmoic orbitals and the bonding and antibonding molecular orbitals.

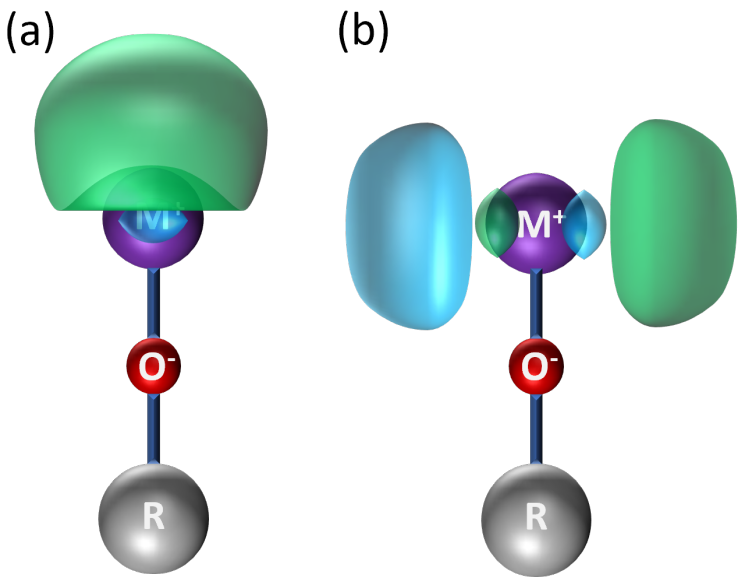

Figure 2.2: Illustration of (a) HOMO and (b) LUMO for M-O-R type molecule.

metal-centered radical electron forms the highest-occupied and lowest-unoccupied molecular orbitals, HOMO and LUMO. Figure 2.2 shows a sketch of the HOMO and LUMO of a typical M-O-R type molecule.

As shown that the HOMO and LUMOs of M-O-R type molecules are significantly decoupled from the majority of the molecule's vibrational degrees of freedom [33], it exhibits considerable potential for optical cycling, as well as state preparation and measurement [13, 37, 38]. In this thesis, the molecules of M-O-R type with different ligand R will be studied .

2.3 Vibrational structure

As referred above, the BO approximation allows us to separate the vibrational part from the total wave equation. Note that the vibration of the nuclei can be decomposed into different normal vibrational modes (the normal coordinates are denoted with Q_i), as the harmonic approximation is taken for all these modes, the vibrational Hamiltonian only contains the

momentum and the quadratic potential terms, i.e.,

$$H_v = \sum_{i=1}^{N_v} \left(-\frac{1}{2}\frac{\partial^2}{\partial Q_i^2} + \frac{\lambda_i}{2} Q_i^2 \right). \tag{2.5}$$

Here the upper limit N_v is depending on the vibrational degree of freedom of the molecule. Generally, $N_v = 3N - 6$ since the N nuclei of the molecule provide 3N degrees of freedom, within which 3 are associated with translations and 3 with rotations. This allows us to express the vibrational wave equation as the function of the normal coordinates of the nuclei. For linear molecule, $N_v = 3N - 5$ because there is only two rotational degrees of freedom.

The exact solution for Eq.(2.5) can be found in plenty of quantum mechanics textbooks. However, harmonic potential is too good to be true in molecule. For a straightforward introduction to the actual vibrational levels, we will take the diatomic molecule as our first example. A simple but important analytical potential is the Morse potential[39]:

$$V(R) = D_e \left[1 - e^{-\beta(R-R_e)}\right]^2, \tag{2.6}$$

where R_e is the equilibrium internuclear distance, β is a constant and D_e is the dissociation energy. The vibrational levels of anharmonic oscillator is

$$E_{vib}/\hbar = \omega_e(v + 1/2) - \omega_e x_e (v + 1/2)^2 + \cdots, \tag{2.7}$$

here v is the vibrational quantum number. For Morse oscillator, the sum of the first two terms are already the exact solution of the levels. Here $\omega_e x_e$ is not "ω_e times x_e"; they are as a whole for representing the anharmonic coefficient. Figure 2.3 is an example of the Morse potential as well as the corresponding lowest four bounded states in the potential well.

In polyatomic molecules, the potential can be complicated, but one may still be able to handle the vibrational modes with harmonic model to approximately calculate their corresponding vibrational frequencies if the vibrational levels are much lower than the well depth. However, some anharmonic effects exist as the molecular potential surface is not a

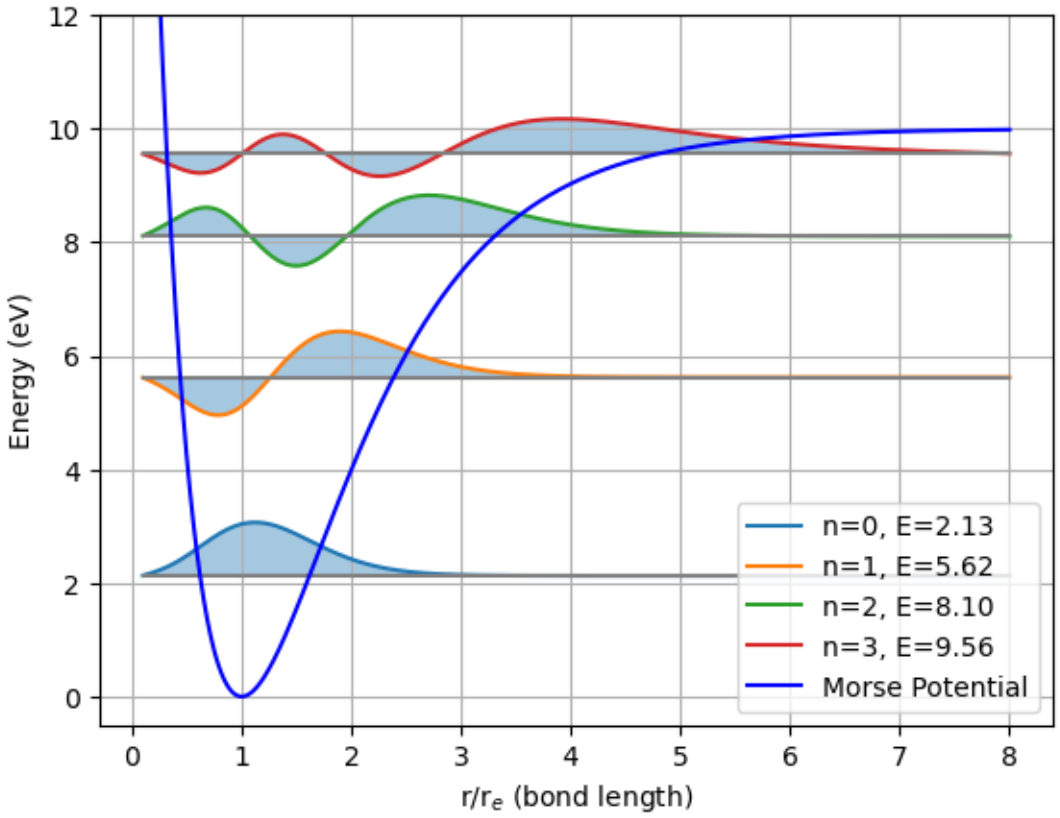

Figure 2.3: Illustration of Morse potential with $D_e = 10eV, \beta = 1/R_e$ and the lowest four bounded states. The levels are indicated with gray lines and the curves in different colors are the corresponding wave functions.

harmonic one. Therefore, one can expect these anharmonic effects come into the molecular Hamiltonian as some higher orders corrections to Eq. (2.5):

$$H_{v,tot} = \sum_{i=1}^{N_v} \left(-\frac{1}{2}\frac{\partial^2}{\partial Q_i^2} + \frac{\lambda_i}{2} Q_i^2 \right) + \sum_{i,j,k=1}^{N_v} \frac{\phi_{ijk}}{6} Q_i Q_j Q_k + ..., \tag{2.8}$$

The anharmonic terms comes from the higher order differentiation of the molecular potential, which is the function of the normal coordinates $\boldsymbol{Q} = (Q_1, \ldots, Q_{N_\nu})$:

$$\phi_{ijk} = \left(\frac{\partial^3 V(\boldsymbol{Q})}{\partial Q_i \partial Q_j \partial Q_k} \right)_{\boldsymbol{Q}=\boldsymbol{0}} \tag{2.9}$$

For simplicity, here we only involve the dominant anhamonic terms which are of the cubic terms of the normal coordinates. By rewriting the equation with creation and annihilation operators of these vibrational modes, the total vibrational Hamiltonian becomes

$$H_{v,tot} = \sum_{i=1}^{N_v} \left(a_i^\dagger a_i + \frac{1}{2} \right) \hbar\omega_i + \sum_{i,j,k=1}^{N_v} \phi'_{ijk} (a_i^\dagger + a_i)(a_j^\dagger + a_j)(a_k^\dagger + a_k)... \tag{2.10}$$

with coefficient ϕ'_{ijk} and ϕ_{ijk} different by a constant ratio omitted for simplicity. One can notice that the anharmonic terms of $a_i a_j^\dagger a_k^\dagger + a_i^\dagger a_j a_k$ connect the fundamental mode ν_i with nearby overtone/combination mode $\nu_j \nu_k$, and such mixing is known as Fermi resonance.

The Fermi resonance gives rise to some interesting spectroscopic phenomenon such as line intensity borrowing effect in experiment[34]. Typically, this effect emerges when the vibrational modes participating in the mixing share the same symmetry, or when the molecules being studied have low or no symmetry[40].

2.4 Rotational structure

A simple model of rotating molecule is ball-and-stick model, in which each atom is represented by a ball and the connections between the atoms are represented by sticks. For example, a diatomic molecule can be represented with a dumbbell model, where two atoms

of mass m_1 and m_2 are regarded as point-like with distance R between them. The rotational energy of the rotor in classical mechanics is

$$E_{rot} = \frac{1}{2}\mu R^2\omega^2 = \frac{1}{2}I\omega^2 = \frac{\boldsymbol{L}^2}{2I}, \tag{2.11}$$

where $\mu = \frac{m_1 m_2}{m_1+m_2}$ is the reduced mass of the diatomic molecule, $I = \mu R^2$ is the moment of inertia and $\boldsymbol{L}$ is the rotational angular momentum.

In quantum mechanics, the rotational Hamiltonian and the corresponding Schrödinger equation are[31]

$$H_{rot} = -\frac{\hbar^2}{2I}\frac{\partial}{\partial R}\left(R^2\frac{\partial}{\partial R}\right) - \frac{\hbar^2}{2I\sin^2\theta}\left[\sin\theta\frac{\partial}{\partial\theta}\left(\sin\theta\frac{\partial}{\partial\theta}\right) + \frac{\partial^2}{\partial^2\phi^2}\right] \tag{2.12}$$

and

$$H_{rot}\psi(R,\theta,\phi) = E\psi(R,\theta,\phi), \tag{2.13}$$

respectively. For a given electronic (vibrational) state, R can be considered as a constant and thus

$$-\frac{\hbar^2}{2I\sin^2\theta}\left[\sin\theta\frac{\partial}{\partial\theta}\left(\sin\theta\frac{\partial}{\partial\theta}\right) + \frac{\partial^2}{\partial^2\phi^2}\right]\psi(\theta,\phi) = E\psi(\theta,\phi). \tag{2.14}$$

The solution of this equation is the spherical harmonics $Y_l^m(\theta,\phi)$, i.e.,

$$Y_l^m(\theta,\phi) = (-1)^m\sqrt{\frac{(2l+1}{4\pi}\frac{(l-|m|)!}{(l+|m|)!}}P_l^m(\cos\theta)e^{im\phi}, \tag{2.15}$$

where $P_l^m(x)$ is the associated Legendre polynomial with degree l and order m. One can show that the eigen values are $\frac{\hbar^2}{2I}l(l+1)$, i.e.,

$$-\frac{\hbar^2}{2I\sin^2\theta}\left[\sin\theta\frac{\partial}{\partial\theta}\left(\sin\theta\frac{\partial}{\partial\theta}\right) + \frac{\partial^2}{\partial^2\phi^2}\right]Y_l^m(\theta,\phi) = \frac{\hbar^2}{2I}l(l+1)Y_l^m(\theta,\phi). \tag{2.16}$$

By defining $B = \frac{\hbar^2}{2I}$, the rotational energy can be represented as

$$E(l) = Bl(l+1). \tag{2.17}$$

The rotational energy levels therefore have energies $0, 2B, 6B, 12B$, etc.

For non-linear molecule, in classical mechanics, the rotation energy is the sum of the energies of the rotation in three principal axes, i.e.,

$$E_{rot} = \frac{L_x^2}{2I_x} + \frac{L_y^2}{2I_y} + \frac{L_z^2}{2I_z}. \tag{2.18}$$

Compared to the diatomic case, for an asymmetric quantum rotor, its rotational Hamiltonian can be similarly written as

$$H_{rot} = B_x L_x^2 + B_y L_y^2 + B_z L_z^2. \tag{2.19}$$

However, as these angular momentum operators do not commute with each other, i.e., $[L_i, L_j] = -i\sum_k \epsilon_{ijk} L_k$ (anomalous commutation rules for rotations of molecule-fixed coordinate system relative to the laboratory, see Ref.[34] and the next section for details), there is no state can be their common eigen-state. To intuitively define a set of eigen-state basis for the rotational Hamiltonian, it would be convenient to rewrite the Hamiltonian with a set of commuting observables, such as $\{L, L_z\}$. By making use of the relation

$$L^2 = L_x^2 + L_y^2 + L_z^2 \tag{2.20}$$

and introducing two operators (the ladder operators):

$$L_\pm = L_x \pm i L_y, \tag{2.21}$$

the rotational Hamiltonian can be written as

$$H_{rot} = B_z L_z^2 + \frac{B_x + B_y}{2}\left(L^2 - L_z^2\right) + \frac{B_x - B_y}{4}(L_+^2 + L_-^2). \tag{2.22}$$

Here we denote the basis of the first two terms on the right-hand side as $|l, m_l\rangle$, where l is the angular momentum quantum number and its projection quantum number is $m_l =$

$l, l-1, \ldots, -l$. Such basis choice is the eigen-basis of the Hamiltonian of symmetric rotor. Note that the ladder operators are not diagonal in this basis, i.e.,

$$L_{\pm}|l, m_l\rangle = \sqrt{l(l+1) - m_l(m_l \mp 1)}\hbar|l, m_l \mp 1\rangle, \tag{2.23}$$

the rotational eigen-states of asymmetric top molecule ($B_x \neq B_y \neq B_z$) are the mixed states of different symmetric top rotational states $|l, m_l\rangle$.

2.5 Hund's cases

Generally, in molecule, the nuclei rotation (denoted as $\boldsymbol{R}$) discussed above is not the only factor to concern, other terms of angular momenta, such as the spins from electron ($\boldsymbol{S}$) and nuclei ($\boldsymbol{I}$) and orbital angular momentum $\boldsymbol{L}$, can have significant affects to the molecular properties. In addition, these angular momenta can couple to one another and therefore affect the spectroscopic patterns in experiment. To understand these patterns and figure out the main and subsequent quantum properties of the molecule, quantum number and state assignments for these features become necessary. Hunds cases[31, 34], the most common method of describing the molecular states so far, provide a way to construct a reduced picture of intramolecular processes and understand how these angular momenta as well as their mutual interactions associate to the patterns in spectroscopy study.

The angular momenta involved in the Hund's cases are listed as follows:

$\boldsymbol{L}$	Electronic orbital angular momentum
$\boldsymbol{S}$	Electronic spin angular momentum
$\boldsymbol{I}$	Nuclear spin angular momentum
$\boldsymbol{J}$	Total angular momentum exclusive of nuclear spin
$\boldsymbol{F}$	Total angular momentum $\boldsymbol{F} = \boldsymbol{J} + \boldsymbol{I}$
$\boldsymbol{J_a}$	Total angular momentum of electron, $\boldsymbol{J_a} = \boldsymbol{L} + \boldsymbol{S}$
$\boldsymbol{N}$	Total angular momentum excluding spins $\boldsymbol{N} = \boldsymbol{J} - \boldsymbol{S}$
$\boldsymbol{R}$	Rotational angular momentum of nuclei, $\boldsymbol{R} = \boldsymbol{N} - \boldsymbol{L}$
Λ	Projection of $\boldsymbol{L}$ on internuclear axis
Σ	Projection of $\boldsymbol{S}$ on internuclear axis
Ω	Projection of $\boldsymbol{J_a}$ on internuclear axis, $\Omega = \Lambda + \Sigma$

According to the hierarchical ordering of electronic (H_{el}), spin-orbital (H_{SO}) and rotational (H_{rot}) Hamiltonians, the corresponding Hund cases (a)-(e) are explained in the table below. Here η represents the rest of the state labels, such as the electronic state and vibration.

Coupling case	H_{el}	H_{SO}	H_{Rot}	Good quantum number
(a)	strong	intermediate	weak	$\eta, \Lambda, S, \Sigma, J, \Omega$
(b)	strong	weak	intermediate	η, Λ, N, S, J
(c)	intermediate	strong	weak	η, J, J_a, Ω
(d)	intermediate	weak	strong	η, L, R, N, S, J
(e)	weak	strong	intermediate	η, J, J_a, R
(e′)	weak	intermediate	strong	η, J, J_a, R

Table 2.1: The classification for Hund's cases

In Hund's case (a), the predominant factor is a strong spin-orbit coupling, complemented by a marginal interaction between the electron and the molecular rotation. Contrarily, case (b) is characterized by the weak spin-orbit coupling and weak electron-nuclear rotational interaction where the electron's spin is oriented with respect to its orbital angular momentum, not the molecular axis. Case (c) represents intermediate situations that don't strictly adhere to the assumptions of cases (a) or (b). In this scenario, neither the electron spin $\boldsymbol{S}$ nor the orbital angular momentum $\boldsymbol{L}$ are rigidly oriented to any particular direction, and they couple strongly to each other and form intermediate quantized angular momentum $\boldsymbol{J_a}$. As a result, the behavior and characterization of molecular states can be more complex. In Hund's Case (d), there is a strong interaction between orbital angular momentum and molecular rotation, and $\boldsymbol{L}$ is non-zero. This case assumes that $\boldsymbol{J}$ orients itself relative to the axis of nuclear rotation. In case (e) and (e′), as $\boldsymbol{S}$ and $\boldsymbol{L}$ couple strongly while their interaction with the internuclear axis is very weak, there is no projection quantum number relative to the internuclear axis like Σ and Ω.

This thesis will be focus on the case (a) and (b) as our primary objective is investigating the optical cycling transitions of molecules, which is the optical transitions between the HOMO and the lowest few LUMOs. The gaps between them are ranging from $60 - 16000$ cm^{-1}, as a consequence, H_{el} often emerges as the most dominant Hamiltonian within the scope of the studies involved. Additionally, even if the choice of the basis does not satisfy

the corresponding conditions in the list, it is feasible to represent the basis functions of one coupling case through those of another, by means of the relationships between the bases, and then consider the state-mixing interaction as some off-diagonal elements or higher order correction in the effective Hamiltonian. For example, the conversion between (a) and (b) can be expressed as [31]

$$|\eta, \Lambda; N, N_a, S, J\rangle = \sum_{\Sigma=-S}^{S} (-1)^{J-S+N_a} \sqrt{2N+1} \begin{pmatrix} J & S & N \\ \Omega & -\Sigma & -N_a \end{pmatrix} |\eta, \Lambda; J, \Omega, S, \Sigma\rangle, \quad (2.24)$$

where N_a is the projection quantum number of N on the same axis as Λ and (:::) is the Wigner 3-j symbols. In addition, the spin-orbit interaction term, an example for illustration, is diagonal in the effective Hamiltonian of Hund's case (a) basis, while it manifests as the off-diagonal elements in the case (b) basis.

The angular momenta involved in this section actually have an important and interesting fact about the commutation rules. Some angular momenta, such as $\boldsymbol{L}$, $\boldsymbol{I}$, $\boldsymbol{S}$ and $\boldsymbol{J_a}$, obey normal commutation rules

$$[A_i, A_j] = i\hbar \sum_k \epsilon_{ijk} A_k, \quad (2.25)$$

while others angular momenta ($\boldsymbol{J}$, $\boldsymbol{N}$, $\boldsymbol{R}$ and $\boldsymbol{F}$) obey the anomalous commutation rules [34]

$$[A_i, A_j] = -i\hbar \sum_k \epsilon_{ijk} A_k. \quad (2.26)$$

This is because the angular momenta $\boldsymbol{L}$, $\boldsymbol{I}$, $\boldsymbol{S}$ and $\boldsymbol{J_a}$ are describing the rotations relative to the molecule-fixed coordinate system while others ($\boldsymbol{J}$, $\boldsymbol{N}$, $\boldsymbol{R}$ and $\boldsymbol{F}$) describe the rotations of the molecule-fixed coordinate system relative to the laboratory. Here we can show the general case that, for two vectors (denoted as $\boldsymbol{A}$ and $\boldsymbol{B}$) fixed in the molecule-fixed coordinate system (denote the operator of rotational angular momentum of the rotor as $\boldsymbol{R}$), their commutation relationship in the laboratory coordinate system is (denote $\hbar = 1$)

$$(\boldsymbol{R}\cdot\boldsymbol{A})(\boldsymbol{R}\cdot\boldsymbol{B}) - (\boldsymbol{R}\cdot\boldsymbol{B})(\boldsymbol{R}\cdot\boldsymbol{A}) = -i\boldsymbol{R}\cdot(\boldsymbol{A}\times\boldsymbol{B}). \quad (2.27)$$

We start by considering the transformation of the vector $\boldsymbol{A}$ under rotation. For component in x direction, A_x, if the rotation is also in x direction, the vector in new frame is unchanged, i.e.,

$$A'_x = A_x, \tag{2.28}$$

therefore, $[R_x, A_x] = 0$. For rotation transformation in y direction with an infinitely small shift denoted by θ, the transformed vector component is

$$A'_x = \hat{R}_y(\theta) A_x \hat{R}_y(\theta)^\dagger = A_x - i\theta[R_y, A_x], \tag{2.29}$$

where rotation operator is $\hat{R}_y(\theta) = e^{-i\theta R_y} = 1 - i\theta R_y$. Because the unit vectors is also rotated from $\hat{\epsilon}_x \to \hat{\epsilon}'_x$ (unit vectors in molecule- and laboratory-fixed coordinates, respectively), i.e.,

$$\hat{\epsilon}'_x = \hat{\epsilon}_x + \theta\hat{\epsilon}_y \times \hat{\epsilon}_x = \hat{\epsilon}_x - \theta\hat{\epsilon}_z, \tag{2.30}$$

the vector component in new coordinates is

$$A'_x = \boldsymbol{A} \cdot \hat{\epsilon}'_x = A_x - \theta A_z. \tag{2.31}$$

Comparing the two equations about A'_x, we have

$$[R_y, A_x] = -iA_z. \tag{2.32}$$

Similar commutation relationships can be worked out for other combinations of the components of the angular momentum and the vectors. Now, we can rewrite the left-hand side

(LHS) of Eq.(2.27):

$$\begin{aligned}
&(\boldsymbol{R}\cdot\boldsymbol{A})(\boldsymbol{R}\cdot\boldsymbol{B})-(\boldsymbol{R}\cdot\boldsymbol{B})(\boldsymbol{R}\cdot\boldsymbol{A})\\
=&(R_xA_x+R_yA_y+R_zA_z)(R_xB_x+R_yB_y+R_zB_z)\\
&-(R_xB_x+R_yB_y+R_zB_z)(R_xA_x+R_yA_y+R_zA_z)\\
=&R_xA_xR_yB_y+R_yA_yR_xB_x-R_xB_xR_yA_y-R_yB_yR_xA_x\\
&+R_xA_xR_zB_z+R_zA_zR_xB_x-R_xB_xR_zA_z-R_zB_zR_xA_x\\
&+R_yA_yR_zB_z+R_zA_zR_yB_y-R_yB_yR_zA_z-R_zB_zR_yA_y=(*),
\end{aligned}\tag{2.33}$$

For the first line in the second equation on the right hand side, we have

$$\begin{aligned}
&R_xA_xR_yB_y+R_yA_yR_xB_x-R_xB_xR_yA_y-R_yB_yR_xA_x\\
=&R_x(R_yA_x+iA_z)B_y+R_y(R_xA_y-iA_z)B_x-R_x(R_yB_x+iB_z)A_y-R_y(R_xB_y-iB_z)A_x\\
=&(R_xR_y-R_yR_x)(A_xB_y-B_xA_y)+iR_x(A_zB_y-B_zA_y)+iR_y(B_zA_x-A_zB_x)\\
=&iR_z(\boldsymbol{A}\times\boldsymbol{B})_z-iR_x(\boldsymbol{A}\times\boldsymbol{B})_x-iR_y(\boldsymbol{A}\times\boldsymbol{B})_y.
\end{aligned}\tag{2.34}$$

Similar derivation can be taken for the rest of two lines, and the sum of the three lines further gives

$$(*)=i\boldsymbol{R}\cdot(\boldsymbol{A}\times\boldsymbol{B})-i\boldsymbol{R}\cdot(\boldsymbol{A}\times\boldsymbol{B})-i\boldsymbol{R}\cdot(\boldsymbol{A}\times\boldsymbol{B})=-i\boldsymbol{R}\cdot(\boldsymbol{A}\times\boldsymbol{B}).\tag{2.35}$$

The anomalous commutation relationship for $\boldsymbol{R}$ can be immediately seen by taking $\boldsymbol{A}=\hat{\epsilon}_i$ and $\boldsymbol{B}=\hat{\epsilon}_j$. From here, we can see that the angular momenta compositing with the nuclei rotation $\boldsymbol{R}$ follow the anomalous commutation rules because of the coordinates transformation under the rotation. This relationship leads to some completely different results when dealing with the ladder operators. It could be very critical and should always be kept in mind when computing with the rotational Hamiltonian matrices.

2.6 Spin-orbit and spin-rotation coupling

The interactions involving electronic spins are neglected as we are taking the Born-Oppenheimer approximation, while these terms can mix levels of different electronic, vibrational and rotational states. As the spin parts in the molecular Hamiltonian have significant effects on the open shell molecule studied in some works involved in this thesis, we will have a brief introduction for them here.

2.6.1 Spin-orbit coupling

Spin-orbit coupling (SOC) describes a quantum mechanical phenomenon where an electron's intrinsic spin angular momentum ($\boldsymbol{S}$) interacts with its orbital angular momentum ($\boldsymbol{L}$) about the nucleus of an atom or molecule. This interaction can be visualized as arising due to the electron's motion in the electric field generated by the nucleus, resulting in the electron experiencing a magnetic field, which subsequently interacts with its spin. In atomic and molecular system, SOC can be rigorously calculated from the Dirac equation in relativistic quantum mechanics and quantum electrodynamics [41, 42]. In materials and molecular systems, SOC plays a significant role in various phenomena, such as the fine structure splitting in atomic spectra[43, 44], the Rashba and Dresselhaus effects in condensed matter physics[45, 46], and the emergence of topological insulators[47, 48]. Furthermore, in molecular systems, SOC can influence the dynamics and outcomes of chemical reactions, particularly when heavy elements are involved[49].

Molecules with open shell electronic states like M-O-R type molecule in this thesis introduce a range of new intramolecular interactions. The most significant of this is spin-orbit coupling, which occurs between the non-zero spin and orbital angular momentum. Depending on the molecular species, spin-orbit interactions range from a few cm^{-1} to several thousand cm^{-1}. Therefore, though spin-orbit coupling may be attributed as a high order correction of the electronic structure, it could mix a few different electronic states as the orbital and spin angular momentum are present, especially when these states are close to one another

in energies.

For the works involved in this thesis, only one valence electron is on the open shell and therefore subject to the spin-orbit effect. Mathematically, the spin-orbit interaction Hamiltonian in the M-O-R type molecule, H_{SO}, is often written as:

$$H_{SO} = \sum_i a_{SO,i} l_i s_i, \tag{2.36}$$

Where $a_{SO,i}$ is the spin-orbit parameter for the coupling in direction $i = x, y, z$, and $l_i s_i$ is the product of the electron's orbital and spin angular momenta in that direction. In molecule, some of the electronic states are separated by orbital angular momentum, therefore SOC can affect these states. We will give further discussion on how the SOC mix electronic states in Chap.5.

2.6.2 Spin-rotation coupling

Spin-rotation coupling (SRC) is a quantum mechanical interaction that pertains to the coupling between an electron's intrinsic spin angular momentum ($\boldsymbol{S}$) and the rotational angular momentum ($\boldsymbol{R}$) of a molecule. This interaction emerges as a consequence of the molecule's rotation modulating the electron's environment, which, in turn, affects its spin dynamics. It's especially relevant in molecular systems where electronic motion and molecular rotations are intimately intertwined.

The strength and effect of spin-rotation coupling depend on the molecular system in question. Typically, SRC is relatively weak compared to the electronic interactions and SOC; however, under certain conditions, especially in high-resolution spectroscopic studies where rotational lines can be distinguished, the effects of SRC become crucial for accurate spectral interpretation[35, 50].

The Hamiltonian representing the spin-rotation interaction, H_{SR}, can generally be expressed as[51]:

$$H_{\mathrm{SR}} = \frac{1}{2} \sum_{\alpha\beta} \varepsilon_{\alpha\beta} \left(N_\alpha S_\beta + S_\beta N_\alpha \right)$$

,

Here, ε denotes the spin-rotation tensor of the molecule. The tensor nature of the ε implies that the strength and directionality of the SRC can vary depending on the electronic and molecular states.

The accurate determination of the SRC parameters can provide insights into the electronic distribution and molecular geometry of the studied system. For example, one interesting fact is, as the precession of the electron spin in the produces a non-zero average magnetic moment which can interact with the rotational magnetic moment, the SR coupling can be induced by the high-order effect from the SO coupling[35, 52]. Such effect will be discussed in Chap.5.

2.7 Hyperfine interaction and nuclear spin statistics in molecule

Historically, the hyperfine structure has provided deep insights into the internal properties of nuclei, including their magnetic moments and nuclear spin[53, 54]. For molecular systems, the hyperfine structure is also evident in molecular spectra, where the interplay between nuclear and electronic motions becomes sophisticated. As it may significantly affect the molecular rotational levels via interaction like spin-rotation coupling, choosing a suitable basis set as well as the best coupling scheme can help building an appropriate form of the effective Hamiltonian.

Another question arises when two or more identical nuclei exist in the molecule. The statistical weights are different for bosonic and fermionic nuclei due to the Pauli exclusion principle, for example, in homonuclear diatomic molecule in which the spin of a single nucleus is I, the number of symmetric and antisymmetric states (denoted with *ortho* and *para*,

respectively) are different:

$$\begin{aligned} \text{number of symmetric states} &= (I+1)(2I+1), \\ \text{number of antisymmetric states} &= I(2I+1). \end{aligned} \tag{2.37}$$

As the rotational states have either even or odd parity and the combination of the parity of the rotational and nuclei states is also subjected to the bosonic or fermionic feature of the molecule, the rotational levels of a given parity will have different statistical weight.

In this section, we will discuss how the spins can affect the analysis of the molecule the Hund's cases (a) and (b) with hyperfine coupling, and the nuclear spin statistics in polyatomic molecule.

2.7.1 Hyperfine Structure in Hund's Case (a)

In Hund's case (a), there are two main possibilities of the coupling. One of them is due to the coupling between the electron spin and orbital moments, $\boldsymbol{J_a} = \boldsymbol{S} + \boldsymbol{L}$, and the nuclear spin, $\boldsymbol{I}$. This scheme is known as case (a_α) and gives rise to the hyperfine Hamiltonian $H_{hf}^{(a)} = a_{hf}(\boldsymbol{J_a} \cdot \boldsymbol{I})$. Here, a_{hf} is the hyperfine coupling constant. The energy levels are then split according to the total F quantum number, where $\boldsymbol{F} = \boldsymbol{J} + \boldsymbol{I} = \boldsymbol{J_a} + \boldsymbol{R} + \boldsymbol{I}$. If we consider such coupling relative to the axis z on which Ω is quantized, the basis can therefore be expressed in the form $|\eta, \Lambda\rangle|S, \Sigma, \Lambda, \Omega\rangle|\Omega, I_z, \Omega'\rangle|\Omega', R, F\rangle$. This case is also known as case (a_α). In general, as spin-spin interaction is interaction between the magnetic moments of the nuclei and electrons, it is very rare to see such a coupling scheme. The other coupling scheme, which is the most common situation and conventionally denoted as case (a_β), is the direct coupling between $\boldsymbol{I}$ and $\boldsymbol{J}$, i.e., $H_{hf}^{(a)} = a_{hf}(\boldsymbol{J} \cdot \boldsymbol{I})$. Such coupling leads to the total angular momentum $\boldsymbol{F}$ and can be regarded as a straightforward extension of Hund's case (a).

2.7.2 Hyperfine Structure in Hund's Case (b)

In Hund's case (b), the electron spin and electron orbital angular momentum are strongly coupled, and both are weakly coupled to the internuclear axis. There are also two sub-cases in this case. The first one is, when the hyperfine interaction is typically between the total rotational angular momentum, $\boldsymbol{N}$, and the nuclear spin, $\boldsymbol{I}$, the hyperfine Hamiltonian in this case can be expressed as $H_{hf}^{(b)} = b_{hf}(\boldsymbol{N} \cdot \boldsymbol{I})$. Here, b_{hf} is the hyperfine coupling constant. This sub-case is known as case ($b_{\beta N}$). As in Case (a), the energy levels are split according to the total F quantum number, where $\boldsymbol{F} = \boldsymbol{N} + \boldsymbol{I} + \boldsymbol{L}$, and the corresponding basis kets take the form $|\eta, \Lambda; N, \Lambda, I, F_1; F_1, S, F\rangle$.

In the second sub-case (conventionally labelled as case ($b_{\beta S}$)), $\boldsymbol{S}$ and $\boldsymbol{I}$ are coupled to form a resultant $\boldsymbol{G}$, which then couples with $\boldsymbol{N}$ to form $\boldsymbol{F}$. The corresponding basis kets can be represented as $|\eta, \Lambda; S, I, G; G, N, F\rangle$. This case is the one chosen for describing the electronic state of SiO^+, which will be introduced with further details in the Chap.3.

Though these coupling schemes are very useful for understanding the hyperfine structure of the molecules, it's worth noting that in many molecular systems, these Hund's cases may be oversimplifications, and a mixture of both might be needed to accurately describe the observed hyperfine structure. Furthermore, additional terms might be needed in the hyperfine Hamiltonian to capture quadrapolar interactions or other effects in more complex molecules. We will have further discussion in Chap.3.

2.7.3 Nuclear spin statistics in polyatomic molecules

For symmetric molecules comprising of identical bosonic nuclei, the permutations lead to symmetric wave functions, which is consistent with the inherent nature of bosons. However, when a symmetric molecule incorporates identical fermionic nuclei, the statistics become more nuanced. The Pauli exclusion principle still holds, and the combined symmetry of the molecular wave function – encompassing rotational, vibrational, electronic, and nuclear spin components – dictates the accessible quantum states. Only certain rotational and vibrational

states will align with the antisymmetric requirements of fermions. The total molecular wavefunction, the product of the electronic, ro-vibrational and nuclear spin wavefunctions, must therefore be either symmetric or antisymmetric with respect to the interchange of the coordinates of the two identical nuclei for bosons or fermions, respectively. As the calculation of the statistical weights varies from one point group symmetry to another as well as from one nuclei species to another, we will discuss the calculation details when necessary, for example in Chap.5. The calculation of the statistical weights for some molecular point groups can be found in Ref. [55, 56].

2.8 Beyond the Born-Oppenheimer approximation: the Jahn-Teller effect

The interaction between electronic configurations and molecular structures lies at the heart of molecular physics, while it is beyond the BO approximation, the center of our discussions in the previous few sections. Moreover, as there are degeneracies in both the electronic states and molecular structures, these degenerate levels may repel one another. Such phenomenon is called the Jahn-Teller effect (JTE)[28, 57, 58]. JTE is a phenomenon that demonstrates how certain molecular systems, when faced with electronic state degeneracy, undergo geometric modifications to achieve stability. This intrinsic drive towards stabilization leads to unique manifestations in various molecular scenarios which can not be well explained under BO condition.

One example is copper(II) complexes [59], in which the central copper ion exhibits a d^9 electronic configuration. The degenerate e_g orbitals can be stabilized by elongating along one axis and compressing along the other, leading to a characteristic tetragonal distortion. This effect can be observed in many copper(II) complexes, such as $[Cu(H_2O)_6]^{2+}$ in aqueous solutions [60]. The Jahn-Teller distortion in these complexes leads to two longer and four shorter Cu-O bond lengths.

Contrastingly, the pseudo Jahn-Teller (pJT) effect strays from traditional Jahn-Teller

dynamics. Instead of inducing geometric alterations, it achieves stability by reallocating electrons among non-degenerate molecular orbitals. An example for illustration is benzene cation $C_6H_6^+$, where the D_{6h} symmetric cation undergoes distortion to a D_6 geometry due to electronic redistributions[61]. Molecule $CaOCH_3$ is also observed to have pJT coupling in between the vibrational ground and bending modes of the $\tilde{A}^2\Pi$ state, which are both doubly-degenerate[62].

The Renner-Teller effect embodies the complex interaction between electronic states and vibrational motions in linear molecules. The doubly-degenerate electronic levels in the linear molecule such as Π and Δ states are split into to two sub-levels by the Renner-Teller effect, and the ro-vibrational levels are therefore affected by some Coriolis terms. This intertwined relationship results in merged vibrational and electronic wavefunctions, causing notable shifts in vibrational energy levels and consequent alterations in spectroscopic characteristics. CO_2 in its excited states, for example, demonstrate the Renner-Teller effect[63]. The $\tilde{A}^2\Pi$ state of CaOH is another example where the Renner-Teller effect causes a mixing of vibrational and electronic states, affecting its spectroscopic properties[64, 65].

2.9 Dipole transition

To understand the molecular structure introduced in the previous few sections, it is critical to figure out the initial and final states of the transitions from the spectra. Following the convention in atomic spectroscopy, these transitions are generally described by specifying the quantum numbers of the upper and lower states, though the complexity in molecular structure such as broken symmetry in the asymmetric top molecules can make these quantization properties be merely nominal. Besides, in molecular spectroscopy study, not only the quantum properties of the initial and final states but also a number of other factors can affect the line intensity. These factors include transition moment, radiative lifetime, transition probabilities, degeneracy and population of the initial states, and so on. Though multiple factors has to be involved, for a straight-forward understanding of the molecule, this section will only focus on the vibrational and rotational transitions between ground and excited

molecular states. We will leave the discussion of other factors affecting the line intensity measured in experiment according to the needs of the projects in the following few chapters.

2.9.1 Vibrational transition, Franck-Condon Factor and vibrational branching ratio

The amplitude of the vibrational transition between ground and excited electronic states of a molecule can be described by

$$A_{e,\nu';g,\nu''} = \langle e, \nu' | \boldsymbol{E} \cdot \boldsymbol{\mu} | g, \nu'' \rangle, \tag{2.38}$$

where dipole transition moment is denoted as $\boldsymbol{\mu}$. The transition probability is proportional to $|A_{e,\nu';g,\nu''}|^2$. For the lowest order of approximation, if we assume that the dipole moment does not changed as the vibrational states, the transition probability is then proportional to the square of the overlapping of the vibrational function, i.e., the Franck-Condon Factor (FCF):

$$q_{e,\nu';g,\nu''} = |\langle e, \nu' | g, \nu'' \rangle|^2. \tag{2.39}$$

The FCFs determine the relative intensities of vibrational lines within one electronic transition and can be computed explicitly in the harmonic approximation. On the other hand, in experiment, the concept of vibrational branching ratios(VBRs), defined as

$$b_{e,\nu';g,\nu''} = \frac{q_{e,\nu';g,\nu''}\omega^3_{e,\nu';g,\nu''}}{\sum_{\nu''} q_{e,\nu';g,\nu''}\omega^3_{e,\nu';g,\nu''}} = \frac{I_{e,\nu';g,\nu''}}{\sum_{\nu''} I_{e,\nu';g,\nu''}}, \tag{2.40}$$

is more frequently used (the ω^3 is due to the frequency dependence of the transition dipole) because the VBR of line $|e, \nu'\rangle \rightarrow |g, \nu''\rangle$ can be directly measured by calculating the intensity ratio of the line versus the sum of all observed lines.

2.9.2 Dipole transition with rotation

Unlike atomic cases, molecule has rotational degree freedom and thus the dipole transition in molecule can happen with initial and final rotational states being different. The dipole transition amplitude, with dipole transition moment denoted as $\boldsymbol{\mu}$, between the initial and final electronic states of a rotor can be described by $A_{iJ_i\Omega_iM_i,fJ_f\Omega_fM_f} = \langle f, J_f, \Omega_f M_f|\boldsymbol{E}\cdot\boldsymbol{\mu}|i, J_i, \Omega_i, M_i\rangle$, where $\boldsymbol{E} = E_0\hat{\epsilon}_z$ is the electric field in z axis of space-fixed coordinate, J_s is the angular momentum, Ω_s and M_s are the projection quantum numbers in molecule- and space-fixed coordinates, respectively. To unravel the rotational transition from the electronic transition amplitude, it is convenient to express the transition in terms of spherical tensors, i.e., $\boldsymbol{E}\cdot\boldsymbol{\mu} = -E_0T^1_{p=0}(\boldsymbol{\mu})$. Then we have

$$A_{iJ_i\Omega_iM_i,fJ_f\Omega_fM_f} = -E_0\langle f, J_f, \Omega_f M_f|T^1_{p=0}(\boldsymbol{\mu})|i, J_i, \Omega_i, M_i\rangle. \tag{2.41}$$

As the permanent electric dipole moment lies along the axes in the molecule-fixed coordinates, we have to rotate the space-fixed component $T^1_{p=0}(\boldsymbol{\mu})$ to the molecular axis system (denoted with subscript q), i.e.,

$$T^1_{p=0}(\boldsymbol{\mu}) = \sum_q \mathfrak{D}^{(1)}_{pq}(\omega)^* T^1_q(\boldsymbol{\mu}) = \sum_q \mathfrak{D}^{(1)}_{0q}(\omega)^* T^1_q(\boldsymbol{\mu}). \tag{2.42}$$

Here $\mathfrak{D}^{(1)}_{pq}(\omega)^*$ is the pq component of the rank-1 rotation matrix $\mathfrak{D}^{(1)}$ with ω denoting the angles of the rotation. With the coordinate conversion, the matrix elements in Eq.(2.41) can be written as

$$\begin{aligned}
&\langle f, J_f, \Omega_f M_f|T^1_{p=0}(\boldsymbol{\mu})|i, J_i, \Omega_i, M_i\rangle \\
=&\sum_{q=-1}^{1}\langle f, J_f, \Omega_f M_f|\mathfrak{D}^{(1)}_{0q}(\omega)^* T^1_q(\boldsymbol{\mu})|i, J_i, \Omega_i, M_i\rangle \\
=&\sum_{q=-1}^{1}\langle f|T^1_q(\boldsymbol{\mu})|i\rangle\langle J_f, \Omega_f, M_f|\mathfrak{D}^{(1)}_{0q}(\omega)^*|J_i, \Omega_i, M_i\rangle.
\end{aligned} \tag{2.43}$$

Here, we can see that the transition matrix element contain two parts: $\langle f|T^1_q(\boldsymbol{\mu})|i\rangle$ is corresponding to the electric dipole transition amplitude and independent from the rotational transition, while the second part $\langle J_f, \Omega_f, M_f|\mathfrak{D}^{(1)}_{0q}(\omega)^*|J_i, \Omega_i, M_i\rangle$ is the pure rotational transition. The rotational transition matrix element can be calculated as follows:

$$\begin{aligned}&\langle J_f, \Omega_f, M_f|\mathfrak{D}^{(1)}_{0q}(\omega)^*|J_i, \Omega_i, M_i\rangle \\ =&(-1)^{J_f-M_f+J_i-M_i}\sqrt{(2J_f+1)(2J_i+1)}\begin{pmatrix} J_f & 1 & J_i \\ -M_f & 0 & M_i\end{pmatrix}\begin{pmatrix} J_f & 1 & J_i \\ -\Omega_f & q & \Omega_i\end{pmatrix}.\end{aligned} \tag{2.44}$$

This expression gives the selection rules immediately: the 3-j symbols are non-zero if $J_f = J_i, J_i \pm 1$ and $\Delta\Omega = \Omega_f - \Omega_i = q$. This also indicates that the change of the rotational projection quantum number during the transition is subjected to the orientation of the electric transition dipole moment of the molecule.

2.10 Optical cycling

In this section, we will focus on the optical cycling in molecules, including the closures in electronic, vibrational and rotational transitions. There are a few ways for effective optical cycling in molecules, such as reducing off-diagonal branching ratios or adding more repumping lasers. The off-diagonal branching ratios can be suppressed by substituting with different functional groups on the molecule[33], and additional repumpers can drive any molecules that have decayed into non-resonant states back into the cycling transition, thereby maintaining the cycling process.

Applications of optical cycling in molecules are vast. For example, by exploiting the momentum transfer during photon absorption and emission, optical cycling can be utilized to cool molecules to ultra-cold temperatures[14, 66, 67]. It also allows for the enhancement of molecular fluorescence signals, enabling precision spectroscopic measurements such as searching for CP violation in molecule[68] and electron electric dipole moment (eEDM) measurement[69, 70].

In general, it is not realistic to have a perfect cycling closure in molecule, and the population on dark states (the loss of population) grows as the molecules are being pumped to the excited state over and over again. Therefore, cycling in molecules is usually considered as "quasi-cycling". Here we will discuss these closures and the strategies of how to minimize the loss in the cycling.

2.10.1 Electronic closure

Molecules have multiple electronic levels on which optical cycling transitions can be addressed. However, the selection rules for electronic transitions may be devoid if the molecule has low or no symmetry, which can be an issue for laser cooling.

Here we may start with the discussion of how the selection rules of electronic transitions vary due to the symmetry. For simplicity, the nuclear spin $\boldsymbol{I}$ is ignored and only dipole transitions are considered here. Due to the spherical symmetry of the atoms, their electronic wavefunctions also follow the spherical symmetry, and the electric spin $\boldsymbol{S}$, orbital angular momentum $\boldsymbol{L}$ and total angular momentum $\boldsymbol{J} = \boldsymbol{L} + \boldsymbol{S}$ are good quantum numbers. The selection rules for atoms are then given by:

- $\Delta J = 0$ or ± 1; $\Delta J = 0$ is forbidden when $J = 0$;
- $\Delta M_J = 0$ or ± 1; $\Delta M_J = 0$ is forbidden when $\Delta J = 0$.

For molecules, as the electronic wavefunctions follow the molecular symmetry, the transition rules are subject to the symmetry of initial and final states. C_{2v} and C_s molecules, for example, do not have specific electronic transition rule regarding to the symmetry of the electronic states, and only have some general rotational transition rules such as $\Delta J = 0$ or ± 1.

Without the selection rules, the number of potential decay paths from a given excited state increases similarly as the number of the levels below it. As a result, if molecular structure has lower symmetry, the cycling with higher excitation levels can lead to some further issues. For example, these levels can decay to the ground state via multiple transitions, while

the undesired rotational transition accompanied with the additional electronic decays can affect the rotational cycling efficiency. Consequently, here we mainly consider the lowest few excited levels for optical cycling to avoid the undesired decays.

2.10.2 Vibrational closure

Given that the number of the vibrational modes grows as the number of the nuclei in molecule increases, it is not realistic to repump all the population in the vibrational dark states of the electronic ground state in large molecule. Therefore, to cool the molecules as efficient as possible, it is reasonable to address the repumping transitions on the ones with the most off-diagonal vibrational branching ratios.

Here we denote p as the sum of the branching ratios of the vibrational levels being addressed. The probability of decaying to dark states is $1-p$, and the average number of photons scattered by molecules in the absorption-emission cycles is $\bar{n} = 1+p+p^2+\cdots = \frac{1}{1-p}$. In general, the laser cooling requires $\bar{n} \approx 10^2 - 10^5$, hence $1-p \approx 10^{-2} - 10^{-5}$. This indicates that the efficiency of vibrational repumping is depending on the vibrational branch ratios as well as the number of the repumpers is used.

2.10.3 Rotational closure

To cool molecule without loss in rotational cycling, each vibrational repumping transition is resonant to the corresponding rotational cooling transition $|g, v'', N''=1\rangle \rightarrow |e, v'=0, N'=0\rangle$. For different molecules and transitions, the choice of the substates for the rotational cycling varies.

Diatomic molecules, for example, have P, Q, and R branches in the rotational spectra, which are corresponding to the transition of $\Delta N = N' - N'' = -1, 0$ and 1, respectively. The rotational cycling transition of diatomic molecule is denoted as P_1 transition, where the subscript indicate the N'' value. However, for some special cases such as $\Sigma \leftarrow \Sigma$ transition, the Q branch is missing due to the selection rule about parity.

Contrastingly, in asymmetric top molecules, rotational levels of $N \neq 0$ states are generally not degenerate. The rotational states in asymmetric top molecule are denoted with $N_{K_a K_c}$, where K_a and K_c are the projection quantum number of the rotational angular momentum $\boldsymbol{N}$ onto the principle axis in prolate and oblate rotor approximation, respectively.

The rotational transition of asymmetric top molecule is relative to the symmetry of the initial and final electronic states. The corresponding selection rules in the dipole approximation are listed in the following table[13]:

	ΔK_a	ΔK_c	Additional rules
a-type	0	± 1	$\Delta N \neq 0$ if $K'_a = K''_a = 0$
b-type	± 1	± 1	
c-type	± 1	0	$\Delta N \neq 0$ if $K'_c = K''_c = 0$

Table 2.2: Selection rules of rotational transitions of the asymmetric top molecule

Here the type of the transition is subject to the orientation of the transition dipole moment. An example for illustration is SrOPh, which is an asymmetric top molecule with ground state $\tilde{X}^2A_1$ and the lowest excited state $\tilde{A}^2B_2$. Because the transition dipole moment is lying along the axis in the molecular plane and perpendicular to the Sr-O bonding (denoted as axis b in the Chap.5), only *b-type* transitions are allowed. As a result, the rotational cooling transition is $|\tilde{X}^2A_1, 1_{11}\rangle \leftrightarrow |\tilde{A}^2B_2, 0_{00}\rangle$. Some further discussion on the rotation cycling transition can be found in Chap. 5.

CHAPTER 3

Laser spectroscopy of diatomic molecular ion $^{28}Si^{16}O^+$ and $^{29}Si^{16}O^+$

Laser cooling and trapping of atoms have been successfully and widely applied in many fields such as quantum information science [71], atomic clocks[5, 72], and probes of fundamental physics. Molecules, possessing richer internal structures than the atoms, have great potential to be laser cooled as well [73, 74] and thus can provide new capabilities in a wide range of fields, including new platforms for quantum simulation and computation [26, 75], tests of fundamental physics [24, 76], and ultracold chemistry and collisions [77, 78].

In 2004, Di Rosa [79] proposed that for direct laser cooling of a molecule, it is essential for the molecule to possess diagonal Franck-Condon factors (FCFs). Molecules with these properties suppress spontaneous decays involving vibrational transitions. This characteristic facilitates closed optical cycling, allowing for the repeated and spontaneous scattering of many photons post-optical excitation. Adhering to these criteria, several molecules, including SrF[14], CaF[80, 81], YbF[22], YO[82], SrOH[17], CaOH[83], YbOH[24], and $CaOCH_3$[18], have been demonstrated to be amenable to laser cooling.

Several molecular ions, including SiO^+ [84, 85], BH^+ [86, 87], AlH^+ [88], and $AlCl^+$ [89], have also gained interest for their potential in laser cooling. In addition to these, computational studies have identified BO^+, PN^+, and YF^+ as potential candidates due to their highly diagonal FCFs [90]. Currently, $^{28}Si^{16}O^+$ is found to be a particularly promising candidate, with research spearheaded by the Odom group [86]. The diagonal branching ratios of the $B^2\Sigma^+ \rightarrow X^2\Sigma^+$ transition were determined via dispersed laser-induced fluorescence (LIF) of a supersonic $^{28}Si^{16}O^+$ beam, resulting in a value of $0.970^{+0.007}_{-0.025}$[91]. Additionally,

rotational cooling of $^{28}Si^{16}O^+$ has been achieved through techniques such as driving the P-branch rotational transitions with a broadband laser[92] and optically pumping trapped $^{28}Si^{16}O^+$ to a super-rotor state.

The electronic structure and spectroscopic attributes of SiO^+ have been thoroughly studied over the years. Pankhurst initially observed a SiO^+ band around 3840 Å in 1940 using a heavy-current hydrogen discharge tube with a quartz constriction [93]. However, it was mistakenly attributed to SiO_2. It wasn't until 1943 that Woods correctly identified this band as the $B^2\Sigma^+ - X^2\Sigma^+$ transition of SiO^+ [94]. Ghosh et al. provided further confirmation in 1979 when they examined the isotope shift measurements of $^{28}Si^{16}O^+$ and $^{28}Si^{18}O^+$ [95], determining molecular constants for both isotopes. Colbourn and his team later estimated the spectroscopic constants of three ionic states of $^{28}Si^{16}O^+$ ($X^2\Sigma^+$, $A^2\Pi$, and $B^2\Sigma^+$) using vacuum UV photoelectron spectroscopy of SiO ($X^1\Sigma^+$) [96]. Subsequent studies by Rosner and colleagues examined high-resolution bands of $A^2\Pi - X^2\Sigma^+$ and $B^2\Sigma^+ - X^2\Sigma^+$ transitions of $^{28}Si^{16}O^+$ through LIF investigations of mass-selected fast ion beams [97–100]. Their analysis, which involved fitting the accumulated data with a Hamiltonian model, yielded highly precise rotational and fine-structure constants for all three states. Alongside these experimental undertakings, several theoretical calculations have delved into the potential energy curves and spectroscopic constants of SiO^+ low-lying electronic states[101–109].

As we consider the prospective applications of SiO^+, an immediate question arises: how can this molecular ion be utilized in quantum information? Typically, the proposal is to embed quantum information within the rotational degrees of freedom of polar molecules. However, when molecular ions are maintained in an ion trap, their thermal motions can result in rotational decoherence. This is primarily due to the Stark shift influenced by the trap's electric fields and other ion monopoles [110]. One could consider housing a qubit within the ground-state Zeeman structure to mitigate Stark-induced decoherence, yet this approach becomes complex given the necessity for magnetic field control [110, 111]. A promising alternative is to employ an isotopologue of $^{28}Si^{16}O^+$ possessing a non-zero hyperfine structure to craft a hyperfine qubit. Conveniently, the naturally occurring isotope ^{29}Si exhibits a

nuclear spin of $I = 1/2$. This gives rise to a ground state marked by total angular momenta of $F = 0$ and $F = 1$. This particular structure introduces a zero-field clock-state qubit in its dual $M = 0$ Zeeman sublevels. In the realm of atomic ion quantum computing, this has demonstrated appealing resistance to decoherence [112, 113]. Furthermore, it offers a frequency-resolved qubit state ($|F = 0\rangle$), which can be prepared and detected via frequency-selective optical pumping.

While $^{29}Si^{16}O^+$ will share the diagonal FCFs of $^{28}Si^{16}O^+$, to the best of our knowledge there has not yet been a spectroscopic study of gas-phase $^{29}Si^{16}O^+$. In this chapter, we focus on the measurement of the spectra of $^{28}Si^{16}O^+$ and $^{29}Si^{16}O^+$ and the quantum logic on $^{29}Si^{16}O^+$. In Sec. 3.1, we introduce the Hamiltonian of the molecular ions, including vibrational, rotational and hyperfine terms. The experiment part, including the production of ions, experimental setup and procedure of measurement, is introduced in Sec. 3.2 and 3.3. The dispersed spectra and high-resolution scan data are shown in Sec. 3.4 and 3.5, respectively, with some discussion about the spectroscopic patterns. Sec. 3.6 introduces the lifetime measurement of the $B^2\Sigma^+$ state of $^{28}Si^{16}O^+$ and $^{29}Si^{16}O^+$. Sec. 3.7 estimates the uncertainties of the measurement and curve fitting, and the discussion about the potential of $^{29}Si^{16}O^+$ in quantum computation can be found in Sec. 3.8.

3.1 Molecular Hamiltonian

Here we start with the level structure of the SiO^+ ion. The potential curves of the ground state $X^2\Sigma^+$ and the two lowest excited levels $A^2\Pi$ and $B^2\Sigma^+$ are plotted in Figure. 3.1, which is produced by the fitting the Morse potential with the calculated D_e and ω_e values in Ref. [85]. The crossing in the $X^2\Sigma^+$ and $A^2\Pi$ curves has some mixing effects in the ro-vibrational states and therefore leads to significant shifts in highly rotational states ($N > 40$) [100]. In this work, however, as the molecular ions are studied at $T \approx 100$K instead of room temperature in previous works[95, 100], the population in highly rotational states is suppressed and therefore the vibrational, rotational and hyperfine Hamiltonians introduced in Chap. 2 can fit the data well. We will introduce these Hamiltonians in the rest of this

section.

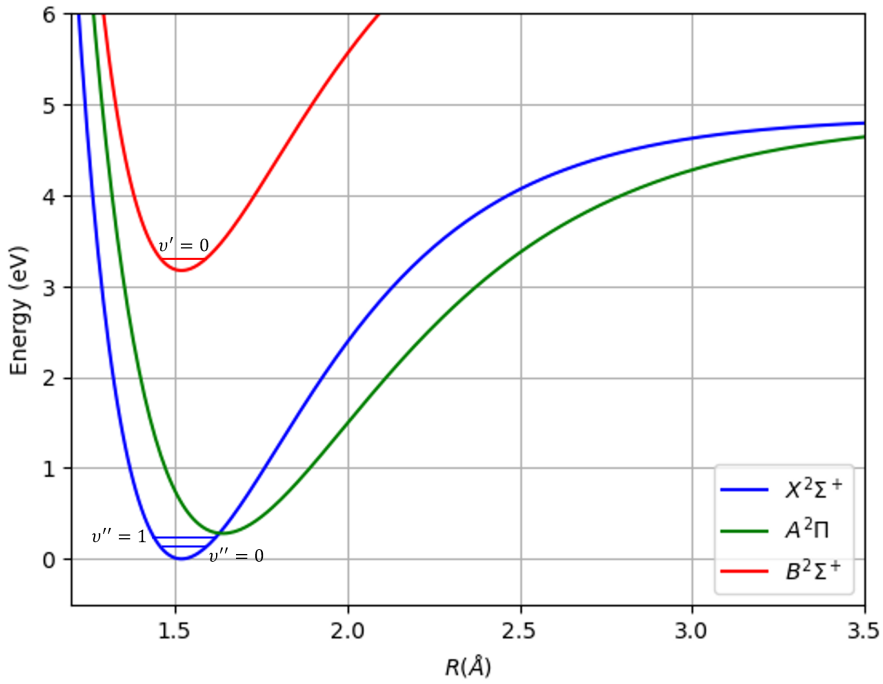

Figure 3.1: Schematic illustration of SiO^+ diabatic potential curves of the $X^2\Sigma^+$, $A^2\Pi$ and $B^2\Sigma^+$ states.

3.1.1 Vibrational Hamiltonian

The energy of electronic state is conventionally denoted as T_e, and the vibrational Hamiltonian is

$$H_{vib}/h = \omega_e \left(v + \frac{1}{2}\right) - \omega_e x_e \left(v + \frac{1}{2}\right)^2, \tag{3.1}$$

where ω_e and $\omega_e x_e$ are vibrational constants, and v is the vibrational quantum number. The vibronic part of the Hamiltonian can then be rearranged as:

$$H_{el}/h + H_{vib}/h = T_0 + [\omega_e - \omega_e x_e (v+1)]v, \tag{3.2}$$

where the electronic energy T_e and the vibrational ground state energy are absorbed into T_0.

3.1.2 Rotational and hyperfine Hamiltonian

The rotational Hamiltonian reads

$$H_{rot}/h = B_v \boldsymbol{N}^2 - D_v \boldsymbol{N}^4 + \gamma T^1(\boldsymbol{N}) \cdot T^1(\boldsymbol{S}), \tag{3.3}$$

where $\boldsymbol{N}$ is the rotational angular momentum of the molecule about its center of mass, $\boldsymbol{S}$ is the electron spin, B_v and D_v are molecular rotational constants of vibrational state $|v\rangle$, and γ is the spin-rotation coupling constant. Here all rotational constants include the contribution from rotation-vibration coupling. The third term in Eq. (5.10) is the electron spin-rotation interaction, represented as the scalar product of two spherical tensors, defined via $T^k(\boldsymbol{A}) \cdot T^k(\boldsymbol{B}) \equiv \sum_p (-1)^p T^k_p(\boldsymbol{A}) T^k_{-p}(\boldsymbol{B})$. The hyperfine Hamiltonian, nonzero for $^{29}Si^{16}O^+$, is

$$H_{hfs}/h = b_F T^1(\boldsymbol{I}) \cdot T^1(\boldsymbol{S}) + \sqrt{6} g_S \mu_B g_N \mu_N (\mu_0/4\pi) T^2(\boldsymbol{S}, \boldsymbol{I}) \cdot T^2(\boldsymbol{C}), \tag{3.4}$$

where T^2 indicates a spherical tensor of rank-2, $T^2(\boldsymbol{C})$ represents a normalized spherical harmonic, $T^2(\boldsymbol{S}, \boldsymbol{I})$ describes the dipolar coupling between spins, and the rest of symbols have their standard meanings [31]. For simplicity, here we only summarize the expressions of the matrix elements for $^{29}Si^{16}O^+$ in the following table. The details about the derivation of these matrix elements can be found in Appendix.A.

	$G' = 1,$ $F' = N+1$	$G' = 1,$ $F' = N$	$G' = 0,$ $F' = N$	$G' = 1,$ $F' = N-1$
$G = 1,$ $F = N+1$	$\frac{\gamma N}{2} + \frac{b_F}{4} - \frac{Nt}{4N+6}$	0	0	0
$G = 1,$ $F = N$	0	$\frac{\gamma N}{2} + \frac{b_F}{4} + \frac{t}{2}$	$\frac{\gamma}{2}\sqrt{N(N+1)}$	0
$G = 0,$ $F = N$	0	$\frac{\gamma}{2}\sqrt{N(N+1)}$	$-\frac{3b_F}{4}$	0
$G = 1,$ $F = N-1$	0	0	0	$-\frac{\gamma(N+1)}{2} + \frac{b_F}{4} - \frac{(N+1)t}{4N-2}$

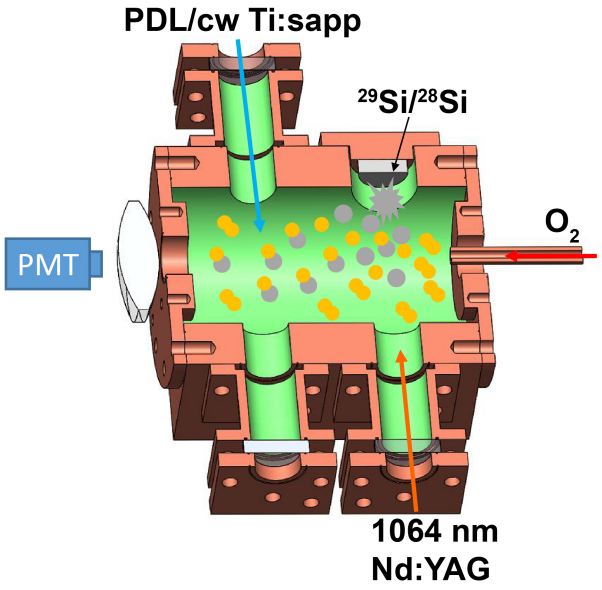

Figure 3.2: Schematic of the cryogenic cell showing the production of SiO^+ and LIF measurement setup.

3.2 Production of SiO^+

In this experiment, SiO^+ ions were produced by direct reaction of Si^+ and O_2 in a cryogenic cell at a temperature $\approx$ 90 K, as schematically shown in Figure 1. Si^+ ions were generated by ablating a Si target using a pulsed Nd:YAG laser at 1064 nm, focused onto the target with a spot size of $\approx$ 1 mm and a pulse energy of $\approx$ 5 mJ. A silicon wafer (Sigma Aldrich, natural isotopic abundance) was used to produce $^{28}Si^+$ and pressed target of ^{29}Si metalloid powder (Buyisotope, isotopic enrichment >99.2%) was used for $^{29}Si^+$. The produced Si^+ ions then reacted with ultrahigh purity O_2 gas (Praxair, 99.993%), which was introduced into the cell at a flow rate $\approx$ 7 standard cubic centimeter per minute (sccm) resulting in a gas density $\approx 10^{15} - 10^{16}$ cm^{-3}, to form SiO^+ ions.

3.3 Measurement procedure

The $^{28}Si^{16}O^+$ ions were first probed at 368 nm and 384 nm, generated by frequency doubling a pulsed dye laser with LDS 751 laser dye (LiopStar-E dye laser, linewidth 0.04 cm^{-1} at

620 nm), to cover the (0,0) and (1,0) bands of the $B^2\Sigma^+ \leftarrow X^2\Sigma^+$ transition, respectively. To avoid scattered light from the ablation plume, the dye laser illuminated the ions roughly 120 μs after the ablation pulse. A Coherent WaveMaster was used to calibrate the absolute wavelength of the dye laser. The resulting fluorescence photons were imaged onto a photomultiplier tube (PMT) via a lens system and counted (Stanford Research Systems, SR430). Both bands were scanned with a step size of 2 GHz near resonance and 4 GHz away from resonance. Each data is the sum of 500 laser pulses at a 10 Hz repetition rate and repeated between two and four times.

Following the dye laser survey spectroscopy, higher resolution spectroscopy was performed on the (0,0) bands of $^{28}Si^{16}O^+$ and $^{29}Si^{16}O^+$ using a doubled, continuous wave Ti:sapphire laser (M Squared Lasers). This laser has an effective linewidth on the order of 10 MHz and was scanned with a step size between 50 MHz and 200 MHz. The laser frequencies were measured and recorded using a High Finesse WS-U wavemeter. The resulting LIF photons were counted over a 5 μs window that was delayed by 120 μs from the ablation pulse and averaged for 300 ablation pulses. Each measurement was repeated between two and four times.

3.4 Dispersed laser-induced spectra

While the main purpose of the pulsed dye laser experiment was to inform the subsequent higher-resolution measurement, analysis of the recorded data provided several useful results. Figure. 3.3 shows the LIF spectra of $^{28}Si^{16}O^+$ along with a least-squares fitting of a Voigt profile to each rotational line, in which the Gaussian and Lorentzian contributions are estimated to be within the ranges of $0.5 - 0.8$ GHz (mostly corresponding to the Doppler broadening) and $3.0 - 6.0$ GHz (mainly corresponding to the laser linewidth), respectively. First, the measurements of the (0,0) and (1,0) bands in $^{28}Si^{16}O^+$ provide a straightforward measurement of the separation of the first two vibrational states of the $B^2\Sigma^+$ vibrational as $\omega_e^B - 2\omega_e x_e^B = 33657.29(13)$ GHz.

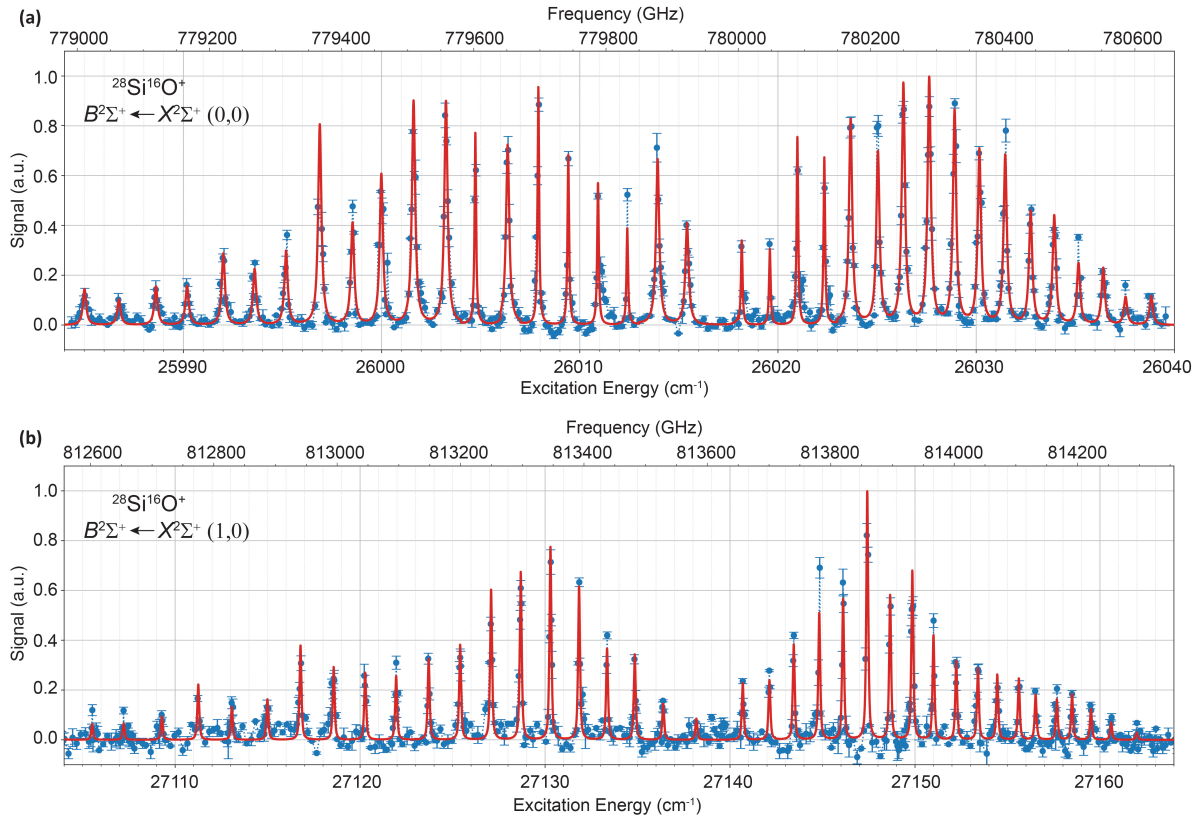

Figure 3.3: The experimental LIF data (blue dots) obtained with a pulsed dye laser and the Voigt fittings (red curves) of $^{28}Si^{16}O^+$ (a) (0,0) band and (b) (1,0) band of the $B^2\Sigma^+ \leftarrow X^2\Sigma^+$ transition.

3.5 High resolution spectra

The higher resolution scans required significantly more time, roughly half of a day per rotational line, and resulted in two changes to the experiment. First, the cryogenic cell temperature was raised to approximately 100 K to prevent O_2 ice from forming over the course of longer runs. And second, long-term drifts in the ion signal, presumably due to changes in the ablation conditions, led to variations of the LIF amplitude from one rotational line to the next, preventing extraction of the molecular rotational temperature. As a result, in our fitting, we fix the relative strengths of the spin-rotational and hyperfine transitions *within* a single rotational transition according to their respective transition moments, and allow a single fitted amplitude for each rotational transition. In this manner, custom software was created that diagonalizes the relevant Hamiltonians, calculates the individual transition

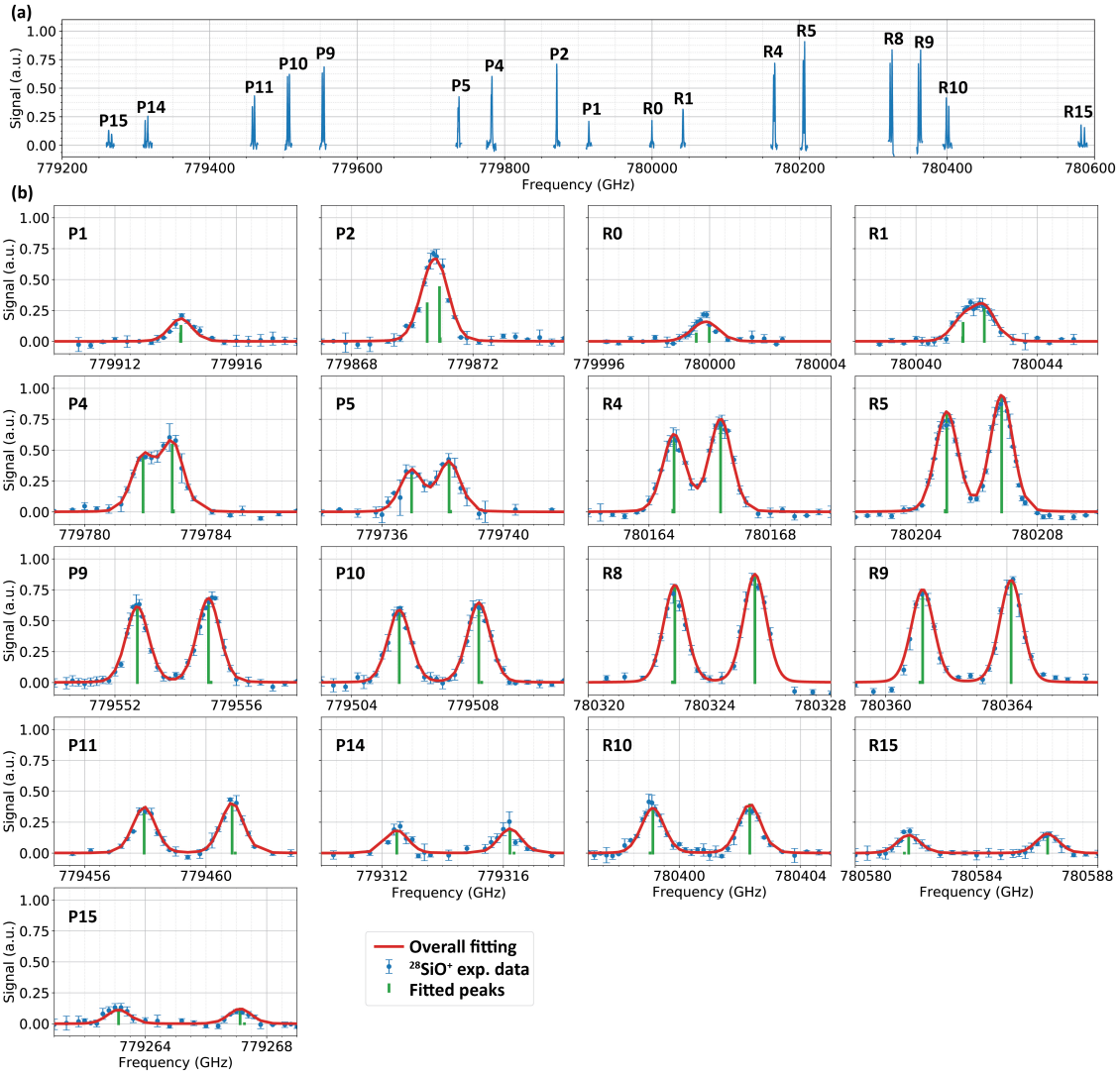

Figure 3.4: High-resolution LIF spectra of $B^2\Sigma^+ \leftarrow X^2\Sigma^+$ (0,0) band of $^{28}Si^{16}O^+$. (a) The overall spectrum of seventeen observed rotational lines, including nine P-branch and eight R-branch rotational lines (b) Seventeen spectra of single rotational lines and the corresponding fittings. The observed rotational lines are plotted by blue dots with error bars. The backgrounds are subtracted and the signal strengths are normalized to unity, which corresponds to the maximum signal strength detected in the experiment. The red curves are the overall fittings and the green lines indicate the positions of the rotational transitions, which are calculated by substituting the fitted molecular constants into the theoretical model. The relative strengths of the peaks in each rotational line are calculated from the square of the transition dipole moment between the ground and excited states.

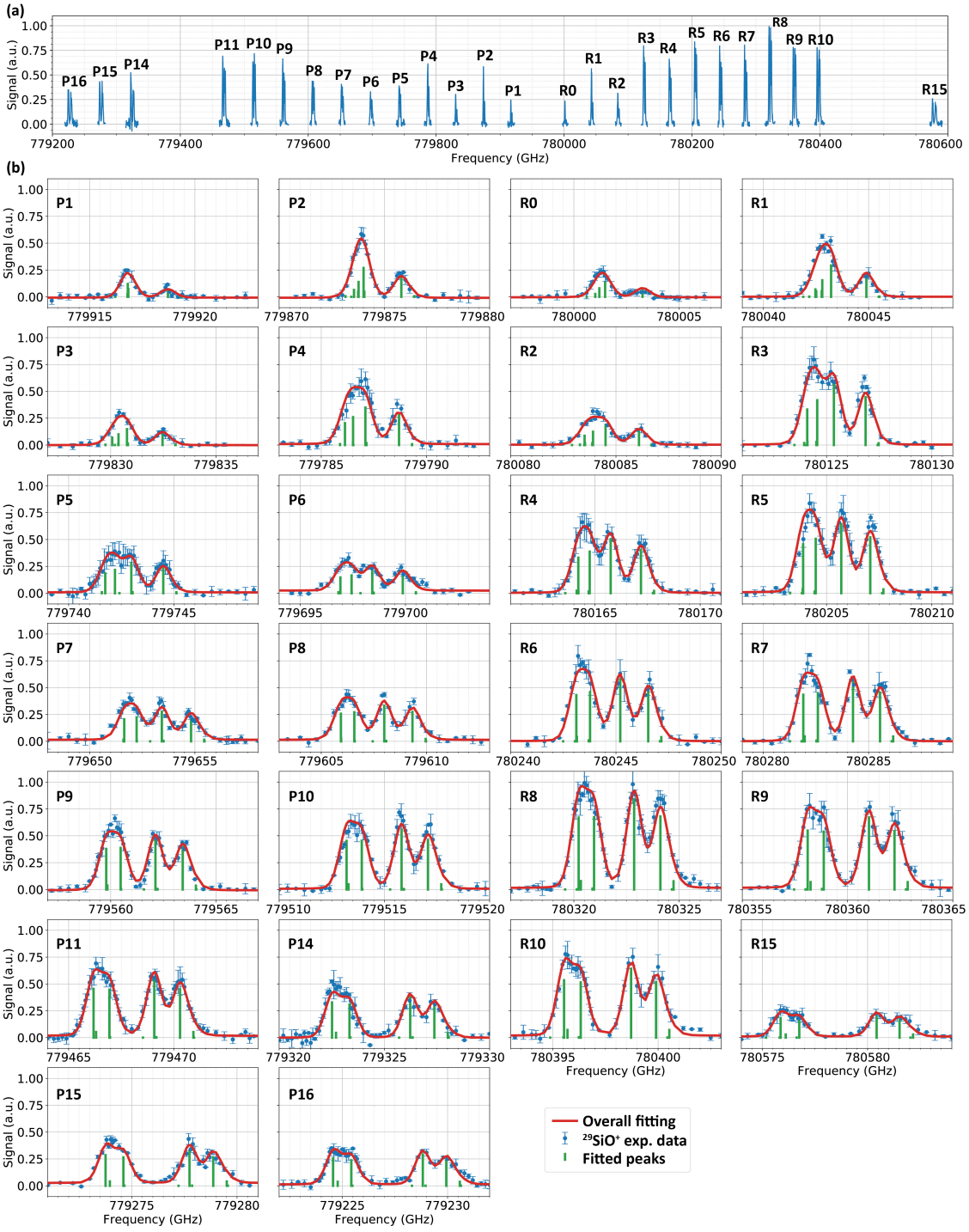

Figure 3.5: High-resolution LIF spectra of $B^2\Sigma^+ \leftarrow X^2\Sigma^+$ (0,0) band of $^{29}Si^{16}O^+$. (a) The overall spectrum of twenty-six observed rotational lines, including fourteen P-branch and twelve R-branch lines. (b) Twenty-six spectra of single rotational transitions and the respective fits.

strengths between states, convolves those transition lines with a Gaussian lineshape of full width at half maximum (FWHM) of 840 MHz, which is consistent with the expected Doppler broadening of ≈ 800 MHz,and fits to the data by minimizing χ^2 with a gradient descent algorithm. Once the best fit values were found, 68% confidence intervals were found for each fitted parameter using the profiling method [114].

Parameters	$^{28}Si^{16}O^+$			$^{29}Si^{16}O^+$	
	PDL	CW	Ref.	CW	Ref.
T_0^B	779962.32(5)	779957.19(8)	779948.27(6)[a]	779959.78(11)	
			779957.30(12)[b]		
$\omega_e^B - 2\omega_e x_e^B$	33657.29(13)		33659.32(10)[a]		
B_0^X	21.513(4)[c]	21.5137(9)	21.51341(30)[a]	21.2435(12)	21.2447(9)[f]
	21.555(4)[d]		21.5137(21)[b]		
B_0^B	21.279(4)	21.2897(9)	21.28796(30)[a]	21.0217(12)	21.0236(9)[f]
			21.2901(21)[b]		
α_e^B	0.123(5)		0.174139(14)[a]		
D_0^X		$3.3(7) \times 10^{-5}$	$3.223(9) \times 10^{-5}$ [a]	$3.2(7) \times 10^{-5}$	$3.2(7) \times 10^{-5}$ [f]
			$3.27(6) \times 10^{-5}$ [b]		
D_0^B		$3.5(7) \times 10^{-5}$	$3.292(6) \times 10^{-5}$ [a]	$3.2(8) \times 10^{-5}$	$3.4(7) \times 10^{-5}$ [f]
			$3.32(6) \times 10^{-5}$ [b]		
γ^X		0.009(18)	0.006(25)[e]	0.012(25)	0.009(18)[f]
			0.12(12)[b]		
γ^B		0.286(18)	0.287(24)[e]	0.288(25)	0.279(18)[f]
			0.420(12)[b]		
b_F^X				−0.60(22)	−0.797(1)[g]
b_F^B				−2.49(25)	
t^X				−0.04(30)	−0.064(1)[g]
t^B				0.04(33)	

[a] Ref. [98, 99], from a deperturbation analysis.
[b] Ref. [95].
[c] Our fitted results from $B^2\Sigma^+ \leftarrow X^2\Sigma^+(0,0)$ band.
[d] Our fitted result from $B^2\Sigma^+ \leftarrow X^2\Sigma^+(1,0)$ band.
[e] Extracted from (0,0) band data of Ref. [98, 99].
[f] Predictions by scaling isotope constants of $^{28}Si^{16}O^+$ measured in the CW experiment.
[g] Ref. [115].

Table 3.1: $^{28}Si^{16}O^+$ and $^{29}Si^{16}O^+$ molecular constants (Unit: GHz). PDL denotes constants extracted from the low-resolution pulsed-dye laser measurement, while CW denotes constants extracted from the higher resolution continuous wave laser measurement. The constants in the CW column denote our recommended values.

The resulting fits for $^{28}Si^{16}O^+$ are shown in Figure 3.4. The fits yield χ^2 per degree of freedom (DOF) of $\chi^2/DOF = 0.96$ when assuming the data is Poissonian distributed, indicating a stable, well-behaved experiment and reasonable fit. The fits also appear to satisfactorily reproduce the observed spectra.

Figure 3.5 shows a high-resolution spectra of $^{29}Si^{16}O^+$. The data are fitted in the same way as the $^{28}Si^{16}O^+$ with the addition of the relevant hyperfine Hamiltonians for each state. If the data are assumed to be Poissionian distributed, the best fit value yields a $\chi^2/DOF = 1.34$, which for the current number of degrees of freedom (1366) must be rejected. As the resulting fit reproduces the data reasonably well, we conclude that the data are likely super-Poissonian, presumably due to extra fluctuations introduced by ablation of the pressed ^{29}Si target, and increase the standard deviation in our fits such that the $\chi^2/DOF = 1$. While this procedure does not change the best fit values, it does increase the confidence intervals on the reported parameters. This result means that the experimental data should have a greater standard deviation than our estimation, in which we have assumed the measurement follows the Poisson distribution, i.e., the standard deviation for a measured value n is $\sqrt{n}$.

The extracted molecular constants are shown and compared to previous results in Table 3.1. Comparing to the molecular constants of $^{28}Si^{16}O^+$, the $^{29}Si^{16}O^+$ transition energy T_0^B has an isotope shift of 2.59(14) GHz, which is due to the shifts in T_e and the zero-point energy. Further, the rotational constants are a few percent smaller due to the greater reduced mass. The spin-rotation constants are indistinguishable from those of $^{28}Si^{16}O^+$ at the current experimental resolution. In order to fit the hyperfine constants b_F and t for $^{29}Si^{16}O^+$, we first used the experiment values in Ref.[115], in which the hyperfine constants of the $X^2\Sigma^+$ state were measured in Neon-matrix method, as the initial values of the hyperfine constants of X states in the fitting program, then we repeated the hyperfine constants fitting process multiple times with different initial values assigned to the other molecular constants. This is to ensure that the fitting can reach the global minimum of the total error, and check whether the output is consistent and independent from the input. By using the relative transition strength in the fitting procedure we are able to resolve the Fermi contact parameters for both the X and B states to be $-0.60(22)$ GHz and $-2.49(25)$ GHz, respectively. The larger Fermi contact interaction in the B state is consistent with the molecular orbital description provided in Refs. [91, 105], where the $B^2\Sigma^+ \leftarrow X^2\Sigma^+$ transition involves electron promotion to an orbital with a larger Si contribution. The dipolar hyperfine parameters for both states

are merely constrained by our fit.

While there has been no previous measurement of the hyperfine structure of the $^{29}Si^{16}O^+$ $B^2\Sigma^+$ state to our knowledge, Knight et al. [115] reported measurements of the $X^2\Sigma^+$ state hyperfine parameters in a neon matrix. These values are in agreement with our measured values. A review of the literature to compare hyperfine parameters determined in a neon matrix to those measured in gas phase suggests that the values are typically within a few percent of one another [116]. Therefore, the more accurate values of Knight et al. [115] likely provide the best estimate of the $^{29}Si^{16}O^+$ ground state hyperfine structure. If we fix b_F^X and t^X to the Knight et al. values [115], our estimates of the B state hyperfine parameters become $b_F^B = -2.72(21)$ GHz and $t^B = -0.03(32)$ GHz.

3.6 Lifetime of the $B^2\Sigma^+$ state

The recorded LIF data with pulsed dye laser excitation can also be fitted by an exponential decay function to determine the spontaneous emission lifetime of the excited $B^2\Sigma^+$ state, as shown in Figure 3.6. From this data, we observe the lifetime of $B^2\Sigma^+(v = 0)$ of $^{28}Si^{16}O^+$ to be 67.4(0.8) ns, which is consistent with the previously reported value of 66(2) ns [91], but in tension with the value of 69.5(0.6) ns reported by Ref. [117]. For the first-excited vibrational level $v = 1$ we observe a longer lifetime of 74.5(2.3) ns, which is in good agreement with the previous value of 72.4 (0.5) ns [117]. The longer lifetime of the excited vibrational level is due to a decrease in the transition dipole moment with the increased internuclear distance, as shown in the theoretical calculations [85, 104, 106]. The same lifetime trend is also observed in CO^+, where it is due to the mixing of a low-lying electronic configuration ($...4\sigma^2 1\pi^3 5\sigma^1 2\pi^1$) with the $B^2\Sigma^+$ state configuration of $...4\sigma^1 1\pi^4 5\sigma^2$ with increasing internuclear distance [117, 118]. Finally, the lifetime of $B^2\Sigma^+(v = 0)$ of $^{29}Si^{16}O^+$ is determined to be 67.5(4.1) ns.

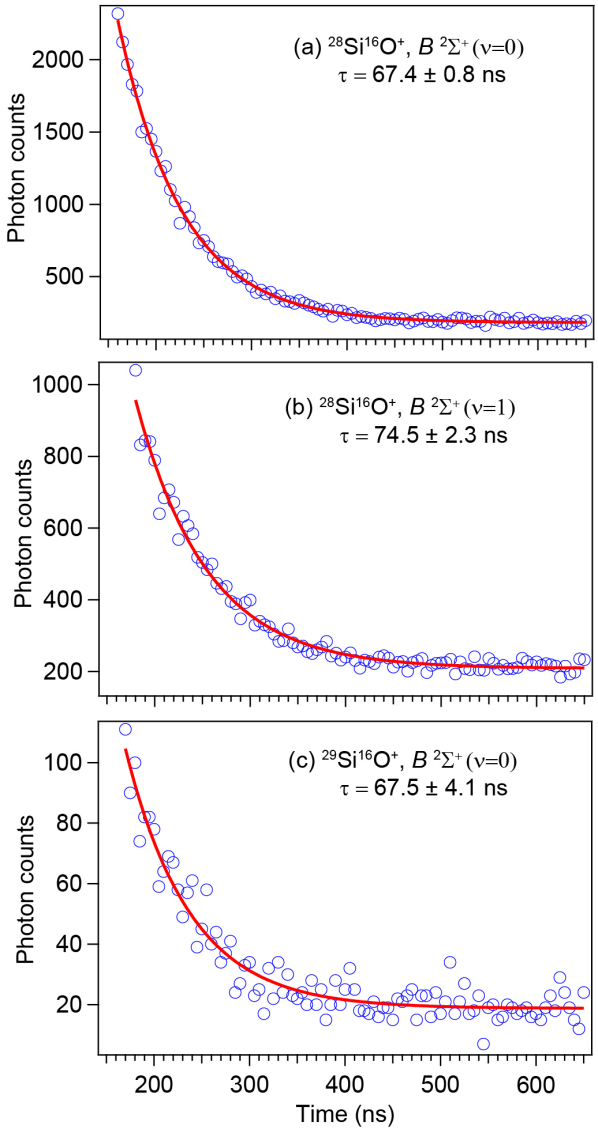

Figure 3.6: Fluorescence decays (blue circles) and exponential fits (red traces) from (a) $^{28}Si^{16}O^+$ $B^2\Sigma^+(v = 0)$, (b) $^{28}Si^{16}O^+$ $B^2\Sigma^+(v = 1)$ and (c) $^{29}Si^{16}O^+$ $B^2\Sigma^+(v = 0)$. The lifetimes are determined to be 67.4 (0.8) ns, 74.5 (2.3) ns and 67.5 (4.1) ns, respectively.

3.7 Error analysis

The transition energy T_0^B, vibrational term $\omega_e^B - 2\omega_e x_e^B$ and the rotational constants are in agreement with the previous results, however, the extracted spin-rotational constants γ^X and γ^B show some deviation from previously reported results. For γ^X, our result agrees with that reported by Ghosh et al. [95]. Cameron et al. [98, 99] and the later work of the same group [100], also reported $\gamma^X = 0.34416(30)$ GHz and 0.41629(129) GHz, respectively. But their values came from a deperturbation analysis that considered the perturbations in the $X^2\Sigma^+$ state from the nearby $A^2\Pi$ state. Thus, their γ^X cannot be directly compared to the one reported here. Therefore, we refitted the low-lying rotational transitions ($N < 40$) of the (0,0) band reported by Cameron et al. [98] with our phenomenological model and found $\gamma^X = 0.006(25)$ GHz, which agrees with our reported value.

Cameron et al. [98, 99] also reported data for $\gamma^B = 0.2986(27)$ GHz. When we refitted their reported low-lying rotational transitions, in the same manner as we did for the X state, we find $\gamma^B = 0.287(24)$ GHz, which is compatible with our result. The small change with refitting is presumably due to the lack of perturbation of the B state in their analysis. The value reported by Ghosh et al. [95] is incompatible with our result, but those workers did not appear to use the relative line strengths as employed here and were therefore sensitive only to $|\gamma^B - \gamma^X|$. This leads to significant covariance in the two spin-rotation parameters and they therefore stated that "the individual [spin-rotation parameters] can not be obtained with any certainty".

The error bars reported here are statistical standard errors. Systematic shifts, which could include, e.g., Zeeman and Stark shifts, non-uniform Doppler shifts, and laser wavelength calibration, are possible. An order of magnitude estimate of the systematic error can be made by the following considerations. Given typical laboratory stray fields, Zeeman and Stark shifts on the order of a few MHz are possible. The ablation process could lead to a non-uniform gas flow and therefore a Doppler shift of the observed lines. Analysis of the residual of a typical lineshape suggests that such a shift is likely < 5 MHz. Finally, the wavemeter reported inaccuracies are ≈ 2 MHz and the laser frequency fluctuation is within

~ 10 MHz. From the covariance matrix resulting from the aforementioned fit, we estimate that fluctuations of this order would likely lead to corrections to B_0, D_0, γ, and b_F of roughly < 50 kHz, < 0.25 kHz, < 0.5 MHz, and < 20 MHz, respectively.

3.8 Rotational cycling and quantum logic with $^{29}SiO^+$

With the presented spectroscopic data, the relevant structure for using $^{29}Si^{16}O^+$ in quantum logic operations is determined and shown in Figure 3.7. Each rotational state in the X and B electronic states is split into two hyperfine states $G = 0$ and 1, and the $G = 1$ state is split into three states with different total angular momentum, F, when $N > 0$.

The presence of $F = 0$ states provides convenient means for qubit state-preparation and measurement. Namely, state preparation can be accomplished by first rotationally cooling the molecule to the $N = 0$ state [92], followed by optical pumping on the weakly-allowed $|B, N = 1, G = 0, F = 1\rangle \leftarrow |X, N = 0, G = 1, F = 1\rangle$ transition, while applying rotational and vibrational repumping. Because $\Delta G \neq 0$ transitions are weak, the $|B, N = 1, G = 0, F = 1\rangle$ state decays to the the $|\downarrow\rangle \equiv |X, N = 0, G = 0, F = 0\rangle$ with 99.994% probability. In this manner, the molecular qubit can be initialized in the $|\downarrow\rangle$ state with high fidelity after a single scattering event. Defining the other state of the qubit as $|\uparrow\rangle \equiv |X, N = 0, F = 1, m_F = 0\rangle$, preparation of an arbitrary qubit state can be realized by driving a microwave M1 or optically stimulated Raman transition resonant on the ≈ 800 MHz hyperfine transition frequency.

Measurement of the qubit state can be accomplished by applying a laser on resonance with the $|B, N = 1, G = 1, F = 0\rangle \leftarrow |X, N = 0, G = 1, F = 1\rangle$ transition, while applying the appropriate vibrational and rotational repumping. Because spontaneous emission between two $F = 0$ levels is strictly forbidden by angular momentum conservation, this will lead to scattering of photons only if the qubit is found in $|\uparrow\rangle$. Detecting any resulting fluorescence, thus allows the determination of the qubit state. Alternatively, state detection could also be performed by using laserless electric field gradient gates and monitoring a co-trapped atomic ion [119], or pumping the $|\uparrow\rangle$ state to the $|B, N = 0, G = 1, F = 1\rangle$ state

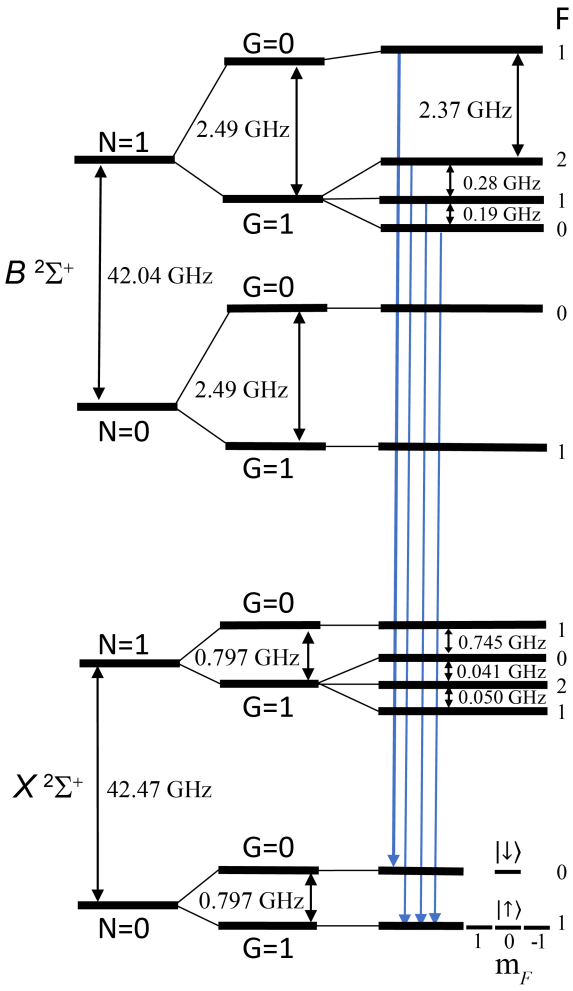

Figure 3.7: Low-lying structures of the $B^2\Sigma^+$ and $X^2\Sigma^+$ states of $^{29}Si^{16}O^+$. Blue arrows show the strong $\Delta G = 0$ electric dipole transitions. $\Delta G = 1$ transitions are allowed, but are significantly weaker due to the small spin-rotation interaction (relative to the hyperfine interaction). The qubit states are defined as $|\downarrow\rangle \equiv |X, N = 0, G = 0, F = 0\rangle$ and $|\uparrow\rangle \equiv |X, N = 0, F = 1, m_F = 0\rangle$.

via a microwave transition $|X, N = 1\rangle \leftrightarrow |X, N = 0\rangle$ and detecting fluorescence on the $P1$ transition $|B, N = 0\rangle \leftrightarrow |X, N = 1\rangle$.

Single qubit gates can be accomplished with microwave radiation at the ≈ 800 MHz qubit frequency or via a laser-driven Raman transition.

Two-qubit gates can be realized in a number of ways. The laser-based Raman gates employed in atomic ion quantum computing, e.g., the Mølmer-Sørensen gate [120, 121], can be applied to molecules without modification. While these gates are well understood, they require near motional ground state cooling and stablization of the relative phase between two laser frequency. A potentially less technologically demanding alternative is to use the recently proposed electric field gradient gates (EGGs) [119], which requires only the application of microwave gradient electric field that is near resonance with the $|X, N = 1\rangle \leftarrow |X, N = 0\rangle$ rotational transition at ≈ 42.5 GHz.

The EGGs interaction proceeds by applying an oscillating quadrupole electric field via the ion trap itself, which results in a position-dependent electric field that couples the internal state of the qubit to the ion motion. This can be used to entangle two trapped $^{29}Si^{16}O^+$ ions as follows. For two trapped $^{29}Si^{16}O^+$ ions, microwave radiation is used to transfer population from $|\uparrow\uparrow\rangle \rightarrow |ee\rangle$, where $|e\rangle$ is some excited state that also couples to $|\downarrow\rangle$. This excited state is necessary since the $|\uparrow\rangle \leftrightarrow |\downarrow\rangle$ transition is electric dipole forbidden. For $^{29}Si^{16}O^+$, we choose $|e\rangle$ to be $|X, N = 1, G = 0\rangle$ due to its strong coupling to the $|\downarrow\rangle$ state. A Mølmer-Sørensen gate can then be applied via the EGGs interaction on the $|e\rangle \leftrightarrow |\downarrow\rangle$ transition, producing $|\psi\rangle = \frac{1}{\sqrt{2}}(|ee\rangle + i|\downarrow\downarrow\rangle)$. The weak coupling between the $|e\rangle$ and $|\uparrow\rangle$ states can be remedied by simply increasing the voltage applied to the rods since the Mølmer-Sørensen gate is highly sensitive to detuning errors. Finally, microwave radiation can be used to produce $|\psi\rangle = \frac{1}{\sqrt{2}}(|\uparrow\uparrow\rangle + i|\downarrow\downarrow\rangle)$. Simulations show that this sequence can reasonably yield Bell-state fidelities ≥ 0.99 with gate times on the order of a few milliseconds. Decoherence of $\{\downarrow, \uparrow\}$ qubits can be anticipated from a variety of sources, including blackbody radiation, collisions with background gas, and Zeeman and Stark shifts. Ref. [92] observes that $^{28}Si^{16}O^+$ prepared in the $N = 0$ state is lost with a time constant of tens of seconds and suggests this may be

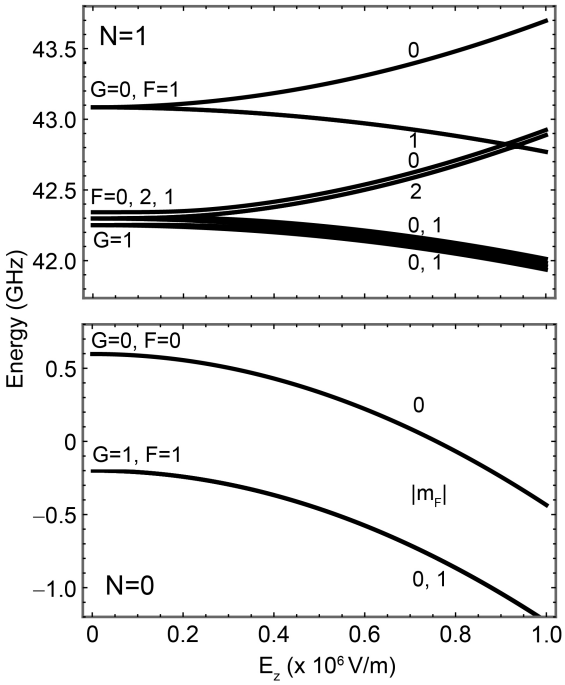

Figure 3.8: Calculated DC Stark shift of the $X^2\Sigma^+$ state of $^{29}Si^{16}O^+$ based on the spectroscopically determined structure parameters. The qubit is first-order insensitive to electric and magnetic field noise, allowing long coherence times, even in an ion trap environment.

due to a combination of blackbody radiation and background gas collisions. As the qubit states are zero-field clock states, magnetically-limited coherence times in excess of a second are expected [112]. Finally, with the structure of $^{29}Si^{16}O^+$ determined, the Stark shift may be calculated as shown in Figure 3.8. As expected for a Hund's $(b)_{\beta S}$ molecule [110], the chosen qubit states exhibit a small differential Stark shift of $\approx 6.8 \times 10^{-7} E^2$ [Hz/(V/m)^2]. Thus, in total qubit coherence time in excess of seconds should be expected.

3.9 Summary

We have performed laser-induced fluorescence spectroscopy of the $B^2\Sigma^+ \leftarrow X^2\Sigma^+$ transition in both $^{28}Si^{16}O^+$ and $^{29}Si^{16}O^+$. The ions were produced by reaction of Si^+ with O_2 in a cryogenic cell at roughly 100 K. Low-resolution spectra of the (0,0) and (1,0) bands of $^{28}Si^{16}O^+$ and the (0,0) band of $^{29}Si^{16}O^+$ were obtained with a pulsed dye laser ($\approx$ 1.2 GHz linewidth), yielding molecular constants of both states, the lifetimes of $B^2\Sigma^+(v = 0, 1)$

states of $^{28}Si^{16}O^+$, and the lifetime of the $B^2\Sigma^+(v = 0)$ of $^{29}Si^{16}O^+$. Using a narrowband cw Ti:sapphire laser ($\approx$ 10 MHz linewidth), we have observed seventeen and twenty-six high-resolution rotational lines of the (0,0) band of $^{28}Si^{16}O^+$ and $^{29}Si^{16}O^+$, respectively. These data are used to extract more precise molecular constants for both ions, including the determination of the Fermi contact interaction constant for both the $B^2\Sigma^+$ and $X^2\Sigma^+$ states in the gas phase. The observed spin-rotation constants show some disagreement with two previous conflicting reports. We show this disagreement is due to a lack of experimental resolution in one case and a differing model in the other. Finally, we outline how the determined and fortuitous structure of $^{29}Si^{16}O^+$ can be used to perform state preparation and measurement of a qubit and one/two-qubit gates, as well as discuss several potential sources of decoherence.

CHAPTER 4

Vibrational branching ratios measurement of molecules with optical cycling centers

Optical cycling transitions in atoms allow laser cooling of the center-of-mass motion, laser state preparation, and laser-induced fluorescence (LIF) state detection. Laser-cooled atoms enable channel operations at the heart of many promising applications of quantum technology, including quantum computation[122, 123], atomic clocks[5, 124], and quantum simulation[6, 125]. Optical cycling and cooling schemes have also been demonstrated in diatomic [32, 126] and even some small polyatomic molecules [127, 128], including SrF [14], YO[15], CaF [16, 81], YbF [22], BaF [129, 130], MgF [131], AlF [132], SrOH [17], CaOH [83], YbOH [24], and $CaOCH_3$ [18]. Because they possess rich internal structures and complex interactions, molecules provide new opportunities in studies of dark matter detection [133, 134], measurement of electron's electric-dipole moment [23, 70, 135], parity violation tests [136, 137], and changes to fundamental constants [138, 139].

The atom-like transitions supporting optical cycling and cooling in these small molecules have inspired searches for similar transitions in complex polyatomic molecules with an M-O-R structure [128], where M is an alkaline-earth metal atom ionically bonded to oxygen (O) forming an optical cycling center (OCC) and R is a molecular ligand [13, 140, 141]. In these molecules, the remaining metal-centered radical electron forms the highest-occupied molecular orbital (HOMO) and the lowest-unoccupied molecular orbital (LUMO). For molecules with R having strong electron withdrawing capability, the HOMO and LUMO are localized on M, which typically indicates that the OCC is highly decoupled from the vibrational degrees of freedom. As a result, the diagonal vibrational branching ratio (VBR, which is to

say the probability that spontaneous decay occurs on the 0-0 transition) is high, indicating that the spontaneous emission happens without a vibrational state change. This allows such molecules to repeatedly scatter photons before being pumped to the vibrational dark states, enabling mechanical control and state detection of single molecules via laser illumination.

Since optical cycling in this motif is predicted to be enhanced by the electron-withdrawing strength of the ligand, the diagonal VBR of M-O-R molecules could be tuned by functionalizing the ligand to promote this effect [33]. In this chapter, we will introduce the experiments about the measurement of VBRs of calcium phenoxides (CaOPh-X) and strontium phenoxides (SrOPh-X), where X is the substituent tuning the electron-withdrawing strength of the ligand.

4.1 Measurement procedure

Prior to the measurements in the cryogenic buffer beam cells [37, 38], the optical transitions of CaOPh-X and SrOPh-X molecules were identified under room temperature in a vacuum chamber in our lab. Later, the dispersed laser induced fluorescence (DLIF) spectroscopy measurements for CaOPh-X and SrOPh-X were taken in cryogenic environment for better signal-to-noise ratios, with the CaOPh-X measurement completed in Doyle lab at Harvard University [37] and the SrOPh-X measurement done in our lab [38], respectively. Therefore, the experimental setups described in the two papers are different. On the other hand, due to the similarities in the molecular structures being studied and the VBRs analysis methods, the two separate experiments are put together in this chapter for better comparison and comprehension.

Theoretical results, such as the Franck-Condon factors and the frequencies of the vibrational modes, were obtained by Dr. Claire E. Dickerson from Prof. Anastasia Alexandrova's group. The measured results and the calculation which are not involved in this chapter can be found in the Appendix. B.

Molecule production. The studied molecules of CaOPh-X and SrOPh-X were pro-

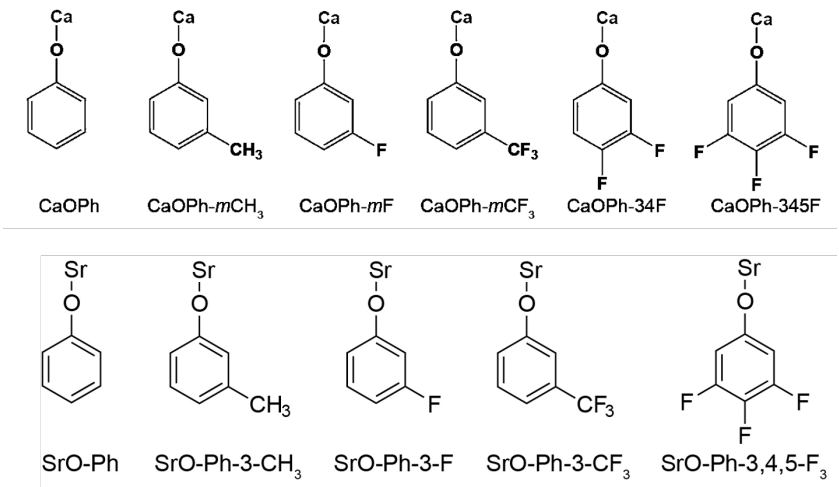

Figure 4.1: Molecular structures of calcium and strontium phenoxide and derivatives involved in this chapter.

duced by the reaction of Ca or Sr atoms with ligand precursors in a cryogenic buffer-gas cell. Because the buffer gas species used for CaOPh-X and SrOPh-X are helium and neon, respectively, the cell operating temperature is ≈ 9 K [142] for CaOPh-X and ≈ 23 K for SrOPh-X. Five precursor molecules – phenol, *m*-cresol, 3-fluorophenol, 3-(trifluoromethyl)phenol and 3,4,5-trifluorophenol – were purchased commercially and used without further purification. Gas-phase metal atoms were introduced into the buffer gas by laser ablation of a metallic Ca or Sr target. The position of the ablation laser was continuously swept over the target with a moving mirror to avoid ablation-induced yield drifts. A reservoir containing the ligand precursors was heated to a temperature between 300 K and 350 K to maintain a vapor pressure of 3-5 Torr (melting points of precursors given in Table B.3). The resulting vapor was flowed into the cryogenic cell via a thermally isolated, heated fill line. The reaction products were cooled via collisions with the buffer gas, which was continuously flowed into the cell at a rate of 10-20 standard cubic centimeters per minute (sccm), leading to a gas density of density $\approx 10^{15-16}$ cm^{-3}.

CaOPh-X DLIF measurement in the cryogenic cell. The resulting CaOPh-X molecules were studied using two-dimensional (2D) spectroscopy via excitation and dispersed fluorescence [143–146], DLIF spectroscopy, and radiative decay. A tunable, pulsed optical parametric oscillator (OPO)(with approximate parameters 5 cm^{-1} linewidth, 10 ns pulse

duration, and 1 mJ pulse energy) illuminated the molecules at a delay of $\approx$ 1 ms after the ablation pulse. The OPO wavelength was continuously tunable from 500 nm to 700 nm, and the absolute wavelength was determined by a spectrum analyzer with a measurement accuracy of 0.5 nm. Molecular fluorescence was collected into a 0.67 m focal length Czerny-Turner style monochromator (McPherson Model 207, numerical aperture $\approx$0.1) equipped with a 300 lines/mm grating (500 nm blaze). The dispersed fluorescence was imaged onto a gated, intensified charge-coupled device (Andor iStar 320T ICCD) camera cooled to -30 °C. Given the system passband, a roughly 80 nm wide spectral region of the DLIF could be recorded in a single image.

SrOPh-X DLIF measurement in the cryogenic cell. The resulting SrOPh-X molecules have two low-lying electronic states proposed for laser cooling. To look for those states, a tunable, pulsed dye laser (10 Hz, LiopStar-E dye laser, linewidth 0.04 cm^{-1} at 620 nm) were used to excite molecules in the cryogenic cell and the laser wavelength was scanned. When the laser wavelength hit electronic resonance, the molecule was excited and followed by the emission of molecular fluorescence. The fluorescence was then collected via an imaging system into a model 2035 McPherson monochromator equipped with a 1200 lines/mm grating and detected by a PMT. The dispersed measurement were done by parking the laser wavelength at the electronic resonance and continuously scanning the grating of the spectrometer at an increment of 0.10 nm while monitoring the fluorescence photons. The entrance and exit slit widths were both set at 0.20 mm, resulting in a spectrometer resolution of $\approx$ 20 cm^{-1}.

4.2 Linear relationship between pKa and excitation energy of Phenoxide molecule

The excitation energies of the molecules are measured via For phenoxide-type molecule, we observed that there is a linear relationship between the pK_a of the molecule and the excitation energy. The acid dissociation constant, pK_a is a convenient parameter that indicates the

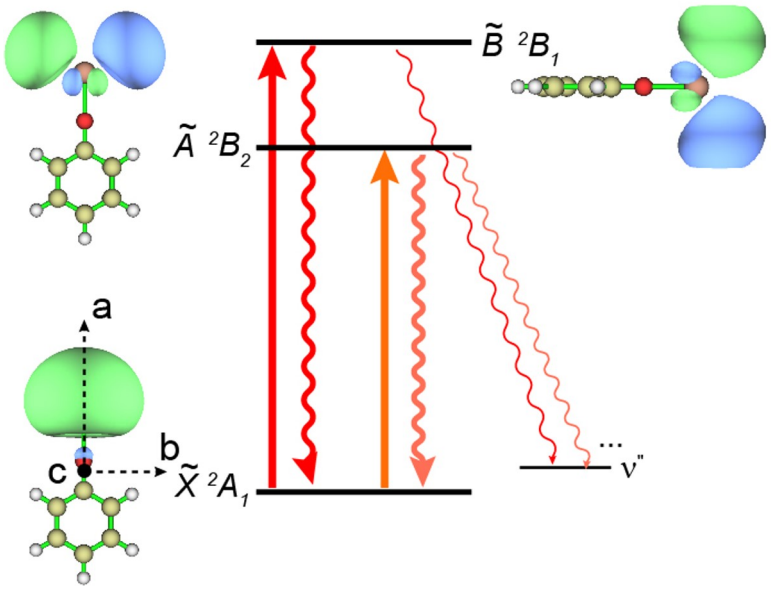

Figure 4.2: Molecular orbital and schematic energy levels of SrOPh. All other molecules have similar orbitals and energy levels.

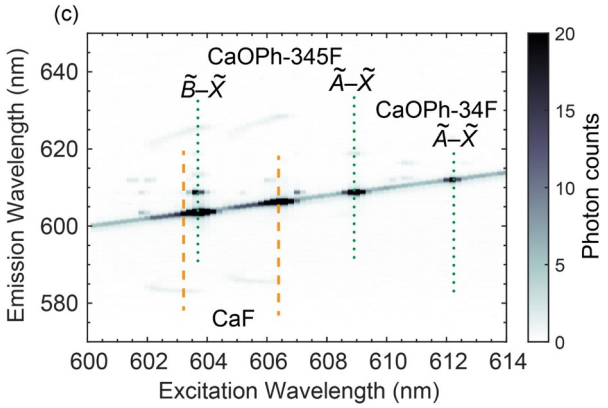

Figure 4.3: 2D DLIF spectrum following the reaction of Ca with 3,4,5-trifluorophenol. The orange dashed lines indicate the resonance bands of CaF while green dotted lines indicate the bands of CaOPh-3,4,5-F and CaO-3,4-F.

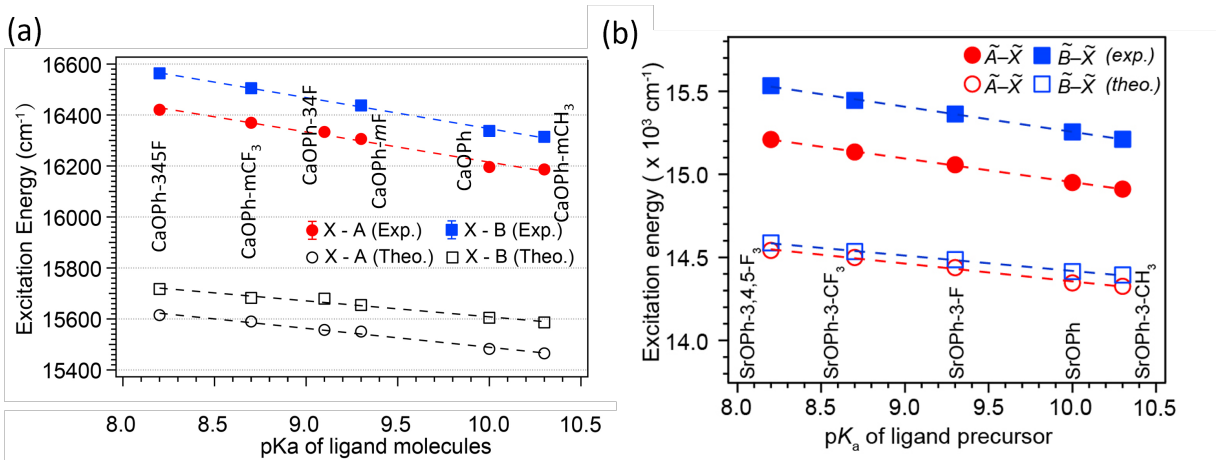

Figure 4.4: (a) $\widetilde{A} \leftarrow \widetilde{X}$ and $\widetilde{B} \leftarrow \widetilde{X}$ transition energies versus pKa for all CaOPh-X molecules studied here. The linear fits to the experimental data yield $E_A = 17400 - 118{\times}\mathrm{pK}_a$ (cm^{-1}) and $E_B = 17561 - 121.49{\times}\mathrm{pK}_a$ (cm^{-1}).(b) Excitation energy versus pK_a for $\widetilde{A} - \widetilde{X}$ and $\widetilde{B} - \widetilde{X}$ transition for SrOPh-X in an increasing order of ligand pK_a. The linear fits of the experimental values yield $E_{\widetilde{A}-\widetilde{X}} = (16,372 - 142\,\mathrm{p}K_\mathrm{a})$ cm^{-1} and $E_{\widetilde{B}-\widetilde{X}} = (16,769 - 151\,\mathrm{p}K_\mathrm{a})$ cm^{-1}.

strength of an acid R−OH, and therefore quantifies the electron-withdrawing capability of the R−O$^-$ ligand. Lower pK_a implies higher electron-withdrawing capability of the R-O$^-$ ligand, which pulls the single electron away from the Sr atom, making it more ionic and increasing the HOMO-LUMO gap [33]. The measured transition energies of CaOPh-X as a function of the precursor pK_a in solution in Figure 4.4(a). Similarly, as can be seen in Figure 4.4(b), the excitation energies of SrOPh-X follow a monotonic and apparently linear trend with pK_a. Also shown are excitation energies calculated by time-dependent density functional theory which give a similar trend but systematically undershoot the excitation energies likely due to self-interaction error and approximate treatment of electronic correlation [147]. The calculated energy gap of $\widetilde{A} - \widetilde{B}$ ($36 - 68$ cm^{-1}) is much smaller than the measured gap ($300 - 324$ cm^{-1}), similar to what was observed in CaOPh-X species but with a wider difference between the theory and measurement [37]. The theory-experiment discrepancies of the $\widetilde{A} - \widetilde{B}$ energy gap are likely due to the lack of spin-orbit coupling in calculations [35] and the wider difference in SrOPh-X is due to the stronger SOC effects in Sr.

4.3 DLIF spectroscopy measurement

Typically, the laser cooling of molecule requires the repumping of the population in the vibrational excited state to the $\nu = 0$ state of the low-lying electronic excited states. The effectiveness of repumping is governed by the vibrational branching ratios (VBRs) from these excited states. To measure the VBRs from the electronic states, we conducted Dispersed Laser-Induced Fluorescence (DLIF) spectroscopy, as detailed in Figure 4.1. Here, a sample of molecules is optically pumped to an excited electronic state, which then relaxes by spontaneously emitting photons that correspond in wavelength to the energy gap between the excited state and various vibrational levels of the ground state. The likelihood of each emission wavelength—governed by the VBRs—reflects the probability of the molecule decaying into each possible vibrational ground state. In the CaOPh-X DLIF experiment, the fluorescence is collected, wavelength-sorted through a diffraction grating, and then recorded by an Electron-Multiplying CCD (EMCCD) camera, while in the SrOPh DLIF measurements, a Photon-multiplier tube (PMT) is employed to capture the emissions. This process yields an image with discrete peaks, each representing a different emission wavelength. The relative intensity of these peaks provides a direct measure of the VBRs, which, after appropriate calibration, can be quantitatively determined.

4.3.1 CaOPh-X DLIF measurement

CaOPh-X DLIF measurements were recorded by tuning the OPO to a selected resonance and accumulating a large number of ICCD exposures (typically between 4000-8000 excitation pulses). Background light due to the excitation laser was determined separately by recording spectra with the ablation laser off and subtracted from the recorded DLIF. Representative DLIF spectra for CaOPh-3,4,5-F are shown in Figs. 4.5(a-b), while those of all other studied molecules are presented in Figure 4.6. All spectra are plotted in terms of the energy difference (in cm^{-1}) relative to the excitation energy and are normalized to the peak at the origin. Given the low vibrational temperature, this peak mainly consists of the "diagonal" $\nu' = 0 \rightarrow \nu'' = 0$

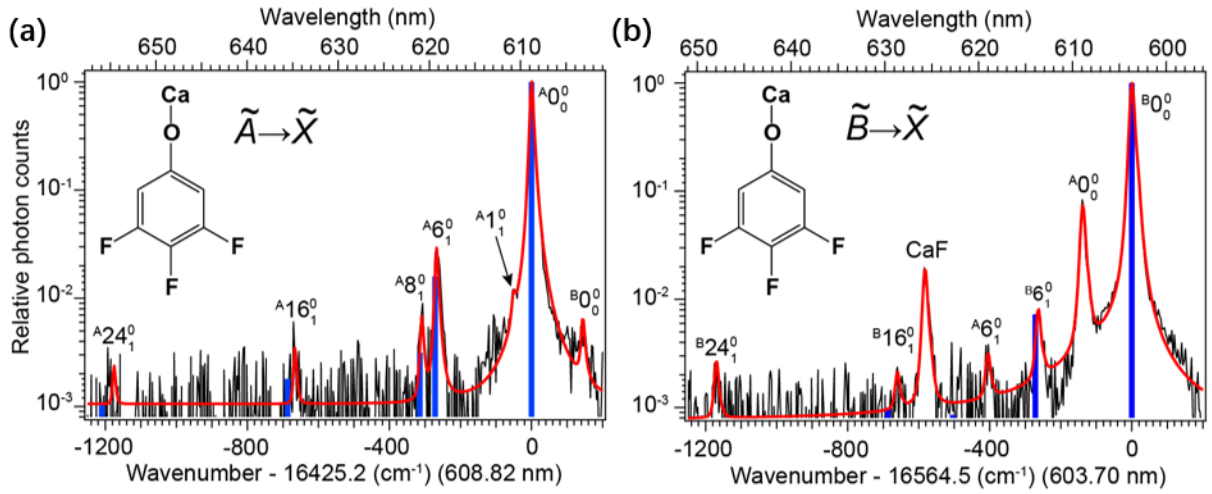

Figure 4.5: DLIF spectra of CaOPh-3,4,5-F_3 when exciting the (a) $\widetilde{A} \leftarrow \widetilde{X}$ at 608.82 nm and (b) $\widetilde{B} \leftarrow \widetilde{X}$ at 603.70 nm. Experimental data (black) is overlaid with a Pearson distribution fit (red). The blue vertical lines in the DLIF spectra indicate the calculated frequencies of the vibrational modes and the height of the lines reflect their calculated relative strengths. The green traces indicate the background due to scattered OPO laser photons. The assignments of the resolved vibrational peaks are also given.

transition. Figure 4.5(a) shows the DLIF spectrum of CaOPh-3,4,5-F when exciting the $\widetilde{A} \leftarrow \widetilde{X}$ transition at 608.82 nm. The peak, labeled as $^{A}0_0^0$, represents the decay from the excited $\widetilde{A}(\nu' = 0)$ state to the ground $\widetilde{X}(\nu'' = 0)$ state. The strongest vibration-changing decay, observed at -267 cm^{-1} and labeled $^{A}6_1^0$, is assigned to the Ca-O stretching mode. This is the sixth smallest-frequency vibrational mode in the $\widetilde{X}$ state and has a theoretically predicted harmonic frequency of 272 cm^{-1}(Figure 4.9(a)) Comparing to the theoretically calculated frequencies and VBRs, two peaks at -307 cm^{-1}and -670 cm^{-1}can be assigned to 8_1^0 and 16_1^0, respectively, which are both symmetric stretching modes involving the benzene ring (Figure B.2(a)). A weak decay at -1184 cm^{-1}is attributed to the high-frequency stretching mode 24_1^0 (Figure 4.9(a)) The small shoulder next to the diagonal peak is due to decays to the lowest-frequency fundamental bending mode, 1_1^0. The vertical blue lines are the theoretically calculated VBRs (see SI) normalized by the predicted value for the 0-0 decay. Interestingly, as noted by the absence of a predicted VBR for the 1_1^0 peak, theoretical calculations predict this decay pathway to be negligible. The observed strength of this decay is likely due to vibronic couplings among and anharmonicities within the low-frequency

modes [33, 148, 149], which have not been considered in the present calculations (see SI).

The DLIF spectrum of CaOPh-345F from the $\widetilde{B}$ state is shown in Figure 4.5(b). In addition to the non-vibration-changing decay ${}^{B}0_0^0$ and the dominant vibration-changing decay ${}^{B}6_1^0$, a relatively strong peak is observed with a shift of -139 cm^{-1}. This redshift is not compatible with the calculated frequencies of any vibrational modes of the molecule, though the peak occurs at the same emission wavelength as the $\widetilde{A}(\nu' = 0) \rightarrow \widetilde{X}(\nu'' = 0)$ transition. The assignment of this peak as emission from $\widetilde{A}(\nu' = 0)$ is further confirmed with the observation of a feature, attributable to ${}^{A}6_1^0$, at -407 cm^{-1}and with the expected relative intensity. The presence of peaks originating from the $\widetilde{A}$ state when exciting to the $\widetilde{B}$ state has been observed in the spectra of all other molecules measured in this work (Figure 4.6) and we attribute it to collision-induced de-excitation from the B to A state [62, 150]. Interestingly, we also see the opposite process of collision-induced excitation when exciting to the A state; as seen in Figure 4.5(a), a small peak at a positive shift of 140 cm^{-1} can be assigned to the ${}^{B}0_0^0$ decay. This excitation process is presumably due to collisions occurring before the hot ablation plume is fully thermalized. Lastly, a weak peak at -1172 cm^{-1} is attributed to the stretching mode 24_1^0, while the strong peak at -584 cm^{-1} is assigned to CaF $A^2\Pi_{1/2}(\nu' = 0) \rightarrow X^2\Sigma^+(\nu'' = 1)$ decay.

4.3.2 SrOPh-X DLIF measurement

For SrOPh-X, the electronic excitation is provided by a pulsed dye laser (PDL) tuned to the 0-0 line and the spectrometer grating was scanned in time (over repeated excitation) to select the wavelength of LIF photons sent to a photomultiplier tube (PMT). Figure 4.7 shows the representative DLIF spectra of SrOPh while those of other species are presented in Figure 4.8. Figure 4.7a shows the spectrum of $\widetilde{A}\ {}^2B_2 \rightarrow \widetilde{X}\ {}^2A_1$ of SrOPh (Figure 4.4a) at an excitation of 668.90 nm. The strongest peak at the origin, labeled as ${}^{A}0_0^0$, is due to the diagonal decay from $\widetilde{A}(\nu' = 0)$ to $\widetilde{X}(\nu'' = 0)$. The strong peak at -440 cm^{-1} is from excited atomic Sr created during laser ablation [151]. The peak at -238 cm^{-1} is assigned to the strongest off-diagonal stretching mode ν_3 (theo. 241 cm^{-1}) and the weak peak at -54

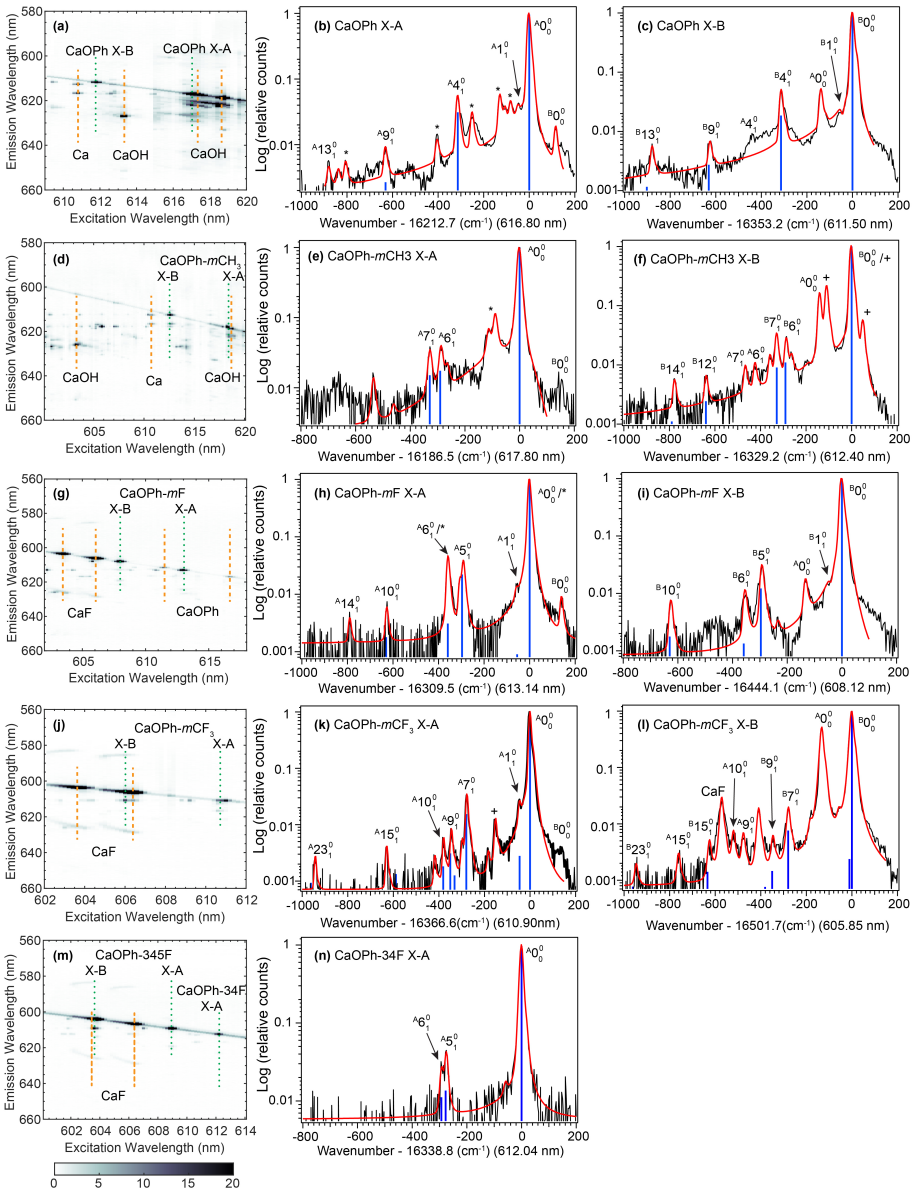

Figure 4.6: 2D spectra and dispersed LIF spectra of all CaOPh-X species. In the 2D spectra, the orange dashed lines mark features due to CaOH or CaF, while the green dotted lines indicate features from CaOPh-X species. In the corresponding dispersed LIF spectra, the experimental curves (black) are fitted with Pearson functions (red). The blue sticks illustrate the vibrational branching ratios of different vibrational modes. The assignments of resolved vibrational peaks are also given. The symbols * and + indicate features due to CaOH and Ca, respectively.

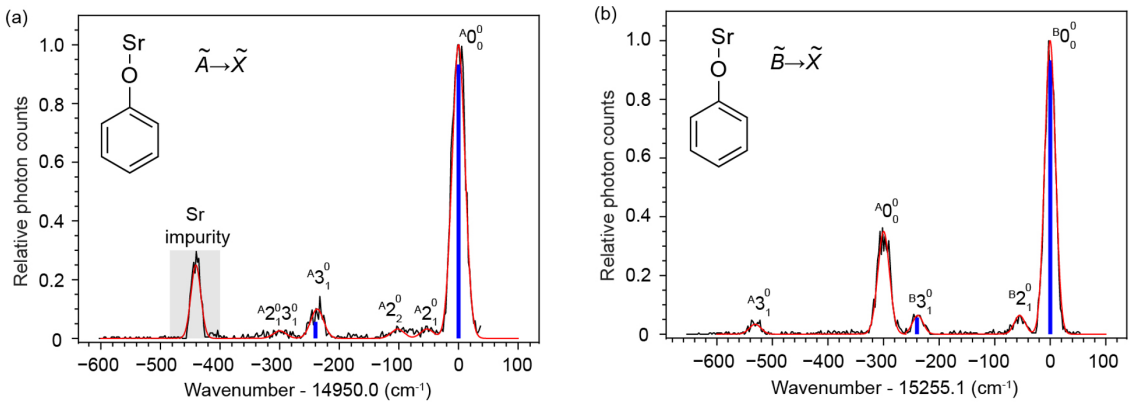

Figure 4.7: (a) and (b) Dispersed spectra of $\widetilde{A} \rightarrow \widetilde{X}$ and $\widetilde{B} \rightarrow \widetilde{X}$, respectively, of SrOPh excited by pulsed dye laser and measured by a spectrometer coupled with PMT. The experimental curves (black) are fitted with the Gaussian functions (red). The positions of the blue, vertical lines illustrate the theoretical frequencies while the intensities show the vibrational branching ratios of different vibrational modes of SrOPh. The Sr impurity peak in (a) is from the Sr emission of $5s5p\ ^3\mathrm{P}_1^o \rightarrow 5s^2\ ^1\mathrm{S}_0$ at 689 nm. The assignments of all resolved vibrational peaks are indicated.

cm^{-1} is assigned to the low-frequency bending mode ν_1 (theo. 54 cm^{-1}). The other two weak peaks at -100 cm^{-1} and -297 cm^{-1}, which do not match the calculated frequencies of any fundamental vibrational modes, are assigned to the overtone of the bending mode $^{A}2_2^0$ and a combinational mode of $^{A}2_1^0 3_1^0$, respectively.

Figure 4.7b shows the spectrum of $\widetilde{B}\ ^2B_1 \rightarrow \widetilde{X}\ ^2A_1$ of SrOPh (Figure 4.4a) at 655.52 nm. Aside from the strongest diagonal peak $^{B}0_0^0$, four peaks are observed. The strong peak with a shift of -300 cm^{-1} is due to a diagonal decay $^{A}0_0^0$ from the $\widetilde{A}$ state. The origin of the appearance of $^{A}0_0^0$ when exciting the $\widetilde{B} \leftarrow \widetilde{X}$ is unknown, but could be due to the collisional relaxation from $\widetilde{B}$ to $\widetilde{A}$ followed by fluorescence decay to the ground state $\widetilde{X}$ [37, 62, 152]. The identification of this feature as originating from the $\widetilde{A}$ state is further confirmed by the observation of the decay to the stretching mode ν_3 at -534 cm^{-1} from $\widetilde{A}$. The other two weak peaks, -238 cm^{-1} and -55 cm^{-1}, are due to the vibrational decay to the stretching mode ν_3 and bending mode ν_1, respectively. The full width at half maximum of all peaks is ≈ 22 cm^{-1} mainly due to the spectrometer resolution of approximately 20 cm^{-1}. Another measurement using a narrow-band continuous-wave (cw) laser to excite the $\widetilde{B} \leftarrow \widetilde{X}$ of SrOPh and an electron-multiplying charge-coupled device (EMCCD) camera to

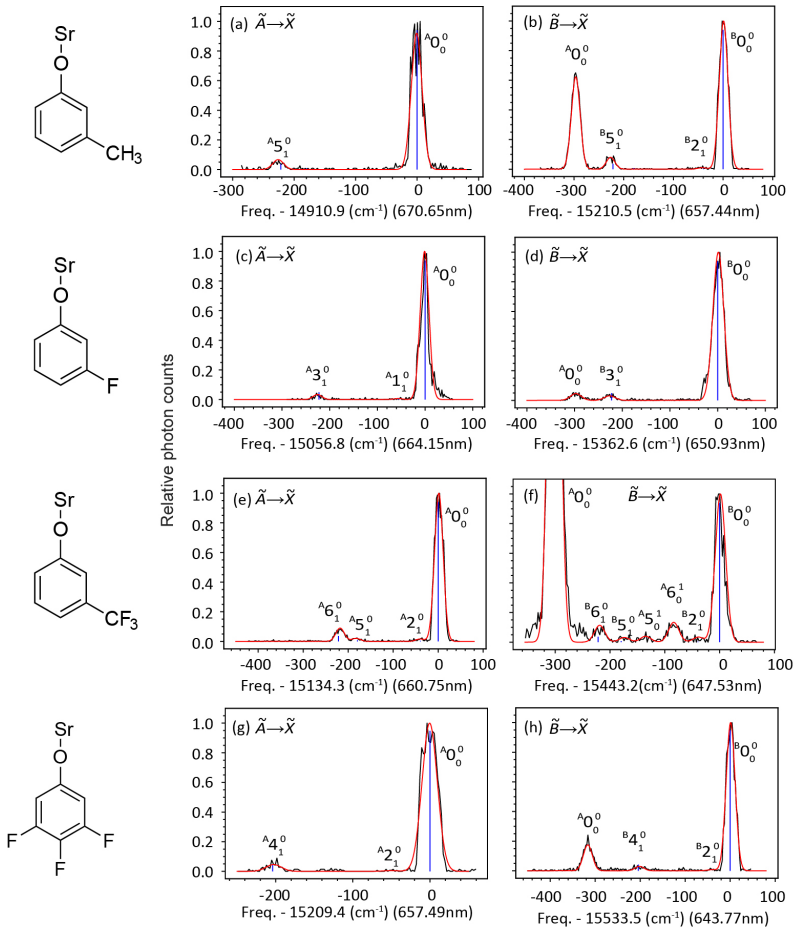

Figure 4.8: Dispersed fluorescence spectra of all SrOPh-X species. The experimental curves (black) are fitted with the Gaussian functions (red). The blue sticks illustrate the vibrational branching ratios of different vibrational modes. The assignments of resolved vibrational peaks are also given.

capture the fluorescence photons dispersed by the spectrometer. This technique obtained a better spectral resolution (≈ 5 cm^{-1}), allowing the resolution the combinational vibrational mode of $^{B}2_1^0 3_1^0$ (Figure B.1), which is overlapped with the diagonal decay $^{A}0_0^0$ from the $\widetilde{A}$ state and not observed in Figure 4.7b.

4.4 VBRs data analysis

The promising potential for optical cycling of both $\widetilde{A} \rightarrow \widetilde{X}$ and $\widetilde{B} \rightarrow \widetilde{X}$ transitions is evidenced by the comparative heights of the $^{A}0_0^0$ and $^{B}0_0^0$ peaks in Figs. 4.5, 4.6, 4.7, and

4.8. To accurately determine the VBRs for these molecules, we employ a maximum likelihood method to fit the peak profiles, subsequently extracting the area under each decay curve. For the CaOPh-X spectra, a Pearson distribution fitting is utilized to account for the observed slight skewness in the line shapes, the specifics of which are detailed in Appendix B. In contrast, the peaks in the SrOPh-X spectra are characterized using Gaussian fits with the parameters of peak location, height and width.

To compare with the theory, the calculated FCFs were converted to the VBRs using the formula [13, 37]:

$$\begin{aligned} b_{i\nu',f\nu''} &= \frac{A_{i\nu',f\nu''}}{\sum_{f\nu''} A_{i\nu',f\nu''}} \\ &= \frac{|\mu_{i\nu',f\nu''}|^2 \ \times \ (\nu_{i\nu',f\nu''})^3}{\sum_{f\nu''} |\mu_{i\nu',f\nu''}|^2 \ \times \ (\nu_{i\nu',f\nu''})^3} \\ &\approx \frac{\mathrm{FCF}_{i\nu',f\nu''} \ \times \ \nu^3_{i\nu',f\nu''}}{\sum_{f\nu''} \mathrm{FCF}_{i\nu',f\nu''} \ \times \ \nu^3_{i\nu',f\nu''}} \end{aligned} \tag{4.1}$$

The VBRs for $\widetilde{A} \rightarrow \widetilde{X}$ and $\widetilde{B} \rightarrow \widetilde{X}$ transitions of the CaOPh-X are shown in Figure 4.9, and the relation of diagonal VBR and the pK_a of the ligand molecule is plotted in Figure 4.10. Remarkably, across all six ligands and a considerable range of pK_a, the VBRs are relatively unchanged and always $\gtrsim 90$ %, indicating that the OCC function can indeed be made orthogonal to the ligand molecule. The theoretical calculations in Figure 4.10 show an increase in VBR for stronger acids, as was previously predicted [33]. This trend is consistent with the experimental data, and is understood as the localization of the electronic wavefunction on the Ca atom with a more ionic Ca−O bond, leading to further isolation of the electronic and vibrational degrees of freedom [33]. This suggests that while an OCC can be successfully attached to a wide range of molecules, performance may still be optimized by choosing ligands with strong electron withdrawing character.

Figure 4.11 displays the VBRs of the SrOPh-X molecules. For the ith peak in each spectrum, the peak area (M_i) is extracted and the error of the area (δM_i) is estimated from the covariance matrix of the fitting parameters. The intensity ratios of each peak, as shown

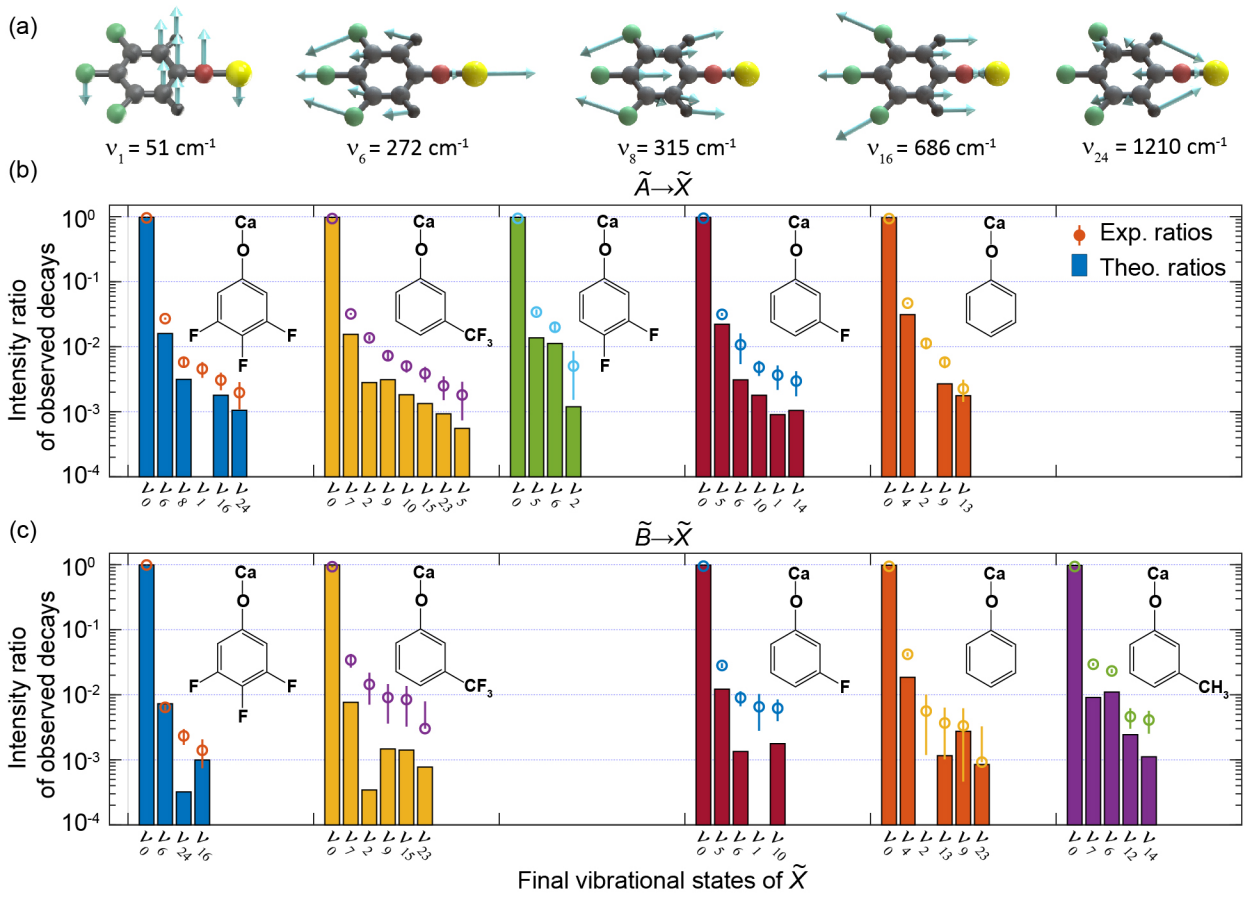

Figure 4.9: (a) Schematic illustrations of the resolved fundamental normal vibrational modes of CaOPh-3,4,5-F. The arrows indicate the direction of vibrational displacements. The corresponding theoretical frequencies are also given. Intensity ratio of observed decays, relative to total observed decays, for (b) $\widetilde{A} \rightarrow \widetilde{X}$ and (c) $\widetilde{B} \rightarrow \widetilde{X}$ transitions for all molecules and modes studied in this work arranged in order of increasing pK_a. . Experimental values are denoted with circles while calculated values are depicted as bars for clarity. Error bars are statistical standard errors. The vibrational mode denoted as ν_I indicates the decay to the final vibrational state of I_1^0. ν_0 implies the decay to the ground vibrational level of $\widetilde{X}$. The $\widetilde{A} \rightarrow \widetilde{X}$ decay of CaOPh-mCH$_3$ and $\widetilde{B} \rightarrow \widetilde{X}$ decay of CaOPh-34F are omitted due to coincidences with CaOH and CaF decays, respectively.

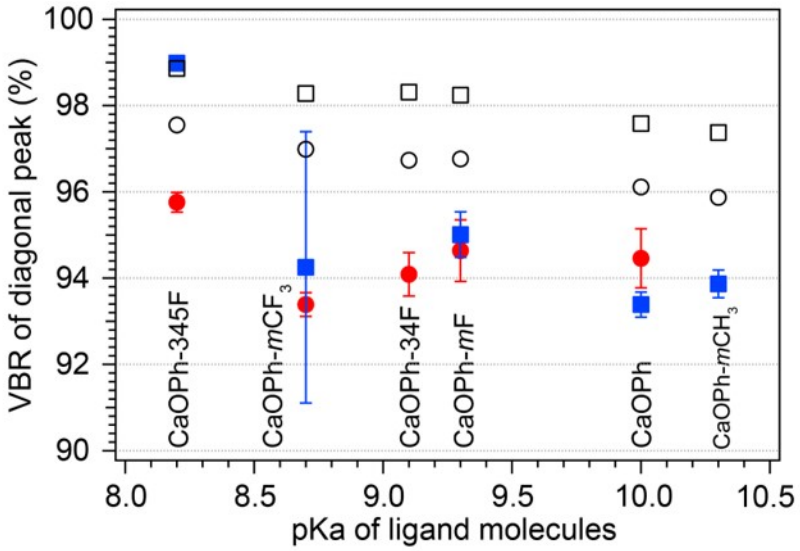

Figure 4.10: Scaled VBR for diagonal decay as a function of pK_a. Error bars on experimental points include the combined uncertainties from statistical and unobserved peaks. The large error bar for $\widetilde{B} \rightarrow \widetilde{X}$ decay of CaOPh-mCF$_3$ is due to a partial spectral overlap with CaF.

VBRs measurement error source	Percentage
Contributions from unobserved peaks	$1.1\% - 3.2\%$
Signal fluctuation	1.0%
Instrument wavelength response	1.0%
Diagonal excitation	0.5%
Total error	$1.9\% - 3.5\%$

Table 4.1: Systematic error budget for the vibrational branching ratio measurements.

in Figure 4.11a, is obtained from the ratio of M_i and the total area of all the observed peaks, $\sum_{i=0}^{p} M_i$. The statistical error of each intensity ratio is then calculated from the relative uncertainties $\delta M_i / M_i$. Besides the statistical fitting errors, several sources of systematic error in the DLIF measurement are evaluated in Appendix B and listed in Table 4.1.

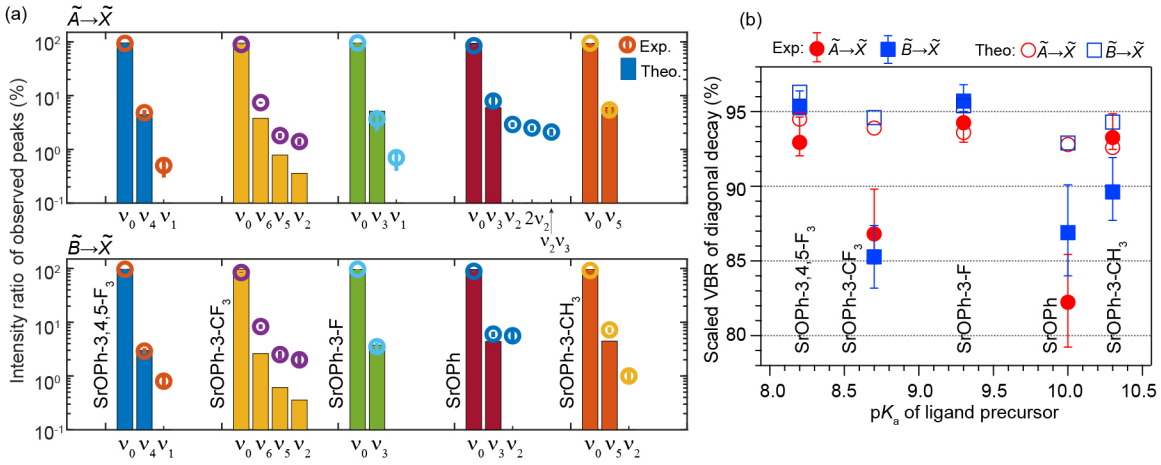

Figure 4.11: (a) Intensity ratio of observed decays for $\widetilde{A} \rightarrow \widetilde{X}$ and $\widetilde{B} \rightarrow \widetilde{X}$ transitions. Error bars are statistical errors from Gaussian fits. The vibrational label ν_i indicates the final vibrational modes of the $\widetilde{X}$ state. ν_0 implies the decay that doesn't change the vibrational state. (b) Scaled 0_0^0 VBRs as a function of p$K_a$of all species. The scaling adds the contributions of those unobserved vibrational decays predicted by the theory to the observed intensity ratios of 0_0^0 in (a). Error bars include the statistical errors from Gaussian fits and the systematic errors from the unobserved peaks.

4.5 Lifetime of excited states

The radiative lifetimes of the CaOPh-X molecules were measured by driving the 0-0 transition and recording the DLIF spectrum at variable time delay after the excitation. In Figure 4.12, the decay trace of each transition has been measured 2-4 times. The experimental data points show the averaged values of all normalized measurements at the same gate delay and the error bar of each point represents the standard deviations. The experimental points are fitted with an exponential function to extract the lifetime and the corresponding error bars are obtained by bootstrapping the data.

For SrOPh-X molecules, the lifetime were measured by analyzing the PMT signal counts at different time after the excitation is driven. The temporal resolution of the PMT used in experiment is $\approx$ 5ns. The experimental data points (red circles) in Figure 4.13 are obtained from the sum of PMT signal for the $0-0$ decay in the DLIF measurements and the respective error bar represents the standard errors. For each trace, the data points are normalized to the maximum signal counts. The radiative lifetimes τ and errors for all species are estimated

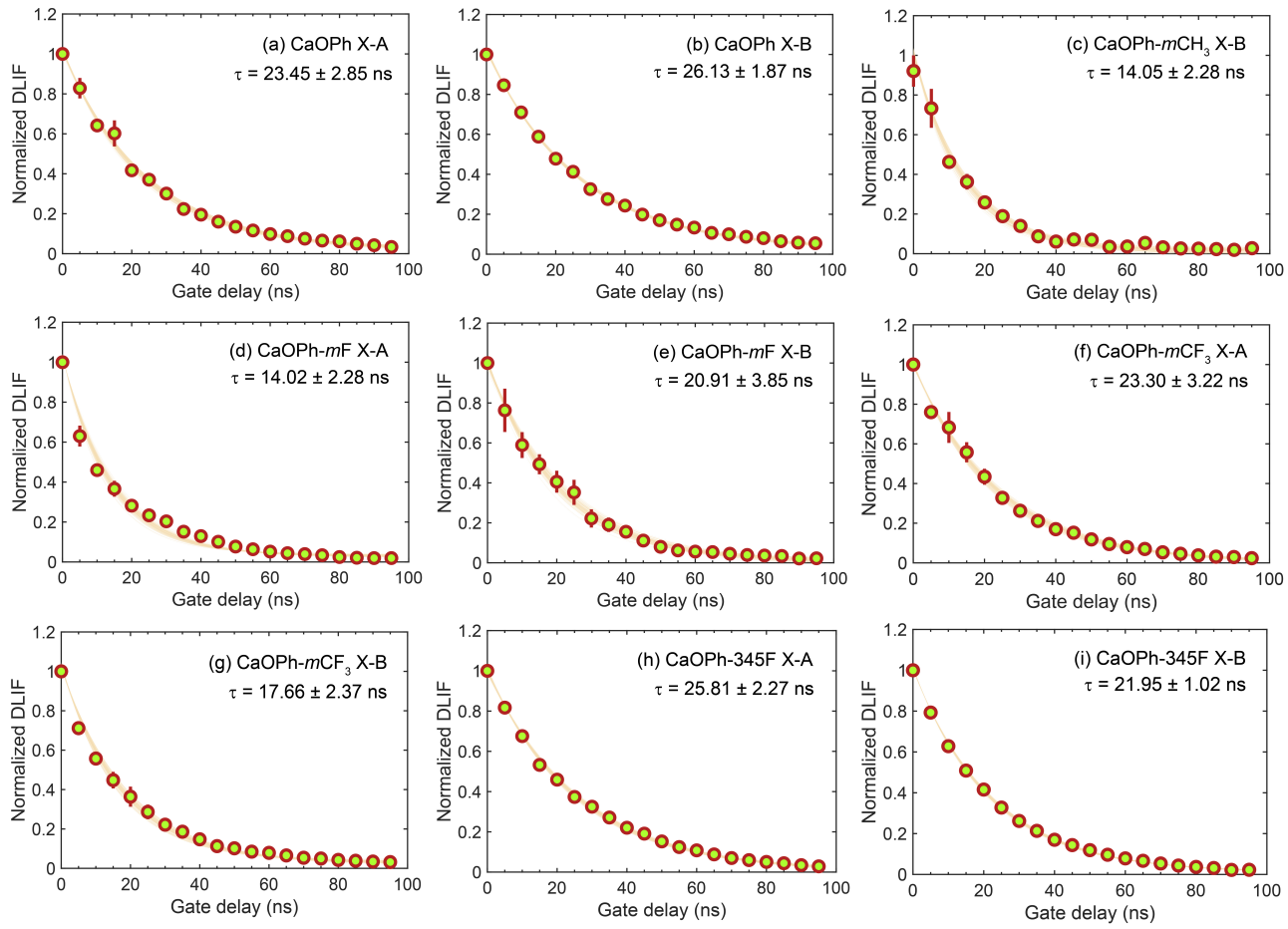

Figure 4.12: Fluorescence decay traces used to determine radiative lifetimes for all CaOPh-X molecules observed in this work.

from exponential fits (green curves) by bootstrapping the data.

4.6 Conclusion

We have produced calcium and strontium (I) phenoxide and derivatives featuring electron-withdrawing groups in a cryogenic cell, and measured the VBRs of the excited states of these molecules. Two proposed laser cooling transitions ($\widetilde{A}-\widetilde{X}$ and $\widetilde{B}-\widetilde{X}$) of each molecule have been identified and the transition energies show linear trends as the ligand pK_{a}, which can be used to look for transitions of new molecules containing the alkaline-earth metal atom. The overall vibrational branching ratios are estimated to be $82.2\% - 99.0\%$. Among them,

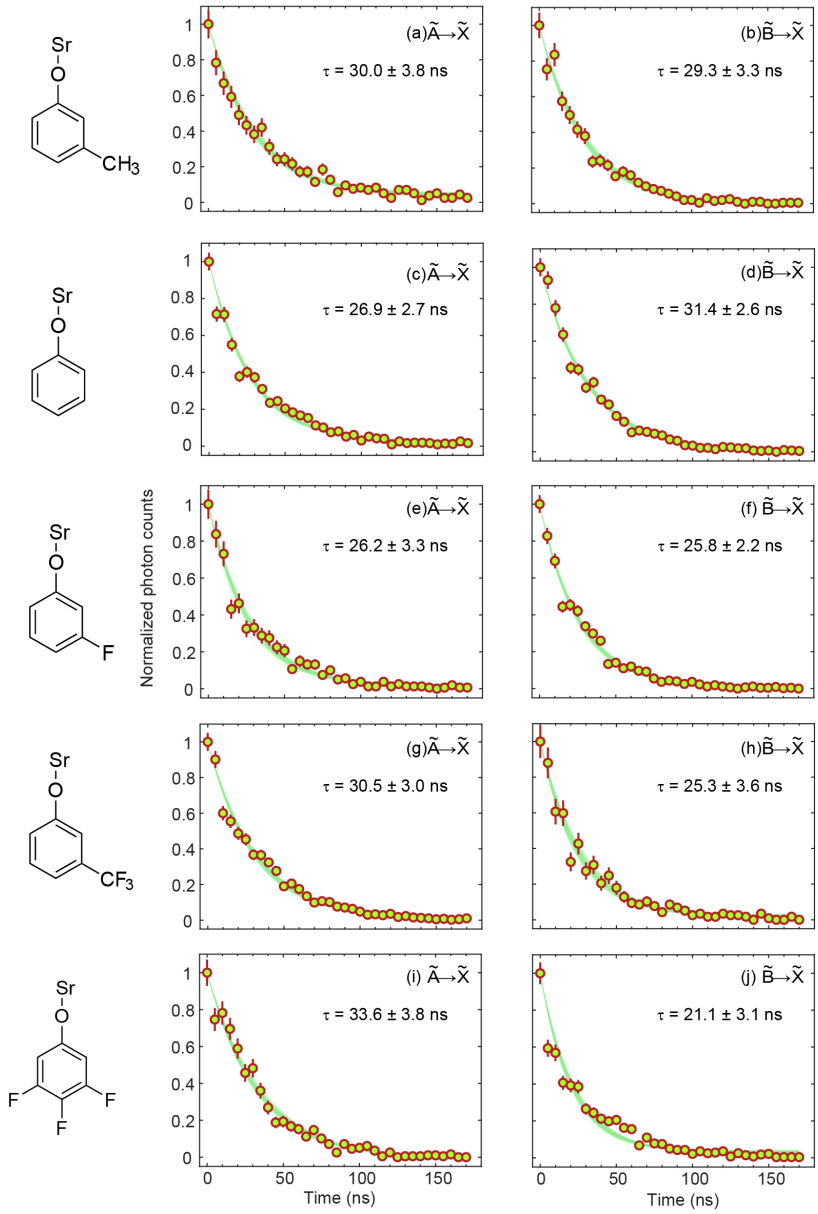

Figure 4.13: Fluorescence decay traces of all the SrOPh-X transitions studied in this work.

CaOPh-3,4,5-F_3 molecules show diagonal VBRs of $\approx 99\%$, potentially enabling laser cooling with fewer than five vibrational repumping lasers.

Generally, as shown in this work, the vibrational branching ratios were largely unaffected by the choice of ligand and at a level sufficient for laser cooling and trapping as well as quantum state preparation and measurement. This demonstration of the orthogonality of the OCC function to the ligand function lays the ground work for functionalizing molecules with quantum functional groups and establishes principles of chemical design that can be used to build molecules of increasing size, complexity, and function for quantum science and technology.

To achieve laser cooling of the molecule referred, rotational cycling transitions is the key and therefore it is necessary to obtain rotationally-resolved spectra and identify the these transitions. We will introduce the theory and measurement of the rotationally-resolved spectrum of SrOPh in the next chapter.

CHAPTER 5

High-resolution laser spectroscopy of asymmetric top molecule, SrOPh

The technique of laser cooling molecules necessitates rotational closure to ensure the efficiency of the cooling process. This requirement arises because effective cooling depends on the scattering of photons by molecules without dissipating into rotational states that are outside the cooling cycle [13]. Fortunately, the principles governing rotational transitions are well-defined by the selection rules. As a result, it is usually sufficient to employ just a single repumping laser to address the $N'' = 1 \rightarrow N' = 0$ transition. This strategy facilitates the efficient recycling of molecular states back into the cooling cycle, thereby enhancing the overall cooling efficiency.

To accurately identify the appropriate rotational closure transitions within a molecule, a typical method is to obtain its high-resolution rotational spectroscopy, where different rotational lines or even the rotational band structures can be well resolved. By fitting the observed spectral lines to the rotational model described in Chapter 2, one can identify the necessary transitions for effective laser cooling. In our research, we conduct high-resolution excitation spectroscopy on the SrOPh molecule, specifically investigating the $\widetilde{B}(v' = 0) - \widetilde{X}(v'' = 0)$ transition. The collected spectra were analyzed with multiple data-fitting techniques and algorithms to identify the necessary rotational transitions for cooling and to understand the molecular structure of SrOPh.

5.1 Experimental setup

The SrOPh molecules formed in the cryogenic cell were extracted out via a 9 mm cell aperture and entrained into a neon buffer gas beam. The excitation zone is $\approx$ 23 cm downstream the cell aperture. A cw laser from an ECDL was scanned with an increment of $25 - 50$ MHz near the $\widetilde{B}(v' = 0) - \widetilde{X}(v'' = 0)$ transition of SrOPh determined by the low-resolution PDL measurement. The fluorescence were collected by a PMT placed in the perpendicular direction. Due to the cooling effect in the expansion, SrOPh molecules in the beam are colder than those thermalized in the cell, at a temperature $\approx$ 23 K.

5.2 Rotational spectrum

The high resolution rotational spectrum is recorded in the Figure 5.1. Rotational states are labeled as $N_{K_aK_c}$, where N is the rotational angular momentum, a and c label the inertial axes lying along the Sr-O bond and perpendicular to the molecular plane, respectively, K_a and K_c are the projection of N onto the two axes in the prolate and oblate limits, respectively. Figure 5.1a shows the expansion of the two congested bands at 15238.5 cm^{-1}, while Figures 5.1b,c show two well-resolved rotational bands. A full rotational analysis is difficult due to the high density of rotational lines in the middle of the spectrum (Figure 5.1a) , but the individually resolved lines (Figures 5.1b,c) make it possible to fit the spectrum and extract some spectroscopic constants. Using a custom program to fit the spectral contour and PGOPHER[153] to refine and iterate the line assignments, we have assigned nearly 400 rotational transitions and obtained the final fitted spectrum given as the black traces in Figure 5.1. The fitting is in agreement with the experimental measurement for the middle broad bands and the $K'_a = 3 \leftarrow K''_a = 2$ and $K'_a = 4 \leftarrow K''_a = 3$ bands, as expanded in Figures 5.1a-c. The following few sections will focus on the calculation and simulation process of this work.

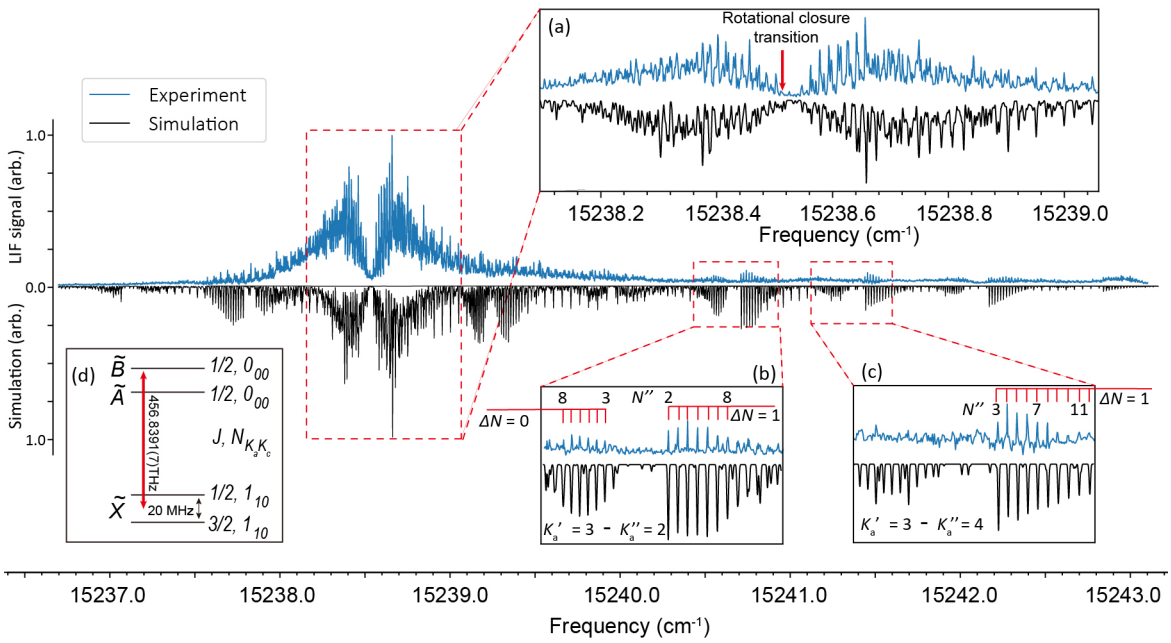

Figure 5.1: High-resolution rotationally-resolved excitation spectrum of the $\widetilde{B} \leftarrow \widetilde{X}$ transition of SrOPh. The upper trace (blue) shows the experimental spectrum and the lower trace (black) is the simulated spectrum with a Gaussian linewidth of 70 MHz and a rotational temperature $T_{\mathrm{sim}} = 2.5$ K. Insets (a), (b) and (c) are expansions of some local features. (a) displays detailed spectrum near 0-0 transition, while (b) and (c) show the $K_a' = 3 \leftarrow K_a'' = 2$ and $K_a' = 4 \leftarrow K_a'' = 3$ rotational bandheads, respectively. (d) shows the inferred position of the candidate rotational cycling transition between the spin-rotation manifold of the $N'' = 1$ state and $N' = 0$ state.

5.3 Molecular Hamiltonian

Consider the transition between $\tilde{X}^2A_1$ and $\tilde{A}^2B_2$. The transition amplitude is proportional to the following term:

$$\langle \tilde{A}^2B_2|(-e)r_c|\tilde{X}^2A_1\rangle, \tag{5.1}$$

where r_c is the coordinate of the electron on the axis c (the axis in the molecular plane and vertical to the Sr - O bond), and $(-e)r_c$ is the dipole moment along the axis c. As we take axis a (on which the Sr - O bond is lying) as our principle axis of the spherical coordinate, we may represent the dipole moment in the form of spherical tensor:

$$r_c = r\sin\theta\sin\phi = i\sqrt{\frac{2\pi}{3}}r\left[Y_1^{-1}(\theta,\phi) + Y_1^1(\theta,\phi)\right]. \tag{5.2}$$

We expect that the ground state $\tilde{X}^2A_1$ is similar to the $|\Lambda = 0\rangle$ state of a diatomic molecule, like the CaF X state, so we have:

$$|\tilde{X}^2A_1\rangle = |\eta_X\rangle|\Lambda = 0\rangle|S, \Sigma\rangle, \tag{5.3}$$

here η_X represents the radial electronic wavefunction, and other symbols follow their standard meanings. Notice that, the $Y_1^{-1}(\theta, \phi)$ and $Y_1^1(\theta, \phi)$ terms change the Λ value from 0 to -1 and 1, respectively, thus excited state $\tilde{A}^2B_2$ could be described by the superposition state of $\Lambda = 1$ and $\Lambda = -1$:

$$|\tilde{A}^2B_2\rangle = \frac{1}{\sqrt{2}}|\eta_A\rangle \left[|\Lambda = 1\rangle + |\Lambda = -1\rangle\right] |S, \Sigma\rangle, \tag{5.4}$$

similarly, for transition between X and B, the transition amplitude $\langle\tilde{B}^2B_1|(-e)r_b|\tilde{X}^2A_1\rangle$ is proportional to $\langle\tilde{B}^2B_1|[Y_1^1(\theta, \phi) - Y_1^{-1}(\theta, \phi)]|\tilde{X}^2A_1\rangle$, thus

$$|\tilde{B}^2B_1\rangle = \frac{1}{\sqrt{2}}|\eta_B\rangle \left[|\Lambda = 1\rangle - |\Lambda = -1\rangle\right] |S, \Sigma\rangle. \tag{5.5}$$

For simplicity, we define following notations:

$$|\Lambda_x\rangle = \frac{1}{\sqrt{2}}[|\Lambda = 1\rangle + |\Lambda = -1\rangle], \tag{5.6}$$

$$|\Lambda_y\rangle = \frac{1}{\sqrt{2}}[|\Lambda = 1\rangle - |\Lambda = -1\rangle]. \tag{5.7}$$

5.3.1 Rotational Hamiltonian

Here we follow the notation used in Ref. [13], with N, L to be the rotational and orbital angular momentum, respectively, and the subscripts denote the projection of these angular

momenta:

$$\begin{aligned} H_{Rot} =& B_a(N_a - L_a)^2 + B_b(N_b - L_b)^2 + B_c(N_c - L_c)^2 \\ =& B_a R_a^2 + B_b N_b^2 + B_c N_c^2 - 2(B_b N_b L_b + B_c N_c L_c) \\ =& B_a K^2 + B_b N_b^2 + B_c N_c^2 + H'. \end{aligned} \tag{5.8}$$

For SrOPh, $B_a \approx 0.192\text{cm}^{-1}$, $B_c \approx 0.0157\text{cm}^{-1}$, and $B_b \approx 0.0145\text{cm}^{-1}$. The perturbation terms $H' = -2(B_b N_b L_b + B_c N_c L_c)$ do not have first order contribution to the effective Hamiltonian: by replacing N_b, N_c, L_b and L_c with the creation and annihilation operators $N_\pm = N_b \pm iN_c$ and $L_\pm = L_b \pm iL_c$, we have

$$H' = -\frac{1}{2}(B_b + B_c)(N_+ L_+ + N_- L_-) - \frac{1}{2}(B_b - B_c)(N_+ L_- + N_- L_+), \tag{5.9}$$

we can see that $|\Lambda = 0\rangle$, $|\Lambda_x\rangle$ and $|\Lambda_y\rangle$ are not the eigen states of H', and H' mixes different electronic states. Due to the huge energy difference between X and A (or B) states, we can ignore the mixing between these X and A (or B) states, which is corresponding to the last two terms in Eq.(5.9).Therefore, we can rewrite the rotational Hamiltonian as follows:

$$\begin{aligned} H_{Rot} =& \left[\frac{1}{2}(B_b + B_c)(\mathbf{N}^2 - N_a^2) + B_a K^2\right] + \frac{1}{4}(B_b - B_c)(N_+^2 + N_-^2) \\ =& \left[\frac{1}{2}(B_b + B_c)(\mathbf{N}^2 - K^2 - \Lambda^2) + B_a K^2\right] \\ & - (B_b + B_c)K\Lambda + \frac{1}{4}(B_b - B_c)(N_+^2 + N_-^2), \end{aligned} \tag{5.10}$$

The rotational-orbital coupling term $-(B_b + B_c)K\Lambda$ may need further discussion, and we just skip it here. The diagonal elements of the rest of the rotational Hamiltonian are (set $\hbar = 1$):

$$\langle N, \Lambda, R, K | H_{Rot} | N, \Lambda, R, K \rangle = \frac{1}{2}(B_b + B_c)[N(N+1) - K^2 - \Lambda^2] + B_a K^2, \tag{5.11}$$

and the off diagonal elements are:

$$\langle N, K|H_{Rot}|N, K \pm 2\rangle = \frac{B_b - B_c}{4}\sqrt{(N \mp K)(N \pm K + 1)(N \mp K - 1)(N \pm K + 2)}, \quad (5.12)$$

where the anomalous commutation rules of different components of N in molecule-fixed coordinate system are applied (see Ref.[34], p.74):

$$[N_i, N_j] = -i\sum_k \epsilon_{ijk} N_k. \quad (5.13)$$

For SrOPh, since $|B_b - B_c|$ is much smaller than rotational constants B_b, B_c and B_a, we can apply the perturbation theory to obtain the rotational eigenstates. For example, for $N - 2 > |K| > 1$, the rotational eigenstate with the perturbation terms is

$$\begin{aligned}|\varphi_{Rot}(N, K)\rangle \approx & |N, K\rangle + \sum_{K'} \frac{\langle N, K'|H_{Rot}|N, K\rangle}{E_K^{(N)} - E_{K'}^{(N)}}|N, K'\rangle \\ = & |N, K\rangle + \frac{\lambda}{-K-1}\sqrt{(N-K)(N+K+1)(N-K-1)(N+K+2)}|N, K+2\rangle \\ & + \frac{\lambda}{K-1}\sqrt{(N+K)(N-K+1)(N+K-1)(N-K+2)}|N, K-2\rangle,\end{aligned} \quad (5.14)$$

where the dimensionless factor $\lambda = \frac{(B_b - B_c)}{4[4B_a - 2(B_b + B_c)]} \approx -4.0 \times 10^{-4}$. In low N approximation, the rotational eigenfunction $|\varphi_{Rot}(N, K)\rangle \approx |N, K\rangle$.

For basis choice $|R, K = R_a, L, \Lambda, S, \Sigma\rangle$, the rotational Hamiltonian is

$$\begin{aligned}H_{Rot} = & B_a R_a^2 + B_b R_b^2 + B_c R_c^2 \\ = & \left[\frac{1}{2}(B_b + B_c)(\mathbf{R}^2 - K^2) + B_a K^2\right] + \frac{1}{4}(B_b - B_c)(R_+^2 + R_-^2).\end{aligned} \quad (5.15)$$

5.3.1.1 Rotational Hamiltonian expressed in Hund's case (a) basis

An alternative choice is using Hund's case (a) and take $N = J - S$, which could be reasonable for SrOPh since it is close to a prolate type symmetric top and the the spin-orbital coupling

is significant. In this basis, the state representation is $|J,\Omega,\Lambda,K=\Omega-\Lambda-\Sigma,S,\Sigma\rangle$, and the rotational Hamiltonian reads

$$\begin{aligned}
H_{Rot} &= \sum_{i=a,b,c} B_i(J_i-L_i-S_i)^2 = \sum_{i=a,b,c} B_i(N_i-L_i)^2 \\
&= \left[\frac{1}{2}(B_b+B_c)(\mathbf{R}^2-R_a^2)+B_aR_a^2\right]+\frac{1}{4}(B_b-B_c)(R_+^2+R_-^2) \\
&= \left[\frac{1}{2}(B_b+B_c)[(\mathbf{J}-\mathbf{L}-\mathbf{S})^2-(J_a-L_a-S_a)^2]+B_a(J_a-L_a-S_a)^2\right] \\
&\quad +\frac{1}{4}(B_b-B_c)[(J_+-L_+-S_+)^2+(J_--L_--S_-)^2] \\
&= \frac{1}{2}(B_b+B_c)[J(J+1)+\mathbf{L}^2+\frac{3}{4}-2\mathbf{J}\cdot\mathbf{L}-2\mathbf{J}\cdot\mathbf{S}+2\mathbf{L}\cdot\mathbf{S}-K^2)]+B_aK^2 \\
&\quad +\frac{1}{4}(B_b-B_c)[(J_+-L_+-S_+)^2+(J_--L_--S_-)^2],
\end{aligned} \tag{5.16}$$

here we can omit the terms with $\mathbf{J}\cdot\mathbf{L}$, $\mathbf{S}_\pm{}^2$, $\mathbf{L^2}$, $\mathbf{L_\pm^2}$, $J_\pm L_\pm$ and $L_\pm S_\pm$ since they have almost no effect within the electronic state that we are considering, and the $\mathbf{L}\cdot\mathbf{S}$ term can be absorbed into the spin-orbital coupling Hamiltonian, so the rotational Hamiltonian could be written as:

$$\begin{aligned}
H_{rot} &= \frac{1}{2}(B_b+B_c)[J(J+1)-2\mathbf{J}\cdot\mathbf{S}-K^2)]+B_aK^2 \\
&\quad +\frac{1}{4}(B_b-B_c)[J_+^2-2J_+S_++J_-^2-2J_-S_-], \\
&= \frac{1}{2}(B_b+B_c)[J(J+1)-2J_a\Sigma-K^2)]+B_aK^2 \\
&\quad -\frac{1}{2}(B_b+B_c)(J_+S_-+J_-S_+)+\frac{1}{4}(B_b-B_c)[J_+^2-2J_+S_++J_-^2-2J_-S_-].
\end{aligned} \tag{5.17}$$

In this Hamiltonian, the diagonal terms are shown in the first line of the second equation on the right-hand side, in which the $J_a\Sigma$ term indicates the energy splitting of $N=J\pm\frac{1}{2}$ states. The off-diagonal terms are in the last line: $-\frac{1}{2}(B_b+B_c)(J_+S_-+J_-S_+)$ mixes the states $|J,\Omega\pm1,\Lambda,K,S,\Sigma\pm1\rangle$ and $|J,\Omega,\Lambda,K,S,\Sigma\rangle$, $J_\pm^2$ terms mix $|J,\Omega,\Lambda,K,S,\Sigma\rangle$ and $|J,\Omega\mp2,\Omega,\Lambda,K\mp2,S,\Sigma\rangle$ states, and $J_\pm S_\pm$ mixes $\Delta\Omega=\mp1,\Delta\Sigma=\pm1$ states:

$$\langle J,\Omega\pm1,\Lambda,K,S,\Sigma'|J_\mp S_\pm|J,\Omega,\Lambda,K,S,\Sigma\rangle=\delta_{\Sigma',\Sigma\pm1}\sqrt{J(J+1)-\Omega(\Omega\pm1)}, \tag{5.18}$$

$$\langle J,\Omega,\Lambda,K\mp2,S,\Sigma|J_{\pm}^2|J,\Omega,\Lambda,K,S,\Sigma\rangle=\sqrt{(J\mp\Omega)(J\pm\Omega+1)(J\mp\Omega-1)(J\pm\Omega+2)}, \tag{5.19}$$

$$\langle J,\Omega',\Lambda',K',S,\Sigma'|J_{\pm}S_{\pm}|J,\Omega,\Lambda,K,S,\Sigma\rangle=\delta_{\Lambda',\Lambda}\delta_{\Omega',\Omega\mp1}\delta_{\Sigma',\Sigma\pm1}\sqrt{J(J+1)-\Omega(\Omega\mp1)}. \tag{5.20}$$

According to Ref.[27] and Ref.[154], the rotational Hamiltonian should have a few correction terms regarding to the mixing of different Λ states:

$$\begin{aligned}H_{rot}=&B_aN_a^2+B_bN_b^2+B_cN_c^2+h_1(L_-^2N_+^2+L_+^2N_-^2)\\&+h_2[L_-^2(N_aN_-+N_-N_a)+L_+^2(N_aN_++N_+N_a)].\end{aligned} \tag{5.21}$$

We can rewrite the correction by taking $\mathbf{N}=\mathbf{J}-\mathbf{S}$:

$$h_1(L_-^2N_+^2+L_+^2N_-^2)=h_1L_-^2(J_+^2-2J_+S_+)+h_1L_+^2(J_-^2-2J_-S_-), \tag{5.22}$$

and

$$\begin{aligned}&h_2[L_-^2(N_aN_-+N_-N_a)+L_+^2(N_aN_++N_+N_a)]\\=&h_2L_-^2(J_aJ_-+J_-J_a-J_aS_--J_-S_a-S_aJ_--S_-J_a+S_aS_-+S_-S_a)\\&+h_2L_+^2(J_aJ_++J_+J_a-J_aS_+-J_+S_a-S_aJ_+-S_+J_a+S_aS_++S_+S_a)\\=&h_2L_-^2[(2J_a-1-2S_a)J_--2J_aS_-]+h_2L_+^2[(2J_a+1-2S_a)J_+-2J_aS_+].\end{aligned} \tag{5.23}$$

5.3.1.2 H_{rot} expression in Hund's case (b) basis

According to the fitting result based on the case (a) basis, we found that the spin-orbital coupling effect is negligible ($A_{SO}\approx0.1$ cm^{-1}, about three orders of magnitude smaller than the energy gap betweeen A and B states), thus the Hund's case (b) basis is better for state description. The basis expression is $|N,N_a,\Lambda,S,J\rangle$, in which N_a denotes the projection quantum number of N with respect to the rotational principle axis a. The relation between

case (a) and (b) basis is (adopted from Eq.(6.149) in Ref.[31])

$$|N, N_a, \Lambda, S, J\rangle = \sum_{\Sigma=-S}^{S} (-1)^{J-S+N_a} \sqrt{2N+1} \begin{pmatrix} J & S & N \\ \Omega & -\Sigma & -N_a \end{pmatrix} |J, \Omega, \Lambda, S, \Sigma\rangle. \tag{5.24}$$

here we omit the quantum number K for simplicity, but we should keep in mind that $K = \Omega - \Lambda - \Sigma = N_a - \Lambda$. Also, the sum should be taken over all possible value of Ω, though this is not indicated in the equation. The case (b) expression allows us to denote the molecular state with $N(K_a, K_c)J$, and we will update the notation in future analysis.

With the case (b) basis, the rotational Hamiltonian could be expressed as

$$H_{Rot} = \left[\frac{1}{2}(B_b + B_c)(\mathbf{N}^2 - N_a^2) + B_a(N_a - \Lambda)^2\right] + \frac{1}{4}(B_b - B_c)(N_+^2 + N_-^2). \tag{5.25}$$

5.3.2 Centrifugal distortion correction

According to the fitting result, we should consider some correction terms to fit better. Here we considered the centrifugal distortion terms first:

$$H_{\mathrm{CD}} = -D_N\mathbf{N}^4 - D_{NK}\mathbf{N}^2N_a^2 - D_KN_a^4 + H_NN^6 + H_{NK}N^4N_a^2 + H_{KN}N^2N_a^4 + H_KN_a^6 \tag{5.26}$$

In case (b) basis, the correction terms could be directly applied to the diagonal matrix elements. In Hund's case (a) basis, $\mathbf{N}^2$ could be expressed as

$$\mathbf{N}^2 = (\mathbf{J} - \mathbf{S})^2 = \mathbf{J}^2 - 2\mathbf{J}\cdot\mathbf{S} + \frac{3}{4} = \mathbf{J}^2 - 2J_aS_a + \frac{3}{4} - J_+S_- - J_-S_+. \tag{5.27}$$

For the off-diagonal matrix elements induced by the $\mathbf{N}^4$ operator, we may only keep the dominating terms (J^4 and J^3 terms):

$$\mathbf{N}^4 = \left[\mathbf{J}^2 - 2J_aS_a + \frac{3}{4} - J_+S_- - J_-S_+\right]^2 \approx \left[\mathbf{J}^2 - 2J_aS_a + \frac{3}{4}\right]^2 - 2\mathbf{J}^2\left(J_+S_- + J_-S_+\right), \tag{5.28}$$

$$N^6 \approx \left[\mathbf{J}^2 - 2J_aS_a + \frac{3}{4}\right]^3 - 3\mathbf{J}^4\left(J_+S_- + J_-S_+\right) \tag{5.29}$$

$$\begin{aligned} H_{\mathrm{CD}} \approx & -D_N\left[\mathbf{J}^2 - 2J_aS_a + \frac{3}{4}\right]^2 - D_{NK}N_a^2\left[\mathbf{J}^2 - 2J_aS_a + \frac{3}{4}\right] - D_KN_a^4 \\ & + \left(2D_N\mathbf{J}^2 + D_{NK}N_a^2\right)\left(J_+S_- + J_-S_+\right) \\ & + H_N\left[\mathbf{J}^2 - 2J_aS_a + \frac{3}{4}\right]^3 - 3H_N\mathbf{J^4}\left(J_+S_- + J_-S_+\right) \\ & + H_{NK}\left[\mathbf{J}^2 - 2J_aS_a + \frac{3}{4}\right]^2 N_a^2 - 2H_{NK}\mathbf{J}^2N_a^2\left(J_+S_- + J_-S_+\right) \\ & + H_{KN}\left[\mathbf{J}^2 - 2J_aS_a + \frac{3}{4}\right]N_a^4 - H_{KN}\left(J_+S_- + J_-S_+\right)N_a^4 + H_KN_a^6. \end{aligned} \tag{5.30}$$

When orbital angular momentum exists, the rotational distortion correction is [27]

$$\begin{aligned} H_{CD} = & -D_N\mathbf{N}^4 - D_{NK}N^2N_a^2 - D_KN_a^4 + \\ & + (h_{1N}/2)[\mathbf{N}^2, L_-^2N_+^2 + L_+^2N_-^2]_+ + (h_{1K}/2)[\mathbf{N}_a^2, L_-^2N_+^2 + L_+^2N_-^2]_+ \\ & + h_{2N}/2[\mathbf{N}^2, L_-^2(N_aN_- + N_-N_a) + L_+^2(N_aN_+ + N_+N_a)]_+ \\ & + h_{2K}/2[\mathbf{N}_a^2, L_-^2(N_aN_- + N_-N_a) + L_+^2(N_aN_+ + N_+N_a)]_+ \end{aligned} \tag{5.31}$$

where $[A,B]_+ = AB + BA$. Now we will investigate the matrix elements of these terms:

$$
\begin{aligned}
&(h_{1N}/2)[\mathbf{N}^2, L_-^2 N_+^2]_+ \\
=&(h_{1N}/2)L_-^2[\mathbf{J}^2 - 2J_aS_a + \frac{3}{4} - J_-S_+ - J_+S_-, J_+^2 - 2J_+S_+]_+ \\
=&(h_{1N}/2)L_-^2\left[2\left(\mathbf{J}^2 + \frac{3}{4}\right)(J_+^2 - 2J_+S_+) - 2[J_aS_a, J_+^2 - 2J_+S_+]_+\right. \\
&\left.-[J_-S_+ + J_+S_-, J_+^2 - 2J_+S_+]_+\right] \\
=&(h_{1N}/2)L_-^2\left[2\left(\mathbf{J}^2 + \frac{3}{4}\right)(J_+^2 - 2J_+S_+) - 4(J_a+1)S_aJ_+^2 - 4S_aJ_+S_+\right. \\
&\left.-2(\mathbf{J}^2J_+ - J_a^2J_+ + J_+J_a)S_+ - 2J_+^3S_- + 2J_+^2\right] \\
=&h_{1N}L_-^2\left[\left(\mathbf{J}^2 + \frac{3}{4}\right)(J_+^2 - 2J_+S_+) - 2(J_a+1)S_aJ_+^2 - 2S_aJ_+S_+\right. \\
&\left.-(\mathbf{J}^2J_+S_+ - J_a^2J_+S_+ - J_aJ_+S_+ - J_+S_+) - J_+^3S_- + J_+^2\right] \\
=&h_{1N}L_-^2\left[\left(\mathbf{J}^2 + \frac{7}{4} - 2J_aS_a - 2S_a\right)J_+^2 - \left(3\mathbf{J}^2 - J_a^2 - J_a + \frac{3}{2}\right)J_+S_+ - J_+^3S_-\right]
\end{aligned}
\tag{5.32}
$$

similarly,

$$
\begin{aligned}
&(h_{1N}/2)[\mathbf{N}^2, L_+^2 N_-^2]_+ \\
=&(h_{1N}/2)L_+^2[\mathbf{J}^2 - 2J_aS_a + \frac{3}{4} - J_-S_+ - J_+S_-, J_-^2 - 2J_-S_-]_+ \\
=&(h_{1N}/2)L_+^2\left[2\left(\mathbf{J}^2 + \frac{3}{4}\right)(J_-^2 - 2J_-S_-) - 2[J_aS_a, J_-^2 - 2J_-S_-]_+\right. \\
&\left.-[J_-S_+ + J_+S_-, J_-^2 - 2J_-S_-]_+\right] \\
=&(h_{1N}/2)L_+^2\left[2\left(\mathbf{J}^2 + \frac{3}{4}\right)(J_-^2 - 2J_-S_-) - 4(J_a-1)S_aJ_-^2 + 4S_aJ_-S_-\right. \\
&\left.-2(\mathbf{J}^2 - J_a^2 + J_a - 1)J_-S_- - 2J_-^3S_+ + 2J_-^2\right] \\
=&h_{1N}L_+^2\left[\left(\mathbf{J}^2 + \frac{3}{4}\right)(J_-^2 - 2J_-S_-) - 2(J_a-1)S_aJ_-^2 + 2S_aJ_-S_-\right. \\
&\left.-(\mathbf{J}^2 - J_a^2 + J_a - 1)J_-S_- - J_-^3S_+ + J_-^2\right] \\
=&h_{1N}L_+^2\left[\left(\mathbf{J}^2 + \frac{7}{4} - 2J_aS_a + 2S_a\right)J_-^2 - \left(3\mathbf{J}^2 - J_a^2 + J_a + \frac{3}{2}\right)J_-S_- - J_-^3S_+\right]
\end{aligned}
\tag{5.33}
$$

h_{1K} term:

$$
\begin{aligned}
&(h_{1K}/2)[N_a^2, L_-^2 N_+^2 + L_+^2 N_-^2]_+ \\
=&(h_{1K}/2)[(J_a - S_a)^2, L_-^2 (J_+^2 - 2J_+ S_+) + L_+^2 (J_-^2 - 2J_- S_-)]_+ \\
=&(h_{1K}/2) L_-^2 [(J_a - S_a)^2, (J_+^2 - 2J_+ S_+)]_+ + (h_{1K}/2) L_+^2 [(J_a - S_a)^2, (J_-^2 - 2J_- S_-)]_+ \\
=&h_{1K} L_-^2 \Bigg\{ \left[J_a^2 + 2J_a + \frac{9}{4} - 2(J_a+1)S_a \right] J_+^2 - \left(2J_a^2 + 2J_a + \frac{5}{2} \right) J_+ S_+ \Bigg\} \\
&+ h_{1K} L_+^2 \Bigg\{ \left[J_a^2 - 2J_a + \frac{9}{4} - 2(J_a-1)S_a \right] J_-^2 - \left(2J_a^2 - 2J_a + \frac{5}{2} \right) J_- S_- \Bigg\}.
\end{aligned}
\tag{5.34}
$$

h_{2N} terms:

$$
\begin{aligned}
&(h_{2N}/2)[\mathbf{N}^2, L_-^2 (N_a N_- + N_- N_a)]_+ \\
=&(h_{2N}/2) L_-^2 \left[\mathbf{J}^2 - 2J_a S_a + \frac{3}{4} - J_- S_+ - J_+ S_-, (J_a J_- + J_- J_a - 2J_- S_a - 2J_a S_-) \right]_+ \\
=&(h_{2N}/2) L_-^2 \Bigg\{ \left[\mathbf{J}^2 - 2J_a S_a + \frac{3}{4}, (2J_a - 1 - 2S_a) J_- \right]_+ + \left[\mathbf{J}^2 - 2J_a S_a + \frac{3}{4}, -2J_a S_- \right]_+ \\
&- [J_- S_+ + J_+ S_-, (2J_a - 1 - 2S_a) J_- - 2J_a S_-]_+ \Bigg\} \\
=&h_{2N} L_-^2 \Bigg[\left(2\mathbf{J}^2 - 4J_a S_a + \frac{5}{2} + 2S_a \right) (J_a - 1/2 - S_a) J_- \\
&+ \left(-4\mathbf{J}^2 - \frac{3}{2} + 2J_a^2 \right) J_a S_- - 2(J_a - 1) J_-^2 S_+ \Bigg],
\end{aligned}
\tag{5.35}
$$

and

$$
\begin{aligned}
&(h_{2N}/2)[\mathbf{N}^2, L_+^2(N_aN_+ + N_+N_a)]_+ \\
=&(h_{2N}/2)L_+^2\left[\mathbf{J}^2 - 2J_aS_a + \frac{3}{4} - J_-S_+ - J_+S_-, (J_aJ_+ + J_+J_a - 2J_+S_a - 2J_aS_+)\right]_+ \\
=&(h_{2N}L_+^2)\Bigg[(J_a + 1/2 - S_a)\left(2\mathbf{J}^2 + \frac{3}{2} - 4J_aS_a - 2S_a\right)J_+ - 2\left(\mathbf{J}^2 + \frac{3}{4}\right)J_aS_+ \\
&- 2(J_a+1)J_+^2S_- - 2J_aJ_+J_-S_+ - J_a(2J_a - 1 + 2S_a)S_+ + J_+S_-S_+ + J_aJ_+\Bigg] \\
=&h_{2N}L_+^2(J_a + 1/2 - S_a)\left(2\mathbf{J}^2 + \frac{5}{2} - 4J_aS_a - 2S_a\right)J_+ \\
&+ h_{2N}L_+^2\left(-4\mathbf{J}^2 - \frac{3}{2} + 2J_a^2\right)J_aS_+ - 2h_{2N}L_+^2(J_a+1)J_+^2S_-.
\end{aligned}
\tag{5.36}
$$

h_{2K} terms:

$$
\begin{aligned}
&(h_{2K}/2)[N_a^2, L_-^2(N_aN_- + N_-N_a)]_+ \\
=&(h_{2K}/2)L_-^2[J_a^2 - 2J_aS_a + 1/4, (J_aJ_- + J_-J_a - 2J_-S_a - 2J_aS_-)]_+ \\
=&h_{2K}L_-^2\left[(2J_a - 1 - 2S_a)(J_a^2 - J_a - 2J_aS_a + S_a + 3/4)J_- - (2J_a^2 + 1/2)J_aS_-\right],
\end{aligned}
\tag{5.37}
$$

and

$$
\begin{aligned}
&(h_{2K}/2)[N_a^2, L_+^2(N_aN_+ + N_+N_a)]_+ \\
=&(h_{2K}/2)L_+^2[J_a^2 - 2J_aS_a + 1/4, (J_aJ_+ + J_+J_a - 2J_+S_a - 2J_aS_+)]_+ \\
=&h_{2K}L_+^2\left[(2J_a + 1 - 2S_a)(J_a^2 + J_a - 2J_aS_a - S_a + 3/4)J_+ - (2J_a^2 + 1/2)J_aS_+\right].
\end{aligned}
\tag{5.38}
$$

5.3.3 Spin-orbital coupling

Noticed that the SrOPh molecule is very close to a prolate symmetric top molecule (Ray's asymmetry parameter for SrOPh is $\kappa = \frac{2B_b - B_a - B_c}{B_a - B_c} \approx -0.988$, and $\kappa = -1$ for prolate symmetric top), and the rotational constants are about 3 to 4 orders of magnitude smaller than the spin-orbital coupling coefficients of SrOH (≈ 263 cm^{-1}), it is possible that $|A_a\Lambda| \gg |B_aN|$ in SrOPh and thus Hund's case (a) basis is more suitable for the description of the lowest few rotational states, which are of our interest.To handle this situation, we separate

the L and R from the total rotational angular moment N, and $N = |J \pm \frac{1}{2}|$ denotes the splitting of J level, as indicated in the previous subsection. In such basis, the L-S coupling Hamiltonian reads

$$H_{LS} = A_a L_a S_a. \tag{5.39}$$

Here A_a is the spin-orbital coupling factor. The other two terms $A_b L_b S_b$ and $A_c L_c S_c$ are omitted since they are mixing X and A (or B) states and have no effect on rotational level. With the expression, we have:

$$\langle \tilde{B}^2 B_1, S, \Sigma' | H_{LS} | \tilde{A}^2 B_2, S, \Sigma'' \rangle = \delta_{\Sigma''\Sigma'} \Sigma'' \langle \Lambda_y | A_a L_a | \Lambda_x \rangle = A_a \delta_{\Sigma''\Sigma'} \Sigma''. \tag{5.40}$$

Thus, we could write down the molecular Hamiltonian with LS coupling term, in basis of the molecular electronic states $\{|\tilde{A}^2 B_2, S, \Sigma\rangle, |\tilde{B}^2 B_1, S, \Sigma\rangle\}$:

$$H_{el} + H_{SO} = \begin{pmatrix} E_A & A_a \Sigma \\ A_a \Sigma & E_B \end{pmatrix}, \tag{5.41}$$

from the Hamiltonian, we can obtain the energies

$$E_{\pm} = \frac{E_A + E_B}{2} \pm \frac{1}{2} \sqrt{(E_B - E_A)^2 + 4 A_a^2 \Sigma^2} \tag{5.42}$$

as well as the new eigenstate vectors

$$\phi_- = [\cos\beta |\tilde{A}^2 B_2\rangle + \sin\beta |\tilde{B}^2 B_1\rangle] |S, \Sigma\rangle, \tag{5.43}$$

$$\phi_+ = [-\sin\beta |\tilde{A}^2 B_2\rangle + \cos\beta |\tilde{B}^2 B_1\rangle] |S, \Sigma\rangle, \tag{5.44}$$

where the parameter β satisfies following equations

$$\sin 2\beta = -\frac{2 A_a \Sigma}{\sqrt{(E_B - E_A)^2 + 4 A_a^2 \Sigma^2}} \text{ and } \cos 2\beta = \frac{E_B - E_A}{\sqrt{(E_B - E_A)^2 + 4 A_a^2 \Sigma^2}}, \tag{5.45}$$

and $\beta \in \left[-\frac{\pi}{4}, \frac{\pi}{4}\right]$, and the sign of β is opposite to Σ. In Eq.(5.42), if we take $A_a \approx 263\text{cm}^{-1}$ (based on SrOH measurement) and the energy splitting between $\tilde{A}$ and $\tilde{B}$ states $E_+ - E_- = \sqrt{(E_B - E_A)^2 + A_a^2} \approx 390\text{cm}^{-1}$ (based on the experiment), we can find $E_A - E_B \approx 288\text{cm}^{-1}$ (this energy difference is in the approximation of ignoring the spin-orbital coupling effect), which is close to the spin-orbital coupling strength in magnitude. This shows that the molecular symmetry and the spin-orbital coupling effect together decide the electronic eigenstate vectors and energies in SrOPh. Therefore, we may re-define the two electronic states $|\tilde{A}\rangle$ and $|\tilde{B}\rangle$ as Eq.(5.43) and Eq.(5.44), respectively:

$$\begin{aligned} |\tilde{A}\rangle =& |\eta\rangle \left[\cos\left(\frac{\pi}{4} - \beta\right)|\Lambda = 1\rangle + \sin\left(\frac{\pi}{4} - \beta\right)|\Lambda = -1\rangle\right]|S, \Sigma\rangle \\ =& \sum_{\Lambda=-1,1} \cos\left(\frac{\pi}{4} - \Lambda\beta\right)|\eta\rangle|\Lambda\rangle|S, \Sigma\rangle \end{aligned} \tag{5.46}$$

$$\begin{aligned} |\tilde{B}\rangle =& |\eta\rangle \left[\cos\left(\frac{\pi}{4} + \beta\right)|\Lambda = 1\rangle - \sin\left(\frac{\pi}{4} + \beta\right)|\Lambda = -1\rangle\right]|S, \Sigma\rangle \\ =& \sum_{\Lambda=-1,1} \Lambda\cos\left(\frac{\pi}{4} + \Lambda\beta\right)|\eta\rangle|\Lambda\rangle|S, \Sigma\rangle. \end{aligned} \tag{5.47}$$

Actually, these two electronic states are both double degenerate. For example, in A states,

$$\phi_{A,1} = |\eta\rangle \left[\cos\left(\frac{\pi}{4} - \beta\right)|\Lambda = 1\rangle + \sin\left(\frac{\pi}{4} - \beta\right)|\Lambda = -1\rangle\right]|S, \Sigma\rangle \tag{5.48}$$

has the same energy as the state

$$\phi_{A,2} = |\eta\rangle \left[\cos\left(\frac{\pi}{4} + \beta\right)|\Lambda = 1\rangle + \sin\left(\frac{\pi}{4} + \beta\right)|\Lambda = -1\rangle\right]|S, -\Sigma\rangle. \tag{5.49}$$

We can introduce an operator $\hat{P}$ which reflects the wavefunction across the molecular plane σ_v:

$$\hat{P}|\tilde{A}, \pm\rangle = \pm|\tilde{A}, \pm\rangle, \tag{5.50}$$

where $\pm$ denotes the parity of the basis functions. For concreteness, we can define the eigenstates as follows:

$$\begin{aligned}|\tilde{A},\pm\rangle =&\frac{1}{\sqrt{2}}\cos\left(\frac{\pi}{4}-\beta\right)\left[|\eta,\Lambda=1,S,\Sigma=1/2\rangle \pm |\eta,\Lambda=-1,S,\Sigma=-1/2\rangle\right]\\ &+\frac{1}{\sqrt{2}}\sin\left(\frac{\pi}{4}-\beta\right)\left[\pm|\eta,\Lambda=1,S,\Sigma=-1/2\rangle + |\eta,\Lambda=-1,S,\Sigma=1/2\rangle\right],\end{aligned} \tag{5.51}$$

and similarly, for B state, the definition is

$$\begin{aligned}|\tilde{B},\pm\rangle =&\frac{1}{\sqrt{2}}\cos\left(\frac{\pi}{4}+\beta\right)\left[|\eta,\Lambda=1,S,\Sigma=1/2\rangle \pm |\eta,\Lambda=-1,S,\Sigma=-1/2\rangle\right]\\ &-\frac{1}{\sqrt{2}}\sin\left(\frac{\pi}{4}+\beta\right)\left[\pm|\eta,\Lambda=1,S,\Sigma=-1/2\rangle + |\eta,\Lambda=-1,S,\Sigma=1/2\rangle\right],\end{aligned} \tag{5.52}$$

and X state:

$$|\tilde{X},\Lambda=0,\pm\rangle = \frac{1}{\sqrt{2}}\left[\eta_X,\Lambda=0,S,\Sigma=1/2\rangle \pm |\eta_X,\Lambda=0,S,\Sigma=-1/2\rangle\right]. \tag{5.53}$$

Note: in the simulation later then March 1, we will take $\beta = 0$ since the SO coupling is weak, unless the value is indicated.

5.3.3.1 Spin-orbital coupling Hamiltonian in Hund's case (b) basis

Combine the basis transform Eq.(5.24) and the Hamiltonian Eq.(5.39), we can obtain the matrix elements:

$$\begin{aligned}
&\langle N', N'_a, \Lambda', S, J'|H_{LS}|N, N_a, \Lambda, S, J\rangle \\
=&\sum_{\Sigma=-S}^{S}\sum_{\Sigma'=-S}^{S}(-1)^{J+J'+N_a+N'_a-1}\sqrt{(2N+1)(2N'+1)} \\
&\times \begin{pmatrix} J' & S & N' \\ \Sigma'+N'_a & -\Sigma' & -N'_a \end{pmatrix}\begin{pmatrix} J & S & N \\ \Sigma+N_a & -\Sigma & -N_a \end{pmatrix} \\
&\times \delta_{JJ'}\delta_{N_aN'_a}\delta_{\Sigma\Sigma'}\delta_{\Lambda\Lambda'}A_{SO}\Lambda\Sigma \\
=&\sum_{\Sigma=-S}^{S}\delta_{JJ'}\delta_{N_aN'_a}\delta_{\Lambda\Lambda'}A_{SO}\Lambda\Sigma\sqrt{(2N+1)(2N'+1)} \\
&\times \begin{pmatrix} J & S & N' \\ \Sigma+N_a & -\Sigma & -N_a \end{pmatrix}\begin{pmatrix} J & S & N \\ \Sigma+N_a & -\Sigma & -N_a \end{pmatrix},
\end{aligned} \tag{5.54}$$

and we can see that the spin-orbital coupling terms mix the $N = J \pm \frac{1}{2}$ states.

5.3.4 Spin-rotational coupling

The spin-rotational coupling Hamiltonian in C_{2v} molecule is

$$\begin{aligned}
H_{SR} =&\epsilon_{aa}N_aS_a + \epsilon_{bb}N_bS_b + \epsilon_{cc}N_cS_c \\
=&\epsilon_{aa}(J_a - S_a)S_a + \epsilon_{bb}(J_b - S_b)S_b + \epsilon_{cc}(J_c - S_c)S_c,
\end{aligned} \tag{5.55}$$

In case (a) basis, we can omit the $S^2_{a,b,c}$ terms because they do not split rotational levels and only shift the electronic states, and then rewrite it in form of raising and lowering operators:

$$H_{SR} = \epsilon_{aa}J_aS_a + \frac{\epsilon_{bb}+\epsilon_{cc}}{4}(J_+S_- + J_-S_+) + \frac{\epsilon_{bb}-\epsilon_{cc}}{4}(J_+S_+ + J_-S_-). \tag{5.56}$$

In case (b) basis, the expression is

$$H_{SR} = \epsilon_{aa} N_a S_a + \frac{\epsilon_{bb} + \epsilon_{cc}}{4}(N_+ S_- + N_- S_+) + \frac{\epsilon_{bb} - \epsilon_{cc}}{4}(N_+ S_+ + N_- S_-). \tag{5.57}$$

The spin-rotation Hamiltonian mntrix elements are given in Ref.[155]:

$$\begin{aligned}
&\langle N', N'_a, \Lambda, S, J | H_{SR} | N, N_a, \Lambda, S, J \rangle \\
&= \sum_{k=0}^{2} \sqrt{\frac{3}{2}(2k+1)(2N+1)(2N'+1)}(-1)^{J+S-N'_a} \begin{Bmatrix} N & S & J \\ S & N' & 1 \end{Bmatrix} \sum_q T_q^k(\epsilon) \begin{pmatrix} N' & k & N \\ -N'_a & q & N_a \end{pmatrix} \\
&\times \frac{1}{2} \left[(-1)^k \sqrt{N(N+1)(2N+1)} \begin{Bmatrix} 1 & 1 & k \\ N' & N & N \end{Bmatrix} + \sqrt{N'(N'+1)(2N'+1)} \begin{Bmatrix} 1 & 1 & k \\ N & N' & N' \end{Bmatrix} \right],
\end{aligned} \tag{5.58}$$

where $T_q^k(\epsilon)$ is

$$T_q^k(\epsilon) = \begin{cases} -\frac{1}{\sqrt{3}}(\epsilon_{aa} + \epsilon_{bb} + \epsilon_{cc}), & k = 0, q = 0 \\ \frac{1}{2}(\epsilon_{bb} - \epsilon_{cc}), & k = 2, q = \pm 2 \\ \frac{1}{\sqrt{6}}(2\epsilon_{aa} - \epsilon_{bb} - \epsilon_{cc}), & k = 2, q = 0 \\ 0, & \text{other cases} \end{cases} \tag{5.59}$$

The diagonal matrix element is

$$
\begin{aligned}
&\langle N, N_a, \Lambda, S, J | H_{SR} | N, N_a, \Lambda, S, J \rangle \\
&= \sum_{k=0,2} \sqrt{\frac{3}{2}(2k+1)}(2N+1)(-1)^{N-N'_a+1} \frac{\frac{3}{4}+N(N+1)-J(J+1)}{\sqrt{6N(N+1)(2N+1)}} \sum_q T_0^k(\epsilon) \begin{pmatrix} N & k & N \\ -N_a & 0 & N_a \end{pmatrix} \\
&\quad \times \frac{1}{2} \left[\sqrt{N(N+1)(2N+1)} \begin{Bmatrix} 1 & 1 & k \\ N & N & N \end{Bmatrix} + \sqrt{N(N+1)(2N+1)} \begin{Bmatrix} 1 & 1 & k \\ N & N & N \end{Bmatrix} \right] \\
&= \sum_{k=0,2} \sqrt{\frac{2k+1}{4}}(2N+1)(-1)^{N-N'_a+1} \sum_q T_0^k(\epsilon) \begin{pmatrix} N & k & N \\ -N_a & 0 & N_a \end{pmatrix} \\
&\quad \times \begin{Bmatrix} 1 & 1 & k \\ N & N & N \end{Bmatrix} \left[\frac{3}{4} + N(N+1) - J(J+1) \right] \\
&= \sum_{k=0,2} \sqrt{\frac{2k+1}{4}}(2N+1)(-1)^{N-N'_a+1} T_0^k(\epsilon) \begin{pmatrix} N & k & N \\ -N_a & 0 & N_a \end{pmatrix} \\
&\quad \times \begin{Bmatrix} 1 & 1 & k \\ N & N & N \end{Bmatrix} \left[\frac{3}{4} + N(N+1) - J(J+1) \right]
\end{aligned}
\tag{5.60}
$$

By using the following formulas

$$
\begin{Bmatrix} 1 & 1 & 0 \\ N & N & N \end{Bmatrix} = -\frac{1}{\sqrt{3(2N+1)}} \tag{5.61}
$$

$$
\begin{pmatrix} N & 0 & N \\ -N_a & 0 & N_a \end{pmatrix} = (-1)^{N-N_a} \frac{1}{\sqrt{2N+1}} \tag{5.62}
$$

$$
\begin{Bmatrix} 1 & 1 & 2 \\ N & N & N \end{Bmatrix} = \frac{-3+4N(N+1)}{\sqrt{30(2N-1)N(N+1)(2N+1)(2N+3)}}, \tag{5.63}
$$

we have

$$\begin{aligned}
&\langle N, N_a, \Lambda, S, J|H_{SR}|N, N_a, \Lambda, S, J\rangle \\
&= \left[-\frac{T_0^0(\epsilon)}{2\sqrt{3}} + T_0^2(\epsilon)(-1)^{N-N_a'+1}\frac{\sqrt{2N+1}[4N(N+1)-3]}{2\sqrt{6(2N-1)N(N+1)(2N+3)}}\begin{pmatrix} N & 2 & N \\ -N_a & 0 & N_a\end{pmatrix}\right] \\
&\times \left[\frac{3}{4} + N(N+1) - J(J+1)\right].
\end{aligned} \tag{5.64}$$

The off diagonal matrix elements are related to $T_{\pm 2}^2(\epsilon)$, which connect states with $\Delta N_a = \pm 2$. Since the energy gap between different N_a states is much greater than $T_{\pm 2}^2(\epsilon)$, For simplicity, we may just ignore them (This means that the difference between ϵ_{bb} and ϵ_{cc} is not going to be measured or fitted).

5.3.5 Centrifugal distortion correction for spin-rotation

The correction for centrifugal distortion to the spin-rotation in Hund's case (b) is [156]:

$$\begin{aligned}
H_{SR}' =& \Delta_N^s \mathbf{N}^4(\mathbf{N}\cdot\mathbf{S}) + \Delta_{KN}^s(\mathbf{N}\cdot\mathbf{S})\mathbf{N}^2N_a^2 + \Delta_{NK}^s(\mathbf{N}^2N_aS_a + N_aS_a\mathbf{N}^2) \\
&+ \Delta_K^s N_a^3 S_a + \delta_K^s N_a S_a(N_+^2 + N_-^2)
\end{aligned} \tag{5.65}$$

In Hund's case (a) basis, the correction is [27]

$$\begin{aligned}
H_{SR}' =& \epsilon_1(L_-^2N_+S_+ + L_+^2N_-S_-) + \epsilon_{2a}[L_-^2(N_aS_- + S_-N_a) + L_+^2(N_aS_+ + S_+N_a)] \\
&+ \epsilon_{2b}[L_-^2(N_-S_a + S_aN_-) + L_+^2(N_+S_a + S_aN_+)]
\end{aligned} \tag{5.66}$$

The correction terms are only applied to the excited states since the $L_{\pm}^2$ operator connect the $\Lambda = \pm 1$ states. Noticed that $N_{\pm} = J_{\pm} - S_{\pm}$:

$$\begin{aligned}
H'_{SR} =&\epsilon_1(L_-^2 J_+ S_+ + L_+^2 J_- S_-) \\
&+ \epsilon_{2a}[L_-^2(J_a S_- + S_- J_a - S_a S_- - S_- S_a) + L_+^2(J_a S_+ + S_+ J_a - S_a S_+ - S_+ S_a)] \\
&+ \epsilon_{2b}[L_-^2(J_- S_a + S_a J_- - S_a S_- - S_- S_a) + L_+^2(J_+ S_a + S_a J_+ - S_a S_+ - S_+ S_a)] \\
=&\epsilon_1(L_-^2 J_+ S_+ + L_+^2 J_- S_-) + \epsilon_{2a}[L_-^2(J_a S_- + S_- J_a) + L_+^2(J_a S_+ + S_+ J_a)] \\
&+ \epsilon_{2b}[L_-^2(J_- S_a + S_a J_-) + L_+^2(J_+ S_a + S_a J_+)] \\
=&\epsilon_1(L_-^2 J_+ S_+ + L_+^2 J_- S_-) + \epsilon_{2a}[L_-^2(J_a S_- + S_- J_a) + L_+^2(J_a S_+ + S_+ J_a)] \\
&+ \epsilon_{2b}[L_-^2(J_- S_a + S_a J_-) + L_+^2(J_+ S_a + S_a J_+)].
\end{aligned} \tag{5.67}$$

5.3.6 Coriolis term

The spin-orbital coupling does not affect the relative positions of the rotational lines, since it does not split any rotational levels or change their degeneracy. However, the Coriolis term

$$H_{Cor} = -2A_{Cor} N_a L_a = -2A_{Cor}(J_a - S_a)L_a \tag{5.68}$$

can have non-zero contribution to the rotational Hamiltonian:

$$\langle J, \Omega, \Lambda, S, \Sigma | H_{Cor} | J, \Omega, \Lambda, S, \Sigma \rangle = -2A_{Cor}\Omega\Lambda. \tag{5.69}$$

In case (b) basis, the contribution is

$$\langle N, N_a, \Lambda, S, J | H_{Cor} | N, N_a, \Lambda, S, J \rangle = -2A_{Cor} N_a \Lambda. \tag{5.70}$$

5.4 Molecular state representation and transition

Combining the Hamiltonian we have discussed above, the molecular Hamiltonian is

$$H = H_{el} + H_{SO} + H_{Rot} + H_{SR} + H_{Cor}, \tag{5.71}$$

where the five terms on the right hand side are corresponding to electronic, spin-orbital coupling, rotational, spin-rotational and rotation-orbital coupling Hamiltonian. In case (a) basis, the three lowest eigenstates of $H_{el} + H_{SO}$, $|\tilde{X}\rangle$, $|\tilde{A}\rangle$ and $|\tilde{B}\rangle$ could be described by Eq.(5.53), Eq.(5.51) and Eq.(5.52), respectively. After combining the rotational states and the electronic state representation and fixing the parity definition for the rotational state $|J, \Omega\rangle$, we can obtain a set of basis for the X state which satisfies the C_{2v} symmetry:

$$|\eta_X, J, \Omega, \pm\rangle = \frac{1}{\sqrt{2}} \left[|\eta_X, J, \Omega, S, \Sigma = 1/2\rangle \pm (-1)^{J-\Omega+S-\Sigma} |\eta_X, J, -\Omega, S, \Sigma = -1/2\rangle \right], \tag{5.72}$$

(Note: comparing to the last version, here we remove the S, Σ label on the left because we should keep the dimensions of the vector space on the both sides to be the same ($d = 4J + 2$ for each J).) For A and B states, the molecular eigenbasis is a little bit complicated since Ω is not a good quantum number for the asymmetric top molecule. However, we may still define a set of parity eigenstates, in which Ω is a good quantum number, as follows:

$$|\eta, J, \Omega, S, \Sigma, \pm\rangle = \frac{1}{\sqrt{2}} \left[|\eta, J, \Omega, \Lambda = 1, S, \Sigma\rangle \pm (-1)^{J-\Omega+S-\Sigma} |\eta, J, -\Omega, \Lambda = -1, S, -\Sigma\rangle \right] \tag{5.73}$$

In Hund's case (b) basis $|N, N_a, \Lambda, S, J\rangle$, the electronic Hamiltonian actually has off-diagonal terms:

$$\begin{aligned} H_{el} =& \frac{E_A}{2}(|\Lambda = +1\rangle + |\Lambda = -1\rangle)(\langle\Lambda = +1| + \langle\Lambda = -1|) \\ &+ \frac{E_B}{2}(|\Lambda = +1\rangle - |\Lambda = -1\rangle)(\langle\Lambda = +1| - \langle\Lambda = -1|) \\ =& \frac{E_A + E_B}{2} - \frac{E_B - E_A}{2}(|\Lambda = 1\rangle\langle\Lambda = -1| + |\Lambda = -1\rangle\langle\Lambda = 1|). \end{aligned} \tag{5.74}$$

It is easy to check that H_{SR} and H_{Cor} are still diagonal in this basis. The A and B eigenstates could be described as the combination of these state vectors with the same parity, with the coefficients determined by diagonalization of the Hamiltonian matrices. We will have some further analysis in the following few subsections.

5.4.1 Molecular state

In this section, we will express the asymmetric top molecular state $|\eta, J, K_a, K_c, S, \Sigma, \pm\rangle$ as the superposition of several symmetric top molecular states. K_a and K_c are the projection rotation quantum number of J in the limits of prolate and oblate symmetric tops, and here they are only used for labeling the energy levels obtained from matrix diagonalization. Combining the expressions of electronic and rotational states, we have:

X state:

$$|\tilde{X}, J, K_a, K_c, S, \Sigma\rangle = \sum_{\Sigma'=\pm 1/2} \sum_{\Omega=1/2}^{J} g_{\Omega\Sigma'}^{(X,JK_aK_c)} |\eta_X, J, \Omega, S, \Sigma', \pm\rangle, \tag{5.75}$$

A state:

$$|\tilde{A}, J, K_a, K_c, S, \Sigma\rangle = \sum_{\Sigma'=\pm 1/2} \sum_{\Omega=1/2}^{J} g_{\Omega\Sigma'}^{(A,JK_aK_c)} |\eta_A, J, \Omega, S, \Sigma', \pm\rangle, \tag{5.76}$$

and B state:

$$|\tilde{B}, J, K_a, K_c, S, \Sigma\rangle = \sum_{\Sigma'=\pm 1/2} \sum_{\Omega=1/2}^{J} g_{\Omega\Sigma'}^{(B,JK_aK_c)} |\eta_B, J, \Omega, S, \Sigma', \pm\rangle. \tag{5.77}$$

The meaning of these equations is to express the asymmetric top molecular state as the superposition of several symmetric top molecular states, which allows us to handle the spectrum of asymmetric top molecule with the knowledge of symmetric top molecule. Generally, we may use a unitary matrix U_G to represent such basis transformation, and the matrix elements could be determined by diagonalizing the Hamiltonian in the basis of Eq.(5.72) and Eq.(5.73). Given that the symmetry of the rotational wavefunction could be discussed in terms of K_a and K_c, we may assume the parity is $+$ for even value of $K_a - K_c$ and $-$ for

odd $K_a - K_c$.

5.4.2 Basis representation

In the first section, the Hamiltonian matrix elements are calculated in basis of $|J, \Omega, \Lambda, S, \Sigma\rangle$. To calculate the eigenstate vectors in the basis Eq.(5.72) and Eq.(5.73), we can construct a unitary transform $U_{(\pm)}$:

$$|\eta, J, \Omega, S, \Sigma, \pm\rangle = U_{(\pm)}|J, \Omega, \Lambda, S, \Sigma\rangle \tag{5.78}$$

with the matrix elements defined as follows:

$$\langle \eta, J', \Omega', S, \Sigma', \pm| \, U_{(\pm)}|J, \Omega, \Lambda, S, \Sigma\rangle = \frac{\delta_{J'J}}{\sqrt{2}}[\delta_{\Omega'\Omega}\delta_{\Sigma'\Sigma} \pm (-1)^{J-\Omega+S-\Sigma}\delta_{-\Omega'\Omega}\delta_{-\Sigma'\Sigma}], \tag{5.79}$$

and thus $U_{(\pm)}HU^{\dagger}_{(\pm)}$ represents the Hamiltonian in the new basis.

For each J in X state, Σ and Ω can be eigher positive or negative, and thus there are two $(4J+2) \times (4J+2)$ matrices (one for each parity) to be diagonalized. If we neglect the population of the rotational states with high Ω, we can reduce the dimension of the matrix and thus reduce the unnecessary calculation of the weak lines, which is an issue in the simulation program of current version. For example, in SrOPh, if we exclude the rotational states with energy over 1000K, the limit for Ω value is around $\sqrt{1000k_B/B_a} \approx 60$. Therefore, for each J over 60, we only need to diagonalize two 60×60 matrices. This idea could be used for limiting the sizes of the states matrices involved in the fitting and accelerate the simulation.

For A and B states, the eigenstate vectors of parity and electronic states could be determined by comparing the coefficients of Eq.(5.51), Eq.(5.52) with Eq.(5.73):

$$|\tilde{A}, J, \Omega, S, \Sigma, \pm\rangle = \cos\left(\frac{\pi}{4} - \beta\right)|\eta_A, J, \Omega, S, \Sigma, \pm\rangle + \sin\left(\frac{\pi}{4} - \beta\right)|\eta_A, J, \Omega - 2\Sigma, S, -\Sigma, \pm\rangle, \tag{5.80}$$

$$|\tilde{B}, J, \Omega, S, \Sigma, \pm\rangle = \cos\left(\frac{\pi}{4} - \beta\right)|\eta_B, J, \Omega, S, -\Sigma, \pm\rangle - \sin\left(\frac{\pi}{4} - \beta\right)|\eta_B, J, \Omega + 2\Sigma, S, \Sigma, \pm\rangle. \tag{5.81}$$

The two equations indicate that, when spin-orbital coupling is weak (or zero), $\beta \approx 0$ and the electronic wavefunction follows the C_{2v} symmetry, the rotational eigenstates are the mixing states of different Ω, and the molecule behaves like an asymmetric top rotor; however, when spin-orbital coupling is strong and dominates the electronic levels ($\beta \approx \pi/4$), the molecule is close to a symmetric top and the second terms on the right-hand side of both equations vanish, therefore the rotational eigenstates are just the symmetric top wavefunctions $|J, \Omega, S, \Sigma, \pm\rangle$. These two equations describe how the C_{2v} symmetry and the spin-orbital coupling affect the rotational eigenstates, and β could be defined as a parameter in the fitting which reflects the spin-orbital coupling strength in SrOPh.

5.4.3 Transition

Now we consider the transition between two symmetric top rotational states $|i, J', \Omega', M_{J'}\rangle$ and $|f, J'', \Omega'', M_{J''}\rangle$[31]:

$$\begin{aligned}
A^{fi}_{J''\Omega''M_{J''}-J'\Omega'M_{J'}} &= \sum_{p=-1}^{1}(-1)^p\langle f, J'', \Omega'', M_{J''}|T^1_p(\mu_e)T^1_{-p}(E)|i, J', \Omega', M_{J'}\rangle \\
&= \sum_{p=-1}^{1}\sum_{q=-1}^{1}(-1)^pT^1_{-p}(E)\langle f, J'', \Omega'', M_{J''}|D^{(1)}_{pq}(\omega)^*T^1_q(\mu_e)|i, J', \Omega', M_{J'}\rangle \\
&= \sum_{p=-1}^{1}\sum_{q=-1}^{1}(-1)^pT^1_{-p}(E)\langle f|T^1_q(\mu_e)|i\rangle\langle J'', \Omega'', M_{J''}|D^{(1)}_{pq}(\omega)^*|J', \Omega', M_{J'}\rangle \\
&= \sum_{p=-1}^{1}\sum_{q=-1}^{1}(-1)^pT^1_{-p}(E)\langle f|T^1_q(\mu_e)|i\rangle \\
&\quad \times (-1)^{J''-M_{J''}}\langle J'', \Omega''||D^{(1)}_{\cdot q}(\omega)^*||J', \Omega'\rangle \begin{pmatrix} J'' & 1 & J' \\ -M_{J''} & p & M_{J'} \end{pmatrix}, \\
&= \sum_{p=-1}^{1}\sum_{q=-1}^{1}(-1)^pT^1_{-p}(E)\langle f|T^1_q(\mu_e)|i\rangle \\
&\quad \times (-1)^{M_{J''}-\Omega''}\sqrt{(2J''+1)(2J'+1)}\begin{pmatrix} J'' & 1 & J' \\ -\Omega'' & q & \Omega' \end{pmatrix}\begin{pmatrix} J'' & 1 & J' \\ -M_{J''} & p & M_{J'} \end{pmatrix}
\end{aligned} \tag{5.82}$$

where $M_{J'}$ and $M_{J''}$ are the projection quantum number of J' and J'' in the space-fixed coordinates, respectively, $D^{(1)}_{pq}(\omega)^*$ is the complex conjugate of the pq element of the 1st rank rotation matrix $D^{(1)}(\omega)$ (see Eq.(5.143) in Brown & Carrington). Here q labels the molecule-fixed components of the tensors. The dipole transition operator is expressed in form of spherical tensor in molecule-fixed coordinates, $T^1_q(\mu_e)$, with polarization of the field denoted by $p = 0, \pm 1$. Since we are using linear polarized beam in experiment, we can take $p = 0$, and therefore the total transition probability (as well as the line intensity) is

proportional to [153]

$$
\begin{aligned}
S_{fi} =& \sum_{M_{J''},M_{J'}} |\langle f, J'', \Omega'', M_{J''}|T^1_{p=0}(\mu_e)|i, J', \Omega', M_{J'}\rangle|^2 \\
=& \left|\sum_{q=-1}^{1} \langle f|T^1_q(\mu_e)|i\rangle \langle J'', \Omega''||D^{(1)}_{.q}(\omega)^*||J', \Omega'\rangle\right|^2 \sum_{M_{J''},M_{J'}} \begin{pmatrix} J'' & 1 & J' \\ -M_{J''} & 0 & M_{J'} \end{pmatrix}^2 \\
=& \frac{1}{3}(2J''+1)(2J+1)\left|\sum_{q=-1}^{1} \langle f|T^1_q(\mu_e)|i\rangle \begin{pmatrix} J'' & 1 & J' \\ -\Omega'' & q & \Omega' \end{pmatrix}\right|^2 \\
=& \frac{1}{3}(2J''+1)(2J+1)\sum_{q=-1}^{1} |\langle f|T^1_q(\mu_e)|i\rangle|^2 \begin{pmatrix} J'' & 1 & J' \\ -\Omega'' & q & \Omega' \end{pmatrix}^2
\end{aligned}
\tag{5.83}
$$

here we sum over $M_{J''}$ and $M_{J'}$ to obtain the total transition probability, omit the electric field $T^1_0(E)$, and use a standard property of Wigner 3-j symbols[153]

$$
\sum_{M_{J''},M_{J'}} \begin{pmatrix} J'' & k & J' \\ -M_{J''} & p & M_{J'} \end{pmatrix}^2 = \frac{1}{2k+1}. \tag{5.84}
$$

5.4.3.1 Transition strength in Hund's case (a) basis

For the transition between $|\eta_X, J', K'_a, K'_c, S, \Sigma\rangle$ and $|\eta_A, J'', K''_a, K''_c, S, \Sigma\rangle$, it is straightforward to substitute the equations above into the amplitude formula:

$$
\begin{aligned}
& A^{A-X}_{(J''K''_aK''_c)-(J'K'_aK'_c)} \\
=& \langle \eta_A, J'', K''_a, K''_c, S, \Sigma|T^1_{p=0}(\mu_e)|\eta_X, J', K'_a, K'_c, S, \Sigma\rangle \\
=& \sum_{\Sigma',\Sigma''} \sum_{\Omega'=1/2}^{J'} \sum_{\Omega''=1/2}^{J''} g^{(A,J''K''_aK''_c)}_{\Omega''\Sigma''} g^{(X,J'K'_aK'_c)}_{\Omega'\Sigma'} \\
& \times \langle \eta_A, J'', \Omega'', S, \Sigma'', \mp|T^1_{p=0}(\mu_e)|\eta_X, J', \Omega', S, \Sigma', \pm\rangle,
\end{aligned}
\tag{5.85}
$$

The matrix element can be evaluated as follows:

$$
\begin{aligned}
&\langle \eta_A, J'', \Omega'', M_{J''}, S, \Sigma'', \mp | T^1_{p=0}(\mu_e) | \eta_X, J', \Omega', M_{J'}, S, \Sigma', \pm \rangle \\
=&\frac{1}{2}\Big[\langle \eta_A, J'', \Omega'', M_{J''}, \Lambda = 1, S, \Sigma'' | T^1_{p=0}(\mu_e) | \eta_X, J', \Omega', M_{J'}, S, \Sigma' \rangle \\
&\pm (-1)^{J'-\Omega'+S-\Sigma'} \langle \eta_A, J'', \Omega'', M_{J''}, \Lambda = 1, S, \Sigma'' | T^1_{p=0}(\mu_e) | \eta_X, J', -\Omega', M_{J'}, S, -\Sigma' \rangle \\
&\mp (-1)^{J''-\Omega''+S-\Sigma''} \langle \eta_A, J'', -\Omega'', M_{J''}, \Lambda = -1, S, -\Sigma'' | T^1_{p=0}(\mu_e) | \eta_X, J', \Omega', M_{J'}, S, \Sigma' \rangle \\
&+ (-1)^{J'+J''-\Omega''-\Omega'-\Sigma''-\Sigma'} \langle \eta_A, J'', -\Omega'', M_{J''}, \Lambda = -1, S, -\Sigma'' | T^1_{p=0}(\mu_e) | \eta_X, J', -\Omega', M_{J'}, S, -\Sigma' \rangle \Big] \\
=&\frac{1}{2} \sum_{q=-1}^{1} (-1)^{J''-M_{J''}} \langle \eta_A | T^1_q(\mu_e) | \eta_X \rangle \begin{pmatrix} J'' & 1 & J' \\ -M_{J''} & 0 & M_{J'} \end{pmatrix} \\
&\times \left[\delta_{\Sigma''\Sigma'} \langle J'', \Omega'' || D^{(1)}_{\cdot q}(\omega)^* || J', \Omega' \rangle \pm (-1)^{J'-\Omega'+S-\Sigma'} \delta_{\Sigma'',-\Sigma'} \langle J'', \Omega'' || D^{(1)}_{\cdot q}(\omega)^* || J', -\Omega' \rangle \right. \\
&\mp (-1)^{J''-\Omega''+S-\Sigma''} \delta_{-\Sigma'',\Sigma'} \langle J'', -\Omega'' || D^{(1)}_{\cdot q}(\omega)^* || J', \Omega' \rangle \\
&\left. + (-1)^{J'+J''-\Omega''-\Omega'} \delta_{\Sigma''\Sigma'} \langle J'', -\Omega'' || D^{(1)}_{\cdot q}(\omega)^* || J', -\Omega' \rangle \right]
\end{aligned}
\tag{5.86}
$$

here the reduced matrix element is

$$
\langle J'', \Omega'' || D^{(1)}_{\cdot q}(\omega)^* || J', \Omega' \rangle = (-1)^{J''-\Omega''} \sqrt{(2J''+1)(2J'+1)} \begin{pmatrix} J'' & 1 & J' \\ -\Omega'' & q & \Omega' \end{pmatrix}. \tag{5.87}
$$

For the SrOPh A-X transition, $\langle \eta_A | T^1_{q=0}(\mu_e) | \eta_X \rangle = 0$ because the transition dipole moment is perpendicular to axis a. Therefore, the rotational transition of the symmetric top has the selection rule $\Delta\Omega = \pm 1$, which is a result of the change of parity. With this condition as well as the symmetry of the 3-j symbol, we can further simplify Eq.(5.86):

$$
\begin{aligned}
&\langle \eta_A, J'', \Omega'', M_{J''}, S, \Sigma'', \mp | T^1_{p=0}(\mu_e) | \eta_X, J', \Omega', M_{J'}, S, \Sigma', \pm \rangle \\
=&\sum_{q=\pm 1} (-1)^{\Omega''-M_{J''}} \delta_{\Sigma',\Sigma''} \sqrt{(2J''+1)(2J'+1)} \langle \eta_A | T^1_q(\mu_e) | \eta_X \rangle \\
&\times \begin{pmatrix} J'' & 1 & J' \\ -M_{J''} & 0 & M_{J'} \end{pmatrix} \begin{pmatrix} J'' & 1 & J' \\ -\Omega'' & q & \Omega' \end{pmatrix},
\end{aligned}
\tag{5.88}
$$

where the terms indicating transition between states with opposite electronic spin are cancelled out. Thus, the transition amplitude is

$$A^{A-X}_{(J''K''_aK''_c)-(J'K'_aK'_c)} = \sum_{q=\pm1}\sum_{\Sigma',\Sigma''}\sum_{\Omega'=1/2}^{J'}\sum_{\Omega''=1/2}^{J''}(-1)^{\Omega''-M_{J''}} g^{(A,J''K''_aK''_c)}_{\Omega''\Sigma''} g^{(X,J'K'_aK'_c)}_{\Omega'\Sigma'}$$
$$\times \delta_{\Sigma',\Sigma''}\sqrt{(2J''+1)(2J'+1)}\langle\eta_A|T^1_q(\mu_e)|\eta_X\rangle \begin{pmatrix} J'' & 1 & J' \\ -M_{J''} & 0 & M_{J'}\end{pmatrix}\begin{pmatrix} J'' & 1 & J' \\ -\Omega'' & q & \Omega'\end{pmatrix}, \tag{5.89}$$

The corresponding transition probability is proportional to the transition amplitude squared (here we have summed over the probability for all the $M_{J'}$ and $M_{J''}$ states):

$$\begin{aligned} &S^{A-X}_{(J''R''K''_a)-(J'R'K'_a)} \\ =&|\langle\eta_A, J'', K''_a, K''_c, S, \Sigma|T^1_{p=0}(\mu_e)|\eta_X, J', K'_a, K'_c, S, \Sigma\rangle|^2 \\ =&\frac{1}{3}\Bigg[\sum_{q=\pm1}\sum_{\Omega'=1/2}^{J'}\sum_{\Omega''=1/2}^{J''} g^{(A,J''K''_aK''_c)}_{\Omega''\Sigma''} g^{(X,J'K'_aK'_c)}_{\Omega'\Sigma'}\langle\eta_A|T^1_q(\mu_e)|\eta_X\rangle \\ &\times(-1)^{J''-\Omega''}\sqrt{(2J''+1)(2J+1)}\begin{pmatrix} J'' & 1 & J' \\ -\Omega'' & q & \Omega'\end{pmatrix}\Bigg]^2. \end{aligned} \tag{5.90}$$

Similarily, the transition probability in B-X branch is proportional to

$$\begin{aligned} &S^{B-X}_{(J''R''K''_a)-(J'R'K'_a)} \\ =&|\langle\eta_B, J'', K''_a, K''_c, S, \Sigma|T^1_{p=0}(\mu_e)|\eta_X, J', K'_a, K'_c, S, \Sigma\rangle|^2 \\ =&\frac{1}{3}\Bigg[\sum_{q=\pm1}\sum_{\Omega'=1/2}^{J'}\sum_{\Omega''=1/2}^{J''} g^{(B,J''K''_aK''_c)}_{\Omega''\Sigma''} g^{(X,J'K'_aK'_c)}_{\Omega'\Sigma'}\langle\eta_B|T^1_q(\mu_e)|\eta_X\rangle \\ &\times(-1)^{J''-\Omega''}\sqrt{(2J''+1)(2J+1)}\begin{pmatrix} J'' & 1 & J' \\ -\Omega'' & q & \Omega'\end{pmatrix}\Bigg]^2. \end{aligned} \tag{5.91}$$

5.4.3.2 Transition strength in Hund's case (b) basis

Similarly, for the transition expressed in case (b) basis, we can start with the transition amplitude:

$$
\begin{aligned}
&A^{fi}_{J''N''N''_aM_{J''}-J'N'N'_aM_{J'}} \\
&= \sum_{M_{J''},M_{J'}} \langle \eta'', N'', N''_a, \Lambda'', S, J'', M_{J''}| \sum_p (-1)^p T^1_p(\mu) T^1_{-p}(E) |\eta', N', N'_a, \Lambda', S, J', M_{J'}\rangle \\
&= \sum_{p,M_{J''},M_{J'}} (-1)^p T^1_{-p}(E) (-1)^{J''-M_{J''}} \begin{pmatrix} J'' & 1 & J' \\ -M_{J''} & p & M_{J'} \end{pmatrix} \\
&\quad \times \langle \eta'', N'', N''_a, \Lambda'', S, J''||T^1(\mu)||\eta', N', N'_a, \Lambda', S, J'\rangle \\
&= \sum_{p,M_{J'},M_{J''}} (-1)^p T^1_{-p}(E) (-1)^{J''-M_{J''}+N''+S+J'+1} \begin{pmatrix} J'' & 1 & J' \\ -M_{J''} & p & M_{J'} \end{pmatrix} \\
&\quad \times \sqrt{(2J''+1)(2J'+1)} \begin{Bmatrix} N'' & J'' & S \\ J' & N' & 1 \end{Bmatrix} \langle \eta'', N'', N''_a, \Lambda''||T^1(\mu)||\eta', N', N'_a, \Lambda'\rangle,
\end{aligned}
\tag{5.92}
$$

The reduced matrix element could be computed as follows (adopted from Eq.(8.31) and Eq.(8.213) in Ref.[31]):

$$
\begin{aligned}
&\langle \eta'', N'', N''_a, \Lambda''||T^1(\mu)||\eta', N', N'_a, \Lambda'\rangle \\
&= \sum_q \langle N'', N''_a||D^{(1)}_{\cdot q}(\omega)^*||N', N'_a\rangle \langle \eta'', \Lambda''|T^1_q(\mu)|\eta', \Lambda'\rangle \\
&= \sum_q (-1)^{N''-N''_a} \sqrt{(2N''+1)(2N'+1)} \begin{pmatrix} N'' & 1 & N' \\ -N''_a & q & N'_a \end{pmatrix} \langle \eta'', \Lambda''|T^1_q(\mu)|\eta', \Lambda'\rangle \\
&= (-1)^{N''-N''_a} \sqrt{(2N''+1)(2N'+1)} \begin{pmatrix} N'' & 1 & N' \\ -N''_a & \Lambda'' & N'_a \end{pmatrix} \langle \eta'', \Lambda''|T^1_{\Lambda''}(\mu)|\eta', \Lambda'=0\rangle.
\end{aligned}
\tag{5.93}
$$

The transition probability is proportional to the square of amplitude (here we assume our laser is linear polarized and thus only $p = 0$ component is considered):

$$\begin{aligned} S^{fi}_{J''N''N''_a\Lambda''-J'N'N'_a\Lambda'} &= |\sum_{M_{J''},M_{J'}} A^{fi}_{J''N''N''_aM_{J''}-J'N'N'_aM_{J'}}|^2 \\ \propto &\frac{1}{3}(2J''+1)(2J'+1)\left|\begin{Bmatrix} N'' & J'' & S \\ J' & N' & 1 \end{Bmatrix}\right|^2 (2N''+1)(2N'+1)\begin{pmatrix} N'' & 1 & N' \\ -N''_a & \Lambda'' & N'_a \end{pmatrix}^2 . \end{aligned} \tag{5.94}$$

To avoid calculating 6j-symbol during the fitting (our current python high performance compiler, Numba, does not support the sympy package, which can calculate the 6j symbol), we can use the following formula

$$\begin{Bmatrix} N'' & J'' & S \\ J' & N' & 1 \end{Bmatrix} = \begin{cases} \frac{-1}{2}\sqrt{\frac{2}{N'(2N'+1)}}, & J''-N''=J'-N'=1/2 \text{ and } N''=N'-1, \\ \frac{1}{2}\sqrt{\frac{2}{N'(2N'-1)}}, & J''-N''=J'-N'=-1/2 \text{ and } N''=N'-1, \\ \frac{-1}{2}\sqrt{\frac{2}{(N'+1)(2N'+3)}}, & J''-N''=J'-N'=1/2 \text{ and } N''=N'+1, \\ \frac{1}{2}\sqrt{\frac{2}{(N'+1)(2N'+1)}}, & J''-N''=J'-N'=-1/2 \text{ and } N''=N'+1, \\ \frac{1}{2N'}\sqrt{\frac{2}{(2N'+1)(2N'-1)}}, & J''=J', N''=N'-1, \\ \frac{1}{2(N'+1)}\sqrt{\frac{2}{(2N'+3)(2N'+1)}}, & J''=J', N''=N'+1 \\ 0. & \text{other cases} \end{cases} \tag{5.95}$$

5.4.4 Line intensity

After calculating the transition probability with Eq.(5.90) or Eq.(5.91), we are getting closer to obtain the line intensity in the spectrum. In this section, we will consider the degeneracy due to the nuclear spin statistics and the thermal distribution of the molecular population, and then apply all these factors to obtain the formula of the line intensity.

5.4.4.1 Nuclear spin statistical weight g_{ns}

Generally, the transition between two given molecular states is subjected to the total symmetry of the molecular wavefunction, which is the product of the ro-vibronic state and the nuclear spin wavefunction. In the previous discussion, we only considered the role of the rotational wavefunction but haven't investigated how the nuclear spins would affect the line intensity. According to the theory [55, 56, 157], the nuclear spin statistical weight could be analyzed in the following procedure:

1. Determine the nuclear spin characters: in SrOPh, there are two pairs of H atoms locating on the σ_v plane, and one H atom on the C_2 axis. This gives the following results:

$$\chi_S(E) = (2I_H + 1)^5 = 32, \chi_S(C_2) = (2I_H + 1)^3 = 8,$$
$$\chi_S(\sigma_v) = (2I_H + 1)^3 = 8, \chi_S(\sigma_d) = (2I_H + 1)^3 = 8.$$

2. Compute the weights according to the symmetry of rotational wavefunction: for C_{2v} molecule with two pairs of identical atoms, the formula is

$$g_{ns} = \begin{cases} \chi_S(E) + \chi_S(C_2), & K = 2n, \\ \chi_S(E) - \chi_S(C_2), & K = 2n + 1, \\ [\chi_S(E) + \chi_S(C_2)]/2, & K = 0. \end{cases} \tag{5.96}$$

In SrOPh, the results is

$$g_{ns} = \begin{cases} 40, & K = 2n, \\ 24, & K = 2n + 1, \\ 20, & K = 0. \end{cases} \tag{5.97}$$

We can just take $g_{ns} = 5$ for states with even K and $g_{ns} = 3$ for the odd K states.

5.5 Calculation of matrices of molecular Hamiltonian and rotational line intensity in Python

In order to produce consistent results as PGopher in Python, the molecular Hamiltonian used in the fitting program is in the Hund's case (b) basis. The Hamiltonian matrix for a given quantum number of J, $H_{rot}(J)$, is constructed with the basis $|N, N_a\rangle$ with the order as follows: The matrix elements are calculated with the eq.xx,xx. The rotational eigen-states

$$\begin{vmatrix} N = J + 1/2, \\ N_a = J + 1/2 \end{vmatrix}, \quad \begin{vmatrix} J + 1/2, \\ J - 1/2 \end{vmatrix}, \quad \cdots \quad \begin{vmatrix} J + 1/2 \\ J - 1/2 \end{vmatrix}, \quad \begin{vmatrix} J - 1/2, \\ J - 1/2 \end{vmatrix}, \quad \cdots \quad \begin{vmatrix} J - 1/2, \\ -J + 1/2 \end{vmatrix}.$$

and levels of a given J are then obtained by the diagonalization the Hamiltonian matrix $H_{rot}(J)$.

Next, to involve the rotational levels and eigen-states of different J values, the procedure above is repeatedly run for all the J values of interested. Typically, rotational states and levels with J smaller than a upper bound J_{max} are calculated in this step, where J_{max} can be varied in range of $30 - 80$ according to the needs, such as the running time or the calculation accuracy.

After the levels and states are obtained for the ground and excited electronic states, the transition amplitudes and line intensities between the initial and final rotational states are calculated in the following procedure:

1. For the two rotational manifolds in ground and excited states (the angular momentum quantum number of the initial and final states are denoted as J_i and J_f, respectively), calculate the transition amplitudes with eq.xx and recorded these value in a matrix T_{J_f,J_i} in size of $(2J_f + 1) \times (2J_i + 1)$.

2. Diagonalize the Hamiltonian matrices of the initial and final states to obtain the eigen-state vectors. Here we record the initial and final states as the column vectors in two square matrices V_i and V_f, respectively, and the energies of the initial and final rotational states are recorded as the diagonal elements of two square matrices E_i and

E_f, respectively.

3. Calculate the nucleus statistical weight for each eigen-state of the initial state and record these weights in a column vector g_{ns} with length $2J_i + 1$, and then multiply V_i with $\sqrt{g_{ns}}$ in the elementwise manner (denoted as $\sqrt{g_{ns}^T} * V_i$) to involve the degeneracy in the rotational states. Here the square root of g_{ns} is applied in order to avoid the calculation of the elementwise multiplication of two different matrices when calculating the line intensity, which increase the complexity in the codes.

4. The transition amplitudes and energies are calculated via the following equations:

$$A_{f,i} = V_f^\dagger T_{J_f,J_i}(\sqrt{g_{ns}^T} * V_i), \Delta E_{f,i} = E_f - E_i. \tag{5.98}$$

5. The line intensity can be calculated by the elementwise square of the transition amplitudes times the Boltzamann coefficient $e^{-E_i/kT}$:

$$I_{f,i} = e^{-E_i/kT}|A_{f,i}| * |A_{f,i}|, \tag{5.99}$$

and then these matrices are reshaped into a one-dimension array to form the list of rotational lines. Transition energies are also listed in another array of the same size. Then, only pick out the lines with strength greater than some threshold (in this program, a typical threshold is 10^{-6} of the strongest line). Typically, the size of the list is about $10^5 - 10^6$.

6. To plot the simulated spectrum, one can calculate the convolution of the lines with the Gaussian, Lorentzian or Voigt line shape with line width $\approx 30 - 80$ MHz.

Optimization for Wigner nj-symbols calculation. Although there is not much difficulty in the calculations of nj-symbols for small quantum numbers, the various difficulties arise for large quantum numbers as it can exceed the 64-bit integer size limit in the computer. In order to compute the nj-symbols efficiently, we compute the nj-symbols from the binary coefficients [158], which can be stored and read from memory easily.

The binary coefficient, denoted as $F_m(n)$, can be calculated as follows:

$$F_m(n) = \begin{cases} \frac{n!}{m!(n-m)!} & \text{for } 0 \le m \le n, \\ 0 & \text{for } m < 0 \text{ and } m > n. \end{cases} \tag{5.100}$$

For $3j$ symbols, the formula is

$$\begin{aligned} \begin{pmatrix} l_1 & l_2 & l_3 \\ m_1 & m_2 & m_3 \end{pmatrix} =& \delta_{-m_3, m_1+m_2}(-1)^{l_1-l_2-m_3}\Delta(l_1 l_2 l_3) \\ & \times \left[\frac{F_{l_1-l_2+l_3}(2l_1)F_{l_1+l_2-l_3}(2l_2)F_{-l_1+l_2+l_3}(2l_3)}{F_{l_1+m_1}(2l_1)F_{l_2+m_2}(2l_2)F_{l_3+m_3}(2l_3)}\right]^{\frac{1}{2}} \\ & \times \sum_k (-1)^k F_k(l_1+l_2-l_3)F_{l_1-m_1-k}(l_1-l_2+l_3) \\ & \times F_{l_2+m_2-k}(-l_1+l_2+l_3), \end{aligned} \tag{5.101}$$

the $6j$ symbol formula is

$$\begin{Bmatrix} a & b & c \\ d & e & f \end{Bmatrix} = \frac{\Delta(abc)\Delta(cde)\Delta(bdf)}{\Delta(aef)} \begin{bmatrix} a & b & c \\ d & e & f \end{bmatrix}, \tag{5.102}$$

here the quantities $\Delta(abc)$ and $\begin{bmatrix} a & b & c \\ d & e & f \end{bmatrix}$ are defined as follows:

$$\Delta(abc) = \left[F_{a+b+c}(a+b+c+1)F_{2c}(2c+1)F_{b+c-a}(2c)\right]^{-\frac{1}{2}}, \tag{5.103}$$

and

$$\begin{aligned} \begin{bmatrix} a & b & c \\ d & e & f \end{bmatrix} =& \sum_n (-1)^n F_{n-a-e-f}(n+1)F_{n-b-d-f}(a+e-f) \\ & \times F_{n-c-d-e}(a-e+f)F_{n-a-b-c}(-a+e+f), \end{aligned} \tag{5.104}$$

where $\max(a+e+f, b+d+f, c+d+e, a+b+c) \le n \le \min(a+b+d+e, a+c+d+f, b+c+e+f)$.

As the model we use only involve three angular momentum, N, S and J, we do not need to calculate the $9j$ symbol which is for the coupling of four angular momentum vectors. Further details for the corresponding formula can be found in Ref. [158].

In python, the platform we used for the data fitting, the calculation of these formula can be boosted with the njit command of the Numba package, a compiler for Python array and numerical functions. Therefore the algorithm above has a better performance than the Wigner function provided by the Sympy package, which is unsupported for acceleration.

5.6 Data fitting

5.6.1 Gradient descent algorithm

The gradient descent algorithm was applied as the first attempt to search for the optimal values of the molecular constants. It is a first-order optimization algorithm commonly used to find the minimum of a function. The idea is to move iteratively towards the minimum of the function by taking steps proportional to the negative of the gradient (or approximate gradient) of the function at the current point. Here is the procedure of how the algorithm runs:

Gradient Descent Algorithm used in this work

1. Choose initial parameters: start with initial guesses for the parameters such as rotational constants, spin-rotation coupling constants, etc. Here we represent these parameters as a vector $\boldsymbol{\theta}$. We set the initial guess for rotational constants as the theoretical values, while the rest of the parameters are randomly set;
2. Select learning rate: choose a learning rate ($\boldsymbol{\alpha_\theta}$), which controls how big each step is during the optimization. Typically, the learning rates are set to be $10^{-}4$ of the parameters;
3. Calculate gradient: compute the gradient of the loss function with respect to the parameters, $\nabla_{\boldsymbol{\theta}} F(\boldsymbol{\theta})$, where $F(\boldsymbol{\theta})$ is some loss function to minimize. The loss function we use have multiple forms, which will be introduce later;
4. Update parameters: adjust the parameters in the direction that reduces the loss function: $\boldsymbol{\theta} := \boldsymbol{\theta} - \boldsymbol{\alpha_\theta} \cdot \nabla_{\boldsymbol{\theta}} F(\boldsymbol{\theta})$;
5. Check convergence: determine whether the algorithm has converged. This could be based on the change in the loss function being below a threshold, or after a predetermined number of iterations;
6. Repeat Steps 3-5: if convergence criteria are not met, repeat the process starting from step 3.

The loss function. To compare with the measured rotational spectrum, we applied several kinds of the loss functions in the fitting. The first one, which takes the experimental and calculated spectra as two vectors and computes the loss as the difference between unity and the similarity in the contour, is defined as follows:

$$L_{fg}(\boldsymbol{\theta}) = 1 - \frac{(\boldsymbol{f}, \boldsymbol{g}(\boldsymbol{\theta}))}{||\boldsymbol{f}||\ ||\boldsymbol{g}(\boldsymbol{\theta})||} = 1 - \frac{\sum_{i=1}^{N} f_i g_i}{\sum_{i=1}^{N} f_i^2 \sum_{i=1}^{N} g_i^2}, \tag{5.105}$$

here $\boldsymbol{f} = (f_1, f_2, \ldots, f_N)^T$ and $\boldsymbol{g}(\boldsymbol{\theta}) = (g_1, g_2, \ldots, g_N)^T$ represent the experimental and calculated spectra, respectively, index i indicates the ith data point in the spectra, $(\boldsymbol{f}, \boldsymbol{g})$ is the inner product of the vectors, and the norm of $\boldsymbol{f}$ is defined as $||\boldsymbol{f}|| = \sqrt{(\boldsymbol{f}, \boldsymbol{f})}$. We omit the notation of $\boldsymbol{\theta}$ in all the data point g_i in the calculated spectra, for simplicity, but we

should keep in mind that they are the functions of the molecular parameters.

Given the complexity of the spectra, with approximately a thousand peaks and each displaying a narrow linewidth—a ratio of measured range to linewidth on the order of 10,000—it becomes exceedingly difficult to pinpoint the global minimum of the loss function due to the prevalence of numerous local minima. This challenge is analogous to attempting to align a long comb with a spectrum profile: a slight shift by even one tooth's spacing could seemingly offer another satisfactory fit to the local pattern. Such shifts make it arduous to ensure that the fitting obtained is truly the optimal global fit, rather than just a locally convenient alignment.

To avoid being trapped by the local minima, in the second loss function we tried, another definition for the inner product is used:

$$(\boldsymbol{f}, \boldsymbol{g}) = \boldsymbol{f}^{\boldsymbol{T}} \boldsymbol{W} \boldsymbol{g}, \tag{5.106}$$

here the matrix $\boldsymbol{W}$, defined for describing the sensitivity to the shift of the two spectra relative to one another, is a function of the indices:

$$W_{ij} = \begin{cases} 1 - |i-j|/c, & |i-j| \leq c, \\ 0, & |i-j| > c. \end{cases} \tag{5.107}$$

and the corresponding definition for the second loss function is

$$L_{fg}(\boldsymbol{\theta}) = 1 - \frac{\sum_{i,j}^{N} f_i W_{ij} g_j}{\sum_{i,j}^{N} f_i W_{ij} f_j \sum_{i,j}^{N} g_i W_{ij} g_j}. \tag{5.108}$$

The third loss function we use is the norm of the difference of the normalized $\boldsymbol{f}$ and $\boldsymbol{g}$:

$$L_{fg}(\boldsymbol{\theta}) = \left|\left| \frac{\boldsymbol{f}}{||\boldsymbol{f}||} - \frac{\boldsymbol{g}}{||\boldsymbol{g}||} \right|\right|. \tag{5.109}$$

The loss functions listed above are used alternatively. The first one have a good performance when the loss is close to the global minimum while the other two can search for the global

minimum in a larger range of the parameter space. Other forms of loss functions may also be useful.

5.6.2 Mini-batch stochastic gradient descent algorithm

Except for the multiple loss functions, the Mini-batch stochastic gradient descent (MSGD) algorithm is also applied in the updated versions of the program to enhance its performance of jumping out of the local minima. MSGD is a variation of the stochastic gradient descent algorithm, which is used for optimizing a differentiable objective function. It's a compromise between computing the gradient based on the full dataset (as in batch gradient descent) and computing the gradient based on a single sample (as in true stochastic gradient descent).

Instead of using the entire dataset or a single example to perform a parameter update, MSGD uses a subset of the dataset $\boldsymbol{g}(\boldsymbol{\theta})$. This subset, or mini-batch, typically contains a small, randomly selected subset of the data. The size of the mini-batch is a hyperparameter and can range from a few samples to several hundred. Sizes like 32, 64, and 128 are common.

A typical MSGD cycle, in our program, repeats the following procedure over all the mini-batches: for each mini-batch, the gradients are computed and the parameters of the model are updated based on these gradients. This update is typically performed using an update rule like the aforementioned gradient descent method, but with only the mini-batch's data influencing the gradient calculation. The cycle is executed over and over again until some convergence criterion is met (like a certain accuracy or a small change in loss function).

MSGD maintains a level of stochasticity that can help escape local minima in the loss landscape, unlike gradient descent which can get stuck easily in this spectra fitting problem. In addition, it is more memory-friendly because it doesn't require loading the entire dataset into memory, and therefore the running time can be reduced. In practice, with appropriate learning rate schedules, MSGD often converges faster than gradient descent because it updates the weights more frequently.

5.6.3 Genetic algorithm

As the parameter space in our problem is large ($\approx 26 - 32$ parameters to fit), the gradient descent algorithm doesn't work well if we set a large searching range for these parameters, as the gradients can be 0 or infinite and then the fitting program goes wrong. Then, we realized that it is necessary to use additional algorithm specifically for searching in a large parameter space. We found that, the genetic algorithm (GA), a search heuristic that mimics the process of natural selection, is a reasonable choice for our study.

The GA in this work run with the following steps:

Genetic Algorithm used in this work
1. Generate a certain number of vectors of all "genes" (molecular parameter set) and form the first generation. This population, typically of size 300-500, is usually randomly generated;
2. Evaluate with fitness function for all the parameter sets. For each parameter set, a fitness score is assigned based on how good a fit to the measured spectrum it is;
3. Select a pair of genes to reproduce next individual via crossover and mutation, and the gene with better fitness has higher probability to be chosen;
4. Obtain the next generation by repeating the previous two steps;
5. After enough times of iteration, the individual with the best fitness score represents the best fit to the spectrum.

The power of genetic algorithms comes from the fact that they can effectively search large, non-linear, and complex spaces where other methods might fail to find a good solution. They are particularly useful when the form of the global optimum is unknown or when the problem is highly complex with many local optima. However, GA do not guarantee an optimal solution, and they can be computationally expensive. They are often used when approximate solutions are sufficient or as part of a larger problem-solving strategy that includes other optimization techniques.

5.6.4 Data fitting procedure and results

Although a few rotational bands recognized in the SrOPh excitation spectrum can determine a few rotational constants in good accuracy, the high density of rotational line near 0-0 transition ($\sim 10^2$/GHz in the computing limit of $J_{max} = 30$) is the main challenge for fitting the rest of the parameters. Therefore, we used a homemade program first to search for parameters that can roughly fit the spectrum in contour and limit the searching range of the parameters for PGOPHER's subsequent fitting[153]. To avoid the program being trapped by local minima, two algorithms were used in turns: the mini-batch gradient descent (MBGD) [159] and the genetic algorithm (GA)[160]. MBGD works similarly as the well-known gradient descent method, while its gradient is computed from a batch of randomly chosen data instead of the whole data set during each iteration to jump out of local minima with semi-stochastic steps. MBGD is the main algorithm that searches for a potential solution iteratively, and GA checks whether the MBGD result is optimal within a larger parameter space. The target functions of the two algorithms are different, with the purpose of making their local minima to be also different.

A contour fitting result is accepted as the initial input of PGOPHERif it is agreed by both MBGD and GA. In PGOPHER, the fitting of molecular constants is done in following procedure: first, the clearly observed bandheads are matched to the simulated rotational bands, such as the lines labeled in Figure 5.1b and 5.1c. With such assignment PGOPHERcan calculate parameters T_0, A, $\bar{B}$, ϵ_{aa}, D_K and H_K in a better accuracy than the contour fitting. Next, the rest of the parameters are obtained by some details of the spectrum near the 0-0 transition, such as the spacing of lines in different rotational bands, shape of peaks, and the order of line strength. For concreteness, some strong peaks in the middle of the spectrum (Figure 5.2a) are assigned to the transitions with $K_a'' = 0, 1, 2$ and different P, Q and R branches (P, Q, and R labels refer transitions with $\Delta J = -1, 0$ and 1, respectively): the strongest few peaks in Q branch are assigned to some observed peaks, see Figure 5.2b; and for the P and R branch transitions, the line assignment could be made according to some local features, see Figure 5.2c. Fine adjustment of fitting is achieved by adjusting the

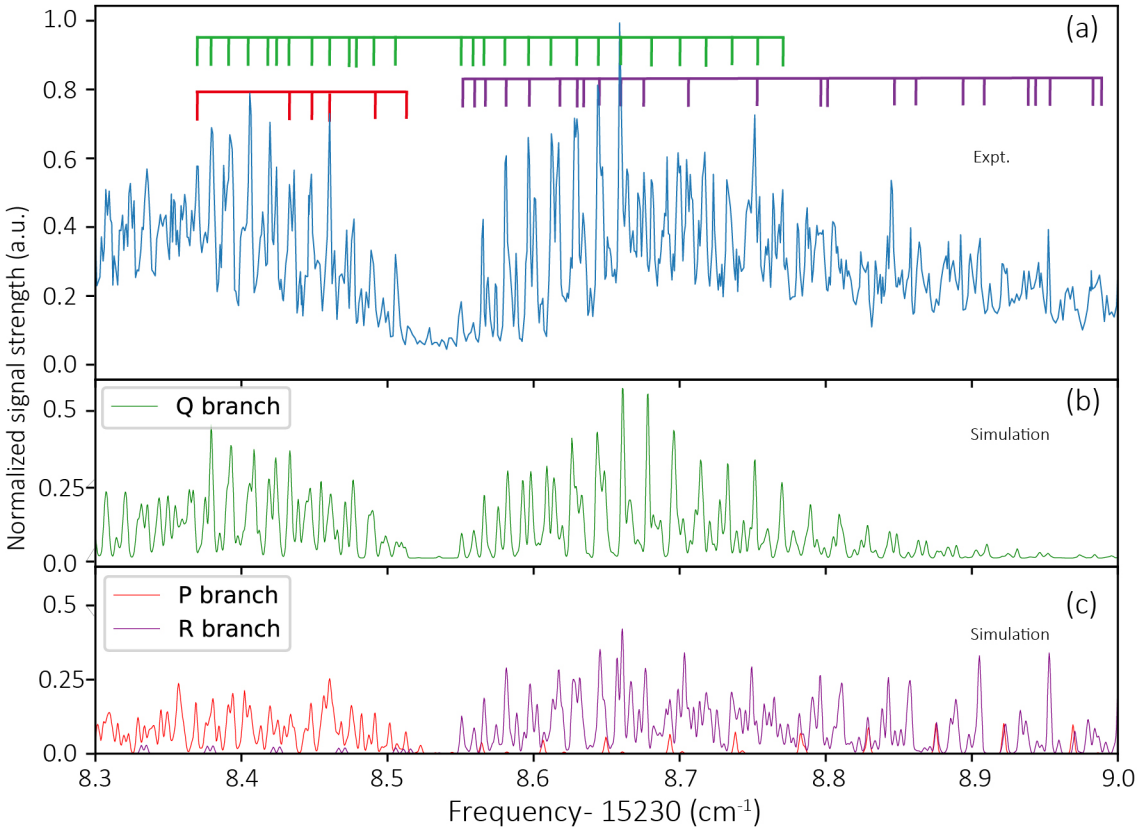

Figure 5.2: A typical line assignment near 0-0 transition of SrOPh. The experimental (a) and simulated data (b,c) are normalized to the maximum signal strength in experiment and simulation, respectively. The observed peaks labeled with green, purple and red ticks in the (a) measured spectrum are assigned to the simulation peaks of (b) Q, (c) R and P branch transitions, respectively. The Gaussian linewidth for the simulation is set as 70 MHz to roughly fit the contour, with the rotational temperature set as $T_{\mathrm{sim}} = 2.5$ K. Each simulation peak in this range usually contains multiple rotational lines, to avoid overfitting, only the strongest 2 - 4 lines in each peak are assigned to the corresponding observed peak.

parameters, re-assigning some lines or bands tentatively, and running the fit based on the updated assignment. This procedure should be repeated multiple times before the parameters become converged.

The rotational temperature in PGOPHERsimulation is set based on the normalized strength of the rotational bandhead of $K'_a = 6 \leftarrow K''_a = 5$, the farthest band we can recognize in experiment. It is found to be close to the experimental results when T_{sim} is around $2 - 3$ K. In the contour fitting procedure, the rotational temperature is estimated to be $4 - 7$ K, depending on the fitting condition such as linewidth and the upper limit of the rotational quantum number J_{max}.

The estimated molecular constants reported in Table 5.1 are from the best fit result whose simulated spectrum pattern matches most of observed peaks near the 0-0 transition, with the assignment error bars calculated from the standard errors of the estimated values given by multiple fitting attempts. These attempts follow the same rotational bandhead assignment in the first step and have a similar P, Q, R line distributions depicted in Figure 5.2, while the numbers and the positions of assigned lines near the 0-0 transition are varied to reflect the parameter fluctuations caused by different assignments. During the procedure of varying the line assignment, we noticed that the fitted values of the centrifugal distortion constants D_N, D_{NK} are very sensitive to the line assignment near the 0-0 transition, while their values could be determined if a set of rotational line assignment is given. In our best fit, PGOPHERreports that $D_{NK} = -2.8(5) \times 10^{-6}$ and $D_N = -1.4(5) \times 10^{-7}$ for the X state, and $D_{NK} = -5(2) \times 10^{-7}$ and $D_N = -1.4(5) \times 10^{-7}$ for the B state, respectively.

We also examined how much the quality of fitting would be changed if we fixed these centrifugal distortion constants to 0. Since the fitting in pgopher is based on the assigned rotational line positions, one straightforward way of comparing the fitting results is to compare the average error of these assigned lines, which is the average difference between the assigned and calculated rotational line frequencies. For our best fit, such average error is about 69 MHz; if D_N, D_{NK} in both X and B states are fixed to 0, the average error of the best fitting under such configuration is 73MHz; if H_K is removed for both X and B states

while keeping all the D_N and D_{NK} terms, the average error is 166MHz. The parameter D_K in the X and B states are critical, and no reasonable fitting result could be obtained without them. Given that the linewidth in our fitting is set as 70MHz and the step size of the scan is about 25-50MHz, the average error of the assigned lines in our best fit is acceptable.

The best fit molecular constants, including the transition energy, rotational constants, spin-rotational constants and centrifugal distortion corrections, are reported in Table 5.1. The measured rotational constants are in good agreement with the calculated values. The spin-rotation constant ϵ_{aa} in the ground state is too small to be determined from the spectrum, and ϵ_{aa} in the $\widetilde{B}$ state is large because of the coupling to the $\widetilde{A}$ state. The larger value of spin-rotational constant than the rotational constants in $\widetilde{B}$ implys a strong SOC effect apart from the direct coupling between the spin and molecular rotation. Based on the second order perturbation theory [161, 162] and the measured constants, the SOC constant in SrOPh is estimated to be $\approx$ 272 cm^{-1}, which is close to that of SrOH ($A^2\Pi$, $\approx$ 265 cm^{-1}).[163] The large SOC also dominates the energy separation of $\widetilde{A} - \widetilde{B}$, elucidating the discrepancy between the calculation and the measurement in Figure 4.4b.[35]

While involving more parameters has been able to enhance the accuracy of fitting, many parameters in such scenarios tended to fit to values consistent with zero, and we therefore omit those in our analysis. The large error bars of some of the centrifugal distortion constants are due to the uncertainty of the line assignment near the 0-0 transition. The rotational temperature from the fit is 2.5 K. The colder temperature is due to the free expansion of neon buffer gas from the cryogenic cell ($\approx$ 23 K) to form a beam with SrOPh entrained.[142] As the SrOPh $\widetilde{B} \leftarrow \widetilde{X}$ transition dipole moment lies along the principle axis c (Figure 4.4b), the rotationally closed photon cycling transition is the c-type transition $N'_{K'_aK_c} = 0_{00} - N''_{K''_aK''_c} = 1_{10}$[13], which is estimated to be at 456.8391(7) THz based on the fitting results and shown in Figure 5.1d.

Constant	$\widetilde{B}\ ^2B_2$		$\widetilde{X}\ ^2A_1$	
	Exp.	Cal.	Exp.	Cal.
T_0	15238.7155(23)			
A	0.1923(6)	0.1915	0.1934(11)	0.1916
$\frac{1}{2}(B+C)$	0.01520(36)	0.01522	0.01508(36)	0.01513
$(B-C)\times 10^3$	1.28(20)	1.21	1.13(12)	1.19
ϵ_{aa}	$-0.6894(6)$		-	
$\epsilon_{bb}\times 10^3$	34(10)		1.3(1.7)	
$\epsilon_{cc}\times 10^3$	16(7)		$-1.3(1.8)$	
$D_N\times 10^8$	$-14(8)$		$-14(8)$	
$D_{NK}\times 10^7$	$-5(11)$		$-28(23)$	
$D_K\times 10^4$	1.3(5)		5.2(1.1)	
$H_K\times 10^6$	3.0(1.4)		21(4)	

Table 5.1: Molecular constants of SrOPh obtained by fitting the rotationally-resolved excitation spectrum in Figure 5.1 with PGOPHER. T_0: electronic transition energy; A, B, C: molecular rotational constants; $\epsilon_{aa}, \epsilon_{bb}, \epsilon_{cc}$: spin-rotation coupling constants; D_N, D_{NK}, D_K: centrifugal distortion constants; H_K: sextic centrifugal distortion correction. All quantities are presented in cm^{-1}.

CHAPTER 6

Extending the Large Molecule Limit: The Role of Fermi Resonance in Developing a Quantum Functional Group

Functionalizing large molecules with optical cycling centers (OCCs) is being explored as a means to extend the exquisite control available in quantum information science to the chemical domain [13, 33, 37, 127, 128, 140, 141, 164–171]. Success requires that these OCCs absorb and emit many photons without changing vibrational states. To accomplish this task, molecular design rules are being developed, aided and validated by experiments, to guide the creation of the ideal quantum functional groups[37, 38, 152, 172]. For example, prior work has demonstrated that alkaline earth alkoxides provide a general and versatile chemical moiety for optical cycling applications, as the alkaline earth radical electron can be excited without perturbing the vibrational structure of the molecule [37, 38, 152, 167, 168]. Similarly, traditional physical organic principles, such as electron-withdrawing, have been shown to improve OCCs performance [33, 37]. Further, experimental and theoretical extensions to more complex acenes, [152, 166] diamondoids [169] and even surfaces [173] suggest an exciting path forward for creating increasingly complex and functional quantum systems.

However, an open question for this work is: what role intramolecular vibrational energy redistribution (IVR) will play as the molecule size is further increased [30, 174, 175]? In the typical description of IVR, the normal modes of molecular vibrations are treated within the harmonic approximation, while any anharmonic couplings between these modes are treated as a perturbation. Laser excitation to an excited (harmonic) vibrational state is then followed by the redistribution of the vibrational energy driven by the anharmonic couplings. This

outflow of energy from one vibrational mode to other modes arises from the selection of basis states that are not eigenstates of the molecular Hamiltonian, and thus not stationary.

An alternate, and equivalent, description of IVR takes the vibrational eigenstates of the molecular Hamiltonian as the basis. These basis states are mixtures of the harmonic vibrational modes, with amplitudes set by the anharmonic couplings. As these states are eigenstates of the molecular Hamiltonian, they are, of course, not time-evolving (except for their coupling to the electromagnetic vacuum) and therefore there is no energy redistribution between them unless perturbed by an external field or collision. Instead, the effect of IVR in this picture is simply that there is more than one vibronic state within the spectrum of the exciting laser leading to non-exponential fluorescence as decay from these nearby states interfere.

This latter picture is convenient for understanding the role that IVR will play in functionalizing large molecules with OCCs. If harmonic vibrational states are close together and possess the correct symmetry, then anharmonic couplings will mix them. In this case, a harmonic vibrational state that is initially not optically active becomes optically active by mixing with an optically active harmonic mode. While this does not change the fraction of diagonal decays ($\Delta\nu = 0$, where ν is the number of quanta in a vibrational mode), it does change the number of accessible final vibrational states and requires more repumping lasers to achieve optical cycling [73, 176, 177].

Therefore, to push optical cycling to larger and larger molecules it is desirable to develop molecular design principles for avoiding these vibrational couplings by energy separation and/or symmetry. Here, we explore these phenomena in both the calcium and strontium phenoxides, which have recently been shown as promising candidates for optical cycling [37, 38, 178]. We show that in certain derivatives of these molecules it is possible to find combination modes (within the harmonic approximation), which are not themselves optically active, close to optically-active stretching modes. Anharmonic coupling between these modes, e.g. Fermi resonance [179, 180], which is the simplest instance of IVR, leads to intensity borrowing and the activation of the combination mode so that a new decay

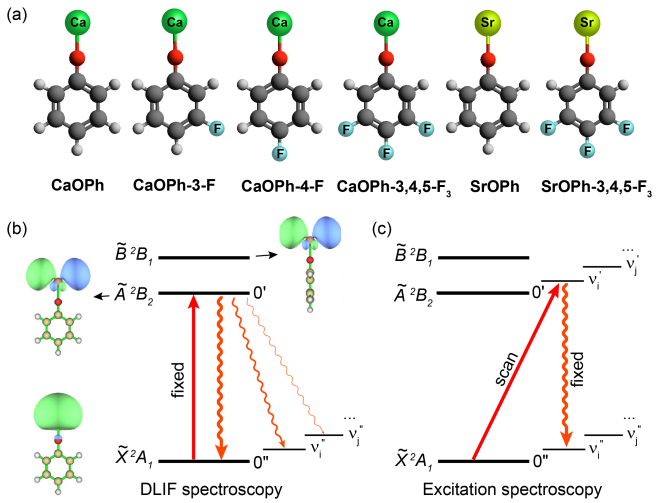

Figure 6.1: (a) Molecular structures of all studied calcium and strontium phenoxide and derivatives. (b) and (c) Schematic diagrams illustrating the DLIF measurement and excitation spectroscopy performed for all molecules in this study, respectively. DLIF measurements were done by fixing the laser wavelength at the transitions of $\widetilde{A}/\widetilde{B}(\nu' = 0) \leftarrow \widetilde{X}(\nu'' = 0)$ and detecting the dispersed fluorescence. Excitation spectroscopy was carried out with off-diagonal excitation scan, $\widetilde{A}/\widetilde{B}(\nu'_n) \leftarrow \widetilde{X}(\nu'' = 0)$, and diagonal fluorescence detection $\widetilde{A}/\widetilde{B}(\nu'_n) \rightarrow \widetilde{X}(\nu''_n)$. The molecular orbital and symmetries of the electronic states are based on the CaOPh molecule with a C_{2v} symmetry.

pathway is opened. Such molecules will require extra repumping lasers for optical cycling. By comparing phenoxides with and without this effect, we present further design rules for functionalizing ever larger molecules with optical cycling centers.

6.1 Experiment

A series of calcium and strontium phenoxides (CaOPh, CaOPh-3-F, CaOPh-4-F, CaOPh-3,4,5-F_3, SrOPh, and SrOPh-3,4,5-F_3, Ph = phenyl group, see Figure 6.1a) were produced via laser ablation of the alkaline earth metal into a mixture of the precursor ligand and Ne buffer gas inside a cryogenic cell operated at a temperature of ∼20 K [38]. The experiments were conducted within a cryogenic buffer-gas cell operated at a temperature range of 20-25 K. Calcium (or strontium) phenoxide and its derivatives were generated by reacting metal atoms with various organic precursors, including phenol, 3-fluorophenol, 4-fluorophenol, and

3,4,5-trifluorophenol, purchased from Sigma Aldrich. Briefly, an Nd:YAG laser (Minilite) operating at 1064 nm with a pulse energy of approximately 6 mJ and a repetition rate of 10 Hz was employed to ablate calcium or strontium metal pellets, generating excited metal atoms. To prevent production yield drifts, the focused spot of the ablation laser was continuously swept over the target using a moving mirror. These excited metal atoms then reacted with organic ligands introduced into the cryogenic cell through a heated gas line originating from a heated reservoir. Each organic ligand was associated with a separate reservoir. The reaction products were subsequently cooled to their vibrational ground states through collisions with neon buffer gas, with a density of approximately $\approx 10^{15-16}$ cm^{-1}. Upon reaching the excitation zone, a tunable pulsed dye laser (LiopStar-E dye laser, operating at 10 Hz) with a linewidth of 0.04 cm^{-1} at 620 nm was utilized to excite molecules to their excited states. Molecules in the excited states underwent spontaneous emission, resulting in fluorescence. This emitted fluorescence was collected by a lens system and directed into a monochromator (McPherson model 2035) equipped with a 1200 lines/mm grating. Finally, the fluorescence was detected by a photomultiplier tube (PMT).

6.2 DLIF and excitation spectra

To investigate the vibrational peak splitting caused by Fermi resonance, we conducted two spectroscopic measurements: dispersed laser-induced fluorescence (DLIF) spectroscopy and excitation spectroscopy. In the DLIF measurement, the laser wavelengths were fixed at the transitions to the vibrational ground level of the electronically excited states, and the fluorescence was dispersed by scanning the grating of the monochromator with an increment of 0.05-0.10 nm. At each grating position, an accumulation of 200-500 shots was taken to ensure reliable signal acquisition. To improve the resolution from the previous measurement [37, 38], where the spectrometer had a resolution of approximately 0.50 nm, narrower slit widths were used. The entrance slit was set at 0.05 mm, while the exit slit was adjusted to 0.03 mm, achieving a better resolution of 0.20 nm (equivalent to 5.5 cm^{-1}). To probe the vibrational decays with low branching ratios, we employed a high laser intensity ($\approx$ 0.2

mJ/pulse) in the DLIF measurement. However, this elevated intensity could potentially saturate the 0-0 emission. To accurately calibrate the vibrational branching ratios, a lower-intensity laser ($\approx$ 0.02 mJ/pulse) was used to measure the relative ratio of the 0-0 peak and the most off-diagonal stretching mode peak in the ground state $\widetilde{X}$. This ratio was used to scale down the 0-0 peak in the DLIF measurement under high laser intensity.

The excitation spectroscopy aimed to detect the vibrational splitting in the excited states $\widetilde{A}$ and $\widetilde{B}$. During this process, the pulsed dye laser wavelengths were scanned at an increment of 0.02-0.10 nm for the $\widetilde{A}(\nu_n')/\widetilde{B}(\nu_n') \leftarrow \widetilde{X}(\nu'' = 0)$, while the grating position remained fixed at the corresponding 0-0 transition. This allowed us to explore the off-diagonal excitation while simultaneously monitoring the diagonal emission.

As sketched in Figs. 6.1b-c, the vibrational structure of these molecules was probed with two types of measurements: dispersed laser-induced fluorescence (DLIF) spectroscopy, which probes the vibrational structure in the electronic ground state ($\widetilde{X}$), and excitation spectroscopy, which examines the vibrational structure in the excited states ($\widetilde{A}$ and $\widetilde{B}$). In DLIF spectroscopy (Figure 6.1b), vibrationally cold molecules are excited to the ground vibrational level of the electronically excited $\widetilde{A}$ and $\widetilde{B}$ states, $\widetilde{A}/\widetilde{B}(\nu' = 0) \leftarrow \widetilde{X}(\nu'' = 0)$, and the resulting fluorescence is recorded as a function of wavelength. In excitation spectroscopy (Figure 6.1c), the exciting laser is tuned to drive excitation to excited vibrational levels of the excited $\widetilde{A}$ and $\widetilde{B}$ states, $\widetilde{A}/\widetilde{B}(\nu_n') \leftarrow \widetilde{X}(\nu'' = 0)$, while simultaneously monitoring the resulting fluorescence from diagonal decays. In both cases, excitation is provided via a tunable pulsed dye laser and the resulting fluorescence is coupled into a grating monochromator and detected using a photomultiplier tube. Compared to previous measurements [37, 38], improvements, such as better source handling techniques to reduce the production of alkaline earth oxide contaminants, provided an increase in signal-to-noise ratio (SNR) of $\sim$3$\times$. This improved SNR enabled spectrometer measurements with a higher resolution of 0.20 nm. Additional experimental details and theoretical methods are provided in the Supporting Information.

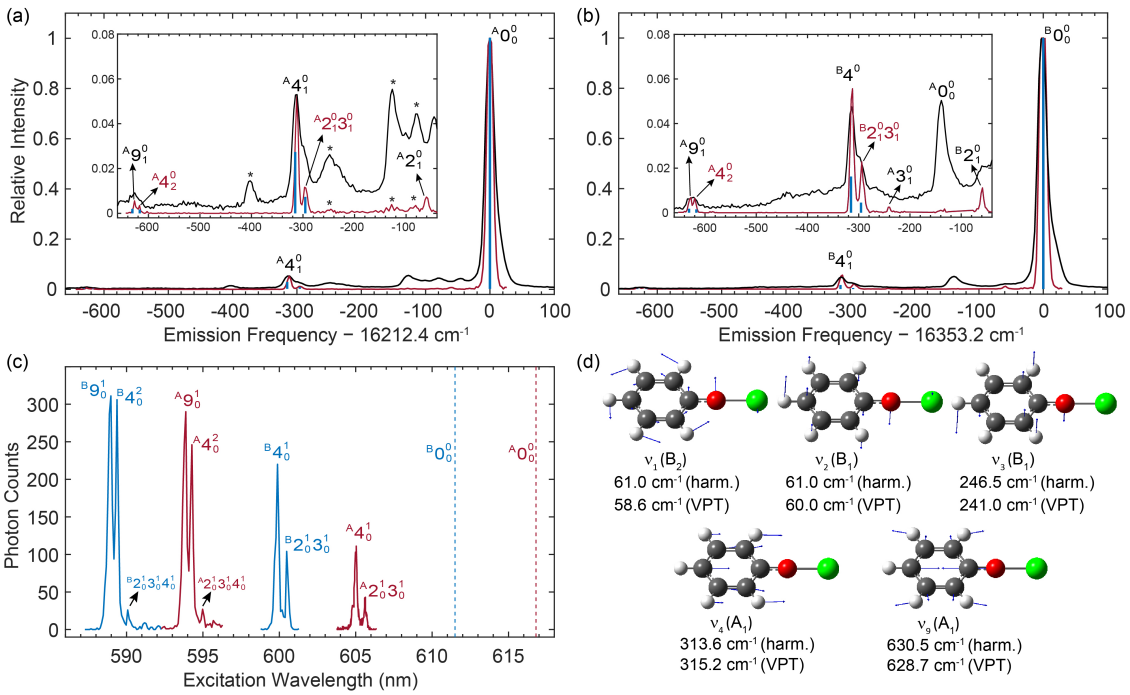

Figure 6.2: (a) and (b) Dispersed fluorescence spectra obtained for the $\widetilde{A} \rightarrow \widetilde{X}$ and $\widetilde{B} \rightarrow \widetilde{X}$ transitions of CaOPh. The black traces, adopted from previous work[37], were obtained with a spectral resolution of ≈ 0.5 nm. The red traces come from an improved measurement with resolution of ≈ 0.20 nm. The insets display the weak peaks in the range of -660 cm^{-1} to -40 cm^{-1} and show the presence of doublet peaks around -300 cm^{-1} and -630 cm^{-1}. The blue sticks depict the calculated frequencies and relative strengths (FCFs) of the vibrational modes using the VPT method. The symbol * indicates CaOH contamination. (c) Excitation spectrum of the $\widetilde{A}(\nu_n') \leftarrow \widetilde{X}(\nu'' = 0)$ (red traces) and $\widetilde{B}(\nu_n') \leftarrow \widetilde{X}(\nu'' = 0)$ (blue traces) transitions. The resulting fluorescence is monitored on diagonal decays. The two dashed lines indicate the excitation wavelengths corresponding to the respective 0-0 transitions. The assignments of all observed vibrational resonances are given. (d) Vibrational displacements of five related fundamental modes. The symmetries and theoretical frequencies in $\widetilde{X}$ using harmonic and VPT methods are provided. All vibrational modes are labeled with increasing frequency regardless of their symmetries.

6.2.1 CaOPh spectra

Using this improved resolution, we recorded DLIF spectra for the $\widetilde{A} \rightarrow \widetilde{X}$ and $\widetilde{B} \rightarrow \widetilde{X}$ transitions of CaOPh, shown as the red lines in Figs. 6.2a and 6.2b, respectively. For comparison, the previously recorded DLIF spectra for this molecule [37] are shown as black lines. Several improvements are immediately clear. First, spectral contamination by CaOH molecules, features denoted by *, is greatly reduced. Second, while in the previous work three fundamental vibrational modes (ν_2, ν_4 and ν_9) were resolved within the frequency range of $\sim$660 cm^{-1} below the respective 0-0 transition, the improved measurements here reveal several new features which were either unresolved in or below the detection limit of the previous measurement. Specifically, the lowest-frequency out-of-plane bending mode ν_2 (Figure 6.2d) is much better resolved at a frequency shift of -60 cm^{-1} (Figs. 6.2a-b). A new weak decay is also observed at -241 cm^{-1} (Figure 6.2b) and readily assigned to the fundamental out-of-plane bending mode ν_3 (Figure 6.2d). Further, the previously assigned peaks due to decay to the Ca-O stretching modes ν_4 and ν_9 are seen to be doublets. While theoretical calculations within the harmonic approximation predict ν_4 should be the strongest off-diagonal decay ($\Delta\nu \neq 0$) and occur at -313.6 cm^{-1} (Table 6.5), the weaker peak at -295 cm^{-1} is not readily assignable. Compared with the theoretical harmonic vibrational frequencies, the weak peak is near the combination modes $\nu_1 + \nu_3$ and $\nu_2 + \nu_3$, as shown in Figure 6.2d, however, the predicted Franck-Condon factors (FCFs) for these decays are $< 10^{-4}$, well below the current detection limit. The observed decay can be explained by an intensity borrowing mechanism [181, 182], which arises from anharmonic coupling between the nearly degenerate stretching mode ν_4 and the combination mode consisting of two bending modes, also known as a Fermi resonance [174, 179, 180]. To corroborate Fermi resonance doublets, vibrational perturbation theory (VPT) with resonances was applied on top of anharmonic frequency calculations to predict corrected frequencies, resonance doublets, and obtain anharmonic FCFs (see the next section for details). As seen in the insets of Figs. 6.2a-b, the predicted separations (vertical blue lines) agree well with the observed vibrational doublets (red traces). Given the requirement that coupled vibrational

modes have the same symmetry, the weaker peak is attributed to the combination mode $\nu_2 + \nu_3$ with A_1 symmetry rather than $\nu_1 + \nu_3$ with A_2 symmetry (Figure 6.2d). Similarly, the doublet near ν_9 is interpreted as a result of vibrational decays to a fundamental mode ν_9, as observed previously [37], and the overtone of the stretching mode ν_4. In the harmonic approximation (Table 6.5), the decay intensity of ν_9 is relatively consistent between $\widetilde{A} \rightarrow \widetilde{X}$ and $\widetilde{B} \rightarrow \widetilde{X}$ transitions, whereas $2\nu_4$ exhibits significant variation. The decay from $\widetilde{A}$ gives a higher intensity for $2\nu_4$, attributed to a larger overlap of vibrational displacement of ν_4 with the in-plane orbital of the $\widetilde{A}$ state (Figure 6.1b). Consequently, this results in an intensity ratio of $\nu_9/2\nu_4$ being four times in the $\widetilde{A} \rightarrow \widetilde{X}$ and ten times in the $\widetilde{B} \rightarrow \widetilde{X}$ transition. The observed nearly equal intensities in both transitions in Figs. 6.2a-b are due to the intensity borrowing via Fermi resonance.

The presence of vibrational doublets due to anharmonic couplings is also observed in the electronically excited $\widetilde{A}$ and $\widetilde{B}$ states by excitation spectroscopy, as presented in Figure 6.2c. Here, it is seen that for both electronically excited states, as in the ground state, the Fermi resonance leads to activation of the combination mode $\nu_2 + \nu_3$ at a spacing of around 16 cm^{-1} from the ν_4 vibrational level (Table 6.5). Similarly, excitations to the excited vibrational levels of ν_9 and $2\nu_4$, as well as a very weak resonance to the combination band of $\nu_2 + \nu_3 + \nu_4$, are observed. The observation of the vibrational anharmonic coupling across different electronic states highlights the significance of Fermi resonances in the spectral characteristics of large molecules like CaOPh.

6.2.2 Substituted CaOPh spectra

To explore the universality of Fermi resonances, we extended our study to the substituted molecules CaOPh-4-F, CaOPh-3-F and CaOPh-3,4,5-F_3. In Figs. 6.3 and 6.6, the DLIF spectra of the $\widetilde{A} \rightarrow \widetilde{X}$ and $\widetilde{B} \rightarrow \widetilde{X}$ transitions for these substituted molecules are presented. Remarkably, with a single fluorine atom substituted at the para-position of the phenyl ring, the DLIF spectra of CaOPh-4F (Figs. 6.3a-b) show only a single peak for the vibrational decay to the stretching mode ν_4 for both transitions. This implies the absence of a Fermi

resonance, which can be attributed to the substantial frequency spacing of 64 cm^{-1} (harm.) or 69 cm^{-1} (VPT) between ν_4 and the symmetry-allowed combination band of $\nu_1+\nu_3$ (Figure 6.3e). Furthermore, the insets in Figs. 6.3a-b reveal two weak peaks at frequencies of around -53 cm^{-1} and -346 cm^{-1}, which can be assigned to mode ν_2 and $\nu_2+\nu_4$, respectively, by comparing with theoretical frequencies (Figure 6.3e). These weak peaks are likely due to the anharmonic mode-coupling involving the low-frequency bending mode ν_2 [37]. Additionally, the complex peaks observed at around -150 cm^{-1} result from collision-induced relaxation from $\widetilde{B} \rightarrow \widetilde{A}$, followed by fluorescence decay to the $\widetilde{X}$ state, and a vibrational decay to mode ν_3 at -170 cm^{-1}.

In the case of CaOPh-3-F, where the *para*-F is replaced with a *meta*-F and the molecular symmetry is reduced from C_{2v} to C_s, the coupling phenomenon is markedly different. While previous DLIF studies [37] of $\widetilde{A} \rightarrow \widetilde{X}$ and $\widetilde{B} \rightarrow \widetilde{X}$ transitions found a broad peak for the stretching mode peak ν_5 at -290 cm^{-1}(black traces in Figs. 6.3c-d), the present, higher resolution spectra, resolve three separate transitions, which are also predicted by the VPT calculation (blue lines in Figs. 6.3c-d). The strongest peak at -284 cm^{-1} corresponds to the vibrational decay to the stretching mode ν_5 (A', Figure 6.3f), while the other two peaks at -291 cm^{-1} and -302 cm^{-1} are assigned to two combination levels, $\nu_2+\nu_3$ (A') and $\nu_2+\nu_4$ (A'), respectively. This more complex coupling behavior can be attributed to the lower C_s symmetry of CaOPh-3-F molecule. All three vibrational modes, ν_2, ν_3 and ν_4, are out-of-plane bending modes with A'' symmetry. The combination levels of $\nu_2+\nu_3$ or $\nu_2+\nu_4$ results in A' symmetry and frequencies close to that of the stretching mode ν_5 (Figure 6.3f), leading to intensity borrowing and activation of these unexpected combination bands.

The absence of Fermi resonance in the CaOPh-4-F stretching mode decay and the presence of complex coupling in CaOPh-3-F are further supported by the excitation spectra obtained for the excited states. Figure 6.4 demonstrates a single peak corresponding to the stretching mode ν_4 in the excitation spectra of CaOPh-4-F, while the excitation spectra of CaOPh-3-F (Figure 6.5) reveal the presence of three transitions in the frequency region associated with the stretching mode ν_5.

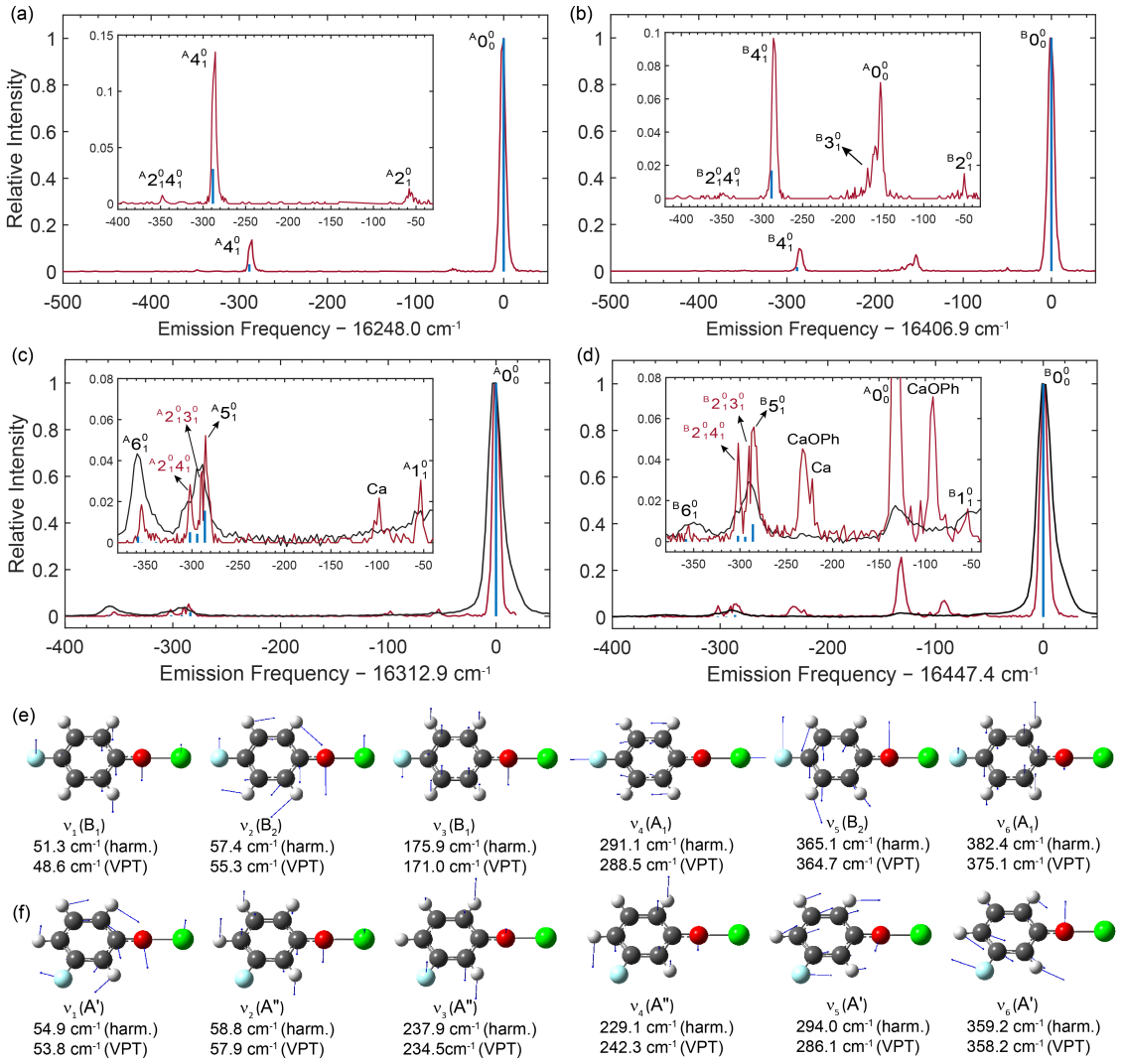

Figure 6.3: (a) and (b) Dispersed spectra for the $\widetilde{A} \rightarrow \widetilde{X}$ and $\widetilde{B} \rightarrow \widetilde{X}$ transitions of CaOPh-4-F molecule, respectively. Only a single peak is observed for the stretching mode ν_4 around -286 cm^{-1}. Due to the absence of Fermi resonance coupling, the theoretical relative strengths (blue vertical lines) are calculated under harmonic approximation. (c) and (d) Dispersed spectra for the $\widetilde{A} \rightarrow \widetilde{X}$ and $\widetilde{B} \rightarrow \widetilde{X}$ transitions of CaOPh-3-F molecule, respectively. The black traces are taken from previous work[37], measured with a spectral resolution of ≈ 0.5 nm, while the red traces represent an improved measurement with resolution of ≈ 0.20 nm. Three decays near -290 cm^{-1} are observed. The blue vertical lines indicate the calculated vibrational frequencies and relative strengths using the VPT method. (e) and (f) Vibrational displacements of the six lowest-frequency fundamental modes in the ground state. Theoretical frequencies and symmetries for these modes are given. All vibrational modes are labeled with increasing frequency regardless of their symmetries.

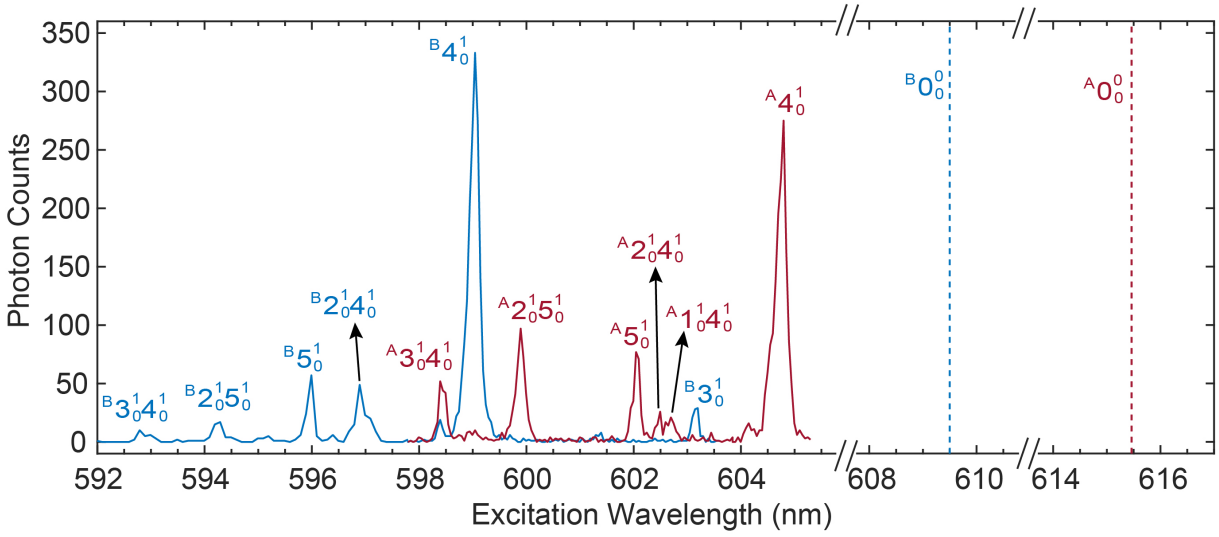

Figure 6.4: Excitation spectra for the excited states of CaOPh-4-F. The excitation wavelengths were scanned off-diagonally for $\widetilde{A}(\nu_n') \leftarrow \widetilde{X}(\nu'' = 0)$ (red trace) or $\widetilde{B}(\nu_n') \leftarrow \widetilde{X}(\nu'' = 0)$ (blue trace) transitions, while simultaneously monitoring the fluorescence photon counts at the diagonal 0-0 transitions. The two dashed lines indicate the excitation wavelengths corresponding to the respective 0-0 transitions. The assignments of all vibrational peaks, obtained by comparing with theoretical vibrational frequencies, are labeled and summarized in Table 6.4.

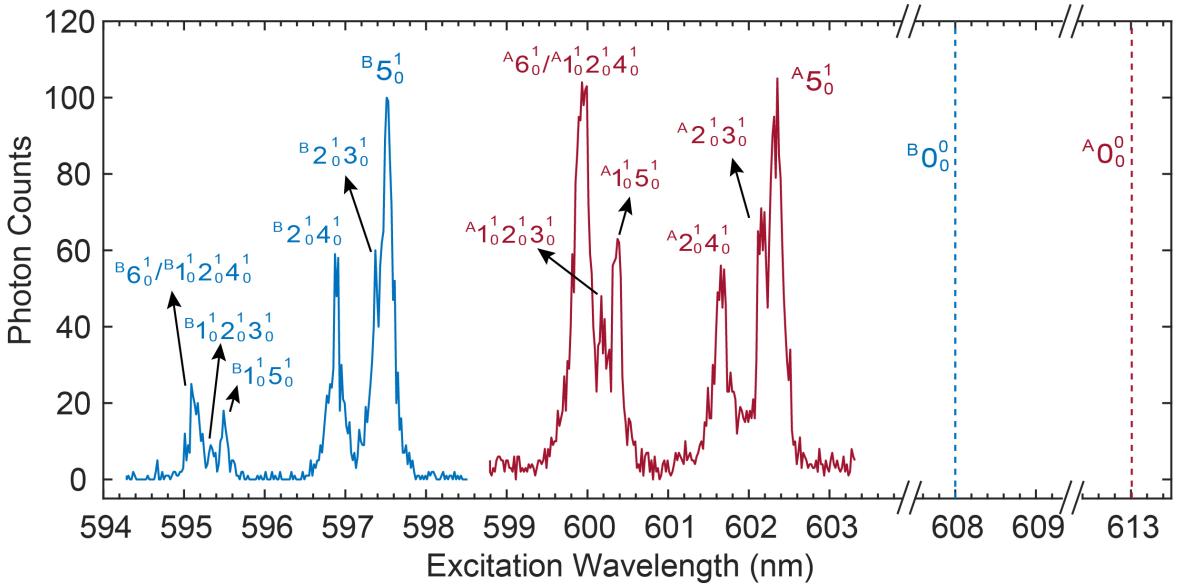

Figure 6.5: Excitation spectra of CaOPh-3-F. For $\widetilde{A}(\nu_n') \leftarrow \widetilde{X}(\nu'' = 0)$ (red trace) or $\widetilde{B}(\nu_n') \leftarrow \widetilde{X}(\nu'' = 0)$ (blue trace) transitions, the excitation wavelengths were scanned off–diagonally while simultaneously monitoring the fluorescence photon counts at the diagonal 0-0 transition. The two dashed lines indicate the excitation wavelengths of the respective 0-0 transitions. The assignments of all vibrational peaks, obtained by comparing with theoretical vibrational frequencies, are labeled and summarized in Table 6.4.

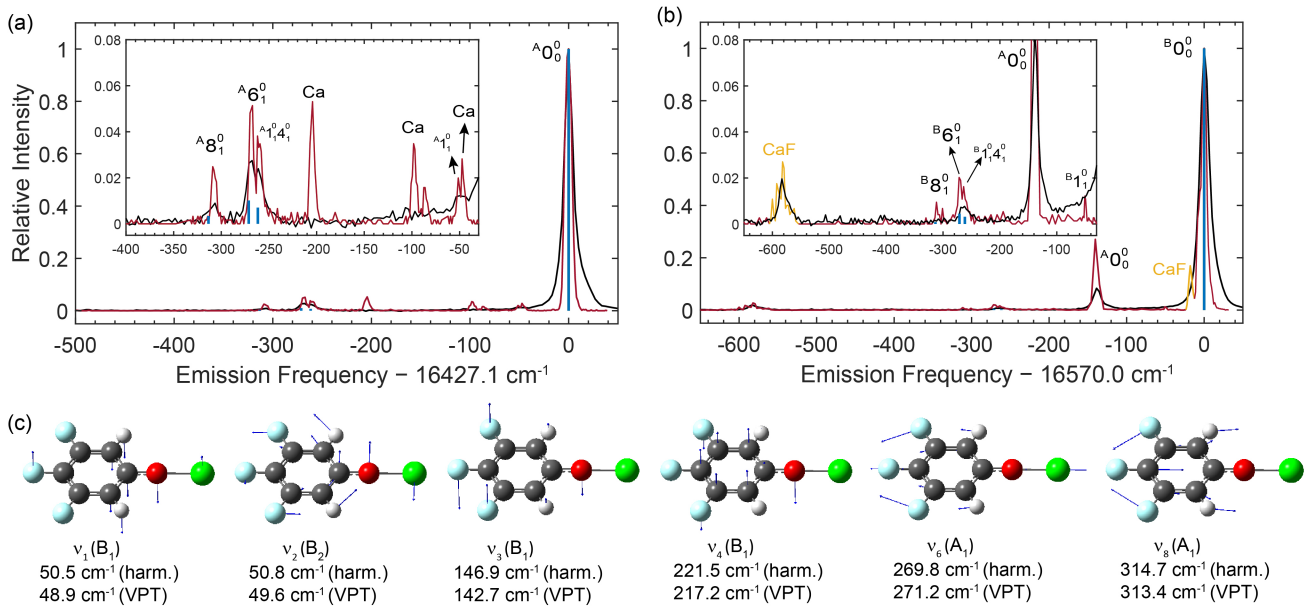

Figure 6.6: (a) and (b) Comparison of dispersed fluorescence spectra obtained for the $\widetilde{A}-\widetilde{X}$ and $\widetilde{B}-\widetilde{X}$ transitions of CaOPh-3,4,5-F_3 molecules, respectively, using two different measurements. The black traces are taken from ref.[37] with a spectral resolution of ≈ 0.5 nm. In contrast, the red traces represent new PMT measurements with an approved resolution of ≈ 0.20 nm. Notably, the red traces clearly exhibit the presence of splitting doublet peaks around -270 cm^{-1}. This is caused by the Fermi resonance between the stretching mode ν_6 and a combination band $\nu_1\nu_4$ based on the vibrational frequencies and symmetries. The contamination of Ca atomic lines and CaF are observed (yellow traces). The blue vertical lines depict the calculated frequencies of the vibrational modes, while the height of the lines reflects their respective calculated strengths using the VPT method. The assignments and vibrational branching ratios of all resolved modes are summarized in Tables 6.2 and 6.3. (c) Vibrational displacements of six vibrational modes. Theoretical frequencies and symmetries for these modes are provided.

A more complex molecule with three F atoms substituted, CaOPh-3,4,5-F_3, has also been revisited, as it is potentially the most attractive calcium phenoxide for optical cycling [37]. The DLIF spectra in Figure 6.6 and excitation spectra of excited states in Figure 6.7 both reveal the presence of doublet vibrational peaks near the stretching mode peak region. One of these peaks corresponds to the stretching mode ν_6 with an A_1 symmetry, while the other peak arises from a combination band involving two out-of-plane bending modes ν_1 (B_1) and ν_4 (B_1).

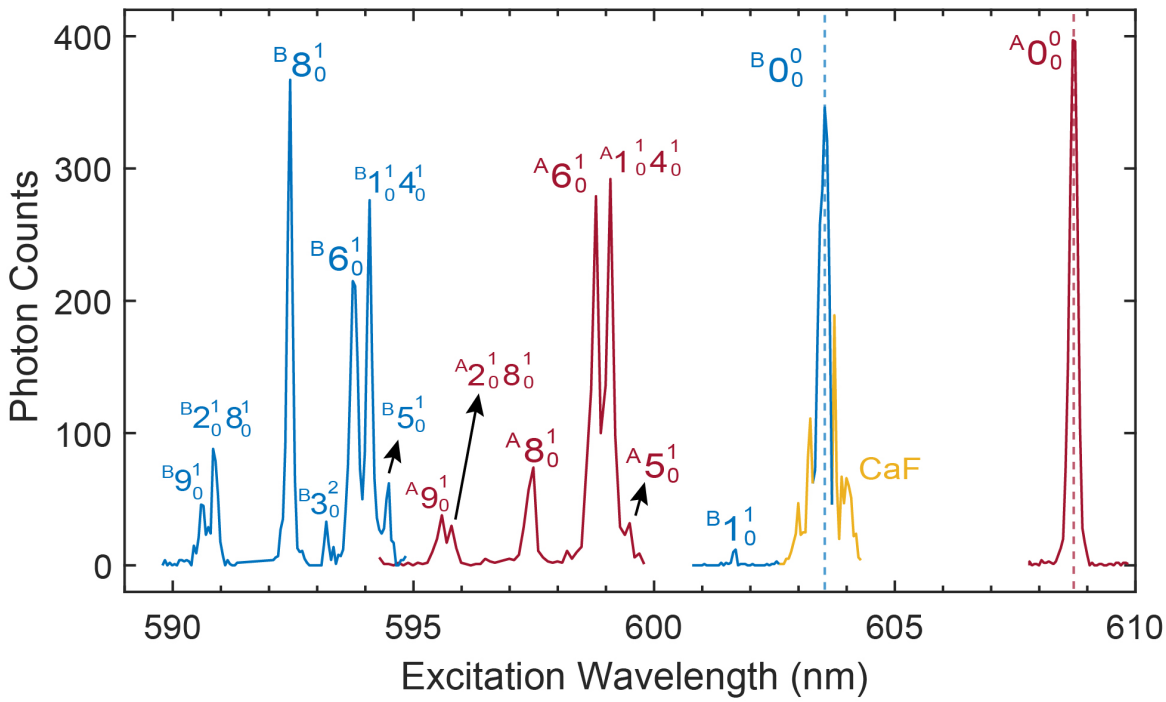

Figure 6.7: (a) Excitation spectra for the excited states of CaOPh-3,4,5-F_3. For $\widetilde{A}(\nu_n') \leftarrow \widetilde{X}(\nu'' = 0)$ (red traces) or $\widetilde{B}(\nu_n') \leftarrow \widetilde{X}(\nu'' = 0)$ (blue traces) transitions, the excitation wavelengths were scanned off-diagonally while simultaneously monitoring the fluorescence photon counts at the diagonal 0-0 transition. The two dashed lines indicate the excitation wavelengths of the respective 0-0 transitions. The $\widetilde{B}(\nu' = 0) \leftarrow \widetilde{X}(\nu'' = 0)$ transition is overlapped with the CaF transition (yellow traces). The assignments of all peaks, obtained by comparing with theoretical vibrational frequencies, are labeled and summarized in Table 6.4.

6.2.3 Strontium phenoxides spectra

To investigate the influence of metal atoms on anharmonic vibrational coupling, we have also studied two strontium phenoxides, SrOPh and SrOPh-3,4,5-F_3. Previous study [38] has provided low-resolution DLIF spectra for these molecules. Figs. 6.8a-b display the higher resolution DLIF spectra recorded here for SrOPh from the excited $\widetilde{A}$ and $\widetilde{B}$ states. Only a single transition is observed for the stretching mode ν_3 at around -235 cm^{-1}, indicating a lack of Fermi resonance. The absence can be explained by the different symmetry of the combination level of $\nu_1 + \nu_2$ (A_2) and the stretching mode ν_3 (A_1), along with a substantial energy gap of either 130 cm^{-1} (harm.) or 132 cm^{-1} (VPT), as shown in Figure 6.8c. This is also validated by the presence of a single stretching mode transition in the excitation spectra of $\widetilde{A} \leftarrow \widetilde{X}$ and $\widetilde{B} \leftarrow \widetilde{X}$ in Figure 6.9.

Contrary to SrOPh, both DLIF spectra (Figure 6.10) and excitation spectra (Figure 6.11) of SrOPh-3,4,5-F_3 exhibit a weak transition assigned to the $\nu_1 + \nu_3$ combination mode close to the stretching-mode peak ν_4, implying the existence of a small anharmonic coupling, as also captured by the VPT calculation.

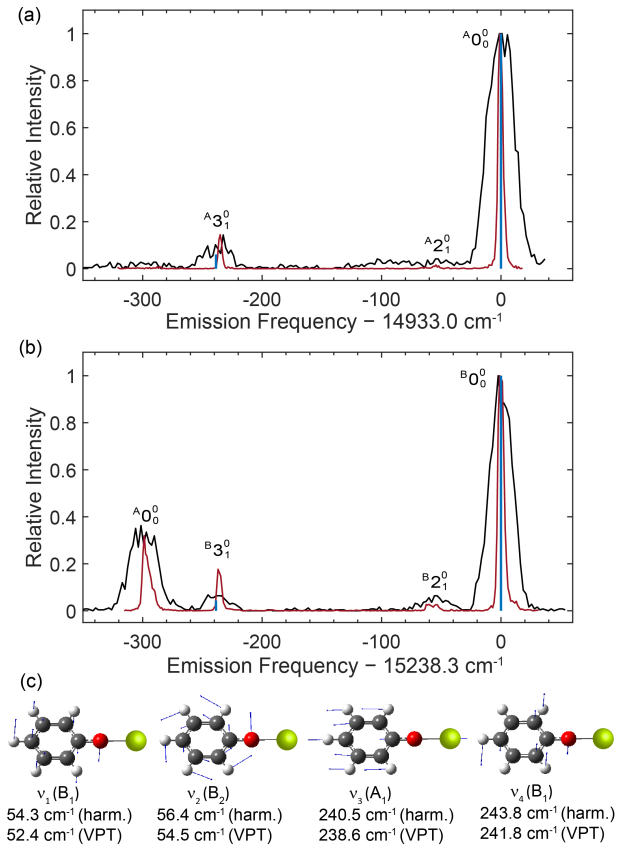

Figure 6.8: (a)-(b) DLIF spectra obtained for the $\widetilde{A} \rightarrow \widetilde{X}$ and $\widetilde{B} \rightarrow \widetilde{X}$ transitions of SrOPh molecules. The black traces are taken from a previous study [38], measured with a spectral resolution of $\approx$ 0.5 nm, while the red traces represent an improved measurement with a resolution of $\approx$ 0.20 nm. The blue sticks show the calculated frequency (VPT) and relative strength (harm.) of vibrational decays. (c) Vibrational displacements of four lowest-frequency fundamental modes. Theoretical frequencies and symmetries for these modes are provided. All vibrational modes are labeled with increasing frequency regardless of their symmetries.

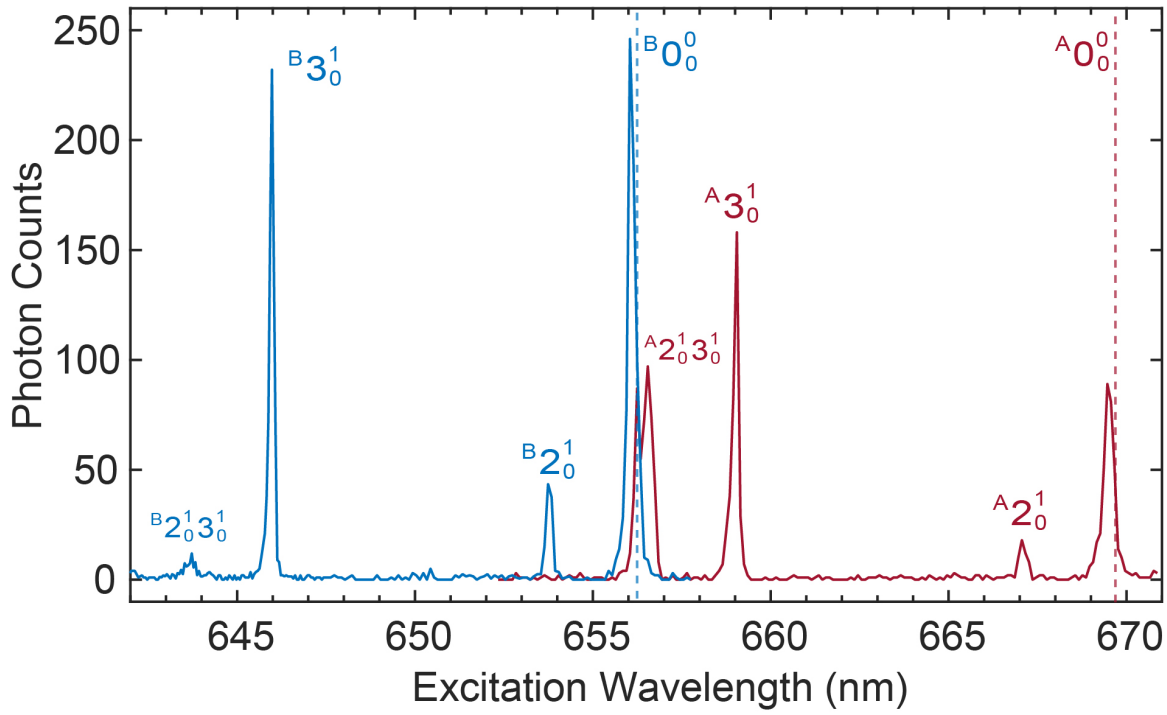

Figure 6.9: Excitation spectra for the excited states of SrOPh. For $\widetilde{A}(\nu_n') \leftarrow \widetilde{X}(\nu'' = 0)$ (red trace) or $\widetilde{B}(\nu_n') \leftarrow \widetilde{X}(\nu'' = 0)$ (blue trace) transitions, the excitation wavelengths were scanned off-diagonally while simultaneously monitoring the fluorescence photon counts at the diagonal 0-0 transition. The two dashed lines indicate the excitation wavelengths corresponding to the respective 0-0 transitions. The assignments of all vibrational peaks, obtained by comparing with theoretical vibrational frequencies, are labeled and summarized in Table 6.5.

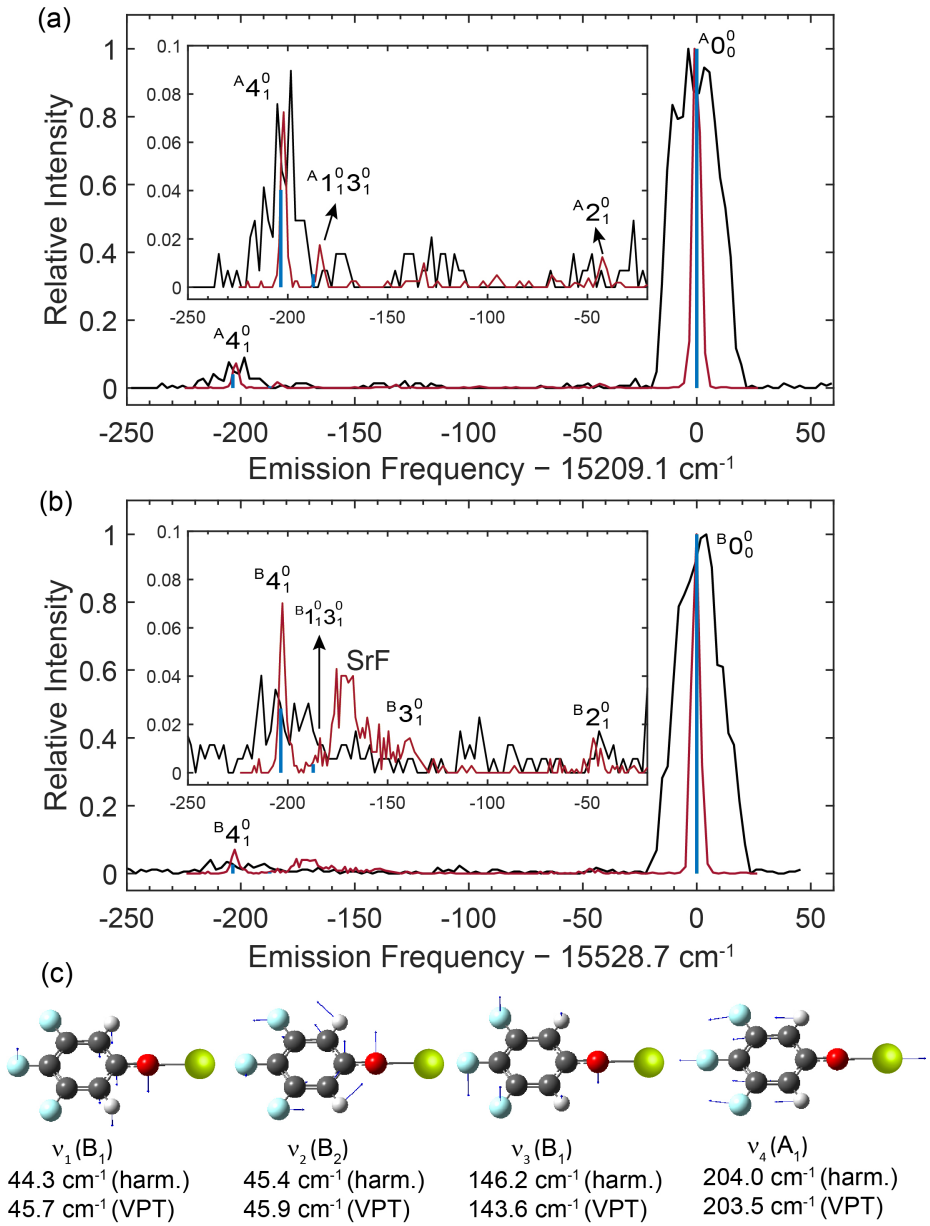

Figure 6.10: (a) and (b) Comparison of dispersed fluorescence spectra obtained for the $\widetilde{A} - \widetilde{X}$ and $\widetilde{B} - \widetilde{X}$ transitions of SrOPh-3,4,5-F_3 molecules, respectively. The black traces, reported previously [38] have a low spectral resolution of $\approx$ 0.5 nm. In contrast, the red traces represent new measurements with a high resolution of $\approx$ 0.20 nm. A weak peak at around -180 cm^{-1}is assigned to the combination band of $\nu_1\nu_3$, which is due to the intensity borrowing from the Fermi resonance coupling with stretching mode ν_4. The blue vertical lines depict the calculated frequencies of the vibrational modes, while the height of the lines reflects their respective calculated relative strengths using the VPT method. (c) Vibrational displacements of four related fundamental modes. Theoretical frequencies and symmetries for these modes are provided.

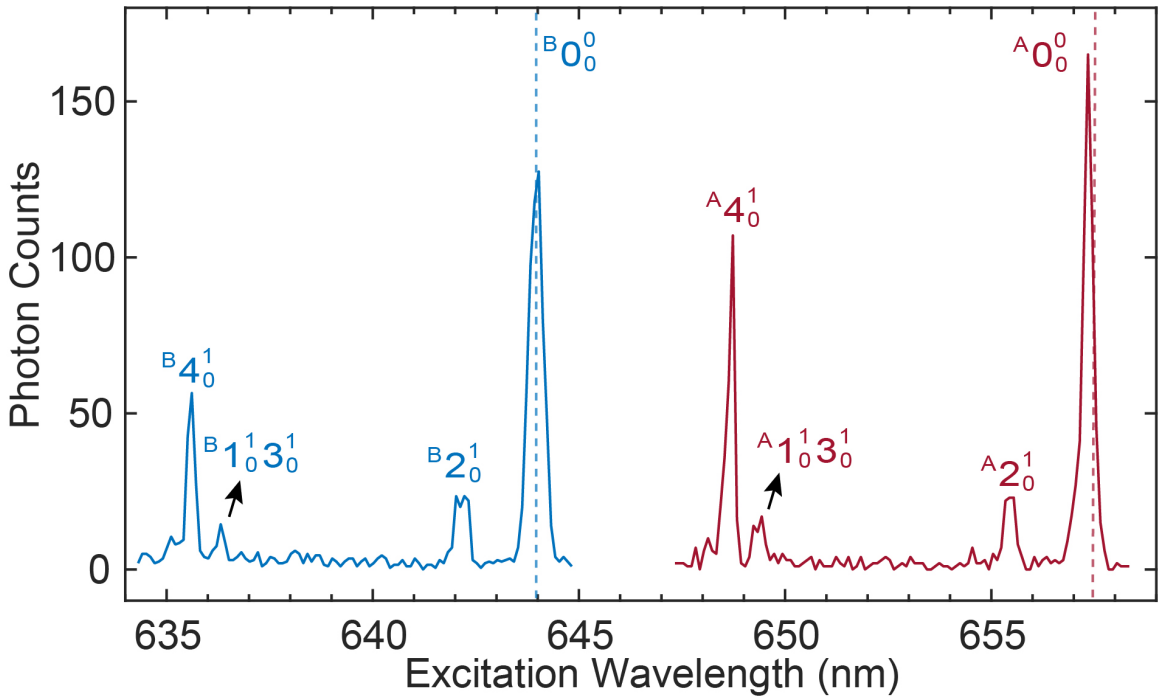

Figure 6.11: Excitation spectra for the excited states of SrOPh-3,4,5-F_3. For $\widetilde{A}(\nu'_n) \leftarrow \widetilde{X}(\nu'' = 0)$ (red trace) or $\widetilde{B}(\nu'_n) \leftarrow \widetilde{X}(\nu'' = 0)$ (blue trace) transitions, the excitation wavelengths were scanned off-diagonally while simultaneously monitoring the fluorescence photon counts at the diagonal 0-0 transition. The two dashed lines indicate the excitation wavelengths corresponding to the respective 0-0 transitions. The assignments of all vibrational peaks, obtained by comparing with theoretical vibrational frequencies, are labeled and summarized in Table 6.5.

Table 6.1: Summary of Fermi resonance for the most off-diagonal decays to the stretching modes in all studied molecules. All frequencies and coupling strengths are given in units of cm^{-1}.

Species	Theo. (VPT)					Exp.		
	ν_i	ν_j	ν_k	$\Delta\nu^{(0)}_{ij,k}$	$\Delta\nu_{ij,k}$	$\Delta\nu'_{ij,k}$	$\beta_{k/ij}$	$\phi^{(\tilde{X})}_{ij,k}$
CaOPh	60.0 (B_1, ν_2)	241.0 (B_1, ν_3)	315.2 (A_1, ν_4)	14.2	19.6	18.0(0.4)	2.9(0.8)	7.9(0.6)
CaOPh-3-F	57.9 (A'', ν_2)	234.5 (A'', ν_3)	286.0 (A', ν_5)	6.4	8.2	6.1(0.6)	3.0(1.0)	-
	57.9 (A'', ν_2)	242.3 (A'', ν_4)	286.0 (A', ν_5)	14.2	16.0	17.4(0.6)	1.9(0.4)	-
CaOPh-3,4,5-F_3	48.9 (B_1, ν_1)	217.2 (B_1, ν_4)	271.2 (A_1, ν_6)	5.1	9.6	8.2(0.4)	1.0(1.0)	4.2(2.4)
SrOPh-3,4,5-F_3	45.7 (B_1, ν_1)	143.6 (B_1, ν_3)	203.5 (A_1, ν_4)	14.2	16.2	18.7(1.0)	9.0(4.0)	6.0(2.6)
CaOPh-4-F	48.6 (B_1, ν_1)	171.0 (B_1, ν_3)	288.5 (A_1, ν_4)	68.9	None	No doublet observed		
SrOPh	52.4 (B_1, ν_1)	54.5 (B_2, ν_2)	238.6 (A_1, ν_3)	131.7	None	No doublet observed		

6.2.4 Summary of the observations

The branching ratios and frequencies of all observed vibrational modes in the DLIF and excitation spectra are summarized in Table 6.2-6.5. From these, a consistent understanding of the role of vibrational coupling in the calcium and strontium phenoxides molecules emerges. As summarized in Tables 6.1, 6.2 and 6.3, except for CaOPh-4-F and SrOPh molecules, all examined molecules show additional off-diagonal decays near the most off-diagonal decays to the stretching mode (ν_k). Specifically, a combination band ($\nu_i + \nu_j$) comprising two low-frequency bending modes, which is absent in the harmonic approximation, is activated by anharmonic vibrational coupling. This occurs in a predictable manner according to the vibrational frequency spacing and vibrational mode symmetry and can be captured by the VPT calculations.

Table 6.2: Experimental vibrational branching ratios and theoretical FCFs of $\widetilde{A} \rightarrow \widetilde{X}$ and $\widetilde{B} \rightarrow \widetilde{X}$ transitions in DLIF spectra (Figs. 6.2, 6.3, 6.8, 6.6 and 6.10) of all molecules studied in this work. The values in parentheses are standard errors in the Gaussian fit to extract the peak areas [37, 38], not including the systematic uncertainties. The theoretical FCFs are obtained under the harmonic approximation (Harm.) and anharmonic-corrected method based on vibrational perturbation theory(Anharm. VPT). The vibrational modes are ordered with increasing frequency. The label * indicates the vibrational modes with Fermi resonance coupling.

Modes	CaOPh					
	Exp. ($\widetilde{A}$)	Harm. ($\widetilde{A}$)	Anharm. VPT ($\widetilde{A}$)	Exp. ($\widetilde{B}$)	Harm. ($\widetilde{B}$)	Anharm. VPT ($\widetilde{B}$)
0	0.930(30)	0.9575	–	0.909(22)	0.9736	–
ν_2	0.009(4)	$<10^{-4}$	–	0.009(3)	$<10^{-4}$	–
ν_3	–	$<10^{-4}$	–	0.002(2)	$<10^{-4}$	–
$\nu_2\nu_3$*	0.013(6)	$<10^{-4}$	0.0071	0.021(5)	$<10^{-4}$	0.0044
ν_4*	0.043(18)	0.0329	0.0264	0.049(12)	0.0196	0.0158
$2\nu_4$*	0.002(2)	0.0007	0.0016	0.004(3)	0.0003	0.0014
ν_9*	0.003(2)	0.0030	0.0019	0.006(3)	0.0031	0.0017
Modes	CaOPh-4-F					
	Exp. ($\widetilde{A}$)	Harm. ($\widetilde{A}$)	Anharm. VPT ($\widetilde{A}$)	Exp. ($\widetilde{B}$)	Harm. ($\widetilde{B}$)	Anharm. VPT ($\widetilde{B}$)
0	0.902(7)	0.9614	–	0.928(4)	0.9773	–
ν_2	0.008(5)	$<10^{-4}$	–	0.004(2)	$<10^{-4}$	–
ν_3	–	$<10^{-4}$	–	0.005(2)	$<10^{-4}$	–
ν_4	0.088(4)	0.0297	–	0.060(3)	0.0165	–
$\nu_2\nu_4$	0.002(4)	$<10^{-4}$	–	0.003(9)	$<10^{-4}$	–
Modes	CaOPh-3-F					
	Exp. ($\widetilde{A}$)	Harm. ($\widetilde{A}$)	Anharm. VPT ($\widetilde{A}$)	Exp. ($\widetilde{B}$)	Harm. ($\widetilde{B}$)	Anharm. VPT ($\widetilde{B}$)
0	0.917(13)	0.9645	–	0.901(11)	0.9806	–
ν_1	0.016(7)	0.0009	–	0.009(5)	$<10^{-4}$	–
ν_5*	0.029(7)	0.0234	0.0150	0.048(7)	0.0129	0.0083
$\nu_2\nu_3$*	0.013(6)	$<10^{-4}$	0.0042	0.013(5)	$<10^{-4}$	0.0023
$\nu_2\nu_4$*	0.015(5)	$<10^{-4}$	0.0049	0.025(4)	$<10^{-4}$	0.0028
$\nu_1\nu_5$*	–	$<10^{-4}$	0.0003	–	$<10^{-4}$	0.0002
ν_6*	0.010(6)	0.0033	0.0028	0.004(4)	0.0014	0.0012
Modes	CaOPh-3,4,5-F_3					
	Exp. ($\widetilde{A}$)	Harm. ($\widetilde{A}$)	Anharm. VPT ($\widetilde{A}$)	Exp. ($\widetilde{B}$)	Harm. ($\widetilde{B}$)	Anharm. VPT ($\widetilde{B}$)
0	0.918(9)	0.9732	–	0.958(39)	0.9875	–
ν_1	0.005(7)	$<10^{-4}$	–	–	$<10^{-4}$	–
$\nu_1\nu_4$*	0.030(5)	$<10^{-4}$	0.0069	0.018(28)	$<10^{-4}$	0.0031
ν_6*	0.030(4)	0.0167	0.0099	0.017(27)	0.0076	0.0044
ν_8	0.017(3)	0.0033	–	0.007(8)	0.0008	–
Modes	SrOPh					
	Exp. ($\widetilde{A}$)	Harm. ($\widetilde{A}$)	Anharm. VPT ($\widetilde{A}$)	Exp. ($\widetilde{B}$)	Harm. ($\widetilde{B}$)	Anharm. VPT ($\widetilde{B}$)
0	0.888(11)	0.9325	–	0.872(13)	0.9497	–
ν_2	0.015(9)	$<10^{-4}$	–	0.016(11)	$<10^{-4}$	–
ν_3	0.097(7)	0.0564	–	0.112(9)	0.0416	–
Modes	SrOPh-3,4,5-F_3					
	Exp. ($\widetilde{A}$)	Harm. ($\widetilde{A}$)	Anharm. VPT ($\widetilde{A}$)	Exp. ($\widetilde{B}$)	Harm. ($\widetilde{B}$)	Anharm. VPT ($\widetilde{B}$)
0	0.929(14)	0.9477	–	0.924(7)	0.9621	–
ν_2	0.010(10)	$<10^{-4}$	–	0.007(3)	$<10^{-4}$	–
ν_3	–	$<10^{-4}$	–	0.017(5)	$<10^{-4}$	–
$\nu_1\nu_3$*	0.011(9)	$<10^{-4}$	0.0051	0.004(2)	$<10^{-4}$	0.0034
ν_4*	0.050(6)	0.0422	0.0382	0.049(3)	0.0285	0.0256

Table 6.3: Resolved vibrational modes for the ground states in the DLIF spectra (Figs. 6.2, 6.3, 6.8, 6.6 and 6.10). The values in the parentheses are statistical errors when fitting resolved peaks with Gaussian functions. The theoretical harmonic frequencies (Harm. freq.) and anharmonic frequencies (VPT freq.) are given for comparison. The harmonic frequencies of combination or overtone bands are simply the sum of frequencies from individual vibrational modes. The label * indicates the vibrational modes with observed Fermi resonance coupling. All values are in units of cm^{-1}.

CaOPh				SrOPh			
Vib. modes	Exp. freq	Harm. freq.	VPT freq.	Vib. modes	Exp. freq	Harm. freq.	VPT freq.
ν_2	59.8 (0.7)	61	60.0	ν_2	54.4 (1.2)	56.4	54.5
ν_3	240.9 (3.1)	246.5	241.0	ν_3	235.5 (0.1)	240.5	238.6
$\nu_2\nu_3$*	294.6 (0.4)	307.5	295.6				
ν_4*	312.6 (0.1)	313.6	315.2				
$2\nu_4$*	621.2 (1.3)	627.3	613.1				
ν_9*	630.3 (1.0)	630.5	628.7				
CaOPh-3-F				CaOPh-4-F			
Vib. modes	Exp. freq	Harm. freq.	VPT freq.	Vib. modes	Exp. freq	Harm. freq.	VPT freq.
ν_1	54.4 (1.0)	58.8	53.8	ν_2	52.9 (1.2)	57.4	55.3
ν_5*	284.4 (0.4)	296.7	286.1	ν_3	169.6 (0.7)	175.9	171.0
$\nu_2\nu_3$*	290.5 (0.4)	296.8	294.3	ν_4	285.9 (0.1)	291.1	288.5
$\nu_2\nu_4$*	301.8 (0.5)	307.9	302.1	$\nu_2\nu_4$	346.3 (6.2)	348.5	343.8
$\nu_1\nu_5$*	–	351.6	338.6				
ν_6*	355.3 (1.3)	359.2	358.4				
CaOPh-3,4,5-F_3				SrOPh-3,4,5-F_3			
Vib. modes	Exp. freq	Harm. freq.	VPT freq.	Vib. modes	Exp. freq	Harm. freq.	VPT freq.
ν_1	50.2 (0.8)	50.5	48.9	ν_2	43.9 (1.1)	45.4	45.9
$\nu_1\nu_4$*	261.6 (0.3)	272.0	261.6	ν_3	138.7 (0.9)	146.2	143.6
ν_6*	269.8 (0.2)	271.6	271.2	$\nu_1\nu_3$*	183.1 (1.0)	190.5	187.3
ν_8	309.4 (0.3)	314.7	313.4	ν_4*	201.8 (0.1)	204	203.5

Table 6.4: The frequencies and assignments of all observed vibrational peaks in the excitation spectra of calcium phenoxides (Figs. 6.2, 6.4, 6.5 and 6.7). The theoretical frequencies are ground-state VPT calcluations. Vibrational modes involved with the Fermi resonance coupling are labeled with *. The uncertainties of observed frequency shifts are within 5 cm^{-1}. All values are in units of cm^{-1}.

CaOPh $\widetilde{A} \leftarrow \widetilde{X}$				CaOPh $\widetilde{B} \leftarrow \widetilde{X}$			
Observed peak wavelength	Freq. above $\widetilde{A}$ (v=0)	Assigned modes	VPT freq.	Observed peak wavelength	Freq. above $\widetilde{B}$ (v=0)	Assigned modes	VPT freq.
605.60	300.1	$\nu_2\nu_3$*	295.6	600.48	300.1	$\nu_2\nu_3$*	295.6
605.00	316.5	ν_4*	315.2	599.88	316.8	ν_4*	315.2
594.98	594.8	$\nu_2\nu_3\nu_4$*	657.4	590.08	593.6	$\nu_2\nu_3\nu_4$*	657.4
594.28	614.6	$2\nu_4$*	613.1	589.38	613.8	$2\nu_4$*	613.1
593.88	626.0	ν_9*	628.7	588.98	625.3	ν_9*	628.7
CaOPh-4-F $\widetilde{A} \leftarrow \widetilde{X}$				CaOPh-4-F $\widetilde{B} \leftarrow \widetilde{X}$			
Observed peak wavelength	Freq. above $\widetilde{A}$ (v=0)	Assigned modes	VPT freq.	Observed peak wavelength	Freq. above $\widetilde{B}$ (v=0)	Assigned modes	VPT freq.
604.80	286.4	ν_4	288.5	603.15	172.7	ν_3	171.0
602.65	345.4	$\nu_1\nu_4$	337.1	599.04	286.5	ν_4	288.5
602.50	349.5	$\nu_2\nu_4$	343.8	596.89	346.6	$\nu_2\nu_4$	343.8
602.05	361.9	ν_5	364.7	595.99	371.9	ν_5	364.7
599.89	421.7	$\nu_2\nu_5$	420.6	594.25	421.0	$\nu_2\nu_5$	420.6
598.44	462.1	$\nu_3\nu_4$	457.9	592.80	462.2	$\nu_3\nu_4$	457.9
CaOPh-3-F $\widetilde{A} \leftarrow \widetilde{X}$				CaOPh-3-F $\widetilde{B} \leftarrow \widetilde{X}$			
Observed peak wavelength	Freq. above $\widetilde{A}$ (v=0)	Assigned modes	VPT freq.	Observed peak wavelength	Freq. above $\widetilde{B}$ (v=0)	Assigned modes	VPT freq.
602.32	289.5	ν_5*	286.1	597.53	288.2	ν_5*	286.1
602.15	294.2	$\nu_2\nu_3$*	294.3	597.37	292.7	$\nu_2\nu_3$*	294.3
601.65	308.0	$\nu_2\nu_4$*	302.1	596.87	306.7	$\nu_2\nu_4$*	302.1
600.37	343.4	$\nu_1\nu_5$*	338.6	595.49	345.5	$\nu_1\nu_5$*	338.6
600.17	349.0	$\nu_1\nu_2\nu_3$*	347.7	595.33	350.0	$\nu_1\nu_2\nu_3$*	347.7
599.93	355.7	ν_6*/$\nu_1\nu_2\nu_4$*	358.4/354.2	595.09	356.8	$\nu_6/\nu_1\nu_2\nu_4$*	358.4/354.2
CaOPh-3,4,5-F_3 $\widetilde{A} \leftarrow \widetilde{X}$				CaOPh-3,4,5-F_3 $\widetilde{A} \leftarrow \widetilde{X}$			
Observed peak wavelength	Freq. above $\widetilde{A}$ (v=0)	Assigned modes	VPT freq.	Observed peak wavelength	Freq. above $\widetilde{B}$ (v=0)	Assigned modes	VPT freq.
599.49	253.7	ν_5	254.8	601.69	49.8	ν_1	48.9
599.09	264.9	$\nu_1\nu_4$*	261.1	594.49	251.1	ν_5	254.8
598.79	273.2	ν_6*	271.2	594.09	262.5	$\nu_1\nu_4$*	261.1
597.49	309.6	ν_8	313.4	593.74	272.4	ν_6*	271.2
595.79	357.3	$\nu_2\nu_8$*	366.0	593.19	288.0	$2\nu_3$	285.4
595.59	363.0	ν_9*	357.4	592.44	309.3	ν_8	313.4
				590.84	355.0	$\nu_2\nu_8$*	366.0
				590.59	362.2	ν_9*	357.4

Table 6.5: The frequencies and assignments of all observed vibrational peaks in the excitation spectra of strontium phenoxides (Figs. 6.9 and 6.11). The theoretical frequencies are ground-state VPT calcluations. The fundamental vibrational modes involved with the Fermi resonance coupling (labeled with *) are given. The uncertainties of observed frequency shifts are within 5 cm^{-1}. The All values are in units of cm^{-1}.

SrOPh $\widetilde{A} \leftarrow \widetilde{X}$				SrOPh $\widetilde{B} \leftarrow \widetilde{X}$			
Observed peak wavelength	Freq. above $\widetilde{A}$ (v=0)	Assigned modes	VPT freq.	Observed peak wavelength	Freq. above $\widetilde{B}$ (v=0)	Assigned modes	VPT freq.
667.06	58.2	ν_2	54.5	653.74	58.3	ν_2	54.5
659.05	240.4	ν_3	238.6	645.98	242.0	ν_3	238.6
656.55	298.2	$\nu_2\nu_3$	294.1	643.73	296.1	$\nu_2\nu_3$	294.1
SrOPh-3,4,5-F_3 $\widetilde{A} \leftarrow \widetilde{X}$				SrOPh-3,4,5-F_3 $\widetilde{B} \leftarrow \widetilde{X}$			
Observed peak wavelength	Freq. above $\widetilde{A}$ (v=0)	Assigned modes	VPT freq.	Observed peak wavelength	Freq. above $\widetilde{B}$ (v=0)	Assigned modes	VPT freq.
655.44	47.8	ν_2	45.9	642.15	44.0	ν_2	45.9
649.33	191.4	$\nu_1\nu_3$*	187.3	636.31	186.9	$\nu_1\nu_3$*	187.3
648.73	205.6	ν_4*	203.5	635.61	204.2	ν_4*	203.5

6.3 Analysis of anharmonic coupling strength and vibrational branching ratios

The strength of this coupling can be estimated from an intensity borrowing model in a molecular system with effects of anharmonicity [183]. Following the convention, the anharmonic vibrational Hamiltonian is expressed as

$$H_{anh}^{(\widetilde{X})} = \frac{1}{6}\sum_{i,j,k}\left(\frac{\partial^3 V^{(\widetilde{X})}}{\partial Q_i \partial Q_j \partial Q_k}\right)_0 Q_i Q_j Q_k + \ldots, \tag{6.1}$$

where the higher-order anharmonic terms in the vibrational potential energy in the $\widetilde{X}$ state ($V^{(\widetilde{X})}$) are negelected. By rewriting the normal coordinates Q_i, Q_j and Q_k with the annihilation and creation operators for the vibration modes, e.g., $Q_i = \frac{1}{\sqrt{2}}\left(\hat{a}_i^\dagger + \hat{a}_i\right)$ [184], the Fermi resonance Hamiltonian affecting the combination mode $\nu_i + \nu_j$ and fundamental mode ν_k in the ground $\widetilde{X}$ state can be expressed as:

$$H_{FR,ij,k}^{(\widetilde{X})} = \phi_{ij,k}^{(\widetilde{X})}\left(\hat{a}_i^\dagger \hat{a}_j^\dagger \hat{a}_k + \hat{a}_i \hat{a}_j \hat{a}_k^\dagger\right), \tag{6.2}$$

where $\phi_{ij,k}^{(\widetilde{X})}$ is the coupling strength. In the absence of the Fermi resonance (i.e. $\phi_{ij,k}^{(\widetilde{X})} = 0$), we assume the probability of decay from the excited state $|e, \nu' = 0\rangle$ to $|\widetilde{X}, \nu_k''\rangle$ (denoted as $I_{e0,X\nu_k}$) is appreciable, while decay to the combination mode $|\widetilde{X}, \nu_i'' + \nu_j''\rangle$ (denoted as $I_{e0,X\nu_i\nu_j}$) is negligible. As $\phi_{ij,k}^{(\widetilde{X})} \neq 0$, the extra and main line intensities can be presented as

$$I'_{e0,X\nu_i\nu_j} = \left(C_{k,ij}^{(X)}\right)^2 I_{e0,g\nu_k} \tag{6.3}$$

and

$$I'_{e0,X\nu_k} = \left[1 - \left(C_{k,ij}^{(X)}\right)^2\right] I_{e0,g\nu_k}, \tag{6.4}$$

respectively, where the coefficient $\left(C_{k,ij}^{(X)}\right)^2$ is the ratio of the borrowed intensity. In experiment, the ratio of the two intensities are measured, i.e., $\beta_{k/ij} = I'_{e0,X\nu_k}/I'_{e0,X\nu_i\nu_j} = \left(C_{k,ij}^{(X)}\right)^{-2} - 1$. Treating the case of only one combination mode mixing with the stretching mode as a simple two level system, one can obtain

$$C_{k,ij}^{(X)} = \sqrt{\frac{1}{2}\left(1 - \frac{\Delta\nu_{ij,k}^{(0)}}{\Delta\nu'_{ij,k}}\right)}, \tag{6.5}$$

and

$$\phi_{ij,k}^{(\widetilde{X})} = \frac{\sqrt{\beta_{k/ij}}}{\beta_{k/ij} + 1}\Delta\nu'_{ij,k}, \tag{6.6}$$

where $\Delta\nu_{ij,k}^{(0)}$ is the unperturbed energy gap between the modes. Using this expression, coupling strengths are extracted and shown in Table 1. In table 1, ν_i and ν_j are two low-frequency out-of-plane bending modes. The combination band of $\nu_i + \nu_j$, FCF-inactive mode under harmonic approximation, is likely to show up due to the intensity borrowing from Fermi resonance coupling with the most-off diagonal decays to the stretching mode ν_k based on the frequency spacing and symmetry. $\Delta\nu_{ij,k}^{(0)} = |\nu_k - \nu_i - \nu_j|$ is the unperturbed frequency separation, and $\Delta\nu_{ij,k} = |\nu_k - \nu_i\nu_j|$ are the predicted Fermi resonance doublets ('None' indicates no Fermi resonance for the mode ν_k). The difference of $|\Delta\nu_{ij,k}^{(0)} - \Delta\nu_{ij,k}|$ indicates the frequency shift due to Fermi resonance. All frequencies are calculated at the

anharmonic-VPT level of theory. $\Delta\nu'_{ij,k}$ is the measured frequency spacing between the combination band and the stretching mode. $\beta_{k/ij}$ is the averaged measured peak intensity ratio of the stretching mode to the combination band in $\widetilde{A} \rightarrow \widetilde{X}$ and $\widetilde{B} \rightarrow \widetilde{X}$ transitions. $\phi_{ij,k}^{(\widetilde{X})}$ is the estimated Fermi resonance coupling strength between the combination band and the stretching mode in the ground state according to equation (6.6). Due to the complexity of coupling between multiple vibrational bands, the coupling strength of CaOPh-3-F could not be estimated from the measurement. For this comparison, though the unperturbed gap $\Delta\nu_{ij,k}^{(0)}$ could be evaluated from the measurement ($\beta_{k/ij}$ and $\Delta\nu'_{ij,k}$) and the above equations, we employ the calculated VPT frequencies for a straightforward comparison of calculated and measured gaps.

Although Fermi resonance occurring between multiple vibrational modes (ν_5, $\nu_2 + \nu_3$, $\nu_2 + \nu_4$) is observed in CaOPh-3-F, evaluating the anharmonic coupling strengths between these modes is challenging. This is due to the mismatch between the numbers of independent elements and available observables: we represent the three-level system with a 3×3 matrix, containing six independent elements, but only have five observables (three frequencies and two relative intensity ratios). Such mismatch results in non-unique solutions from the intensity borrowing model, leading to significant uncertainties in the matrix elements. As a result, the measurement of coupling coefficients of CaOPh-3-F is not available in Table 1.

The observed anharmonic couplings have substantial implications for the laser cooling of these molecules. The presence of additional vibrational decay pathways requires the use of additional repumping lasers to achieve efficient photon scattering [73, 176, 177]. Therefore, it is crucial to design molecules that can minimize or avoid such resonant couplings. Several such strategies for mitigating vibrational anharmonic coupling are readily apparent in these molecules. First, the spacing of vibrational energy levels can be tailored to maintain sufficient separation of *harmonic states* to avoid detrimental Fermi resonances. This can be achieved via several approaches, such as substituting groups on the phenyl ring (e.g. CaOPh-4-F) or altering the metal atom hosting the optical cycling center (e.g. SrOPh). For example, according to theoretical calculations, it is anticipated that CaOPh-4-Cl, CaOPh-4-OH, SrOPh-3-F

and SrOPh-3-OH will not exhibit Fermi resonance coupling between the stretching mode and the bending mode combination band due to their large frequency spacings, as indicated by values exceeding > 60 cm^{-1}, (Table 6.7). Second, choosing molecules with higher symmetry may protect the stretching mode from mixing with other nearby combination modes, as Fermi resonance only affects modes in the same symmetry.

As molecular size and complexity increase above the molecules studied here, the increased density of vibrational states from the increasingly diverse molecular structure will pose challenges for the effectiveness of the mitigation methods discussed here. Selecting suitable ligands with strong electron-withdrawing capability can offer a general suppression of Fermi resonance and higher order couplings. For these molecules, as the orbital motion of the electrons is highly separated from the vibrational degrees of freedom [33, 37], the anharmonic effects induced by these molecular orbitals can be mitigated, therefore the couplings relative to the most off-diagonal decays are suppressed.

6.3.1 Theoretical methods

All calculations in this subsection, done by Dr. Claire E. Dickerson from Prof. Anastasia Alexandrova group, were performed at the PBE0-D3/def2-TZVPPD level of theory [185–188] with a superfine grid in Gaussian16 [189]. An isosurface of 0.03 was used to generate all molecular orbitals with the Multiwfn program [190]. Optimized geometries, vertical excitation energies and frequencies were calculated with density functional theory (DFT)/time-dependent DFT (TD-DFT) methods. Harmonic Franck Condon factors (FCFs) were obtained using the harmonic approximation with Duschinsky rotations up to three quanta in ezFCF [191]. Anharmonic frequencies and anharmonic-corrected FCFs were calculated with vibrational perturbation theory (VPT) [192, 193] using $PyVPT_n$ [194, 195].

As seen in this work, anaharmonic coupling that leads to intensity-borrowing is missed by the harmonic approximation. To predict Fermi resonances and anharmonic-corrected FCFs, we use the numerical, matrix-form VPT as implemented in $PyVPT_n$ with the full $3N-6$ mode basis. Gaussian16 was used to obtain the quartic expansion of the normal

Table 6.6: Ground state vibrational perturbation theory coupling matrices involving the deperturbed frequencies in cm^{-1}. α denotes a deperturbed frequency shift

CaOPh

	ν_4	$\nu_2\nu_3$		ν_9	$2\nu_4$	$\nu_2\nu_3\nu_4$
ν_4	311.052	-7.999	ν_9	624.025	-7.162	-1.06
$\nu_2\nu_3$	-7.999	299.719	$2\nu_4$	-7.162	628.079^{α}	-11.313
			$\nu_2\nu_3\nu_4$	-1.06	-11.313	653.769

CaOPh-3-F

	ν_5	$\nu_2\nu_3$	$\nu_2\nu_4$		ν_6	$\nu_1\nu_5$	$\nu_1\nu_2\nu_4$
ν_5	291.107	-2.821	-6.298	ν_6	357.272	-3.441	-0.509
$\nu_2\nu_3$	-2.821	292.892	-1.356	$\nu_1\nu_5$	-3.441	342.542	-6.298
$\nu_2\nu_4$	-6.298	-1.356	298.489	$\nu_1\nu_2\nu_4$	-0.509	-6.298	351.191

CaOPh-3,4,5-F_3

	ν_6	$\nu_1\nu_4$
ν_6	267.266	4.704
$\nu_1\nu_4$	4.704	265.535

SrOPh-3,4,5-F_3

	ν_4	$\nu_1\nu_3$
ν_4	201.611	5.207
$\nu_1\nu_3$	5.207	189.229

mode potentials by evaluating the first and second derivatives of the Hessian at the PBE0-D3/def2-TZVPPD level of theory. A wavefunction threshold of 0.3 and energy threshold of 500 $cm^{-1}$was used for identifying degenerate subspaces, based on past investigations of these thresholds [196].

Since VPT coupling matrices are sensitive to small changes in the diagonal energies, and diagonal energies are based on the quality of the original Hamiltonian initial inputs of harmonic frequencies and quartic expansions, some frequencies were shifted up to 7 cm^{-1}based on experimental evidence, as done in past work [197, 198]. For CaOPh, the $2\nu_4$ diagonal perturbed anharmonic frequency was shifted $2\nu_4 + 6.8$ cm^{-1}. This shift is incorporated in the resulting coupling matrices in Table 6.6, whose diagonalized matrices gave the corrected frequencies and coefficients used for anharmonic FCFs. For CaOPh-3-F, the original harmonic ν_6 was shifted by $\nu_6 - 2$ cm^{-1}, but no deperturbed anharmonic frequencies were shifted. For all other molecules, no shifts were made.

Table 6.7: Theoretical VPT frequencies of all vibrational modes for the ground state of all molecules. All vibrational modes are ordered with increasing frequency for easy comparison between molecules. All units are in cm^{-1}.

Vib. modes	CaOPh	CaOPh-4-F	CaOPh-3-F	CaOPh-3,4,5-F_3	SrOPh	SrOPh-3,4,5-F_3
ν_1	58.6	48.6	53.8	48.9	52.4	45.7
ν_2	60.0	55.3	57.9	49.6	54.5	45.9
ν_3	241.0	171.0	234.5	142.7	238.6	143.6
ν_4	315.2	288.5	242.3	217.2	241.8	203.5
ν_5	417.1	364.7	291.1	254.8	420.4	219.1
ν_6	445.5	375.1	357.3	271.2	445.7	254.3
ν_7	518.3	428.4	460.3	276.1	524.3	275.9
ν_8	622.1	467.0	500.7	313.4	602.8	309.8
ν_9	628.7	517.4	519.2	358.6	622.7	355.4
ν_{10}	698.8	554.5	622.2	356.9	703.8	361.1
ν_{11}	768.2	645.8	632.1	492.3	764.3	486.9
ν_{12}	819.0	713.8	691.4	514.4	813.0	514.2
ν_{13}	888.8	762.4	766.0	579.5	879.3	580.5
ν_{14}	890.9	795.7	790.6	653.1	879.9	653.6
ν_{15}	962.7	844.9	853.8	646.5	952.9	646.2
ν_{16}	977.8	3275.4	859.7	675.5	944.1	654.4
ν_{17}	998.3	915.1	958.4	716.9	996.6	730.7
ν_{18}	1033.4	938.2	983.7	807.6	1033.7	803.6
ν_{19}	1078.1	1008.0	1007.2	827.7	1076.2	826.9
ν_{20}	1158.4	1091.9	1077.6	845.2	1157.2	854.7
ν_{21}	1166.7	1151.6	1141.5	1008.6	1165.2	1007.7
ν_{22}	1289.4	1233.8	1175.4	1064.8	1288.1	1062.6
ν_{23}	1324.7	1267.1	1266.8	1164.5	1320.4	1188.7
ν_{24}	1324.6	1297.9	1332.5	1188.2	1324.6	1183.6
ν_{25}	1460.9	1332.5	1346.5	1244.9	1460.8	1243.1
ν_{26}	1504.3	1429.5	1464.3	1308.8	1500.4	1308.8
ν_{27}	1595.3	1515.1	1499.3	1424.7	1594.2	1427.5
ν_{28}	1535.1	1614.0	1601.1	1461.4	1619.3	1460.1
ν_{29}	3024.0	1630.0	1633.5	1537.4	3014.7	1535.6
ν_{30}	3051.5	3057.2	3060.9	1529.8	3049.0	1599.1
ν_{31}	2999.3	3062.1	3074.7	1649.0	3050.3	1648.9
ν_{32}	3031.8	3090.1	3079.6	3090.8	3031.9	3087.6
ν_{33}	3087.4	3082.2	3100.0	3102.9	3084.5	3094.6

Table 6.8: The predicted molecules without Fermi resonance coupling for the most-off diagonal stretching mode ν_k. All units are in cm^{-1}. Notes: ν_i and ν_j are two low-frequency out-of–plane bending modes, while ν_j is the most-off diagonal stretching mode.$\Delta\nu^{(0)}_{ij,k} = |\nu_k - \nu_i - \nu_j|$ is the unperturbed frequency spacing. The large splitting can mitigate the Fermi resonance coupling between the combinational band $\nu_i\nu_j$ and the stretching mode ν_k, as shown in Table 1. All frequencies are calculated at the ground-state anharmonic-VPT level of theory.

Species	ν_i	ν_j	ν_k	$\Delta\nu^{(0)}_{ij,k}$
CaOPh-4-Cl	43.7 (B_1, ν_1)	142.6 (B_1, ν_3)	263.0 (A_1, ν_4)	76.7
CaOPh-4-OH	54.6 (A'', ν_1)	172.1 (A'', ν_3)	291.9 (A', ν_4)	65.2
SrOPh-3-F	48.4 (A', ν_1)	53.7 (A'', ν_2)	224.8 (A', ν_3)	122.7
SrOPh-3-OH	48.1 (A', ν_1)	50.8 (A'', ν_2)	228.0 (A', ν_3)	129.1

6.3.2 Anharmonic Franck-Condon Factors

We adopt the same method used in Ref. [198] to include anharmonic corrections based on harmonic FCFs.

Anharmonic vibrational eigenstates are given by:

$$|\chi''\rangle = \sum_j c''_j \left|\Phi''_j\right\rangle \tag{6.7}$$

where c''_j are the eigenstates from the diagonalized VPT coupling matrices (see Table 6.6) and $\left|\Phi''_j\right\rangle$ represents the zeroth-order state basis used in VPT.

Anharmonic FCFs are calculated as a transition form some initial state, j, to final state, k, as:

$$|\langle\chi'|\chi''\rangle|^2 = \left|\sum_{j,k} c'_k c''_j \langle\Phi'_k|\Phi''_j\rangle\right|^2 \tag{6.8}$$

We approximate the zeroth-order wavefunctions used in VPT are approximately the harmonic normal mode wavefunctions, $|\Phi\rangle \approx |\Phi_h\rangle$. This is expected to be a good approximation because $|\Phi\rangle$ are from the deperturbed VPT calculations, which makes other state contributions small compared to the leading term in the expansion. The matrix is then diagonalized to get obtain full state mixing contributions which are incorporated via the mixing coeffi-

cients, $|c|^2$. This gives the revised equation, below:

$$|\langle\chi'|\chi''\rangle|^2 = \left|\sum_{j,k} c'_k c''_j \langle\Phi'_{h,k}|\Phi''_{h,j}\rangle\right|^2 \tag{6.9}$$

Since our excited-state molecule is at its vibrational ground state, we can approximate the initial state as one eigenstate, $|\chi''\rangle \approx |\Phi''_{h,j}\rangle$, so that the FC factor arising from the zeroth-order excited state only involves a single overlap integral between two harmonic states, which is computed analytically in ezFCF:

$$\left|\sum_{j} c''_j \langle\Phi'_k|\Phi''_j\rangle\right|^2 = \left|\langle\Phi'_k|\Phi''_j\rangle\right|^2 \tag{6.10}$$

Using these approximations, anharmonic-corrected FCFs, which we report in Table 6.2, are built using harmonic wavefunctions ($|\phi_h\rangle$) as a basis and mixing coefficients (c'_k) obtained from VPT, using the final equation below:

$$\left|\langle\chi'|\chi''\rangle\right|^2 \approx |c'_k|^2 \left|\langle\Phi'_{h,k}|\Phi''_{h,j}\rangle\right|^2 \tag{6.11}$$

6.3.3 Error analysis of vibrational branching ratios

All peaks observed in the DLIF spectra were fitted with the Gaussian function and the peak areas were extracted to estimate the respective vibrational branching ratios (VBRs) [38]. The corresponding statistical uncertainty is calculated with the following formula

$$S_i = I_i / \sum_{j=0}^{p} I_j \tag{6.12}$$

Table 6.9: Summary of systematic errors in estimating the vibrational branching ratios.

Instrument response	Signal drifting	Unobserved peaks	Diagonal excitations	Total error
1%	1%	3%	0.5%	4%

$$\begin{aligned}\Delta S_i =& \sqrt{\sum_{j=0}^{p}\left(\frac{\partial S_i}{\partial I_j}\right)^2 \Delta I_j^2} \\ =& \frac{1}{S}\sqrt{(1-2S_i)\Delta I_i^2 + S_i^2 \sum_{j=0}^{p} \Delta I_j^2},\end{aligned} \tag{6.13}$$

where S_i and ΔS_i are the VBR and VBR uncertainty of each observed vibrational peak i. p is the number of all observed peaks. I_i and ΔI_i are the intensity (or area) and intensity uncertainty of peak i from the Gaussian fitting. $S = \sum_{j=0}^{p} I_j$ is the total intensity of all observed vibrational decays. The VBR results are summarized in Table 6.2.

The systematic error sources are mainly from the unobserved vibrational decays, signal drifting in the measurement, spectrometer response of the fluorescence detection and the diagonal excitations, as discussed in previous work[38]. For simplicity, the updated errors are summarized in Table 6.9.

The PMT may be saturated if the fluorescence signal is too strong, especially during the detection of diagonal decay signals. This saturation can lead to a decrease in the measured signal strength and lower diagonal VBRs. To address this issue, the DLIF scan is repeated at different excitation powers. The off-diagonal decays are measured from scans with high excitation power, while the diagonal decay signal strength is restored by scaling the scans with low excitation power. The scaling factors are determined by the average ratios of the off-diagonal peak strengths measured in both scans. This scaling method is applied when significant discrepancies in VBRs are observed between scans. The scaling process can introduce larger uncertainties in the diagonal VBRs compared to the off-diagonal VBRs, as

shown in the table, due to larger relative uncertainties in the intensities of the off-diagonal decays obtained under weak excitation.

6.4 Conclusion

In summary, we have studied Fermi resonance coupling of calcium and strontium phenoxides and their derivatives, employing high-resolution dispersed laser-induced fluorescence and excitation spectroscopy. Fermi resonance phenomena were observed in the ground and excited states for CaOPh, CaOPh-3-F, CaOPh-3,4,5-F_3, and SrOPh-3,4,5-F_3 molecules. This resonance led to intensity borrowing, particularly in vibrational combination bands consisting of two low-frequency bending modes close in energy to a stretching mode. The Fermi resonance effect was absent in CaOPh-4-F and SrOPh due to large frequency differences between the combination band and the stretching modes. While Fermi resonance does not significantly alter vibrational branching ratios, it does require additional repumping lasers for effective optical cycling. Several strategies were presented to minimize the impact of Fermi resonance in phenoxide-related molecules, including ligand substitutions and changes in metal atoms. These findings help to provide a roadmap for the design and engineering of ever-larger and more intricate molecular systems with enhanced optical cycling properties for advancing quantum information science.

CHAPTER 7

Bottom-up approach to scalable growth of molecules capable of optical cycling

Quantum information processing (QIP) has been explored in a wide variety of physical platforms, such as superconducting circuits [199], semiconductor spins [200], ultracold neutral atoms [201] and trapped ions [202]. Two major challenges to achieving quantum processing are fidelity and scalability. Among them, molecules offer some unique advantages, including long coherence times, large dipole moments and rich internal degrees of freedom [12]. In particular, molecules containing optical cycling centers (OCCs) [13, 33, 127, 128], which allow repeated absorption and emission of photons without changing the quantum states, enable direct laser cooling [176, 177, 203], and high-fidelity quantum state detection [204, 205]. These features are essential for preparing and measuring qubits, the basic units of QIP.

One possible way to implement QIP with scaled molecules is to use optical tweezer arrays, which can trap and manipulate individual molecules with laser beams [201, 206]. This approach has been successfully demonstrated with ultracold atoms [207, 208], and recently extended to laser-cooled molecules [209, 210]. A specific proposal for a scalable QIP platform based on optical tweezer arrays is to use $CaOCH_3$ molecules [26], where qubit states are encoded in the long-lived rotational levels and gate operations are performed by microwave pulses. The expected gate errors are at the 10^{-3} level, which is close to the fault-tolerant threshold [211]. However, optical tweezer arrays for ultracold molecules are technically difficult, as they require sophisticated laser systems and precise control of molecular interactions. An alternative method to scale up molecular qubits without the need for laser cooling and optical trapping is to couple them with a surface. As theoretically proposed previously [173],

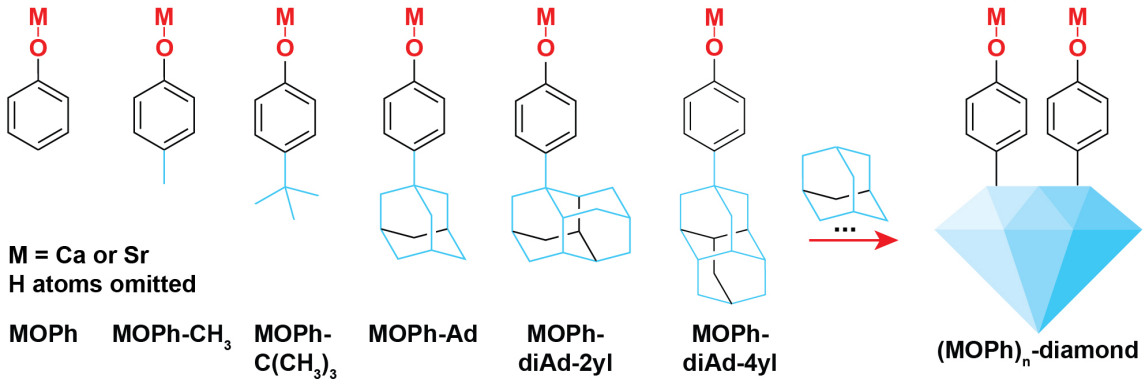

Figure 7.1: Molecular structures of functionalized adamantane and its derivatives as well as the schematic molecular array on the diamond surface. M = Ca or Sr.

the quantum functional group of SrO moiety, bound on a diamond or cubic-BN surface with large scalability, can act as a localized qubit to preserve photon cycling properties for high-fidelity quantum state measurement. The advantage of this approach is that it avoids the complexity of free-space manipulation of molecules, and instead relies on the robustness and tunability of surface chemistry and solid-state devices.

The surface functionalization represents a particular form of molecular functionalization, which has been theoretically proposed [13, 33, 127, 128, 140, 141, 164–166, 169–171] and experimentally demonstrated [37, 38, 152, 178] to potentially bring optical cycling properties to large molecules. As we explore scaling the size of functionalized molecules, we gain insights into how such optical properties may evolve, approaching the ideal scenario achieved through surface binding. However, this scaling raises significant questions: How do molecular size and the complexity of vibrational modes influence optical cycling properties? And, importantly, can optical cycling centers in larger molecules circumvent disruptions from non-Born-Oppenheimer effects, including the Jahn-Teller effect [28] and Fermi resonance [212]? These questions underscore the intricate balance between enhancing molecular capabilities for quantum information processing and navigating the challenges presented by increased molecular complexity. To understand these questions, in this chapter, we investigate the feasibility of implementing surface-bound OCC by functionalizing the adamantane molecule, a subunit of diamond, with MO-Ph (M = Ca or Sr, Ph=phenyl) units as a model system. As

shown in Figure 7.1, the para position of MOPh is substituted with ligands CH3, C(CH3)3, adamantane, diadamantane and diamond. Using the dispersed laser-induced fluorescence (DLIF) spectrosocpy, we measured the diagonal vibrational branching fractions (VBFs, the probability that spontaneous decay occurs on the 0-0 transition) of the SrO-adamantane to be around 0.8. To enhance the optical cycling properties [33, 37], an electron-withdrawing phenyl group (-Ph-) is inserted to form a Ca/SrOPh-adamantane molecule, which results in better diagonal VBFs for Ca/SrOPh-adamantanes.

7.1 Experiment procedure

Two different methods are used for the synthesis of the molecules listed in the scheme. To produce MO-Ad molecules, $\approx$ 5g of 1-adamantanol, serving as the ligand precursor, was heated to approximately 95 °C in a reservoir to produce vapor. The vapor was then introduced into the cryogenic buffer gas cell (running at 20-25K) using helium carrier gas at a flow rate of approximately 0.2 sccm. By ablating the Sr/Ca metal target in the cell, meta-stable Sr/Ca atoms were produced and reacted with the vaporized ligands to synthesize the molecules with OCC. On the other hand, due to the limited amount of the ligands (a few grams of 4-(adamantan-1-yl)phenol for MOPh-Ad and approximately 70 mg of phenol-diadamantane for each MOPh-diAd, respectively), the aforementioned method is not suitable for the synthesis and detection of MOPh-Ad and MOPh-diAd. Hence, we mixed the ligand precursors with the dihydride of the metal (SrH_2 or CaH_2, powder) and silver powder (serves as the binder) in a mass ratio of $m_{\text{ligand}} : m_{\text{MH}_2} : m_{\text{Ag}} \approx 1 : 1 : 3$ and then pressed the mixture into an ablation target. In practice, as the ablation of the composite target in the cell can easily vaporize these ligand precursors with high melting points (estimated to be over 150°C for Phenol-Ad and Phenol-diAd), we found that this method can effectively integrate the ligands into the reaction.

For the carrier gas loading method, the ablation pulse energy $\approx$ 6 mJ is used, and the gas line is heated to $>$ 120 °C to prevent the vapor from freezing in the line. The number density of the ligand precursors in the cell is $\approx 10^{12} - 10^{13}$ cm^{-3}. The reaction products

were cooled by collision with neon buffer gas of density $\approx 10^{15} - 10^{16}$ cm^{-3}. Conversely, for loading through ablation of mixed targets, a higher ablation energy ($15 - 20$ mJ) is essential for observing the vibrational decays with VBR $> 10^{-3}$.

About $0.7 - 2$ ms delay after the ablation, the cooled molecules were then optically pumped to the excited states by a tunable, pulsed dye laser (10 Hz, LiopStar-E dye laser, linewidth 0.04 cm^{-1} at 620 nm). These molecular electronic transitions were identified by scanning the frequencies of the pulsed dye laser (PDL) and detecting the fluorescence signal on resonance with a photo-multiplier tube (PMT) coupled with a grating monochromator[38]. To measure the vibrational branching ratios via DLIF spectra, the 0-0 electronic transitions were driven with PDL, and the fluorescence signals were dispersed by the monochromator and then imaged onto an intensified charge-coupled device camera (ICCD). Here, the delay time was set to maximize the fluorescence signal strength, which depends mostly on the experiment configuration, such as buffer gas flow rate (typical setting is ≈ 20 sccm) and the molecular species. Longer delay time is preferred if any peaks of molecular decays overlap with nearby atomic lines in the spectra.

In experiment, DLIF spectra of the decays from the lowest two electronic excited states for the molecules MO-adamantane , MOPh-4-(adamantan-1-yl) , MOPh-4-(diadamantan-2-yl) and MOPh-4-(diadamantan-4-yl) are recorded in the scheme shown in Figure 7.4 and 7.5. For simplicity, these molecules can be denoted as MO-Ad, MOPh-Ad, MOPh-diAd2, and MOPh-diAd4, respectively. The method of searching for these excited states can be found in the supporting information of previous work[38]. The fluorescence from the excited states was collected via an imaging system into a model 2035 McPherson monochromator equipped with a 1200 lines/mm grating. An Andor i334T intensified charge-coupled device camera (ICCD) is used to record the dispersed spectra, with its gate time set to $\approx 20 - 170$ ns after the laser pulse for capturing the fluorescence signal right after the excitation (pulse duration ≈ 20 ns) while precluding signals of the PDL and ambient light. The entrance slit width was set at ≈ 0.10mm, resulting in a resolution of ≈ 10 cm^{-1} in the spectra.

7.2 DLIF spectra of Ca/SrOPh-4-CH_3 and Ca/SrOPh-4-$C(CH_3)_3$

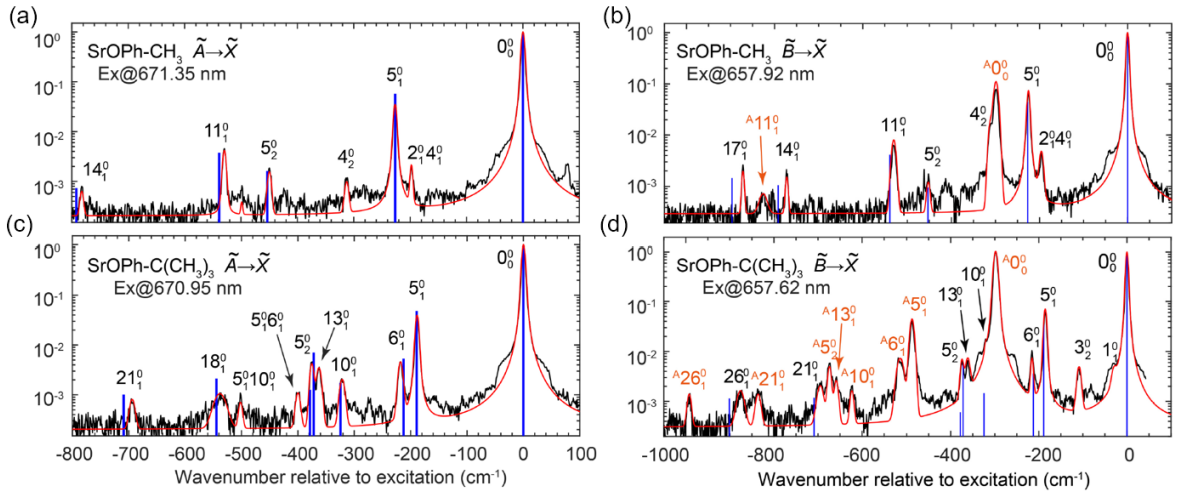

Figure 7.2: DLIF spectra of the SrOPh-CH_3 and SrOPh-$C(CH_3)_3$.

Figure 7.2(a) presents the dispersed spectrum for the $\widetilde{A} \rightarrow \widetilde{X}$ transition of SrOPh-CH_3 at an excitation wavelength of 671.35 nm. The peak at the origin, labeled as 0_0^0, represents the non-vibration-changing diagonal decay ($\widetilde{A}, \nu = n' \rightarrow \widetilde{X}, \nu = n''$). It is primarily from ground state $0' \rightarrow 0''$ decay, with minor contributions ($< 1\%$) from higher vibrational levels $n' \rightarrow n''(n > 0)$ decays due to hot band excitations[37]. The strongest vibration-changing off-diagonal decay is observed at -227 cm^{-1}, corresponding to the theoretical harmonic frequency of the lowest Sr-O and ring stretching mode ν_5 = 227 cm^{-1}. The spectra of the SrOPh-CH_3 $\tilde{B} - \tilde{X}$ transitions were also studied, see Fig. 7.2(b). The spectral line doublet at approximately 200 cm^{-1} indicates the Fermi resonance between the 5_1 and 2_14_1 modes in the ground state [212], which is also observed in the $\tilde{A} - \tilde{X}$ spectra shown in Fig. 7.2(a). Fig. 7.2(c) is SrOPh-$C(CH_3)_3$, which shows a similar decay pattern. Besides the diagonal decay at the origin, the most prominent off-diagonal decay is observed at -189 cm^{-1}, which is attributed to the lowest-frequency Sr-O stretching mode ν_5 = 189 cm^{-1}. Other Sr-O stretching modes, such as ν_6=212 cm^{-1}, ν_{10} = 325 cm^{-1}, ν_{13}=372 $cm^{-1}$and ν_{18} = 544 $cm^{-1}$and ν_{21}=709 cm^{-1}, are observed at shifts of -218 cm^{-1}, -321 cm^{-1}, -363 cm^{-1}, -538 $cm^{-1}$and -694 cm^{-1}, respectively. The presence of additional vibrational decays is likely due

to the flexible structure of the t-butyl moiety.

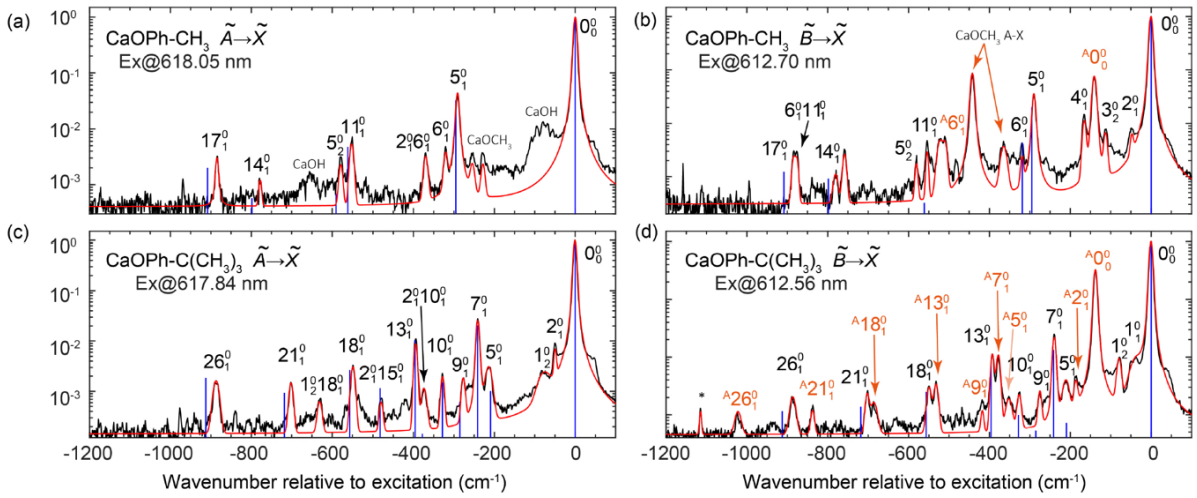

Figure 7.3: DLIF spectra of the CaOPh-CH_3 and CaOPh-$C(CH_3)_3$.

The DLIF spectra of $\tilde{A}/\tilde{B} - \tilde{X}$ transitions for the CaOPh-CH_3 and CaOPh-$C(CH_3)_3$ are shown in Fig. 7.3 (a-d), where most of the observed VBRs of the off-diagonal decays match well with the theoretical prediction indicated by blue sticks. On the other hand, due to the contamination in the chemical, the background signals from CaOH and $CaOCH_3$ with relative intensity around $10^{-2} - 10^{-3}$ were observed, which are recognized by the comparison to the data reported in Ref.[213–215] as well as the broader line shapes (FWHM $= 20 - 40\text{cm}^{-1}$) compared to the lines that can be well assigned to the CaOPh-CH_3 and CaOPh-$C(CH_3)_3$ transitions. The Calcium 616 and 657nm lines were also observed due to the ablation of the Ca/CaH_2 targets.

7.3 DLIF from the lowest excited states of the molecules with adamantane ligands

The DLIF spectra of MO-Ad, MOPh-Ad, MOPh-diAd2 and MOPh-diAd4 from are shown in Figure 7.4. Figure 7.4 (a) displays the CaO-Ad $A^2E_{1/2} - X^2A_1$ DLIF spectrum at excitation of 633.5nm. As there is a strong Jahn-Teller effects between the two $\tilde{A}$ states and the two degenerate bending modes (ν_1 and ν_2) [28], many of the vibrational decays observed in the

spectra come with a side band structure corresponding to the transition in the bending modes (2_1^0). In Figure 7.4(b), the SrO-Ad $\tilde{A}^2E_{1/2} \rightarrow \tilde{X}^2A_1$ transition is driven at 692.1 nm, and the diagonal decay, $\tilde{A}^2E_{1/2}0^0 - \tilde{X}^2A_10_0$, is labeled as 0_0^0. The origin is set at the 0_0^0 peak's center. Decays from the $\tilde{A}^2E_{3/2}0^0$ state to the $\tilde{X}^2A_15_1$ and $\tilde{X}^2A_10_0$ states, labeled with $\circ$ at 75cm^{-1} and -195cm^{-1}, respectively, are observed in the spectrum due to the collision-induced excitation [37]. Decays from the excited bending mode in the excited state $\tilde{A}^2E_{1/2}2^1$ (2_0^1, $2_0^15_1^0$) are also observed at 54cm^{-1} and -216cm^{-1}, respectively.

Figure 7.4 (c), (e) and (g) present the spectra for CaOPh-Ad, CaOPh-diAd2 and CaOPh-diAd4, respectively, originating from the $\widetilde{A}$ state with excitations at 618 nm and 617.7 nm. The calcium 616.2 and 657nm lines are observed and labeled with $*$ in these spectra. Comparing to the spectra of the strontium species, more off-diagonal vibrational decays are observed in the calcium ones. The doublet at approximately -190 cm^{-1} in Figure 7.4 (b) indicates the presence of Fermi resonance between the 6_1 and 3_15_1 states in the CaOPh-Ad. On the other hand, in Figure 7.4 (c), the doublet at -190 cm^{-1} is due to the overlap of the ${}^A6_1^0$ and ${}^A7_1^0$ lines, as the intensity ratios of both of the lines are in good agreement with the theoretical prediction. The peak at +58cm^{-1} on the blue side of the 0_0^0 peak is the 2_0^1 decays of $\tilde{A}^2E_{1/2} \rightarrow \tilde{X}^2A_1$. For the peaks on the red side of the 0_0^0 peak, the strontium atomic transitions of 707nm ($^3S_1 \rightarrow {}^3P_2$) and 710nm ($5s12p$, $^1P_1 \rightarrow 5s6s$, $^1S_0$), labeled with the $+$ signs, are observed at -310cm^{-1} and -366cm^{-1}, respectively. Similarly, the rest of the peaks correspond to the off-diagonal decays of the $\tilde{A}^2E_{1/2} \rightarrow \tilde{X}^2A_1$ transition, with the final states assigned and labeled according to the theoretical results plotted with the blue vertical lines.

Figure 7.4 (d) shows the spectrum of SrOPh-Ad $\tilde{A} \rightarrow \tilde{X}$ excited at 671.3nm. Only three off-diagonal vibrational decays from the A state are observed: 6_1^0 at 154 cm^{-1}, $2_1^05_1^0$ at 170 cm^{-1} and 11_1^0 at 327 cm^{-1}. The $2_1^05_1^0$ decay borrow its line intensity from the 6_1^0 line due to the Fermi resonance [212]. Figure 7.4 (f) and (h) are the DLIF spectrum of $\tilde{A} \rightarrow \tilde{X}$ transition of SrOPh-diAd2 and SrOPh-diAd4, respectively. Fermi resonance is also observed in the both molecules, as the 6_1^0 lines in the both molecule are split into two and three lines, respectively. The lines labeled with "+" signs are the strontium 679 nm, 689 nm, 707nm and

710nm atomic lines, which are produced from the ablation of the SrH_2 in the pressed target. The spectra are cut off at -800cm^{-1}, because the camera sensor quantum efficiency in the range of $\lambda > 710$nm is too low to distinguish the fluorescence signals from the background noise.

7.4 DLIF from the second lowest excited states of the molecules with adamantane ligands

To further verify the experiment results and the line assignments in the adamantanes with SrO/CaO units in the previous section, we measured the DLIF for the transitions from the second lowest excited levels of these molecules, see Figure 7.5. Similar to previous works [37, 38], all the spectra shown in Figure 7.5 come with the lines from the lowest excited levels that are labeled in orange. These lines are likely due to the collisional relaxation or the non-Born-Oppenheimer effects between the vibrational and electronic states. Figure 7.5 (a) shows that the $\tilde{A}^2E_{3/2} - \tilde{X}^2A_1$ spectrum of the CaO-Ad molecule also contains many off-diagonal decays with the transition in bending mode, displaying the Jahn-Teller (JT) interaction between the electronic and bending states. The interaction strength is estimated to be around $10^0 - 10^1$ cm^{-1} according to the results of $CaOCH_3$, another C_{3v} symmetry type molecule in which the electronic and vibrational states of the E symmetry are mixed by the linear JT terms [62]. Figure 7.5 (b) is the $\tilde{A}^2E_{3/2} - \tilde{X}^2A_1$ spectrum of the SrO-Ad molecule. As the spin-orbit effect of the $\tilde{A}$ state in the SrO-Ad (≈ 260 cm^{-1}) is much stronger than that in the CaO-Ad (≈ 70 cm^{-1}), the mixing due to the JT effect is relatively weaker and hence less decays with bending mode transition 2^0_1 were observed.

Figure 7.5 (c-h) are the $\tilde{B} - \tilde{X}$ spectra of all the other phenol-adamantane species studied in this work. In general, the frequencies of observed vibrational modes in these molecules match very well with the corresponding results from $\tilde{A} - \tilde{X}$ scans, and the differences between the two separate measurements do not exceed the systematic uncertainty induced by the spectrometer and ICCD camera (≈ 3 cm^{-1}). The measured frequencies of the fundamental

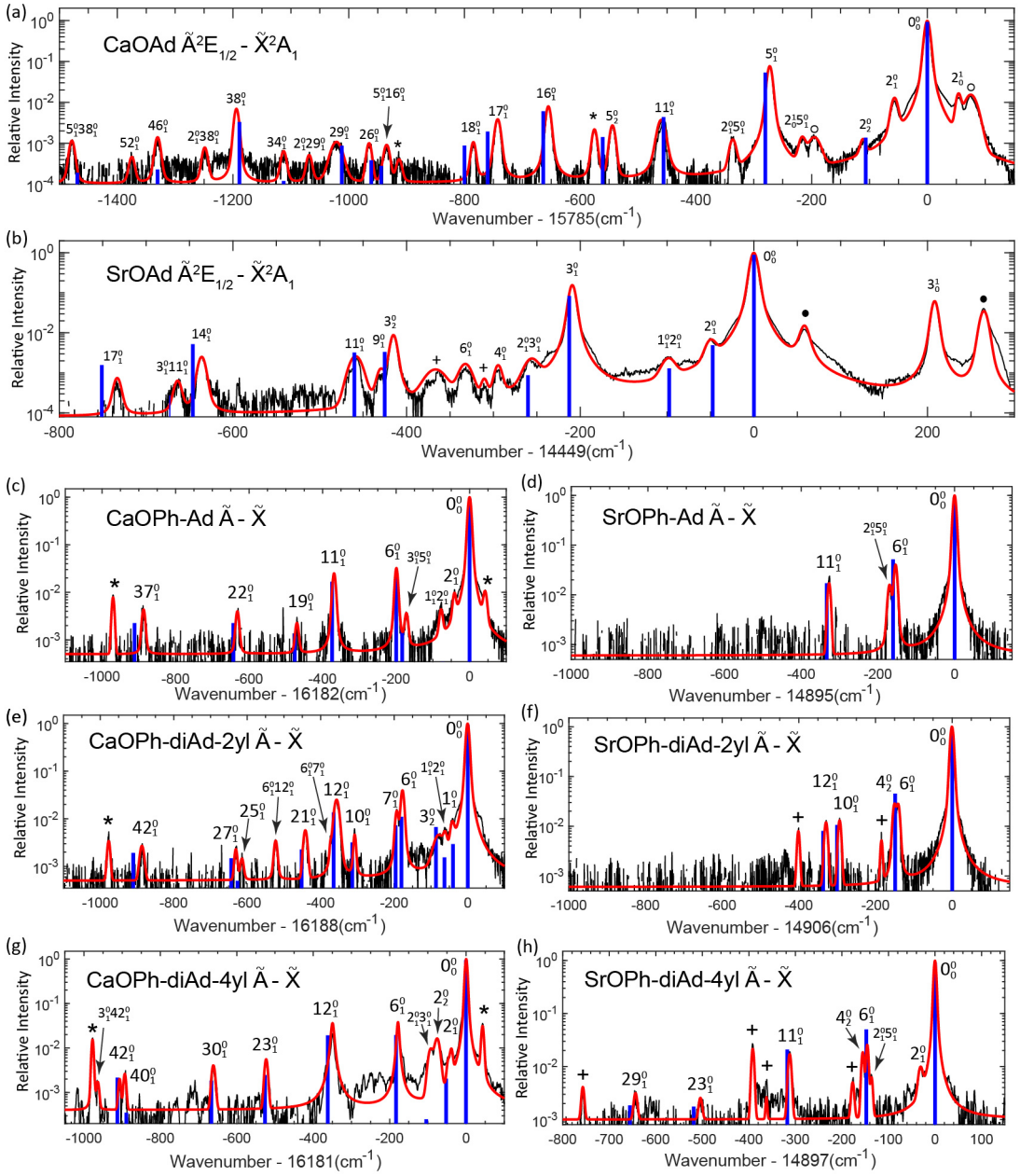

Figure 7.4: DLIF spectra of the $\widetilde{A} \rightarrow \widetilde{X}$ transitions of MOAd, MOPh-Ad, MOPh-diAd2 and MOPh-diAd4.

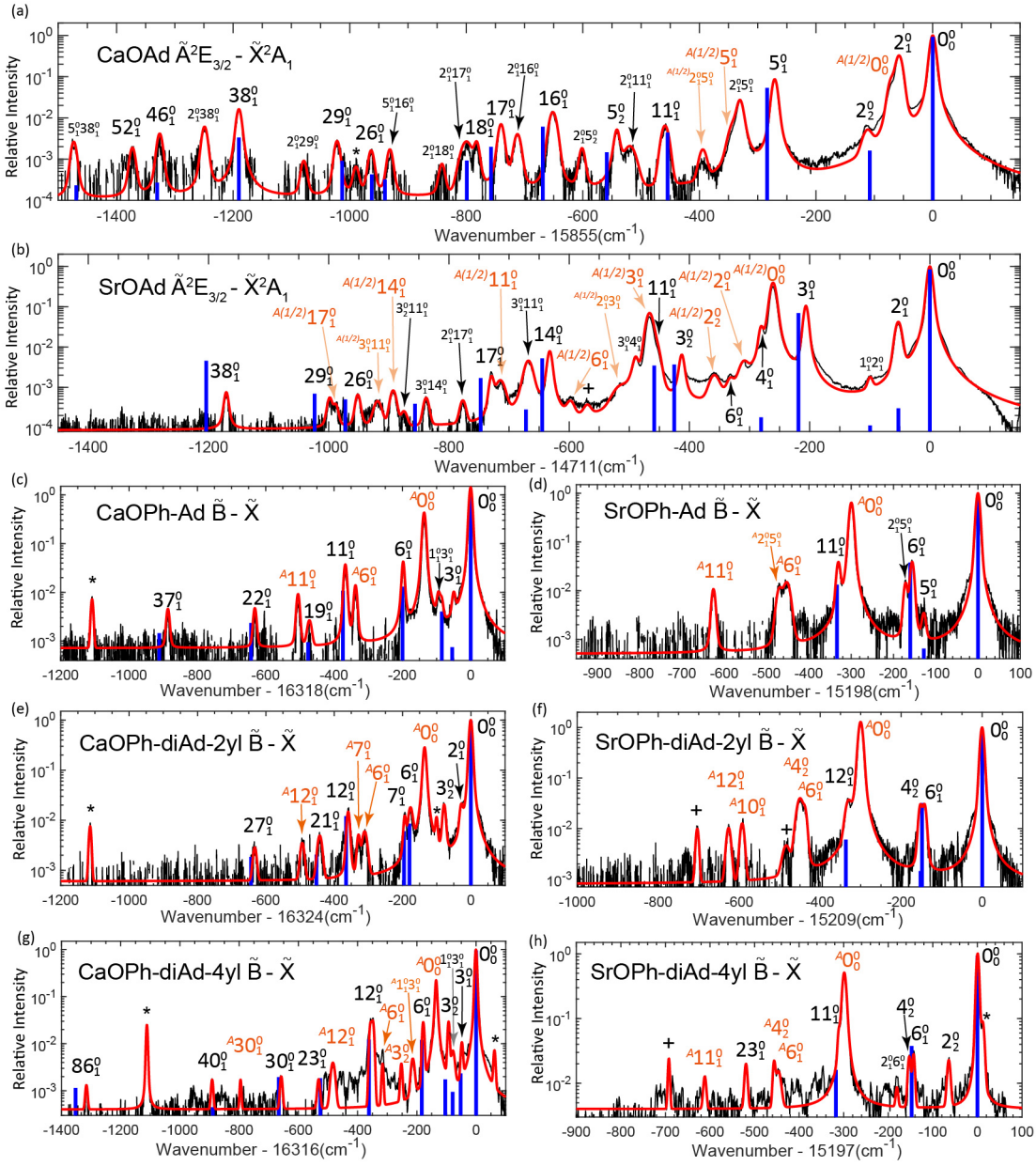

Figure 7.5: DLIF spectra of the $\widetilde{B} \rightarrow \widetilde{X}$ transitions of MOAd, MOPh-Ad, MOPh-diAd2 and MOPh-diAd4.

Vib. Modes	CaO-Adamantane Exp.	Theo.
2_1	57(7)	53
5_1	272(6)	280
11_1	460(8)	456
16_1	653(8)	664
17_1	741(6)	760
18_1	783(5)	801
26_1	964(6)	961
29_1	1021(6)	1012
34_1	1112(6)	1114
38_1	1192(6)	1189
46_1	1328(6)	1330
52_1	1374(6)	1374

Vib. Modes	SrOPh-4-(diAdamantan-2-yl) Exp.	Theo.
6_1	141(4)	149
10_1	293(4)	300
12_1	330(4)	337

Vib. Modes	SrO-Adamantane Exp.	Theo.
2_1	51(5)	75
3_1	208(4)	205
4_1	288(8)	297
6_1	332(6)	336
9_1	430(4)	427
11_1	457(7)	473
14_1	634(4)	644
17_1	731(4)	742
26_1	952(3)	975
29_1	998(3)	1015
38_1	1170(3)	1206

Vib. Modes	SrOPh-4-(diAdamantan-4-yl) Exp.	Theo.
2_1	31(4)	33
6_1	145(3)	148
11_1	312(3)	318
23_1	512(9)	518
29_1	644(3)	655

Vib. Modes	CaOPh-4-(Adamantan-1-yl) Exp.	Theo.
2_1	41(4)	43
3_1	49(4)	54
6_1	198(4)	200
11_1	368(4)	374
19_1	471(4)	476
22_1	632(4)	643
37_1	887(4)	912

Vib. Modes	CaOPh-4-(diAdamantan-2-yl) Exp.	Theo.
2_1	28(4)	31
6_1	177(4)	180
7_1	193(4)	196
10_1	307(3)	314
12_1	358(6)	365
21_1	442(5)	452
25_1	614(4)	626
27_1	631(4)	643
42_1	886(5)	910

Vib. Modes	SrOPh-4-(Adamantan-1-yl) Exp.	Theo.
5_1	128(4)	128
6_1	155(4)	160
11_1	329(4)	333

Vib. Modes	CaOPh-4-(diAdamantan-4-yl) Exp.	Theo.
2_1	39(3)	39
3_1	47(4)	52
6_1	178(3)	183
12_1	349(4)	362
23_1	527(5)	526
30_1	659(5)	666
40_1	892(3)	889
42_1	907(3)	912
86_1	1315(4)	1352

Table 7.1: The observed and calculated frequencies of the resolved fundamental vibrational modes in the electronic ground states of all the molecular species involved in this work (unit: cm $^{-1}$).

modes are calculated from the average values of the observations from the $\tilde{A}-\tilde{X}$ and $\tilde{B}-\tilde{X}$ scans, and their uncertainties are evaluated from the differences in the observations and the aforementioned uncertainty of the experimental setup, see Table. 7.1.

The spectra of decaying from the second lowest excited states agree well with the aforementioned results in the aspects of the vibrational mode frequencies and the positions of the atomic lines. In order to compare to the theoretical calculation for the vibrational branching ratios, we fitted the lines observed in all the aforementioned spectra with the Voigt line shapes and obtained the intensity ratios, with all the experimental and theoretical results shown in Fig. 7.6. In general, the experiment agrees well with the theory, except the vibrational decays induced from the Fermi resonance (e.g., the 4_2^0 line in the SrOPh-diAd spectra) and the Jahn-Teller effect (e.g., the lines with 2_1^0 vibrational transition in the CaOAd spectra).

7.5 Measured VBRs and transition energies of all phenoxide molecules

Fig. 7.6 visually illustrates the intensity ratios of the observed decay channels of the phenoxide molecules. Generally, the experimental results align well with theoretical predictions,

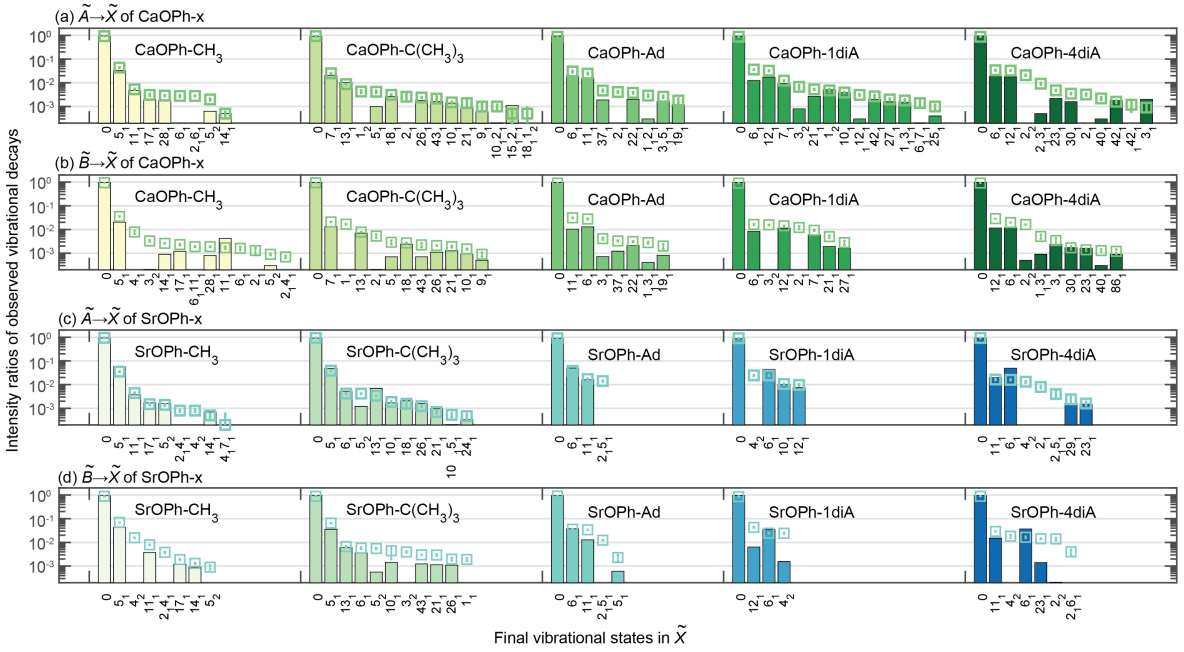

Figure 7.6: Theoretical and experimental results for the intensity ratios of all observed vibrational decays of molecules studied in this work. Each molecule has both $\widetilde{A} \rightarrow \widetilde{X}$ and $\widetilde{B} \rightarrow \widetilde{X}$ transitions. The colored bars indicate the theoretical values while the empty squares show the experimental ratios extracted from the peak areas. Errors are statistical standard errors.

with some exceptions for overtone or combination modes related to Fermi resonance coupling, which eludes the harmonic approximation calculations. Most molecules exhibit only two or three significant vibrational decays with intensities above 10^{-2}, and major decays have intensity ratios between 10^{-3} and 10^{-2}, demonstrating little variation despite the increase in substituent size. According to the calculation results in Table 7.2, the sum of VBRs for the undetected vibrational decays with low VBR is approximately $0.3 - 5\%$, suggesting that OCCs could scatter about $20 - 300$ photons if all the measured vibrational transitions are addressed during repumping. Molecules with the -$C(CH_3)_3$ substituent exhibit a greater number of vibrational decays, likely due to their flexible structures. The Sr-containing molecules show fewer vibrational decays compared to those containing Ca, indicating that heavier metal atoms may dampen the vibrational motions. Across all molecules, the pronounced vibrational decays originate from the low-frequency metal-oxygen stretching modes. To investigate the influence of substituent size and complexity on OCC, we analyzed the transition energies and intensity ratios of diagonal vibrational decays, as depicted in Fig. 7.7. Figs. 7.7(a)-(b) reveal that the transition energies of CaOPh and SrOPh are approximately 40 cm^{-1}higher than those of their derivatives, a discrepancy due to the electron-donating nature of hydrocarbon ligands, in contrast to the strong electron-withdrawing characteristics of groups like -F or -CF_3 [37, 38]. The minimal variation in transition energies, remaining within 10$cm^{-1}$for all derivatives, underscores a consistent electronic structure across different substituents. Projecting this pattern forward, we anticipate that the transition energies for substituents of larger diamondoids and bulk diamonds will remain close. This invariance of the transition energy towards the ligand in the diamonoid series makes it easy to identify the excitation transition in MOPh-diamond complexes.

Figs. 7.7(c)-(d) illustrate the scaled intensity ratios of the diagonal vibrational decay for Ca- and Sr-containing molecules, respectively. For Ca derivatives, the experimental ratios were observed to range $\approx 0.88 - 0.94$, consistently lower than the theoretical predictions. A discernible trend in the theoretical VBRs was observed, with a decrease observed from CaOPh to CaOPh-Ad, followed by an increase with larger diamondoids. Experimentally, the

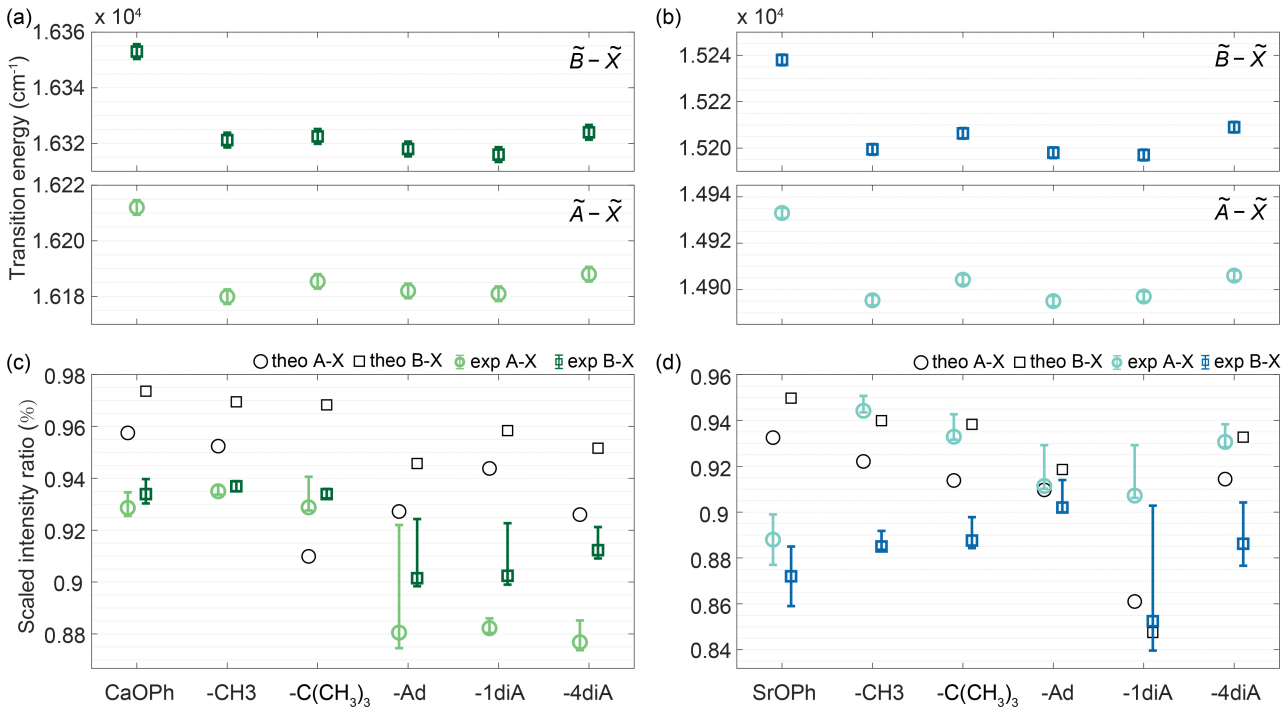

Figure 7.7: (a)-(b) Measured excitation energies of $\widetilde{A} \rightarrow \widetilde{X}$ and $\widetilde{B} \rightarrow \widetilde{X}$ transitions for all molecules studied in this work. (c)-(d) Theoretical and experimental intensity ratios of the diagonal transitions for all molecules. The values of CaOPh and SrOPh are taken from Refs.[37, 38, 212].

ratios for smaller ligands are 0.93 in both transitions, while larger diamondoid substituents exhibit ratios at a range of 0.88-0.92. Interestingly, larger diamondoid substituents appeared to have negligible impact on the diagonal decay ratios. For Sr-containing molecules, the experimental ratio range is broader, spanning from 0.85 to 0.95. The distribution appears more random, showing no discernible trends with increasing ligand size.

7.6 Uncertainty analysis

All observed peaks in DLIF spectra are fitted with the Voigt function in PGopher, with line intensities estimated from the areas under these fitted curves. The statistical uncertainties of the fitting parameters are estimated with the covariance matrix. The Jacobian conversion from wavelength and frequency is performed as a correction to the calculation of line intensities [216]. In addition, as the spectra were taken in a wide wavelength range (610-750nm) while the ICCD sensor quantum efficiency (QE) curve, $> 40\%$ in range of 600-615nm, drops to below 20% as wavelength $>$ 710nm (the QE data was provided by the vendor, Oxford Instrument - Andor Technology), the scaling with the inverse of quantum efficiency is therefore applied to the line intensity calculation. The two corrections, denoted as Δ_J and Δ_{QE}, respectively, are calculated from the differences between the intensity ratios before and after the scaling. The corrections can be larger than the statistical uncertainties, hence we listed these correction terms for the diagonal VBFs in the table 7.5, for comparison.

The unobserved peaks which contribute to the VBRs can lead to system uncertainties [37], as the true VBRs depend on contributions of all possible decay pathways. Due to the limitations of the measurement sensitivity and the detection window, only a few vibrational decays have been observed for each transition. Compared to a complete description of vibrational decays obtained from calculated FCFs, all unobserved vibrational decays are therefore a source of the systematic uncertainty, which is estimated by [37]:

$$S_0' = \frac{S_0^{(c)}}{\sum_{i=0}^{p} S_i^{(c)} + \sum_{i=p+1}^{N} \frac{T_i}{C}}, \tag{7.1}$$

Final state	CaO-Adamantane				Final state	SrO-Adamantane			
	Exp.(A)	Cal.(A)	Exp.(B)	Cal.(B)		Exp.(A)	Cal.(A)	Exp.(B)	Cal.(B)
0	$0.8772^{+0.0024}_{-0.0011}$	0.9239	$0.612^{+0.004}_{-0.002}$		0	$0.811^{+0.013}_{-0.002}$	0.8922	$0.773^{+0.017}_{-0.004}$	0.8886
2_1	0.0087(4)	$< 10^{-4}$	0.2272(22)		2_1	0.0052(15)	0.0348	0.0311(35)	0.0003
2_2	0.0004(1)	0.0014	0.0040(9)		1_12_1	0.0019(1)	0.0004	0.0007(1)	0.0004
5_1	0.0731(7)	0.0535	0.0601(5)		3_1	0.1411(9)	0.0572	0.0855(21)	0.0573
2_15_1	0.0013(1)	$< 10^{-4}$	0.0247(3)		2_13_1	0.0030(2)	0.0034		$< 10^{-4}$
11_1	0.0055(2)	0.0043	0.0043(5)		4_1	0.0008(1)	0.0001	0.0192(13)	0.0001
2_111_1		$< 10^{-4}$	0.0020(1)		6_1	0.0018(3)	$< 10^{-4}$	0.0006(1)	$< 10^{-4}$
5_2	0.0023(2)	0.0014	0.0042(4)		3_2	0.0093(3)	0.0016	0.0056(8)	0.0016
2_15_2		$< 10^{-4}$	0.0008(1)		9_1	0.0011(1)	$< 10^{-4}$		$< 10^{-4}$
16_1	0.0082(2)	0.0060	0.0125(5)		11_1	0.0039(3)	0.0023	0.0076(12)	0.0023
2_116_1		$< 10^{-4}$	0.0032(2)		3_14_1		$< 10^{-4}$	0.0077(2)	$< 10^{-4}$
17_1	0.0045(4)	0.0019	0.0061(5)		14_1	0.0045(5)	0.0023	0.0086(3)	0.0023
18_1	0.0010(1)	0.0009	0.0016(5)		3_111_1	0.0010(1)	0.0001	0.0084(14)	0.0001
2_117_1		$< 10^{-4}$	0.0025(6)		17_1	0.0014(1)	0.0006	0.0027(4)	0.0006
2_118_1		$< 10^{-4}$	0.0005(1)		2_117_1		$< 10^{-4}$	0.0005(1)	$< 10^{-4}$
5_116_1	0.0007(1)	0.0003	0.0010(1)		3_114_1		0.0003	0.0007(1)	0.0001
26_1	0.0007(1)	0.0004	0.0011(1)		3_211_1		$< 10^{-4}$	0.0003(1)	$< 10^{-4}$
29_1	0.0020(3)	0.0009	0.0017(1)		26_1		0.0005	0.0011(1)	0.0001
2_129_1	0.0003(1)	$< 10^{-4}$			29_1		0.0005	0.0010(1)	0.0002
34_1	0.0003(1)	0.0001			38_1		0.0036	0.0034(3)	0.0020
38_1	0.0076(3)	0.0033	0.0147(5)						
2_138_1	0.0005(1)	$< 10^{-4}$	0.0052(2)						
46_1	0.0015(1)	0.0002	0.0021(2)						
52_1	0.0003(1)	$< 10^{-4}$	0.0009(2)						
5_138_1	0.0015(1)	0.0002	0.0028(2)						
Final state	CaOPh-4-(Adamantan-1-yl)				Final state	SrOPh-4-(Adamantan-1-yl)			
	Exp.(A)	Cal.(A)	Exp.(B)	Cal.(B)		Exp.(A)	Cal.(A)	Exp.(B)	Cal.(B)
0	$0.881^{+0.041}_{-0.006}$	0.9330	$0.901^{+0.023}_{-0.003}$	0.9532	0	$0.911^{+0.018}_{-0.001}$	0.9150	$0.902^{+0.012}_{-0.002}$	0.9387
2_1	0.0041(4)	$< 10^{-4}$		$< 10^{-4}$	5_1		0.001	0.0023(7)	0.0006
3_1		0.0003	0.0041(5)	0.0007	6_1	0.0379(13)	0.0502	0.0361(7)	0.0374
1_12_1	0.0029(3)	0.0003		$< 10^{-4}$	2_15_1	0.0142(7)	$< 10^{-4}$	0.0124(5)	$< 10^{-4}$
1_13_1		$< 10^{-4}$	0.0028(3)	0.004	11_1	0.0172(7)	0.0160	0.0341(9)	0.0126
3_15_1	0.0026(3)	0.0017		$< 10^{-4}$					
6_1	0.0300(24)	0.0202	0.0276(17)	0.0126					
11_1	0.0246(18)	0.0157	0.0311(12)	0.0101					
19_1	0.0018(4)	0.0012	0.0020(5)	0.0008					
22_1	0.0038(3)	0.0020	0.0031(2)	0.0021					
37_1	0.0047(4)	0.0019	0.0033(2)	0.0012					

Table 7.2: The intensity ratios of all observed vibrational decays of all molecules with diamondoid substituents. The errors indicate the combined statistical uncertainties from the Voigt fits, sensor quantum efficiency, Jacobian correction and unmeasured lines. The theoretical VBRs are also added for comparison.

where p is the number of observed vibrational decays, T_i is the theoretical VBRs, $C = \frac{1}{p+1}\sum_{i=0}^{p}\frac{T_i}{S_i^{(c)}}$ is a scaling factor, and $S_i^{(c)} = S_i + \Delta_{J,i} + \Delta_{QE,i}$ denotes the intensity ratios with corrections. For a straight forward comparison between the scaled VBFs, S_i', and the intensity ratios, $S_i^{(c)}$, we denote their differences as $\delta_{u,i} = S_i' - S_i^{(c)}$. The values of δ_u for the

Final state	CaOPh-4-(diAdamantan-2-yl) Exp.(A)	Cal.(A)	Exp.(B)	Cal.(B)	Final state	CaOPh-4-(diAdamantan-4-yl) Exp.(A)	Cal.(A)	Exp.(B)	Cal.(B)
0	$0.882^{+0.004}_{-0.002}$	0.9342	$0.902^{+0.020}_{-0.003}$	0.9564	0	$0.877^{+0.008}_{-0.003}$	0.9491	$0.912^{+0.009}_{-0.003}$	0.9616
1_2	0.0048(7)	0.0051		0.0008	2_1	0.0032(3)	$< 10^{-4}$		$< 10^{-4}$
2_1		0.0001	0.0121(18)	$< 10^{-4}$	3_1	0.0009(3)	0.0020	0.0034(10)	0.0023
1_13_1	0.0018(2)	0.0015		$< 10^{-4}$	1_13_1		0.0012	0.0051(11)	0.0009
3_2	0.0068(13)	0.0008	0.0157(7)	$< 10^{-4}$	2_2	0.0210(10)	$< 10^{-4}$	0.0162(5)	0.0005
6_1	0.0362(6)	0.0126	0.0164(10)	0.0083	2_13_1	0.0092(8)	0.0005		$< 10^{-4}$
7_1	0.0123(4)	0.0093	0.0093(7)	0.0058	6_1	0.0339(14)	0.0190	0.0198(5)	0.0117
10_1	0.0039(2)	0.0038		0.0026	12_1	0.0329(9)	0.0180	0.0285(5)	0.0115
12_1	0.0326(7)	0.0171	0.0143(6)	0.0113	23_1	0.0048(2)	0.0022	0.0014(2)	0.0016
6_17_1	0.0014(4)	0.0002		0.0001	30_1	0.0035(2)	0.0016	0.0017(3)	0.0017
21_1	0.0053(2)	0.0027	0.0050(7)	0.0019	40_1	0.0022(3)	0.0003	0.0013(2)	0.0003
6_112_1	0.0031(2)	0.0003		0.0001	42_1	0.0016(2)	0.0018		0.0011
25_1	0.0010(2)	0.0004		0.0004	3_142_1	0.0012(6)	$< 10^{-4}$		$< 10^{-4}$
27_1	0.0020(2)	0.0016	0.0028(6)	0.0016	86_1		0.0015	0.0012(3)	0.0009
42_1	0.0027(4)	0.0020		0.0013					
Final state	SrOPh-4-(diAdamantan-2-yl) Exp.(A)	Cal.(A)	Exp.(B)	Cal.(B)	Final state	SrOPh-4-(diAdamantan-4-yl) Exp.(A)	Cal.(A)	Exp.(B)	Cal.(B)
0	$0.907^{+0.022}_{-0.001}$	0.8682	$0.852^{+0.050}_{-0.013}$	0.8542	0	$0.931^{+0.008}_{-0.002}$	0.9196	$0.886^{+0.018}_{-0.010}$	0.9368
6_1	0.0243(7)	0.0440	$0.0245^{+0.0016}_{-0.0007}$	0.0312	2_1	0.0080(9)	$< 10^{-4}$		$< 10^{-4}$
4_2	0.0246(7)	$< 10^{-4}$	$0.0243^{+0.0015}_{-0.0007}$	0.0014	2_2		0.0002	0.0139(21)	0.0002
10_1	0.0106(5)	0.0100		0.0074	2_15_1	0.0040(12)	$< 10^{-4}$		$< 10^{-4}$
12_1	0.0097(7)	0.0075	$0.0430^{+0.0029}_{-0.0016}$	0.0057	6_1	0.0159(8)	0.0490	0.0165(17)	0.0367
					4_2	0.0132(9)	$< 10^{-4}$	0.0183(31)	$< 10^{-4}$
					2_16_1		$< 10^{-4}$	0.0040(10)	$< 10^{-4}$
					11_1	0.0164(8)	0.0197	0.029(8)	0.0151
					23_1	0.0016(3)	0.0015	0.0143(9)	0.0014
					29_1	0.0024(9)	0.0016		$< 10^{-4}$

Table 7.3: (continued from the Table 7.2)

Final	CaOPh-4-CH_3				Final	SrOPh-4-CH_3			
state	Exp. (A)	Cal. (A)	Exp. (B)	Cal. (B)	state	Exp. (A)	Cal. (A)	Exp. (B)	Cal. (B)
0	0.9350(23)	0.9562	0.9369(20)	0.9718	0	0.9442(65)	0.9269	0.885(7)	0.9438
2_1		$< 10^{-4}$	0.0013(4)	$< 10^{-4}$	2_14_1	0.0008(1)	$< 10^{-4}$	0.0038(3)	$< 10^{-4}$
3_2		$< 10^{-4}$	0.0033(3)	0.0001	5_1	0.0353(5)	0.0571	0.0698(11)	0.0423
4_1		$< 10^{-4}$	0.0078(14)	$< 10^{-4}$	4_2	0.0008(1)	$< 10^{-4}$	0.0158(6)	$< 10^{-4}$
2_24_1		$< 10^{-4}$	0.0007(1)	$< 10^{-4}$	5_2	0.0014(1)	0.0016	0.0009(2)	$< 10^{-4}$
5_1	0.0437(12)	0.0325	0.0356(11)	0.0202	4_17_1	0.00018(4)	$< 10^{-4}$		0.0008
6_1	0.0028(3)	$< 10^{-4}$	0.0016(3)	$< 10^{-4}$	11_1	0.0044(2)	0.0037	0.0080(2)	0.0037
2_16_1	0.0028(1)	$< 10^{-4}$		$< 10^{-4}$	14_1	0.0005(1)	0.0007	0.0013(1)	0.0009
11_1	0.0053(3)	0.0047	0.0017(2)	0.0042	17_1	0.0015(1)	0.0017	0.0019(1)	0.0012
5_2	0.0020(2)	0.00063	0.0009(1)	0.0003					
14_1	0.0005(1)	0.00052	0.0026(1)	0.0009					
6_111_1		$< 10^{-4}$	0.0019(1)	$< 10^{-4}$					
17_1	0.0031(3)	0.002	0.0023(2)	0.0012					
28_1	0.0029(1)	0.0018	0.0019(1)	0.0008					
Final	CaOPh-4-$C(CH_3)_3$				Final	SrOPh-4-$C(CH_3)_3$			
state	Exp. (A)	Cal. (A)	Exp. (B)	Cal. (B)	state	Exp. (A)	Cal. (A)	Exp. (B)	Cal. (B)
0	0.9288(12)	0.9159	0.9489(18)	0.9711	0	0.9329(98)	0.9200	0.8876(102)	0.9431
1_1		$< 10^{-4}$	0.0014(1)	$< 10^{-4}$	1_1		$< 10^{-4}$	0.0019(3)	$< 10^{-4}$
2_1	0.0026(7)	$< 10^{-4}$	0.0054(10)	0.0001	3_2		$< 10^{-4}$	0.0039(3)	$< 10^{-4}$
1_2	0.0043(6)	$< 10^{-4}$		$< 10^{-4}$	5_1	0.0387(7)	0.0481	0.0654(22)	0.0357
5_1	0.0042(5)	0.001	0.0029(6)	0.0007	6_1	0.0042(2)	0.0053	0.0057(5)	0.0036
7_1	0.0252(7)	0.0205	0.0211(8)	0.0133	10_1	0.0019(1)	0.0017	0.0044(24)	0.0014
9_1	0.0010(3)	0.0006	0.0009(2)	0.0005	13_1	0.0034(1)	0.0070	0.0067(5)	0.0060
10_1	0.0015(1)	0.0014	0.0015(1)	0.0009	5_2	0.0042(1)	0.0012	0.0055(4)	0.0006
2_110_1	0.0010(2)	0.0001		$< 10^{-4}$	5_110_1	0.0005(1)	0.0001		$< 10^{-4}$
13_1	0.0088(2)	0.0104	0.0080(2)	0.007	18_1	0.0016(5)	0.0021		0.0020
2_115_1	0.00047(3)	0.0011		$< 10^{-4}$	21_1	0.0007(1)	0.0010	0.0029(3)	0.0011
18_1	0.0031(1)	0.0026	0.0027(1)	0.0024	24_1	0.0005(1)	0.0003		0.0003
18_11_2	0.00052(4)	$< 10^{-4}$		$< 10^{-4}$	26_1	0.0012(1)	0.0016	0.0020(3)	0.0011
21_1	0.0014(4)	0.0009	0.0020(2)	0.0013	43_1		0.0018	0.0030(1)	0.0012
26_1	0.0024(1)	0.0018	0.0021(1)	0.0011					
43_1	0.00217(5)	0.0016	0.00228(5)	0.0007					

Table 7.4: The vibrational branching ratios of all observed vibrational decays of MOPh-CH_3 and MOPh-$C(CH_3)_3$ molecules. The errors indicate the combined statistical uncertainties from the Voigt fits, sensor quantum efficiency, Jacobian correction and unmeasured lines. The theoretical VBRs are also added for comparison.

Molecule	Ca-O-Adamantane		Sr-O-Adamantane		CaOPh-4-(Adamantan-1-yl)		SrOPh-4-(Adamantan-1-yl)	
Transition	$A^2E_{1/2} - X$	$A^2E_{3/2} - X$	$A^2E_{1/2} - X$	$A^2E_{3/2} - X$	$A - X$	$B - X$	$A - X$	$B - X$
0-0 Intensity ratios (S_0)	0.8947	0.6350	0.8510	0.8277	0.9293	0.9308	0.9341	0.9200
Curve fitting uncertainty(δS_0)	0.0010	0.0020	0.0015	0.0036	0.0025	0.0018	0.0011	0.0010
Jacobian correction (Δ_J)	-0.0058	-0.0076	-0.0048	-0.0174	-0.0028	-0.0027	-0.0018	-0.0023
Sensitivity correction (Δ_{QE})	-0.0094	-0.0222	-0.0128	-0.0206	-0.0046	-0.0041	-0.0032	-0.0038
Systematic uncertainty from unobserved decays (δ_u)	-0.0021	-0.0128	-0.0045	-0.0170	-0.0414	-0.0227	-0.0178	-0.0119
Scaled diagonal VBFs $S_0' = S_0 + \Delta_J + \Delta_{QE} + \delta_u$	0.8773	0.6116	0.8112	0.7726	0.8805	0.9015	0.9114	0.9020
Lower estimates of scaled VBFs (S_0'')	0.8772	0.6110	0.8102	0.7705	0.8752	0.8990	0.9113	0.9002
Upper error bar $\sqrt{(\delta S_0)^2 + \delta_u^2}$	0.0024	0.0036	0.0129	0.0174	0.0415	0.0228	0.0178	0.0120
Lower error bar $\sqrt{(\delta S_0)^2 + (S_0' - S_0'')^2}$	0.0011	0.0021	0.0019	0.0042	0.0060	0.0031	0.0012	0.0021
Molecule	CaOPh-4-(diAdamantan-2-yl)		CaOPh-4-(diAdamantan-4-yl)		SrOPh-4-(diAdamantan-2-yl)		SrOPh-4-(diAdamantan-4-yl)	
Transition	$A - X$	$B - X$	$A - X$	$B - X$	$A - X$	$B - X$	$A - X$	$B - X$
0-0 Intensity ratios (S_0)	0.8947	0.9270	0.8903	0.9243	0.9339	0.9098	0.9413	0.9079
Curve fitting uncertainty(δS_0)	0.0018	0.0022	0.0030	0.0031	0.0009	0.0015	0.0021	0.0082
Jacobian correction (Δ_J)	-0.0034	-0.0018	-0.0032	-0.0023	-0.0017	-0.0027	-0.0016	-0.0028
Sensitivity correction (Δ_{QE})	-0.0057	-0.0026	-0.0025	-0.0013	-0.0030	-0.0044	-0.0017	-0.0030
Systematic uncertainty from unobserved decays (δ_u)	-0.0034	-0.0202	-0.0078	-0.0084	-0.0219	-0.0504	-0.0074	-0.0159
Scaled diagonal VBFs $S_0' = S_0 + \Delta_J + \Delta_{QE} + \delta_u$	0.8822	0.9023	0.8768	0.9123	0.9072	0.8524	0.9306	0.8862
Lower estimates of scaled VBFs (S_0'')	0.8821	0.8998	0.8762	0.9117	0.9069	0.8397	0.9299	0.8817
Upper error bar $\sqrt{(\delta S_0)^2 + \delta_u^2}$	0.0038	0.0203	0.0084	0.0089	0.0220	0.0504	0.0077	0.0180
Lower error bar $\sqrt{(\delta S_0)^2 + (S_0' - S_0'')^2}$	0.0018	0.0034	0.0031	0.0032	0.0010	0.0128	0.0023	0.0096

Table 7.5: Measured intensity ratios and scaled VBRs of the diagonal 0-0 decay of all molecules. The scaling process considering contributions of unobserved vibrational decays is detailed in the section of error analysis of VBRs.

diagonal peaks can be found in Table. 7.5. As $S_0^{(c)}$ is always greater than S_0', it is regarded as the estimates for the upper bound of the actual diagonal VBRs, and S_0' is the reported value for the diagonal VBFs in this work. To estimate the lower bound of the VBFs, S_0'', we choose a smaller scaling factor $C' = C - \delta_C$ to replace C in Eq. 7.1, where δ_C is the

uncertainty of the scaling factor, i.e.,

$$\begin{aligned}\delta_C =& \sqrt{\sum_{i=0}^{p}\left(\frac{\partial C}{\partial S_i^{(c)}}\delta S_i^{(c)}\right)^2 + \left(\frac{\partial C}{\partial p}\times 1\right)^2} \\ \approx& \sqrt{\sum_{i=0}^{p} T_i^2\left(\frac{\delta S_i^{(c)}}{(p+1)S_i^{(c)}}\right)^2 + \left(\frac{1-C}{p+1}\right)^2},\end{aligned} \tag{7.2}$$

here, in the last step of Eq.7.2 we replaced the summation with an integral, i.e.

$$\sum_{i=0}^{p} f(i) \approx \int_0^{p+1} f(x)\mathrm{d}x, \tag{7.3}$$

and assumed that $f(p+1) = \frac{T_{p+1}}{S_{p+1}^{(c)}} \approx 1$. $\delta S_i^{(c)}$ is the uncertainty of $S_i^{(c)}$:

$$\begin{aligned}\delta S_i^{(c)} =& \sqrt{\sum_{j=0}^{p}\left(\frac{\partial S_i^{(c)}}{\partial I_j^{(c)}}\right)^2\left(\Delta I_j^{(c)}\right)^2} \\ =& \frac{1}{S}\sqrt{(1-2S_i^{(c)})(\Delta I_i^{(c)})^2 + S_i^2\sum_{j=0}^{p}\left(\Delta I_j^{(c)}\right)^2},\end{aligned} \tag{7.4}$$

where the $I_i^{(c)}$ are the line intensities corrected with the quantum efficiency and Jacobian terms, and $S_i^{(c)}$ are, practically, calculated accordingly with $I_i^{(c)}$:

$$S_i^{(c)} = \frac{I_i^{(c)}}{\sum_{j=0}^{p} I_j^{(c)}}. \tag{7.5}$$

7.7 Discussion

Our investigations into the dispersed laser-induced fluorescence (DLIF) spectra of the A-X transitions in strontium phenol-adamantanes reveal that the diagonal vibrational branching fractions exceed 90%. This significant finding demonstrates that the surface-bound OCCs are capable of scattering multiple photons using just a single pumping laser. Notably, the vibrational decays observed correspond predominantly to a limited number of stretching and

bending modes. This suggests that achieving vibrational cooling for these surface-bound OCCs could be efficiently managed with a minimal set of repumping lasers. Furthermore, the constrained rotational degrees of freedom allow for rotational cooling through straightforward pumping of the P-branch transitions the rotational cooling can be achieved by simply pumping the P-branch transitions $K \rightarrow K-1$ of the surface bound OCCs, where K is the projection quantum number of the rotational angular momentum onto an axis perpendicular to the surface. These experimental insights collectively suggest that cooling surface-bound OCCs to their ground state could be accomplished with only a few lasers, marking a significant step forward in the practical deployment of OCCs in quantum technologies.

Beyond their encouraging optical cycling properties, surface-bound OCCs exhibit another advantage for QIP: multiple quantum degrees of freedom. For example, in the $\tilde{X}$ state, due to the spin-rotational and spin-spin interactions, one can create qubit states with the spin states (S or I) and couple them to the rotational states K for quantum error corrections [217]. The hyperfine qubits can be obtained by selecting a different metal atom for the OCC, such as ^{171}Yb and ^{133}Ba. These potential quantum applications of the surface bound OCCs open new avenues for quantum manipulation and storage, allow the development of large-scale quantum computers that significantly surpass current capabilities in terms of qubit numbers by several orders of magnitude.

7.8 Conclusion

In summary, we we functionalized Ca/SrOPh molecules using ligands ranging in size from 1 to 187 amu, calculated and measured their VBRs, and directly explored the potential for optical cycling and quantum manipulation of surface-bound OCCs in quantum information processing. Calculation and measurements have shown that the diagonal VBRs of most of these molecules remain > 0.85, whereas the number of off-diagonal vibrational decays (VBR$> 10^{-4}$) does not systematically increase with the size of the molecule or the number of potential vibrational states of the molecule. Additionally, such results are indicative of the powerful coupled optical cycling transitions that are nearly size and ligand complexity-

independent, suggesting the possibility that only a minimal number of lasers may be needed for vibrational repumping of surface-bounded OCCs. Furthermore, the multiple quantum degrees of freedom of these molecules could be useful in quantum information processing and storage. By coupling spin states with rotational states, surface-bound OCCs can be used for quantum error corrections, with the potential to create hyperfine qubits using different metal atoms. This feature may allow the development of large-scale quantum computers on surface that significantly surpass current capabilities in terms of qubit numbers by several orders of magnitude.

CHAPTER 8

The Non-Born-Oppenheimer effects: a challenge for optical cycling in molecules with OCCs

The optical cycling property in large organic molecules with OCCs has already been investigated in multiple studies [13, 33, 37, 38, 152]. In the last chapter, we showed that the optical cycling properties of the OCC-functionalized molecules are not systematically affected by the size of the ligands, which indicates that the molecular orbitals localized on the OCCs are highly decoupled from the molecular structural complexity. This gives rise to a series of questions: are all the molecular orbitals localized on the OCCs ($\tilde{X}, \tilde{A}, \tilde{B}, \tilde{C}, ...$) suitable for optical cycling? If yes, what criteria should guide the choice of optical cycling transitions? If not, what challenges arise when addressing the optical cycling transitions with these molecular orbitals?

In addition, as the symmetries and dipole strengths of these states are different, the transition probabilities and selection rules for the rotational cycling transitions are also different. CaOPh, for example, is a C_{2v} type molecule. Its molecular orbitals, represented with the terms of the irreducible representations of the C_{2v} point group symmetry, are $\tilde{X}^2A_1, \tilde{A}^2B_2, \tilde{B}^2B_1, \tilde{C}^2A_1$, and so on. The rotational cycling transitions of the asymmetric top molecules can be categorized into *a-, b-,* and *c-type* transitions based on the symmetries of the initial and final molecular states [24]. We noticed that, because of the spin-orbit coupling between the $\tilde{A}^2B_2$ and $\tilde{B}^2B_1$ states, the two states are mixed, and the C_{2v} symmetries in these two states are broken. For simplicity, the two excited states with broken symmetry are denoted as $\tilde{A}$ and $\tilde{B}$, and we can see that the rotational ground states of the excited states $|\tilde{A}/\tilde{B}, N_{K_aK_c} = 0_{00}\rangle$ can decay to both the $|\tilde{X}^2A_1, N_{K_aK_c} = 1_{11}, 1_{10}\rangle$ states via *b-* and *c-type*

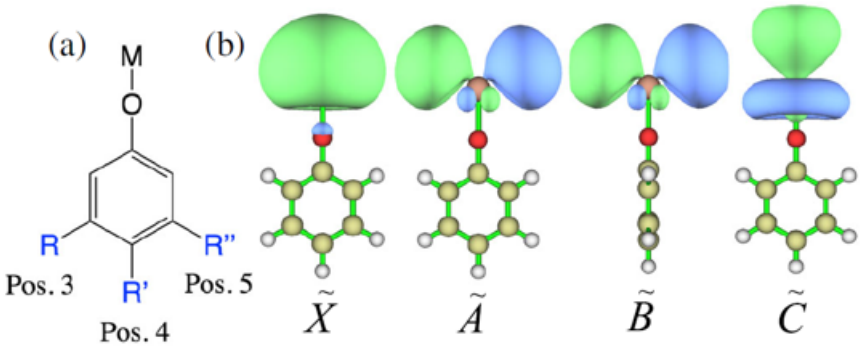

Figure 8.1: The HOMO and lowest few molecular orbitals of the MOPh-X type molecules

rotational transitions, respectively. Assuming that the oscillator strengths of the $\tilde{A}-\tilde{X}$ and $\tilde{B}-\tilde{X}$ transitions are similar, the branching ratios of the two rotational decay pathways are approximately equal to the mixing ratios of the $\tilde{A}^2B_2$ and $\tilde{B}^2B_1$ states. Hence, addressing both the *b*- and *c-type* rotational cycling transitions is necessary for achieving the rotational closure if the following three conditions are met: (i) the molecule is an asymmetric top, (ii) either the $\tilde{A}$ or $\tilde{B}$ state is involved in the cycling scheme, and (iii) the spin-orbit coupling effect between the $\tilde{A}$ and $\tilde{B}$ states can not be ignored.

Conversely, if the $\tilde{C}^2A_1$ and $\tilde{X}^2A_1$ states are selected for the cycling, only one rotational cycling transition needs to be addressed. This is because the molecular symmetries of both the ground and excited states remain unaffected by the spin-orbit coupling effect. To be specific, we need to address only an *a-type* rotational cycling transition ($|\tilde{C}^2A_1, N_{K_aK_c} = 0_{00}\rangle \leftrightarrow |\tilde{X}^2A_1, N_{K_aK_c} = 1_{01}\rangle$) for each of the vibrational repumps. This indicates that selecting suitable initial and final states for the optical cycling transitions can simplify both the vibrational and rotational complexities in the scheme.

To understand these questions and search for the best scheme for laser cooling of large aromatic molecules, it is straightforward to start with the $\tilde{C}$ state of the molecules with Ca-O or Sr-O units as the OCCs, as (i) the $\tilde{C}$ level is more promising for the rotational cycling, and (ii) it is close to the $\tilde{A}/\tilde{B}$ levels we have studied in the previous few chapters, and no significant change to our current experimental setup is needed for the signal detection and measurement. With the experiment scheme similar to previous works, we found that,

though the diagonal VBRs of the $\tilde{C} - \tilde{X}$ transitions of the molecules are better than those of the $\tilde{A}/\tilde{B} - \tilde{X}$ transitions, the $\tilde{C}$ states can couple strongly with the ro-vibrational states of the $\tilde{A}/\tilde{B}$ states via the non-BO effects, and the effectiveness for the optical cycling with the $\tilde{C}$ states is therefore significantly impaired.

8.1 The DLIF spectra of multiple molecules

In this section, we will present the DLIF spectra of DLIF spectra of the Ca/SrOPh-X molecules, where X=H, Cl, F and $3,4,5$-F_3 to further investigate the effectiveness of different excited states for optical cycling schemes. By comparing the spectral features and signal intensities of different molecules with varying ligands and excited states, we aim to gain insights into the optimal conditions for efficient laser cooling of large aromatic molecules.

8.1.1 Ca/SrOPh $\tilde{C}$-$\tilde{X}$ DLIF spectra

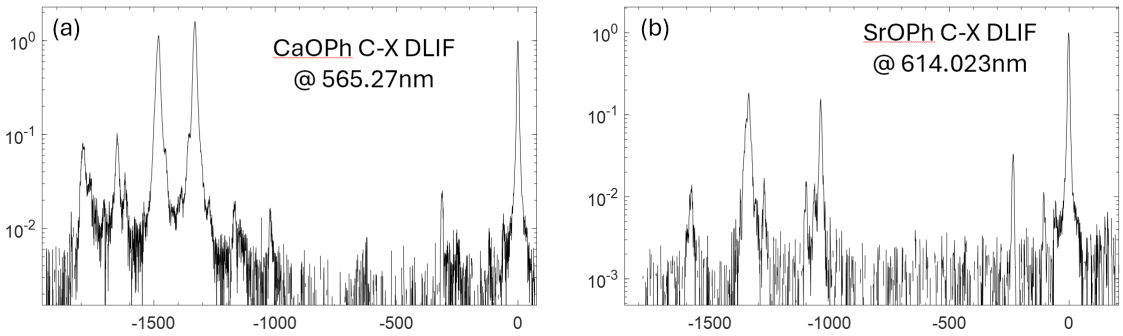

Figure 8.2: (a) CaOPh $\tilde{C}$-$\tilde{X}$ DLIF spectrum. (b) SrOPh $\tilde{C}$-$\tilde{X}$ DLIF spectrum.

Fig. 8.2 shows the $\tilde{C}$-$\tilde{X}$ DLIF spectra of the calcium and strontium phenoxide. Here, we noticed that there are a few great relaxation peaks of decaying via the lower excited states, $\tilde{A}/\tilde{B}$ states, which were presumably populated through the non-BO coupling with the $\tilde{C}$ state and/or the collisional relaxation. On the other hand, in the SrOPh case, such relaxation to the lower excited states is relatively lower compared to the CaOPh, indicated by the lower relative intensity strength of these relaxation peaks. Both spectra show that

the intensity ratios of the decays from the $\tilde{C}$ state to the stretching mode in the ground state are around $3-5\%$, indicating that the diagonal VBRs of the $\tilde{C}$ states of the Ca/SrOPh are higher than those of their $\tilde{A}/\tilde{B}$ states.

8.1.2 CaOPh-4-Cl DLIF spectra

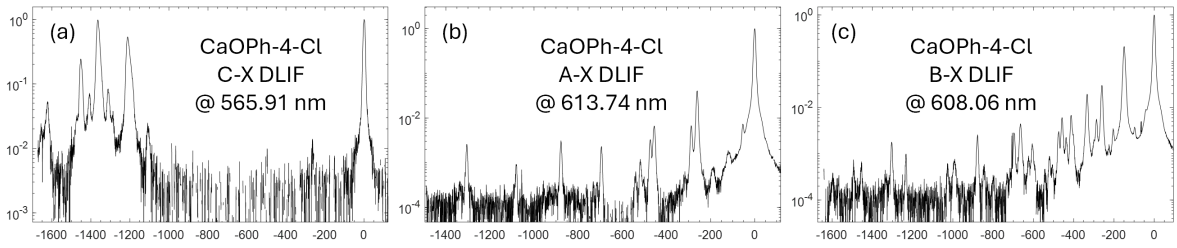

Figure 8.3: CaOPh-4-Cl DLIF spectra

Fig. 8.3 shows the $\tilde{C}$-$\tilde{X}$, $\tilde{A}$-$\tilde{X}$, and $\tilde{B}$-$\tilde{X}$ DLIF spectra of CaOPh-4-Cl. Since the calculations of the mode frequencies for molecules other than Ca/SrOPh were not completed at the time of writing this chapter, we can only briefly discuss the diagonal vibrational branching ratios based on the DLIF spectra. In general, there are multiple off-diagonal decay channels observed in the $\tilde{A}$-$\tilde{X}$, and $\tilde{B}$-$\tilde{X}$ DLIF spectra (Fig. 8.3(b, c), while only the decay to the stretching mode was observed for the $\tilde{C}$-$\tilde{X}$ transition. The strong $\tilde{C}-\tilde{A}/\tilde{B}-\tilde{X}$ peaks in the range of -1600 cm^{-1}– -1000 cm^{-1}in Fig. 8.3(a) indicate that there are significant non-BO effects present in the vibrational coupling of different electronic states. These effects can lead to additional complexity in the optical cycling scheme, potentially reducing the efficiency of laser cooling.

8.1.3 SrOPh-4-Cl DLIF spectra

Fig. 8.4 shows the $\tilde{C}$-$\tilde{X}$, $\tilde{A}$-$\tilde{X}$, and $\tilde{B}$-$\tilde{X}$ DLIF spectra of SrOPh-4-Cl. We noticed the signal from the $\tilde{A}^2\Pi_{1/2}-\tilde{X}^2\Sigma$ transitions of the SrCl, which is at around 662 nm. Similarly, we observed multiple off-diagonal decay channels in the $\tilde{A}-\tilde{X}$ and $\tilde{B}-\tilde{X}$ DLIF spectra of SrOPh-4-Cl, as shown in Fig 8.4(b, c), while only two off-diagonal decay channels were

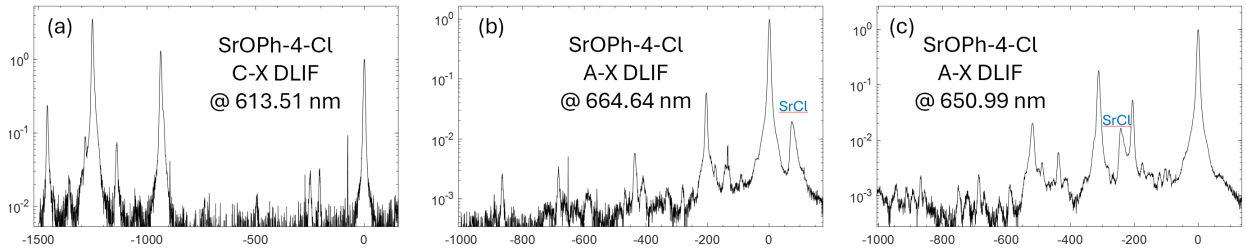

Figure 8.4: SrOPh-4-Cl DLIF spectra

observed for the $\tilde{C}$-$\tilde{X}$ transition, indicated by the lines at ≈ -200 cm^{-1}and at ≈ -250 cm^{-1}in Fig 8.4(a). The sharp line at ≈ -50 cm^{-1}in Fig 8.4(a) is an artifact caused by the reading error of the camera. The presence of strong non-adiabatic effects in the vibrational coupling of different electronic states could impact the laser cooling efficiency of SrOPh-4-Cl. Based on the relative intensity displayed by the DLIF spectra, for molecules decaying from the $\tilde{C}$ state directly to the ground state, only around 1-2 percent of these molecules experience vibrational transitions. However, if we consider the full relaxation pathway involving the $\tilde{A}/\tilde{B}$ states, the overall diagonal vibrational branching ratios from the $\tilde{C}$ state may decrease to roughly $20-30\%$.

8.1.4 CaOPh-4-F DLIF spectra

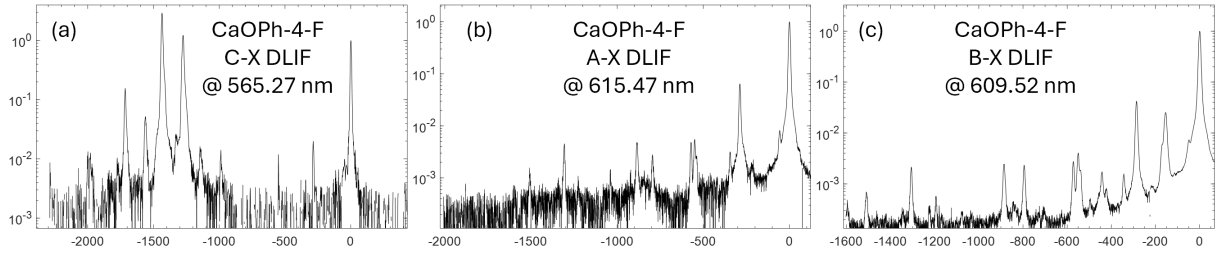

Figure 8.5: CaOPh-4-F DLIF spectra

Next, we change the substituent from chlorine to fluorine to see if the molecular mass can affect such a strong relaxation feature. The $\tilde{C}$-$\tilde{X}$, $\tilde{A}$-$\tilde{X}$, and $\tilde{B}$-$\tilde{X}$ DLIF spectra of CaOPh-4-F are displayed in Fig. 8.5. Similarly, there are several off-diagonal decay channels in the $\tilde{A}-\tilde{X}$ and $\tilde{B}-\tilde{X}$ DLIF spectra of CaOPh-4-F indicated by the line features in Fig. 8.5(b,

c), while only two off-diagonal decays of the $\tilde{C}$ state were observed in Fig. 8.5(a). The relaxation features in the range of -2000 cm^{-1} to -1000 cm^{-1} in the $\tilde{C}$-$\tilde{X}$ DLIF spectra of CaOPh-4-F remain very strong, and the relationship between these relaxation features and the mass of the ligand is still uncertain.

8.1.5 SrOPh-4-F DLIF spectra

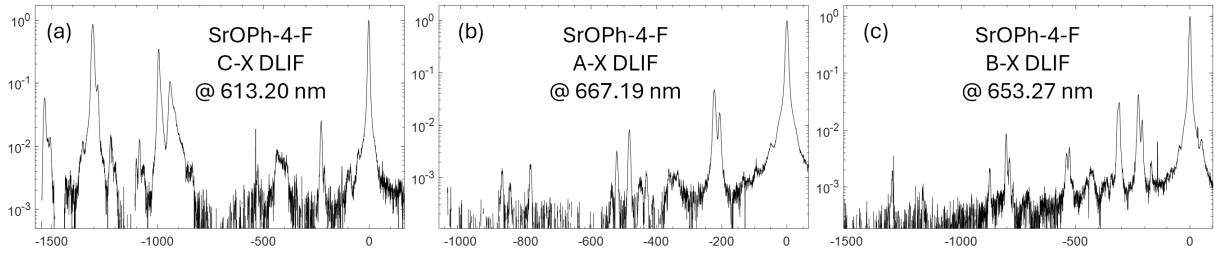

Figure 8.6: SrOPh-4-F DLIF spectra

The $\tilde{C}$-$\tilde{X}$, $\tilde{A}$-$\tilde{X}$, and $\tilde{B}$-$\tilde{X}$ DLIF spectra of SrOPh-4-F are shown in Fig. 8.6. The spectrum shown in Fig. 8.6(a) contains the lines from the two $\tilde{A}$-$\tilde{X}$ transitions of the SrF at 652nm and 664nm, which are observed at -900 $cm^{-1}$and -1230 cm^{-1}, respectively. The broad line feature at -400 $cm^{-1}$is indicating the $\tilde{A}^2\Pi_{1/2}(\nu') - \tilde{X}^2\Sigma(\nu'' = \nu' - 1)$ off-diagonal transition of the SrF, which is inferred by the SrF vibrational constant $\omega_e \approx 500$ cm^{-1}. The SrF fluorescence signal of $\tilde{A}^2\Pi_{1/2}(\nu') - \tilde{X}^2\Sigma(\nu'' = \nu' + 1)$ transition was also observed in the $\tilde{A}$-$\tilde{X}$ DLIF spectra shown in Fig. 8.6(b), indicated by the peak at -350 cm^{-1}. These spectra are all very similar to those introduced in the previous few subsections, indicating that the relaxation feature is a problem that we should consider for the $\tilde{C}$-$\tilde{X}$ transitions of all the phenoxide molecules.

8.1.6 CaOPh-3, 4, 5-F_3 C-X DLIF spectrum

Fig. 8.7 is the C-X DLIF spectra of the CaOPh-3, 4, 5-F_3 molecule. The relaxation peaks are having higher relative intensity comparing to the aforementioned molecules (roughly 90 % of the molecules decay to the ground state indirectly), indicating a possible enhancement

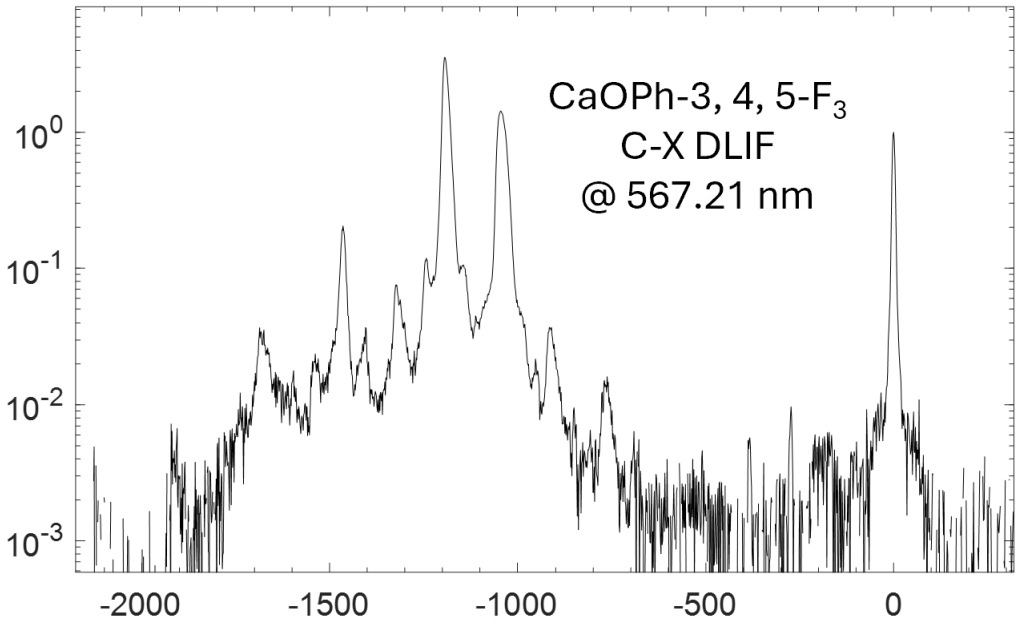

Figure 8.7: CaOPh-3, 4, 5-F_3 C-X DLIF spectra

in the non-adiabatic effects in the vibrational coupling of different electronic states. The multiple off-diagonal decay channels indicated by the feature in the range of -2000cm^{-1}- -800 cm^{-1}corresponding to the $\tilde{A} - \tilde{X}$ and $\tilde{B} - \tilde{X}$ transitions of CaOPh-3, 4, 5-F_3 suggest a complex relaxation pathway for this molecule.

The complexity of the relaxation line features require further investigation to fully understand the implications on the optical cycling of these molecules. To address this issue, we are working on the experiment under different schemes and trying to figure out whether the vibrational coupling of different electronic states can provide insights into potential strategies to mitigate the impact of non-adiabatic effects. One explanation is that, because of the non-BO effect, the spin-orbit coupling effect mix the vibrational states of different electronic states, especially when the these states are close to each other in energy:

$$\langle \tilde{A}, \nu'_A | H_{SO} | \tilde{C}, \nu'_C = 0 \rangle \neq 0, \tag{8.1}$$

$$\langle \tilde{B}, \nu'_B | H_{SO} | \tilde{C}, \nu'_C = 0 \rangle \neq 0. \tag{8.2}$$

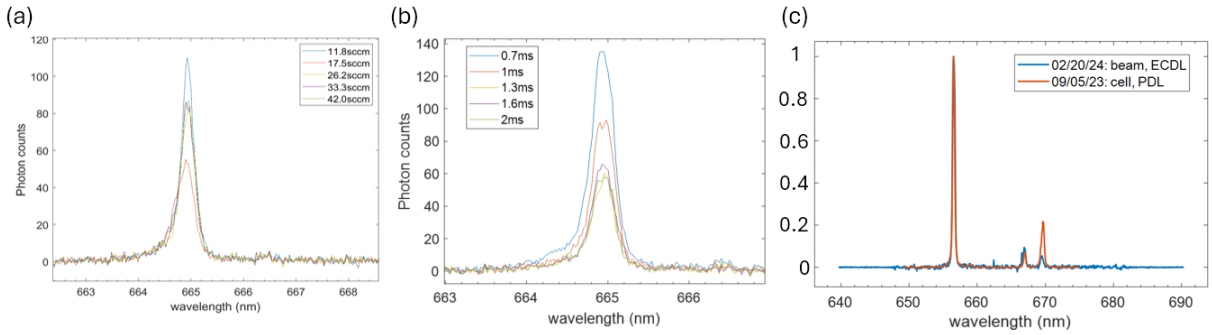

Figure 8.8: Additional experiments for exploring the relaxation mechanism. (a): SrOPh-4-Cl $\tilde{C}-\tilde{A}-\tilde{X}$ signal in different buffer gas flow rate. (b). SrOPh-4-Cl $\tilde{C}-\tilde{A}-\tilde{X}$ signal measured with different gate delay times of the camera. (c). The SrOPh $\tilde{B}-\tilde{A}-\tilde{X}$ DLIF spectra measured in cell (orange) and in beam (blue).

Under such circumstance, the energy level mixing between different electronic states can lead to the complex relaxation pathways observed in the DLIF spectra. In addition, as the molecular orbital of the $\tilde{C}$ state contains more d-type atomic orbitals, the dipole transition strength of the $\tilde{C}-\tilde{X}$ transition may be much weaker compared to the $\tilde{A}-\tilde{X}$ and $\tilde{B}-\tilde{X}$ transitions, which could contribute to the observed differences in the relaxation features.

8.2 Exploring the mechanism of the "relaxation"

To further understand the mechanism of the "relaxation" observed in the DLIF spectra of the phenoxide molecules, we conducted additional experiments as shown in Fig. 8.8. Figure 8.8(a) illustrates the variation of the SrOPh-4-Cl $\tilde{C}-\tilde{A}-\tilde{X}$ signal with the buffer gas flow rate, revealing a dependence that may indicate the role of collisional processes in the relaxation dynamics. Generally, higher flow rate indicates higher collision rate and lower molecular temperature, and we noticed that such a relaxation signal strength was weaken when the buffer gas flow rate increased, which may indicate that lower molecular temperature may help suppressing such a "relaxation" process. In Fig. 8.8(b), the SrOPh-4-Cl $\tilde{C}-\tilde{A}-\tilde{X}$ signal is plotted against the gate delay of the pulsed dye laser, showing a slight trend that suggests a possible temporal aspect to the relaxation process. That is, as the delay time set

to be less than 1.3 ms, the longer decay time we set, the weaker the relaxation feature we observed. On the other hand, the relaxation feature is pretty consistent as the gate delay set to be over 1.3 ms. This further indicates that such a "relaxation" process has relationship with the temperature of the molecules.

However, it remains uncertain whether there are multiple factors that can influence the relaxation process. To address this, we conducted measurements of the SrOPh $\tilde{B} - \tilde{X}$ DLIF spectra both within the cell and in the molecular beam, as depicted in Figure 8.8(c). Typically, the molecules in the beam have lower temperatures, and we observed that the $\tilde{B} - \tilde{A} - \tilde{X}$ relaxation signal strength is less than that of the measurement in the beam. This suggests that lower molecular temperatures may indeed reduce the relaxation process. In addition, as the collision rate of the molecules in the beam is several orders of magnitude lower than that within the cell, the impact of collisions on the relaxation process may be negligible in the beam measurement. The relaxation peak shown in the beam measurement indicates that the collision, the factor believed to lead to the relaxation in our previous works [37, 38], is not the only mechanism that leads to the relaxation. Multiple factors are likely involved in influencing the relaxation process observed in the DLIF spectra, such as temperature, collisions, and non-BO coupling effects. To understand the full picture of the relaxation mechanism in the phenoxide molecules, future studies, such as the DLIF measurement on the deuterated phenoxides (e.g., SrOPh-d5) in cell and in beam and some detailed theoretical calculations, would be necessary.

8.3 Discussion

8.3.1 Difficulties in the optical cycling with the C states

Based on the $\tilde{C} - \tilde{X}$ DLIF spectra shown in Fig. 8.2-8.7, we can clearly observe some challenges associated with optical cycling with the $\tilde{C}$ states. For example, the coupling between the vibrational states of the $\tilde{A}/\tilde{B}$ states and the $\tilde{C}$ states through the non-BO effects can significantly impair the effectiveness of the optical cycling, which leads to a

complex spectral diagram and broadened line shapes ($\approx 20-30$ cm^{-1}) in the $\tilde{C}-\tilde{A}/\tilde{B}-\tilde{X}$ lines. If we consider the problem with the intensity borrowing model, that is, the $\tilde{C}-\tilde{A}/\tilde{B}-\tilde{X}$ lines borrow their intensity from the $\tilde{C}-\tilde{X}$ line, such a coupling should happen between the $|\tilde{C},\nu'=0\rangle$ state and multiple vibrational excited states of the lower electronic states nearby.

This strong coupling behavior can result in a higher demand for laser cooling operations, which thus necessitates the repumps addressing the rotational states of both $\tilde{A}/\tilde{B}$ and $\tilde{C}$ molecular states. More specifically, the coupling between $|\tilde{C},\nu'=0\rangle$ and $|\tilde{A}/\tilde{B},\nu''\rangle$ states can introduce undesired complexity in the vibrational cycling scheme, thereby increasing the difficulty of optical cycling.

8.3.2 Non-BO coupling between the vibrational states belonging to different electronic states

To understand the non-BO effects, here we simplify the non-BO coupling problem with a simple three-level quantum system, where the $\tilde{C}$ state couples to some state nearby and both the states can decay to the $\tilde{X}$ state. Consider a three-level quantum system consisting of levels $|1\rangle$, $|2\rangle$, and $|3\rangle$, with energies E_1, E_2, and E_3, respectively. The energy levels satisfy the condition $E_1 > E_2 \gg E_3$, where $|3\rangle$ is the ground state. The energy difference between $|1\rangle$ and $|2\rangle$ is Δ. The states $|1\rangle$ and $|2\rangle$ are weakly coupled with a coupling strength Ω, and they both decay to the ground state $|3\rangle$ with large spontaneous decay rates Γ_1 and Γ_2, respectively. The decay rates are larger than the coupling strength, i.e., $\Gamma_1, \Gamma_2 > \Omega$. Note: Δ might have the order of $1\text{cm}^{-1} = 30\text{GHz}$, which is much more greater than the Γ_1 and Γ_2.

Master Equations

Under the assumptions mentioned above, the master equations for the density matrix elements can be simplified as:

$$\frac{d\rho_{11}}{dt} = -\Gamma_1\rho_{11} + i\Omega(\rho_{21} - \rho_{12}) \tag{8.3}$$
$$\frac{d\rho_{22}}{dt} = -\Gamma_2\rho_{22} - i\Omega(\rho_{21} - \rho_{12}) \tag{8.4}$$
$$\frac{d\rho_{33}}{dt} = \Gamma_1\rho_{11} + \Gamma_2\rho_{22} \tag{8.5}$$
$$\frac{d\rho_{12}}{dt} = -i\rho_{12}\Delta - \frac{\Gamma_1 + \Gamma_2}{2}\rho_{12} - i\Omega(\rho_{11} - \rho_{22}) \tag{8.6}$$

Here, ρ_{ij} represents the density matrix element for the transition between levels $|i\rangle$ and $|j\rangle$.

Solutions

Case 1. Small energy difference Δ ($\Delta \approx \Gamma$ in the orders of magnitude or $\Delta < \Gamma$). If $\Gamma_1 = \Gamma_2$, we can get analytical solution for the problem. Suppose the initial condition is such that all the population is in level $|1\rangle$, i.e., $\rho_{11}(0) = 1$ and $\rho_{ij}(0) = 0$ for $i \neq j$. Under the situation of $\Gamma_1 = \Gamma_2 = \Gamma$,

$$\frac{d\rho_{11}}{dt} = -\Gamma\rho_{11} + i\Omega(\rho_{21} - \rho_{12}) \tag{8.7}$$

$$\frac{d\rho_{22}}{dt} = -\Gamma\rho_{22} - i\Omega(\rho_{21} - \rho_{12}) \tag{8.8}$$

$$\frac{d\rho_{33}}{dt} = \Gamma(\rho_{11} + \rho_{22}) \tag{8.9}$$

$$\frac{d\rho_{12}}{dt} = -i\Delta\rho_{12} - \Gamma\rho_{12} - i\Omega(\rho_{11} - \rho_{22}) \tag{8.10}$$

$$\frac{d\rho_{21}}{dt} = i\Delta\rho_{21} - \Gamma\rho_{21} + i\Omega(\rho_{11} - \rho_{22}) \tag{8.11}$$

with the initial condition $\rho_{11}(0) = 1$ and $\rho_{ij}(0) = 0$ for $i \neq j$.

To solve these equations, we can use the Laplace transform method, see Sec.8.3.3. The solutions are:

$$\rho_{11}(t) = e^{-\Gamma t} - \frac{2\Omega^2}{\Delta^2 + 4\Omega^2} e^{-\Gamma t}(1 - \cos(\alpha t)) \tag{8.12}$$

$$\rho_{22}(t) = \frac{2\Omega^2}{\Delta^2 + 4\Omega^2} e^{-\Gamma t}\left[1 - \cos(\alpha t)\right]. \tag{8.13}$$

where $\alpha^2 = \Delta^2 + 4\Omega^2$.

In experiment, if $\alpha > 2\pi \times \Gamma$, we are supposed to see at least one node or even an oscillation in the signal of the $B - A - X$ fluorescence lifetime experiment. However, what we observed is that, the $B - A - X$ signal is still very similar to the expontential decay. This gives that $\alpha < 2\pi \times \Gamma$, hence we have

$$\Omega \leq \alpha < 2\pi \times \Gamma. \tag{8.14}$$

For the case of $1/\Gamma = 25$ns, $\Omega < 0.25$ GHz $= 8 \times 10^{-3}\text{cm}^{-1}$.

Case 2: large energy difference Δ. If $\Gamma_1 \approx \Gamma_2$ but not equivalent, the equations would be very difficult to solve. However, under the circumstance of $\Delta \gg \Gamma_1$, we can then set $d\rho_{12}/dt \approx 0$ and $d\rho_{21}/dt \approx 0$ to obtain:

$$\rho_{12}(t) \approx \frac{-i\Omega}{\Gamma + i\Delta}(\rho_{11}(t) - \rho_{22}(t)) \ll 1 \tag{8.15}$$

$$\rho_{21}(t) \approx \frac{i\Omega}{\Gamma - i\Delta}(\rho_{11}(t) - \rho_{22}(t)) \ll 1 \tag{8.16}$$

where $\Gamma = (\Gamma_1 + \Gamma_2)/2$.

Substituting the expressions for $\rho_{12}(t)$ and $\rho_{21}(t)$ into the equations for $\rho_{11}(t)$ and $\rho_{22}(t)$, we get:

$$\frac{d\rho_{11}}{dt} = -\Gamma_1\rho_{11} - \frac{2\Omega^2\Gamma}{\Gamma^2+\Delta^2}(\rho_{11}-\rho_{22}) \tag{8.17}$$

$$\frac{d\rho_{22}}{dt} = -\Gamma_2\rho_{22} + \frac{2\Omega^2\Gamma}{\Gamma^2+\Delta^2}(\rho_{11}-\rho_{22}) \tag{8.18}$$

$$\frac{d\rho_{33}}{dt} = \Gamma_1\rho_{11} + \Gamma_2\rho_{22} \tag{8.19}$$

Since $\Gamma_1 \approx \Gamma_2$, let's define $\delta = (\Gamma_1 - \Gamma_2)/2$. We can rewrite the equations as:

$$\frac{d\rho_{11}}{dt} = -(\Gamma+\delta)\rho_{11} - \frac{2\Omega^2\Gamma}{\Gamma^2+\Delta^2}(\rho_{11}-\rho_{22}) \tag{8.20}$$

$$\frac{d\rho_{22}}{dt} = -(\Gamma-\delta)\rho_{22} + \frac{2\Omega^2\Gamma}{\Gamma^2+\Delta^2}(\rho_{11}-\rho_{22}) \tag{8.21}$$

$$\frac{d\rho_{33}}{dt} = \Gamma(\rho_{11}+\rho_{22}) + \delta(\rho_{11}-\rho_{22}) \tag{8.22}$$

Defining $\Omega' = \frac{2\Omega^2\Gamma}{\Gamma^2+\Delta^2}$ and $\rho_\pm = \rho_{11} \pm \rho_{22}$, we can further simplify the equations:

$$\frac{d\rho_+}{dt} = -\Gamma\rho_+ - \delta\rho_- \tag{8.23}$$

$$\frac{d\rho_-}{dt} = -(\Gamma+2\Omega')\rho_- - \delta\rho_+ \tag{8.24}$$

$$\frac{d\rho_{33}}{dt} = \Gamma\rho_+ + \delta\rho_- \tag{8.25}$$

These equations can be solved analytically using standard methods for linear differential

equations. Defining a coefficient matrix:

$$M = \begin{pmatrix} -\Gamma & -\delta \\ -\delta & -\Gamma - 2\Omega' \end{pmatrix}, \tag{8.26}$$

we have

$$\frac{d}{dt}\begin{pmatrix} \rho_+ \\ \rho_- \end{pmatrix} = M \begin{pmatrix} \rho_+ \\ \rho_- \end{pmatrix}, \tag{8.27}$$

Define $\tan\theta = \frac{\Omega'}{\delta}$ and $\Lambda = V^{-1}MV$ where Λ is a diagonal matrix, we can diagonalize the matrix M with results shown as follows

$$V = \begin{pmatrix} \cos\left(\frac{\theta}{2} - \frac{\pi}{4}\right) & \sin\left(\frac{\theta}{2} - \frac{\pi}{4}\right) \\ -\sin\left(\frac{\theta}{2} - \frac{\pi}{4}\right) & \cos\left(\frac{\theta}{2} - \frac{\pi}{4}\right) \end{pmatrix}, \tag{8.28}$$

$$\Lambda = \begin{pmatrix} \lambda_1 & 0 \\ 0 & \lambda_2 \end{pmatrix}, \tag{8.29}$$

here the eigen-values are $\lambda_{1,2} = -\Gamma - \Omega' \pm \sqrt{\Omega'^2 + \delta^2}$.

The solution of $\rho_\pm$ are

$$\rho_+ = e^{-(\Gamma+\Omega')t}\left[\left(\cos^2\alpha - \cos\alpha\sin\alpha\right)e^{\omega t} + \left(\sin^2\alpha + \cos\alpha\sin\alpha\right)e^{-\omega t}\right], \tag{8.30}$$

$$\rho_- = e^{-(\Gamma+\Omega')t}\left[\left(\sin^2\alpha - \cos\alpha\sin\alpha\right)e^{\omega t} + \left(\cos^2\alpha + \cos\alpha\sin\alpha\right)e^{-\omega t}\right], \tag{8.31}$$

where $\alpha = \left(\frac{\theta}{2} - \frac{\pi}{4}\right)$ and $\omega = \sqrt{\delta^2 + \Omega'^2}$. The solutions, with the initial conditions $\rho_{11}(0) = 1$, $\rho_{22}(0) = \rho_{33}(0) = 0$, are:

$$\rho_{11}(t) = e^{-(\Gamma+\Omega')t}\left[\cosh(\omega t) - \frac{\delta}{\omega}\sinh(\omega t)\right] \tag{8.32}$$

$$\rho_{22}(t) = \frac{\Omega'}{\omega}e^{-(\Gamma+\Omega')t}\sinh(\omega t) \tag{8.33}$$

$$\rho_{33}(t) = 1 - \rho_{11}(t) - \rho_{22}(t) \tag{8.34}$$

The transition intensity for level 1 and 2 are proportional to the integration of the number density over time:

$$\beta = \frac{I_1}{I_2} = \frac{\Gamma_1 \int_0^\infty \rho_{11}(t)\,dt}{\Gamma_2 \int_0^\infty \rho_{22}(t)\,dt}, \tag{8.35}$$

$$\begin{aligned}\int_0^\infty \rho_{11}(t)\,dt &= \frac{1/2}{\Gamma + \Omega' - \omega} + \frac{1/2}{\Gamma + \Omega' + \omega} - \frac{\delta/2\omega}{\Gamma + \Omega' - \omega} + \frac{\delta/2\omega}{\Gamma + \Omega' + \omega} \\ &= \frac{\Gamma + \Omega' - \delta}{(\Gamma + \Omega')^2 - \omega^2},\end{aligned} \tag{8.36}$$

$$\int_0^\infty \rho_{22}(t)\,dt = \frac{\Omega'}{(\Gamma + \Omega')^2 - \omega^2}, \tag{8.37}$$

therefore

$$\beta = \frac{\Gamma + \Omega' + \delta}{\Omega'} = 1 + \frac{\Gamma - \delta}{\Omega'}. \tag{8.38}$$

For the case of $\beta = 10$, decay rate $\Gamma = 40 \times 2\pi\text{MHz}$, if we ignore the decay rate difference δ, we have

$$\begin{aligned}\Omega' &= \frac{\Gamma}{\beta - 1} = 4.4 \times 2\pi\text{MHz} \\ &= \frac{2\Omega^2\Gamma}{\Gamma^2 + \Delta^2}.\end{aligned} \tag{8.39}$$

Estimation of the range of coupling strength

For Case 1, we have the integrals of the population as follows

$$\int_0^\infty \rho_{11}(t)dt = \frac{1}{\Gamma} - \frac{2\Omega^2\Gamma}{(\Gamma^2 + \Delta^2 + 4\Omega^2)(\Delta^2 + 4\Omega^2)} \tag{8.40}$$

$$\int_0^\infty \rho_{22}(t)dt = \frac{2\Omega^2\Gamma}{(\Gamma^2 + \Delta^2 + 4\Omega^2)(\Delta^2 + 4\Omega^2)}, \tag{8.41}$$

hence the intensity ratio is

$$\beta = \frac{(\Gamma^2 + \Delta^2 + 4\Omega^2)(\Delta^2 + 4\Omega^2)}{2\Omega^2\Gamma^2} - 1, \tag{8.42}$$

In fact,

$$\frac{(\Gamma^2 + \Delta^2 + 4\Omega^2)(\Delta^2 + 4\Omega^2)}{2\Omega^2\Gamma^2} > \frac{\Gamma^2 \times 4\Omega^2}{2\Omega^2\Gamma^2} = 2, \tag{8.43}$$

So the intensity ratio β is always greater than 1 if there is only one $|A, v\rangle$ state couples to the B state. This indicates that, for C-X cases, we will have to consider more than three states.

For Case 2,

$$\frac{\Gamma}{\beta - 1} = \frac{2\Omega^2\Gamma}{\Gamma^2 + \Delta^2}, \tag{8.44}$$

we can see that

$$\Omega = \sqrt{\frac{(\Gamma^2 + \Delta^2)}{2(\beta - 1)}}, \tag{8.45}$$

In experiment, Δ can be estimated by the uncertainty of the lines, which is in the range of $0.1 - 10\text{cm}^{-1} = 3 - 300\text{GHz}$ and much more greater than the spontaneous decay rate. Hence, in the example of $\beta = 10$, decay rate $\Gamma = 40 \times 2\pi\text{MHz}$, the range of Ω is

$$0.7 \times 2\pi \text{ GHz} < \Omega < 70 \times 2\pi \text{ GHz}, \tag{8.46}$$

or

$$0.023 \text{ cm}^{-1} < \Omega < 2.3 \text{ cm}^{-1}. \tag{8.47}$$

A smaller Δ can lead to a smaller estimate of the coupling coefficient Ω. Generally, if more vibrational excited states couple to the $\tilde{C}$ state, the numbers of the coupling strength Ω involved in the master equations will need to be scaled up accordingly. Further experimental investigation and consideration of additional vibrational states will be crucial in refining these estimates and understanding the full complexity of the $\tilde{C} - \tilde{X}$ coupling dynamics. The

theoretical framework presented here may serve as a basis for future studies on vibrational excitation and relaxation processes in molecular systems.

8.3.3 The Laplace transform

To solve these differential equations, we can use the Laplace transform method. Let $\tilde{\rho}_{ij}(s)$ be the Laplace transform of $\rho_{ij}(t)$. Applying the Laplace transform to the equations, we get:

$$s\tilde{\rho}_{11}(s) - 1 = -\Gamma\tilde{\rho}_{11}(s) + i\Omega(\tilde{\rho}_{21}(s) - \tilde{\rho}_{12}(s)) \tag{8.48}$$

$$s\tilde{\rho}_{22}(s) = -\Gamma\tilde{\rho}_{22}(s) - i\Omega(\tilde{\rho}_{21}(s) - \tilde{\rho}_{12}(s)) \tag{8.49}$$

$$s\tilde{\rho}_{33}(s) = \Gamma(\tilde{\rho}_{11}(s) + \tilde{\rho}_{22}(s)) \tag{8.50}$$

$$s\tilde{\rho}_{12}(s) = -i\Delta\tilde{\rho}_{12}(s) - \Gamma\tilde{\rho}_{12}(s) - i\Omega(\tilde{\rho}_{11}(s) - \tilde{\rho}_{22}(s)) \tag{8.51}$$

$$s\tilde{\rho}_{21}(s) = i\Delta\tilde{\rho}_{21}(s) - \Gamma\tilde{\rho}_{21}(s) + i\Omega(\tilde{\rho}_{11}(s) - \tilde{\rho}_{22}(s)) \tag{8.52}$$

This is a system of linear equations for $\tilde{\rho}_{ij}(s)$, which can be solved using standard methods. After finding $\tilde{\rho}_{ij}(s)$, we can perform an inverse Laplace transform to obtain the time-domain solutions $\rho_{ij}(t)$.

$$\begin{pmatrix} s+\Gamma & 0 & i\Omega & -i\Omega \\ 0 & s+\Gamma & -i\Omega & i\Omega \\ i\Omega & -i\Omega & s+\Gamma+i\Delta & 0 \\ -i\Omega & i\Omega & 0 & s+\Gamma-i\Delta \end{pmatrix} \begin{pmatrix} \tilde{\rho}_{11}(s) \\ \tilde{\rho}_{22}(s) \\ \tilde{\rho}_{12}(s) \\ \tilde{\rho}_{21}(s) \end{pmatrix} = \begin{pmatrix} 1 \\ 0 \\ 0 \\ 0 \end{pmatrix} \tag{8.53}$$

To solve this system of equations, we can use Cramer's rule. First, we calculate the determinant of the matrix: The determinant of the given 4-by-4 matrix is:

$$\det(A) = (s+\Gamma)^2\left[\Delta^2 + 4\Omega^2 + (s+\Gamma)^2\right] \tag{8.54}$$

Then, we calculate the determinants for each variable:

$$\det(A_{11}) = (s+\Gamma)^3 + 2\Omega^2(s+\Gamma) + \Delta^2(s+\Gamma) \tag{8.55}$$

$$\det(A_{22}) = 2\Omega^2(s+\Gamma) \tag{8.56}$$

$$\det(A_{12}) = -i\Omega(s+\Gamma)(s+\Gamma-i\Delta) \tag{8.57}$$

$$\det(A_{21}) = i\Omega(s+\Gamma)(s+\Gamma+i\Delta) \tag{8.58}$$

Using Cramer's rule, we find the solutions:

$$\tilde{\rho}_{11}(s) = \frac{\det(A_{11})}{\det(A)} = \frac{[(s+\Gamma)^2 + 2\Omega^2 + \Delta^2]}{(s+\Gamma)\left[\Delta^2 + 4\Omega^2 + (s+\Gamma)^2\right]} \tag{8.59}$$

$$\tilde{\rho}_{22}(s) = \frac{\det(A_{22})}{\det(A)} = \frac{2\Omega^2}{(s+\Gamma)\left[\Delta^2 + 4\Omega^2 + (s+\Gamma)^2\right]} \tag{8.60}$$

$$\tilde{\rho}_{12}(s) = \frac{\det(A_{12})}{\det(A)} = \frac{-i\Omega(s+\Gamma-i\Delta)}{(s+\Gamma)\left[\Delta^2 + 4\Omega^2 + (s+\Gamma)^2\right]} \tag{8.61}$$

$$\tilde{\rho}_{21}(s) = \frac{\det(A_{21})}{\det(A)} = \frac{i\Omega(s+\Gamma+i\Delta)}{(s+\Gamma)\left[\Delta^2 + 4\Omega^2 + (s+\Gamma)^2\right]} \tag{8.62}$$

$$\tilde{\rho}_{11}(s) = \frac{(s+\Gamma)^2 + 2\Omega^2 + \Delta^2}{(s+\Gamma)\left[\Delta^2 + 4\Omega^2 + (s+\Gamma)^2\right]} \tag{8.63}$$

To find the inverse Laplace transform, we will use partial fraction decomposition and standard Laplace transform pairs.

First, let's factor the denominator:

$$\tilde{\rho}_{11}(s) = \frac{(s+\Gamma)^2 + 2\Omega^2 + \Delta^2}{(s+\Gamma)\left[(s+\Gamma)^2 + (\Delta^2 + 4\Omega^2)\right]} \tag{8.64}$$

Let $\alpha^2 = \Delta^2 + 4\Omega^2$. Then,

$$\tilde{\rho}_{11}(s) = \frac{(s+\Gamma)^2 + 2\Omega^2 + \Delta^2}{(s+\Gamma)\left[(s+\Gamma)^2 + \alpha^2\right]} \tag{8.65}$$

Now, we can decompose the fraction into partial fractions:

$$\tilde{\rho}_{11}(s) = \frac{A}{s+\Gamma} + \frac{B(s+\Gamma) + C}{(s+\Gamma)^2 + \alpha^2} \tag{8.66}$$

where A, B, and C are constants to be determined.

Equating the coefficients of s and the constant terms, we get:

$$A + B = 1 \tag{8.67}$$

$$A\alpha^2 = 2\Omega^2 + \Delta^2 = \alpha^2 - 2\Omega^2 \tag{8.68}$$

$$C = 0 \tag{8.69}$$

Solving for A and B:

$$A = \frac{\alpha^2 - 2\Omega^2}{\alpha^2} = \frac{\Delta^2 + 2\Omega^2}{\Delta^2 + 4\Omega^2} \tag{8.70}$$

$$B = \frac{2\Omega^2}{\alpha^2} = \frac{2\Omega^2}{\Delta^2 + 4\Omega^2} \tag{8.71}$$

Using standard Laplace transform pairs, we can find the inverse Laplace transform:

$$\mathcal{L}^{-1}\left\{\frac{1}{s+\Gamma}\right\} = e^{-\Gamma t} \tag{8.72}$$

$$\mathcal{L}^{-1}\left\{\frac{s+\Gamma}{(s+\Gamma)^2 + \alpha^2}\right\} = e^{-\Gamma t}\cos(\alpha t) \tag{8.73}$$

$$\mathcal{L}^{-1}\left\{\frac{1}{(s+\Gamma)^2 + \alpha^2}\right\} = \frac{1}{\alpha}e^{-\Gamma t}\sin(\alpha t) \tag{8.74}$$

Therefore, the inverse Laplace transform of $\tilde{\rho}_{11}(s)$ is:

$$\rho_{11}(t) = \frac{\Delta^2 + 2\Omega^2}{\Delta^2 + 4\Omega^2}e^{-\Gamma t} + \frac{2\Omega^2}{\Delta^2 + 4\Omega^2}e^{-\Gamma t}\cos(\alpha t) \tag{8.75}$$

where $\alpha^2 = \Delta^2 + 4\Omega^2$. For $\tilde{\rho}_{22}(s)$, we will use the same approach as before.

$$\tilde{\rho}_{22}(s) = \frac{2\Omega^2}{(s+\Gamma)\left[\Delta^2 + 4\Omega^2 + (s+\Gamma)^2\right]} \tag{8.76}$$

First, we can decompose the fraction into partial fractions:

$$\tilde{\rho}_{22}(s) = \frac{A}{s+\Gamma} + \frac{B(s+\Gamma) + C}{(s+\Gamma)^2 + \alpha^2}, \tag{8.77}$$

where A, B, and C are constants to be determined.

Equating the coefficients of s and the constant terms, we get:

$$A + B = 0 \tag{8.78}$$

$$C = 0 \tag{8.79}$$

$$A\alpha^2 = 2\Omega^2 \tag{8.80}$$

Hence $A = -B = \frac{-2\Omega^2}{\alpha^2}$. Using standard Laplace transform pairs

$$\mathcal{L}^{-1}\left\{\frac{1}{s+\Gamma}\right\} = e^{-\Gamma t} \tag{8.81}$$

$$\mathcal{L}^{-1}\left\{\frac{s+\Gamma}{(s+\Gamma)^2+\alpha^2}\right\} = e^{-\Gamma t}\cos(\alpha t) \tag{8.82}$$

the inverse Laplace transform of $\tilde{\rho}_{22}(s)$ is:

$$\rho_{22}(t) = \frac{2\Omega^2}{\Delta^2 + 4\Omega^2} e^{-\Gamma t}\left[1 - \cos(\alpha t)\right]. \tag{8.83}$$

8.4 Conclusion

In this chapter, our study of the $\tilde{C} - \tilde{X}$ DLIF spectra of multiple phenoxide molecules reveals that while the $\tilde{C} - \tilde{X}$ transition is predominantly diagonal, a significant portion of the molecules in $\tilde{C}$ states undergo transitions to the $\tilde{A}$ and $\tilde{B}$ states before returning to the ground state. This behavior may be attributed to either collisional relaxation processes or non-BO effects. By attributing all relaxation features to non-BO effects, we were able to estimate an upper bound on the coupling strength. We then solve the non-BO coupling strength with a simple three levels model, and the results show that such coupling strength is around a few cm^{-1}. Further investigation is needed to explore the specific contributions of collisional relaxation and non-BO effects to the observed spectra.

APPENDIX A

Effective Hamiltonian of SiO^+

In this appendix, we present the derivation of the rotational and hyperfine Hamiltonian matrix elements. For a comprehensive introduction to the requisite mathematical background, readers are directed to Chapter 5-10 of Ref. [31].

Here we may start with the expression of the effective Hamiltonian. As we know, the X and B states of the diatomic molecule $^{28}Si^{16}O^+$ and $^{29}Si^{16}O^+$ are all of the Σ^+ symmetry, these states can therefore be described by the Hund's case(b) basis $|\eta, \Lambda; N, S, J = S + N, I, F\rangle$. The effective molecular Hamiltonian in such basis reads

$$\begin{aligned} H_{\text{eff}} = &\left(B_\nu - D_\nu \boldsymbol{N}^2\right) \boldsymbol{N}^2 + \gamma_\nu T^1(\boldsymbol{N}) \cdot T^1(\boldsymbol{S}) + b_F T^1(\boldsymbol{I}) \cdot T^1(\boldsymbol{S}) \\ &- \sqrt{10} g_s \mu_B g_N \mu_N \left(\frac{\mu_0}{4\pi}\right) T^1(\boldsymbol{S}, \boldsymbol{C}) \cdot T^1(\boldsymbol{I}) . \end{aligned} \tag{A.1}$$

On the right hand side, the four terms from left to right are the rotation, spin-rotation, hyperfine interaction and dipolar hyperfine Hamiltonians, respectively. As the hyperfine terms are missing in $^{28}Si^{16}O^+$ due to the zero spin in the nuclei while playing an important role in the case of $^{29}Si^{16}O^+$, we will discuss the two isotope species in separate subsections.

A.1 Rotational Hamiltonian of $^{28}Si^{16}O^+$

Here we analyze the molecule $^{28}Si^{16}O^+$ first. As the hyperfine interaction is missing due to the zero nuclear spin in the molecule, we can ignore the hyperfine Hamiltonian for $^{28}Si^{16}O^+$.

For the rotation term, the diagonal matrix elements are

$$\langle \eta, \Lambda; N, S, J, I, F | \left(B_\nu - D_\nu \boldsymbol{N}^2 \right) \boldsymbol{N}^2 | \eta, \Lambda; N, S, J, I, F \rangle = \left[B_\nu - D_\nu N \left(N + 1 \right) \right] N \left(N + 1 \right), \tag{A.2}$$

and the off-diagonal matrix elements in N are 0 if we ignore the coupling between I and N. The spin-rotation interaction term is

$$\begin{aligned} &\langle \eta, \Lambda; I, S, G, N, F | \gamma_\nu T^1 \left(\boldsymbol{N} \right) \cdot T^1 \left(\boldsymbol{S} \right) | \eta, \Lambda; I, S, G, N, F \rangle \\ =&\gamma_\nu (-1)^{N+J+1/2} \left\{ \begin{array}{ccc} 1/2 & N & J \\ N & 1/2 & 1 \end{array} \right\} \left[\frac{3}{2} N \left(N + 1 \right) \left(2N + 1 \right) \right]^{\frac{1}{2}} \\ =&\frac{\gamma_\nu}{2} J \left(J + 1 \right) - N \left(N + 1 \right) - \frac{3}{4} = \left\{ \begin{array}{ll} \frac{N \gamma_\nu}{2}, & \text{when } J = N + \frac{1}{2}, \\ -\frac{(N+1)\gamma_\nu}{2}, & \text{when } J = N - \frac{1}{2} \text{ and } N > 0. \end{array} \right. \end{aligned} \tag{A.3}$$

A.2 Rotational and hyperfine Hamiltonian of $^{29}Si^{16}O^+$

The $^{29}Si^{16}O^+$ molecular ion has a nuclear spin of $I = \frac{1}{2}$ and its hyperfine interaction is larger than the spin-rotation coupling, to suppress the off-diagonal elements the effective Hamiltonian matrix, here we introduce new quantum number $G = I + S$ and use the Hund's case(b_β) basis for illustration.

The matrix elements of the $^{29}Si^{16}O^+$ rotation Hamiltonian is the same as those of $^{28}Si^{16}O^+$, described by Eq.(A.2). However, the spin-rotation term in the new basis set is

not diagonal for G states:

$$\begin{aligned}
&\left\langle \eta,\Lambda;I,S,G,N,F\left|\gamma T^{1}\left(\boldsymbol{N}\right)\cdot T^{1}\left(\boldsymbol{S}\right)\right|\eta,\Lambda;I,S,G',N',F\right\rangle \\
=&\gamma\left(-1\right)^{G'+F+N}\left\{\begin{array}{ccc} N' & G' & F \\ G & N & 1 \end{array}\right\}\left\langle I,S,G\right\|T^{1}\left(\boldsymbol{S}\right)\left\|I,S,G'\right\rangle\left\langle N\right\|T^{1}\left(\boldsymbol{N}\right)\left\|N'\right\rangle \\
=&\gamma\delta_{\mathrm{NN}'}(-1)^{G'+F+N}\left\{\begin{array}{ccc} N' & G' & F \\ G & N & 1 \end{array}\right\}(-1)^{G+I+1+S}[\left(2G'+1\right)\left(2G+1\right)]^{\frac{1}{2}} \\
&\times\left\{\begin{array}{ccc} G & S & I \\ S & G' & 1 \end{array}\right\}[S\left(S+1\right)\left(2S+1\right)N\left(N+1\right)\left(2N+1\right)]^{\frac{1}{2}}.
\end{aligned} \tag{A.4}$$

Substituting $S=\frac{1}{2},I=\frac{1}{2}$ into the equation and ignore off-diagnal terms of $N'\neq N$:

$$\begin{aligned}
&\left\langle \eta,\Lambda;I,S,G,N,F\left|\gamma T^{1}\left(\boldsymbol{N}\right)\cdot T^{1}\left(\boldsymbol{S}\right)\right|\eta,\Lambda;I,S,G',N,F\right\rangle \\
=&\gamma(-1)^{G'+F+N}\left\{\begin{array}{ccc} N & G' & F \\ G & N & 1 \end{array}\right\}(-1)^{G}[\left(2G'+1\right)\left(2G+1\right)]^{\frac{1}{2}} \\
&\times\left\{\begin{array}{ccc} G & 1/2 & 1/2 \\ 1/2 & G' & 1 \end{array}\right\}\left[\frac{3}{2}N\left(N+1\right)\left(2N+1\right)\right]^{\frac{1}{2}}.
\end{aligned} \tag{A.5}$$

Next, we will discuss the matrix elements for different G and G' values. For the $G'=G=0$ case, this term is 0 due to the zero value of the first 6-j symbol. For $G'=G=1$,

$$\begin{aligned}
&\left\langle \eta,\Lambda;I,S,G=1,N,F\left|\gamma T^{1}\left(\boldsymbol{N}\right)\cdot T^{1}\left(\boldsymbol{S}\right)\right|\eta,\Lambda;I,S,G'=1,N',F\right\rangle \\
=&\gamma(-1)^{F+N}\left\{\begin{array}{ccc} F & 1 & N \\ 1 & N & 1 \end{array}\right\}\left\{\begin{array}{ccc} 1 & 1/2 & 1/2 \\ 1/2 & 1 & 1 \end{array}\right\}\left[\frac{27}{2}N\left(N+1\right)\left(2N+1\right)\right]^{\frac{1}{2}} \\
=&-\gamma\frac{[2+N\left(N+1\right)-F\left(F+1\right)]}{4}.
\end{aligned} \tag{A.6}$$

When $G'=0, G=1$ (or $G'=1, G=0$), if $F=N$:

$$\begin{aligned}
&\left\langle \eta,\Lambda;I,S,G=1,N,F\left|\gamma T^{1}\left(\boldsymbol{N}\right)\cdot T^{1}\left(\boldsymbol{S}\right)\right|\eta,\Lambda;I,S,G'=0,N',F\right\rangle \\
=&\gamma(-1)^{F+N+1}\left\{\begin{array}{ccc} F=N & 0 & N \\ 1 & N & 1 \end{array}\right\}\left\{\begin{array}{ccc} 1 & 1/2 & 1/2 \\ 1/2 & 0 & 1 \end{array}\right\}\left[\frac{9}{2}N\left(N+1\right)\left(2N+1\right)\right]^{\frac{1}{2}} \\
=&-\gamma\frac{-1}{\sqrt{3\left(2N+1\right)}}\left[\frac{3}{4}N\left(N+1\right)\left(2N+1\right)\right]^{\frac{1}{2}}=\frac{\gamma}{2}\sqrt{N\left(N+1\right)}.
\end{aligned} \tag{A.7}$$

If $F\neq N$, the spin-rotation term would be 0 because the first 6-j symbol is 0.

The hyperfine term in the Hund's case(b_β) basis is diagonal, i.e.,

$$\begin{aligned}
&\left\langle \eta,\Lambda;I,S,G,N,F\left|b_{F}T^{1}\left(\boldsymbol{I}\right)\cdot T^{1}\left(\boldsymbol{S}\right)\right|\eta,\Lambda;I,S,G',N',F\right\rangle \\
=&b_{F}(-1)^{1+G}\frac{3}{2}\left\{\begin{array}{ccc} 1/2 & 1/2 & G \\ 1/2 & 1/2 & 1 \end{array}\right\}=\left\{\begin{array}{ll} \frac{b_F}{4} & G=1, \\ -\frac{3b_F}{4} & G=0. \end{array}\right.
\end{aligned} \tag{A.8}$$

Because of the change of basis, the revised form of the dipolar hyperfine term is

$$H_{\text{dip}}=\sqrt{6}g_{s}\mu_{B}g_{N}\mu_{N}\left(\frac{\mu_{0}}{4\pi}\right)T^{2}\left(\boldsymbol{C}\right)\cdot T^{2}\left(\boldsymbol{S},\boldsymbol{I}\right), \tag{A.9}$$

and the dipolar hyperfine Hamiltonian matrix element could be calculated by

$$
\begin{aligned}
&\left\langle \eta,\Lambda;I,S,G,N,F\left|\sqrt{6}g_s\mu_B g_N\mu_N\left(\frac{\mu_0}{4\pi}\right)T^2\left(\boldsymbol{C}\right)\cdot T^2\left(\boldsymbol{S},\boldsymbol{I}\right)\right|\eta,\Lambda;I,S,G',N',F\right\rangle \\
=&\sqrt{6}g_s\mu_B g_N\mu_N\left(\frac{\mu_0}{4\pi}\right)(-1)^{G'+F+N}\left\{\begin{array}{ccc} N' & G' & F \\ G & N & 2 \end{array}\right\}\left\langle I,S,G\right\|T^2\left(\boldsymbol{S},\boldsymbol{I}\right)\left\|I,S,G'\right\rangle \\
&\times\left\langle N,\Lambda\right\|T^2\left(\boldsymbol{C}\right)\left\|N',\Lambda\right\rangle \\
=&\sqrt{30}g_s\mu_B g_N\mu_N\left(\frac{\mu_0}{4\pi}\right)(-1)^{G'+F+N}\left\{\begin{array}{ccc} N' & G' & F \\ G & N & 2 \end{array}\right\}\left\{\begin{array}{ccc} G & G' & 2 \\ I & I & 1 \\ S & S & 1 \end{array}\right\} \\
&\times\left[\left(2G'+1\right)\left(2G+1\right)I\left(I+1\right)\left(2I+1\right)S\left(S+1\right)\left(2S+1\right)\right]^{\frac{1}{2}} \\
&\times(-1)^N\left[\left(2N+1\right)\left(2N'+1\right)\right]^{\frac{1}{2}}\left(\begin{array}{ccc} N & 2 & N' \\ 0 & 0 & 0 \end{array}\right)\left\langle\eta,\Lambda\right|C_0^2\left(\theta,\phi\right)r^{-3}\left|\eta,\Lambda\right\rangle \\
=&\frac{\sqrt{30}c}{8\pi}(-1)^{G'+F}\left\{\begin{array}{ccc} N' & G' & F \\ G & N & 2 \end{array}\right\}\left\{\begin{array}{ccc} G & G' & 2 \\ 1/2 & 1/2 & 1 \\ 1/2 & 1/2 & 1 \end{array}\right\}\left(\begin{array}{ccc} N & 2 & N' \\ 0 & 0 & 0 \end{array}\right) \\
&\times\left[\left(2G'+1\right)\left(2G+1\right)\left(2N+1\right)\left(2N'+1\right)\right]^{\frac{1}{2}}=(*),
\end{aligned}
\tag{A.10}
$$

where $c=3g_s\mu_B g_N\mu_N(\mu_0/4\pi)\left\langle\eta,\Lambda\left|C_0^2\left(\theta,\phi\right)r^{-3}\right|\eta,\Lambda\right\rangle$ is a constant depending only on the electronic state. Based on the values of G' and G in the 9-j Wigner symbol, we have

$$
\begin{aligned}
(*)=&\frac{\sqrt{30}c}{2}(-1)^F\left[\left(2N+1\right)\left(2N'+1\right)\right]^{\frac{1}{2}}\left(\begin{array}{ccc} N & 2 & N' \\ 0 & 0 & 0 \end{array}\right) \\
&\times\left\{\begin{array}{ll} 0, & G'G=0, \\ \left\{\begin{array}{ccc} N' & 1 & F \\ 1 & N & 2 \end{array}\right\}, & G'=G=1. \end{array}\right.
\end{aligned}
\tag{A.11}
$$

The 6-j symbol in Eq.(A.11) could be calculated as follows when $N' = N$:

$$\left\{ \begin{array}{ccc} N' & 1 & F \\ 1 & N & 2 \end{array} \right\} = \left\{ \begin{array}{ll} \frac{-6+8N(N+1)}{\sqrt{30(2N+3)!/(2N-2)!}} & F = N, \\ \frac{(N+1)(4N+6)}{\sqrt{30(2N+3)!/(2N-2)!}}, & F = N-1, \\ \frac{2N(2N-1)}{\sqrt{30(2N+3)!/(2N-2)!}}, & F = N+1. \end{array} \right. \tag{A.12}$$

Given that

$$\left(\begin{array}{ccc} N & 2 & N \\ 0 & 0 & 0 \end{array} \right) = (-1)^{N+1} \sqrt{\frac{N\left(N+1\right)}{\left(2N+3\right)\left(2N+1\right)\left(2N-1\right)}}, \tag{A.13}$$

the dipolar hyperfine term could be simplified under different cases (here we only consider the non-zero matrix elements):

(i). $G' = G = 1, F = N$:

$$\begin{aligned} (*) =& \frac{\sqrt{30}c}{6}(-1)^{N+1}\frac{-6+8N\left(N+1\right)}{\sqrt{30\left(2N+3\right)!/\left(2N-2\right)!}}(-1)^{N+1}\sqrt{\frac{4\left(2N-2\right)!}{\left(2N+3\right)!}}\frac{\left(N+1\right)!}{\left(N-1\right)!}\left(2N+1\right) \\ =& \frac{c}{6}\frac{\left[-3+4N\left(N+1\right)\right]}{\left(2N+3\right)\left(2N-1\right)} = \frac{c}{6} = \frac{t}{2}; \end{aligned} \tag{A.14}$$

(ii). $G' = G = 1, F = N-1$:

$$\begin{aligned} (*) =& \frac{\sqrt{30}c}{6}(-1)^{N}\frac{\left(N+1\right)\left(4N+6\right)}{\sqrt{30\left(2N+3\right)!/\left(2N-2\right)!}}(-1)^{N+1}\sqrt{\frac{4\left(2N-2\right)!}{\left(2N+3\right)!}}\frac{\left(N+1\right)!}{\left(N-1\right)!}\left(2N+1\right) \\ =& -\frac{c}{3}\frac{\left(N+1\right)\left(4N+6\right)\left(N+1\right)N}{\left(2N+3\right)\left(2N+2\right)\left(2N+1\right)\left(2N\right)\left(2N-1\right)}\left(2N+1\right) = -\frac{\left(N+1\right)t}{4N-2}; \end{aligned} \tag{A.15}$$

(iii). $G' = G = 1, F = N + 1$:

$$
\begin{aligned}
(*) =& \frac{\sqrt{30}c}{6}(-1)^{N+2}\frac{2N\left(2N-1\right)}{\sqrt{30\left(2N+3\right)!/\left(2N-2\right)!}}(-1)^{N+1}\sqrt{\frac{4\left(2N-2\right)!}{\left(2N+3\right)!}}\frac{\left(N+1\right)!}{\left(N-1\right)!}\left(2N+1\right) \\
=& -\frac{c}{6}\frac{N}{\left(2N+3\right)} = -\frac{Nt}{4N+6}.
\end{aligned}
\tag{A.16}
$$

Here $t = \frac{c}{3}$ is the dipolar hyperfine constant used in this work.

Now we have completed the calculation of all the spin-rotation and hyperfine matrix elements we need. These matrix elements can be summarized as follows:

	$G' = 1,$ $F' = N + 1$	$G' = 1,$ $F' = N$	$G' = 0,$ $F' = N$	$G' = 1,$ $F' = N - 1$
$G = 1,$ $F = N + 1$	$\frac{\gamma N}{2} + \frac{b_F}{4} - \frac{Nt}{4N+6}$	0	0	0
$G = 1,$ $F = N$	0	$\frac{\gamma N}{2} + \frac{b_F}{4} + \frac{t}{2}$	$\frac{\gamma}{2}\sqrt{N(N+1)}$	0
$G = 0,$ $F = N$	0	$\frac{\gamma}{2}\sqrt{N(N+1)}$	$-\frac{3b_F}{4}$	0
$G = 1,$ $F = N - 1$	0	0	0	$-\frac{\gamma(N+1)}{2} + \frac{b_F}{4} - \frac{(N+1)t}{4N-2}$

The expressions of these Hamiltonian matrix elements we have derived here is the same as those in the CO^+ example analyzed in Chapter 10 of Ref. [31], and this section is only a check of the derivation details for these results. We can see that the spin-rotation terms mix the two different G states, and the corresponding perturbed energies of the two G sub-states are

$$
E_G = \frac{t - \gamma - b_F}{4} \pm \frac{1}{2}\sqrt{\left(b_F + \frac{t}{2} - \frac{\gamma}{2}\right)^2 + \gamma^2 N\left(N+1\right)}. \tag{A.17}
$$

APPENDIX B

Supplement information of VBRs measurements

B.1 Uncertainty analysis of SrOPh-X VBRs

The uncertainty analysis for VBRs of the CaOPh-X is done by Doyle group and can be found in Ref. [37], hence here we will only focus on the uncertainty analysis for the SrOPh-X VBRs. The first systematic error come from the unobserved peaks which contribute to the VBRs. A true VBR depends on contributions of all possible decay pathways. Due to a low measurement sensity and a small detection window, only a few vibrational decays have been observed for each transition. Compared to a complete description of vibrational decays obtained from calculated FCFs, all unobserved vibrational decays are therefore a source of the systematic uncertainty, which is estimated by [37]:

$$S_0' = \frac{S_0}{\sum_{i=0}^{p} S_i + \sum_{i=p+1}^{N} \frac{T_i}{C}}, \tag{B.1}$$

where S_0' is the scaled diagonal VBR considering contributions from the unobserved vibrational decays, S_0 is the observed intensity ratio of the diagonal peak, S_i is the observed intensity ratio of the ith vibational decay, T_i is the calculated VBR of the ith vibational decay and C is a scaling factor that averages the ratio of theoretical VBR (T_i) to experimental intensity ratio (S_i) for all observed peaks. Since the VBRs for bending modes are underestimated by theory, T_0 is usually larger than or roughly equal to S_0 , thus the lowest scaled VBR S_0'' can be obtained when excluding the T_0/S_0 in the scaling factor and used as an estimate for the lower bound value of the diagonal VBR. For the measured intensity ratio S_0 is always overestimated and used as the upper bound of the diagonal VBR, while

the scaled VBR S_0' is used as the plot data points in Figure 4.11. As summarized in Table 4.1, the uncertainties of the unobserved peaks as differences of S_0 and S_0'' are in the range of $1.1 - 3.2\%$.

Another source of systematic uncertainty is the signal drifting in the measurement due to the change of experimental conditions. Except for the DLIF measurment of SrOPh $\widetilde{B} \rightarrow \widetilde{X}$ by the cw laser and EMCCD (Figure B.1), all other DLIF spectra were taken by scanning the grating of the spectrometer to disperse photons onto a PMT. This means that the fluorescence photons at different wavelengths were not detected simultaneously. A typical scan of 15 nm wavelength range would take 75 minutes with an increment of 0.1 nm and 300 averages for each wavelength. During the scan, the signal was slowly drifting mainly due to the dust accumulation on the imaging lens and the pulse intensity drifting from both the ablation and the excitation lasers. We kept track of the signals before and after the whole scan and found that the signal change can vary by up to 20%, which can lead to an error of 1.0% in VBR estimation as such signal change mainly affects the off-diagonal vibrational transition signal. In addition, the dispersed photons at different wavelength were detected simultaneously in the EMCCD measurement, which eliminates the error due to signal drifting. The error can be estimated by the difference of the diagonal VBR of SrOPh $\widetilde{B} \rightarrow \widetilde{X}$ from the two different methods, which is 1.2 %.

As discussed in the error analysis of CaOPh-X [37], the wavelength response of the spectrometer and the imperfection of the mirrors and lenses in the imaging system could cause a systematic error up to $\approx 1\%$. The last error source comes from the diagonal excitation of vibrationally excited modes in the ground state. Due to a cell temperature of ≈ 23 K, the thermalized molecules can have thermal populations of $\approx 5\%$ of the low-frequency bending mode and $\approx 10^{-6}$ of the stretching mode. Those vibrationally excited states in the $\widetilde{X}$ state could be near-resonantly excited by the pulsed dye laser to the same vibrational levels of the upper states. The following decays from those diagonal excitations can cause an error up to 0.5%.

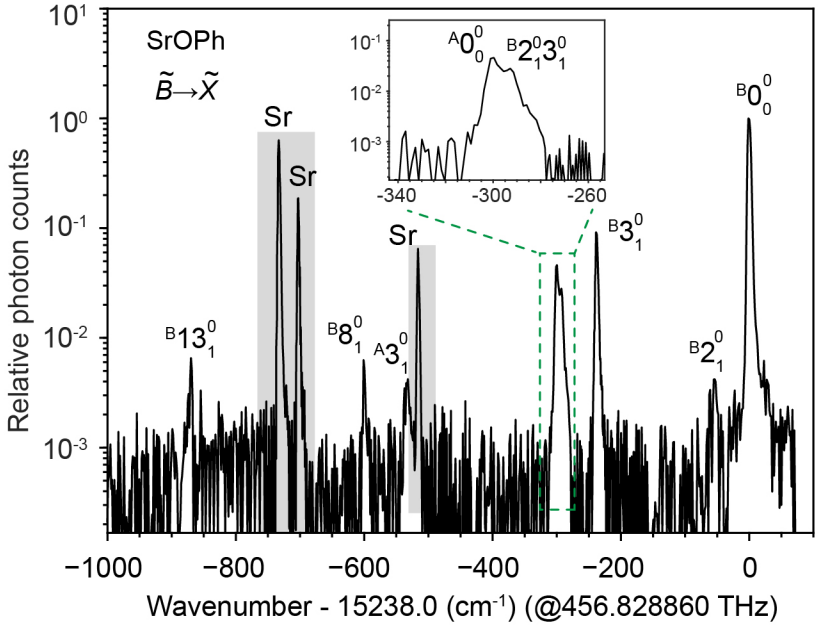

Figure B.1: Dispersed spectrum of SrOPh $\widetilde{B} \rightarrow \widetilde{X}$ excited by cw laser and measured by a spectrometer coupled with an EMCCD camera. The inset shows the expansion of a broad peak at -300 cm^{-1}, which is due to the overlapping of two peaks. The assignments of the resolved vibrational peaks are also given.

B.2 Measured and theoretical results for CaOPh-X and SrOPh-X

Modes	CaOPh			
	Exp. (A)	Theo. (A)	Exp. (B)	Theo. (B)
0	0.9339(29)	0.9611	0.9446(68)	0.9758
ν_2	0.0113(21)	$< 10^{-4}$	0.0056(44)	$< 10^{-4}$
ν_4	0.0468(15)	0.0311	0.0419(29)	0.0185
ν_9	0.0058(11)	0.0027	0.0033(29)	0.0027
ν_{13}	0.0023(8)	0.0018	0.0037(27)	0.0012
ν_{23}		0.0017	0.0009(23)	0.0008
Modes	CaOPh-mCH$_3$			
	Exp. (A)	Theo. (A)	Exp. (B)	Theo. (B)
0		0.9587	0.9387(32)	0.9738
ν_6		0.0175	0.0232(17)	0.0110
ν_7		0.0151	0.0294(16)	0.0090
ν_{12}		0.0024	0.0046(16)	0.0024
ν_{14}		0.006	0.0041(16)	0.0011
Modes	CaOPh-mF			
	Exp. (A)	Theo. (A)	Exp. (B)	Theo. (B)
0	0.9464(71)	0.9676	0.9501(53)	0.9824
ν_1	0.0037(15)	0.0009	0.0065(37)	$< 10^{-4}$
ν_5	0.0314(16)	0.0222	0.0282(23)	0.0122
ν_6	0.0107(53)	0.0031	0.0090(23)	0.0013
ν_{10}	0.0048(13)	0.0018	0.0062(23)	0.0018
ν_{14}	0.0030(12)	0.0010		0.0007
Modes	CaOPh-mCF$_3$			
	Exp. (A)	Theo. (A)	Exp. (B)	Theo. (B)
0	0.9339(28)	0.9699	0.9308(184)	0.9828
ν_2	0.0137(13)	0.0028	0.0144(74)	0.0003
ν_5	0.0018(11)	0.0006		0.0004
ν_7	0.0320(11)	0.0154	0.0343(81)	0.0076
ν_9	0.0073(10)	0.0031	0.0091(55)	0.0002
ν_{10}	0.0050(10)	0.0018		0.0008
ν_{15}	0.0039(10)	0.0013	0.0084(52)	0.0014
ν_{23}	0.0025(10)	0.0009	0.0030(49)	0.0008
Modes	CaOPh-34F			
	Exp. (A)	Theo. (A)	Exp. (B)	Theo. (B)
0	0.9409(51)	0.9674		0.9831
ν_2	0.0050(35)	0.0012		$< 10^{-4}$
ν_5	0.0341(32)	0.0136		0.0073
ν_6	0.0199(32)	0.0112		0.0050
Modes	CaOPh-345F			
	Exp. (A)	Theo. (A)	Exp. (B)	Theo. (B)
0	0.9576(23)	0.9755	0.9899(12)	0.9886
ν_1	0.0046(12)	$< 10^{-4}$		$< 10^{-4}$
ν_6	0.0270(10)	0.0159	0.0064(7)	0.0072
ν_8	0.0058(10)	0.0031		0.0007
ν_{16}	0.0031(9)	0.0018	0.0014(7)	0.0010
ν_{24}	0.0020(9)	0.0011	0.0023(6)	0.0003

Table B.1: Observed and theoretical VBRs for all transitions studied in this work. Errors are standard error of fit and do not include systematic uncertainties.

Modes	SrOPh-CH_3			
	Exp.(A)	Theo.(A)	Exp.(B)	Theo.(B)
0	0.946(6)	0.926	0.918(9)	0.943
ν_2		7×10^{-4}	0.011(2)	2×10^{-4}
ν_5	0.054(6)	0.059	0.072(9)	0.044
Modes	SrOPh			
	Exp.(A)	Theo.(A)	Exp.(B)	Theo.(B)
0	0.845(7)	0.928	0.885(5)	0.945
ν_2	0.029(3)	$< 10^{-4}$	0.054(3)	$< 10^{-4}$
$2\nu_2$	0.025(3)	$< 10^{-4}$		
ν_3	0.079(5)	0.059	0.060(3)	0.043
$\nu_2\nu_3$	0.021(3)	$< 10^{-4}$		
Modes	SrOPh-3-F			
	Exp.(A)	Theo.(A)	Exp.(B)	Theo.(B)
0	0.956(13)	0.936	0.965(3)	0.954
ν_1	0.007(3)	9×10^{-4}		
ν_3	0.037(16)	0.051	0.035(3)	0.037
Modes	SrOPh-CF_3			
	Exp.(A)	Theo.(A)	Exp.(B)	Theo.(B)
0	0.893(5)	0.939	0.867(11)	0.950
ν_2	0.014(2)	0.003	0.021(5)	$< 10^{-4}$
ν_5	0.018(2)	0.007	0.026(6)	0.007
ν_6	0.074(3)	0.037	0.086(8)	0.035
Modes	SrOPh-3,4,5-F			
	Exp.(A)	Theo.(A)	Exp.(B)	Theo.(B)
0	0.946(7)	0.945	0.964(4)	0.963
ν_1	0.005(2)	$< 10^{-4}$	0.008(2)	$< 10^{-4}$
ν_4	0.049(7)	0.044	0.028(4)	0.030

Table B.2: The intensity ratios of all observed vibrational decays of all molecules. The errors indicate the statistical uncertainties from the Gaussian fits. The theoretical VBRs are also added for comparison.

Molecules	PhOH-mCH_3	Phenol	PhOH-3F	PhOH-34F	PhOH-mCF_3	PhOH-35F	PhOH-345F
Melting Point (^{o}C)	12.2(3)	40.89(1)	14(1)	$34-38$	-0.9	$54-58$	57
pKa[218]	10.3	10.0	9.3	9.1	8.7	8.4	8.2
Hammett parameter[33, 219]	-0.07	0	0.34	0.40	0.43	0.67	0.74

Table B.3: Melting points, pKa and Hammett parameters for the different molecular species described in this work. The pKa and Hammett parameter can be linked by the derived Hammett equation [219]: pKa (X) = pKa (H) - $\sigma\rho$, where pKa (X) = $-$ log K (X), pKa (H) = $-$ log K (H), K (X) and K (H) are the equilibrium constants for a substituted species and unsubstituted phenol, respectively. σ is the Hammett parameter and ρ is the reaction constant.

X-A Transition

Molecules	Measured VBR S_0	Scaled VBR S_0'	Scaled VBR exluding main peak S_0''	Upper error bar $(S_0 - S_0')$	Lower error bar $(S_0' - S_0'')$
CaOPh-mCH3					
CaOPh	0.9339	0.9286	0.9274	0.0053	0.0012
CaOPh-mF	0.9464	0.9400	0.9383	0.0064	0.0017
CaOPh-34F	0.9409	0.9298	0.9254	0.0111	0.0044
CaOPh-mCF3	0.9339	0.9250	0.9230	0.0089	0.0021
CaOPh-345F	0.9576	0.9510	0.9493	0.0066	0.0018

X-B Transition

Molecules	Measured VBR S_0	Scaled VBR S_0'	Scaled VBR exluding main peak S_0''	Upper error bar $(S_0 - S_0')$	Lower error bar $(S_0' - S_0'')$
CaOPh-mCH3	0.9387	0.9339	0.9323	0.0048	0.0016
CaOPh	0.9446	0.9422	0.9412	0.0024	0.0010
CaOPh-mF	0.9501	0.9445	0.9403	0.0056	0.0042
CaOPh-34F					
CaOPh-mCF3	0.9308	0.9140	0.9000	0.0168	0.0140
CaOPh-345F	0.9899	0.9867	0.9866	0.0032	0.0002

Table B.4: The comparisons of measured diagonal VBR and scaled diagonal VBR. The differences indicate the systematic uncertainties of unobserved vibrational peaks.

Error source	Percentage
Unobserved peaks	$0.34\% - 3.08\%$
Instrument wavelength response	$\approx 1\%$
Diagonal excitations from excited vibrational levels	$< 0.5\%$
OPO power fluctuation	$< 0.5\%$
Fitting model	$< 1\%$
Totol error	$1.62\% - 3.48\%$

Table B.5: Summary of systematic error sources in the DLIF measurement.

Vib. modes	CaOPh		Vib. modes	CaOPh-mCH$_3$	
	Exp.	Theo.		Exp.	Theo.
ν_2	44(6)	61	ν_6	285(2)	291
ν_4	312(2)	314	ν_7	327(2)	329
ν_9	627(6)	631	ν_{12}	636(4)	640
ν_{13}	878(6)	903	ν_{14}	775(5)	790
ν_{23}	1304(4)	1347			
Vib. modes	CaOPh-mF		Vib. modes	CaOPh-mCF$_3$	
	Exp.	Theo.		Exp.	Theo.
ν_1	47(15)	55	ν_2	51(10)	46
ν_5	290(2)	297	ν_5	182(12)	183
ν_6	355(4)	359	ν_7	277(3)	280
ν_{10}	625(4)	630	ν_9	345(2)	350
ν_{14}	788(4)	802	ν_{10}	379(2)	381
			ν_{15}	626(9)	634
			ν_{23}	942(4)	962
Vib. modes	CaOPh-34F		Vib. modes	CaOPh-345F	
	Exp.	Theo.		Exp.	Theo.
ν_2	58(7)	54	ν_1	51(3)	51
ν_5	275(3)	278	ν_6	266(3)	272
ν_6	292(3)	293	ν_8	309(2)	315
			ν_{16}	663(6)	686
			ν_{24}	1173(6)	1210

Table B.6: Comparison of the observed and calculated frequencies for resolved fundamental vibrational modes of all species studied in this work. Values are given in units of cm^{-1}.

Vib. modes	SrOPh		Vib. modes	SrOPh-3-CF_3	
	Exp.	Theo.		Exp.	Theo.
ν_2	54(2)	54	ν_2	42(5)	39
$2\nu_2$	102(2)	108	ν_5	178(5)	180
ν_3	238(2)	241	ν_6	219(2)	222
$\nu_2\nu_3$	297(2)	294			
Vib. modes	SrOPh-3-F		Vib. modes	SrOPh-3-CH_3	
	Exp.	Theo.		Exp.	Theo.
ν_1	56(5)	56	ν_2	43(5)	50
ν_3	226(2)	222	ν_5	226(2)	230
Vib. modes	SrOPh-3,4,5-F				
	Exp.	Theo.			
ν_2	47(6)	45			
ν_4	203(2)	204			

Table B.7: Comparison of the observed and calculated frequencies for resolved fundamental vibrational modes of all species studied in this work. Values are given in units of cm^{-1}.

CaOPh-mCH$_3$		CaOPh		CaOPh-mF		CaOPh-34F		CaOPh-mCF$_3$		CaOPh-345F	
Modes	Freqs.	Modes	Freqs.	Modes	Freqs.	Modes	Freqs.	Modes	Freqs.	Modes	Freqs.
ν_1	37	ν_1	61	ν_1	55	ν_1	51	ν_1	11	ν_1	50
ν_2	55	ν_2	61	ν_2	59	ν_2	54	ν_2	46	ν_2	51
ν_3	59	ν_3	247	ν_3	238	ν_3	166	ν_3	58	ν_3	147
ν_4	208	ν_4	314	ν_4	249	ν_4	241	ν_4	128	ν_4	222
ν_5	247	ν_5	426	ν_5	297	ν_5	278	ν_5	183	ν_5	260
ν_6	291	ν_6	448	ν_6	359	ν_6	293	ν_6	246	ν_6	272
ν_7	329	ν_7	529	ν_7	471	ν_7	366	ν_7	280	ν_7	277
ν_8	457	ν_8	629	ν_8	502	ν_8	378	ν_8	331	ν_8	315
ν_9	480	ν_9	631	ν_9	523	ν_9	471	ν_9	350	ν_9	363
ν_{10}	527	ν_{10}	714	ν_{10}	630	ν_{10}	486	ν_{10}	381	ν_{10}	364
ν_{11}	594	ν_{11}	782	ν_{11}	642	ν_{11}	590	ν_{11}	470	ν_{11}	604
ν_{12}	640	ν_{12}	837	ν_{12}	706	ν_{12}	604	ν_{12}	477	ν_{12}	518
ν_{13}	715	ν_{13}	903	ν_{13}	781	ν_{13}	646	ν_{13}	536	ν_{13}	589
ν_{14}	790	ν_{14}	910	ν_{14}	802	ν_{14}	716	ν_{14}	588	ν_{14}	658
ν_{15}	796	ν_{15}	985	ν_{15}	878	ν_{15}	790	ν_{15}	634	ν_{15}	658
ν_{16}	876			ν_{16}	883	ν_{16}	820	ν_{16}	669	ν_{16}	686
ν_{17}	901			ν_{17}	989	ν_{17}	827	ν_{17}	676	ν_{17}	729
ν_{18}	976			ν_{18}	998	ν_{18}	879	ν_{18}	721	ν_{18}	817
ν_{19}	991					ν_{19}	955	ν_{19}	779	ν_{19}	849
						ν_{20}	994	ν_{20}	811	ν_{20}	866
								ν_{21}	909		
								ν_{22}	916		
								ν_{23}	962		

Table B.8: Theoretical frequencies of vibrational modes for the $\widetilde{X}$ state of all molecules studied in this work. Only modes with frequencies smaller than 1000 cm^{-1} are listed. Values are given in units of cm^{-1}.

CaOPh-34F				CaOPh-345F			
modes	$\widetilde{A} \rightarrow \widetilde{X}$	modes	$\widetilde{B} \rightarrow \widetilde{X}$	modes	$\widetilde{A} \rightarrow \widetilde{X}$	modes	$\widetilde{B} \rightarrow \widetilde{X}$
0	0.9674	0	0.9831	0	0.9755	0	0.9886
ν_5	0.0136	ν_5	0.0073	ν_6	0.0159	ν_6	0.0072
ν_6	0.0112	ν_6	0.0050	ν_8	0.0031	ν_{16}	0.0010
ν_{11}	0.0023	ν_{11}	0.0017	ν_{16}	0.0018	ν_{11}	0.0009
ν_2	0.0012	ν_{16}	0.0009	ν_{24}	0.0011	ν_8	0.0007
ν_{16}	0.0009	ν_{10}	0.0005	ν_{11}	0.0009	ν_{18}	0.0005
ν_{22}	0.0007	ν_{22}	0.0003	ν_{27}	0.0005	ν_{24}	0.0003
ν_{26}	0.0005	ν_{26}	0.0003	ν_{18}	0.0004	ν_{27}	0.0002
ν_{10}	0.0004	ν_{28}	0.0002	ν_{29}	0.0002	$2\nu_2$	0.0002
ν_{15}	0.0003	$2\nu_2$	0.0002	$2\nu_6$	0.0002	ν_{29}	0.0001
ν_{28}	0.0003	ν_{20}	0.0001	ν_{21}	0.0001	ν_{21}	0.0001
ν_{20}	0.0002	ν_{15}	0.0001	ν_{31}	0.0001	$2\nu_6$	0.0001
ν_{30}	0.0002	ν_{30}	0.0001	$2\nu_1$	0.0001		
$\nu_5\nu_6$	0.0002	ν_{27}	0.0001	ν_{25}	0.0001		
ν_{24}	0.0002	$2\nu_5$	0.0001	$\nu_6\nu_8$	0.0001		
$2\nu_5$	0.0001						
$2\nu_2$	0.0001						
ν_{27}	0.0001						
$2\nu_6$	0.0001						

Table B.9: Theoretical vibrational branching ratios of CaOPh-34F and CaOPh-345F above the level of 10^{-4}.

CaOPh-mF				CaOPh-mCF$_3$			
modes	$\widetilde{A} \rightarrow \widetilde{X}$	modes	$\widetilde{B} \rightarrow \widetilde{X}$	modes	$\widetilde{A} \rightarrow \widetilde{X}$	modes	$\widetilde{B} \rightarrow \widetilde{X}$
0	0.9676	0	0.9824	0	0.9699	0	0.9828
ν_5	0.0222	ν_5	0.0122	ν_7	0.0154	ν_7	0.0076
ν_6	0.0031	$\nu_1 0$	0.0018	ν_9	0.0031	ν_1	0.0024
ν_{10}	0.0018	ν_6	0.0013	ν_2	0.0028	ν_9	0.0015
ν_{14}	0.0010	ν_{14}	0.0007	ν_{10}	0.0018	ν_{15}	0.0014
ν_1	0.0009	ν_{25}	0.0003	ν_{14}	0.0013	ν_{23}	0.0008
ν_{25}	0.0008	ν_{24}	0.0002	ν_8	0.0013	ν_{10}	0.0008
ν_{24}	0.0006	ν_{27}	0.0002	ν_{23}	0.0009	ν_8	0.0005
$2\nu_{24}$	0.0004	ν_{18}	0.0002	ν_5	0.0006	ν_5	0.0004
ν_{18}	0.0003	$2\nu_5$	0.0001	ν_{34}	0.0005	ν_{17}	0.0003
$2\nu_1$	0.0003	$2\nu_1$	0.0001	ν_{19}	0.0004	ν_2	0.0003
ν_{29}	0.0002	ν_{19}	0.0001	$2\nu_2$	0.0004	ν_{19}	0.0002
ν_{22}	0.0002	ν_{29}	0.0001	$2\nu_7$	0.0002	ν_{34}	0.0002
ν_{27}	0.0002	ν_{26}	0.0001	ν_{17}	0.0002	ν_{27}	0.0002
ν_{26}	0.0001	ν_{22}	0.0001	ν_{36}	0.0002	ν_{36}	0.0001
ν_{21}	0.0001	ν_{22}	0.0002	ν_{31}	0.0001	ν_{35}	0.0001
$\nu_4\nu_5$	0.0001	ν_{22}	0.0002	ν_{38}	0.0001	$2\nu_2$	0.0001
$2\nu_2$	0.0001	ν_{22}	0.0002	ν_{33}	0.0001	$2\nu_7$	0.0001
ν_{19}	0.0001	ν_{22}	0.0002	ν_{35}	0.0001	ν_{38}	0.0001
				ν_{32}	0.0001	$2\nu_1$	0.0001
				ν_{14}	0.0001		
				ν_{26}	0.0001		
				ν_1	0.0001		
				ν_{12}	0.0001		

Table B.10: Theoretical vibrational branching ratios of CaOPh-mF and CaOPh-mCF$_3$ above the level of 10^{-4}.

CaOPh				CaOPh-mCH$_3$			
modes	$\widetilde{A} \rightarrow \widetilde{X}$	modes	$\widetilde{B} \rightarrow \widetilde{X}$	modes	$\widetilde{A} \rightarrow \widetilde{X}$	modes	$\widetilde{B} \rightarrow \widetilde{X}$
0	0.9611	0	0.9758	0	0.9587	0	0.9737
ν_4	0.0311	ν_4	0.0185	ν_6	0.0175	ν_6	0.0110
ν_9	0.0027	ν_9	0.0027	ν_7	0.0151	ν_7	0.0090
ν_{13}	0.0018	ν_{13}	0.0012	ν_{12}	0.0024	ν_{12}	0.0024
ν_{23}	0.0017	ν_{23}	0.0008	ν_{14}	0.0016	ν_{14}	0.0014
$2\nu_4$	0.0006	$2\nu_4$	0.0003	ν_{27}	0.0012	ν_{27}	0.0006
ν_{28}	0.0006	ν_{26}	0.0002	ν_2	0.0006	ν_1	0.0003
ν_{26}	0.0006	ν_{28}	0.0001	ν_{18}	0.0003	ν_{33}	0.0002
$2\nu_1$	0.0002	$2\nu_2$	0.0001	$2\nu_2$	0.0003	ν_{21}	0.0002
$\nu_4\nu_9$	0.0001	$\nu_4\nu_9$	0.0001	$\nu_6\nu_7$	0.0003	ν_{18}	0.0002
$2\nu_2$	0.0001			ν_{33}	0.0002	ν_{35}	0.0001
$\nu_4\nu_{23}$	0.0001			ν_{21}	0.0002	ν_{15}	0.0001
$\nu_4\nu_{13}$	0.0001			ν_{25}	0.0002	ν_{30}	0.0001
				ν_{35}	0.0002	$2\nu_2$	0.0001
				$2\nu_6$	0.0002	$\nu_6\nu_7$	0.0001
				ν_{28}	0.0001	ν_{25}	0.0001
				ν_{30}	0.0001	$2\nu_6$	0.0001
				$2\nu_7$	0.0001	ν_{28}	0.0001
				ν_{15}	0.0001	ν_{34}	0.0001
				ν_{34}	0.0001	ν_2	0.0001
				ν_{29}	0.0001	$2\nu_7$	0.0001
				$2\nu_3$	0.0001		

Table B.11: Theoretical vibrational branching ratios of CaOPhand CaOPh-mCH$_3$ above the level of 10^{-4}.

decays from A (v=0)		decays from A (v=1) of mode ν_1		decays from A (v=1) of mode ν_4	
modes	VBR	modes	VBR	modes	VBR
0	0.9611	ν_1	0.9609	ν_4	0.8963
ν_4	0.0311	$\nu_1\nu_4$	0.0311	$2\nu_4$	0.0598
ν_9	0.0027	$\nu_1\nu_9$	0.0027	0	0.0354
ν_{23}	0.0017	$\nu_1\nu_{23}$	0.0017	$\nu_4\nu_9$	0.0025
ν_{13}	0.0018	$\nu_1\nu_{13}$	0.0018	$\nu_4\nu_{23}$	0.0015
$2\nu_4$	0.0006	$\nu_1 2\nu_4$	0.0006	$4\nu_4$	0.0017
ν_{28}	0.0003	$3\nu_1$	0.0005	$\nu_4\nu_{13}$	0.0016
ν_{26}	0.0003	$\nu_1\nu_{28}$	0.0003	$\nu_4\nu_{28}$	0.0003
$2\nu_1$	0.0002	$\nu_1\nu_{26}$	0.0003	$\nu_4\nu_{26}$	0.0003
$\nu_4\nu_9$	0.0001	$\nu_1\nu_4\nu_9$	0.0001	$2\nu_4\nu_9$	0.0002
$2\nu_2$	0.0001	$\nu_1 2\nu_2$	0.0001	$2\nu_1\nu_4$	0.0002
$\nu_4\nu_{23}$	0.0001	$\nu_1\nu_4\nu_{23}$	0.0001	$2\nu_4\nu_{23}$	0.0001

Table B.12: Theoretical vibrational branching ratios from different vibrational levels of $\widetilde{A}$ state of CaOPh above the level of 10^{-4}.

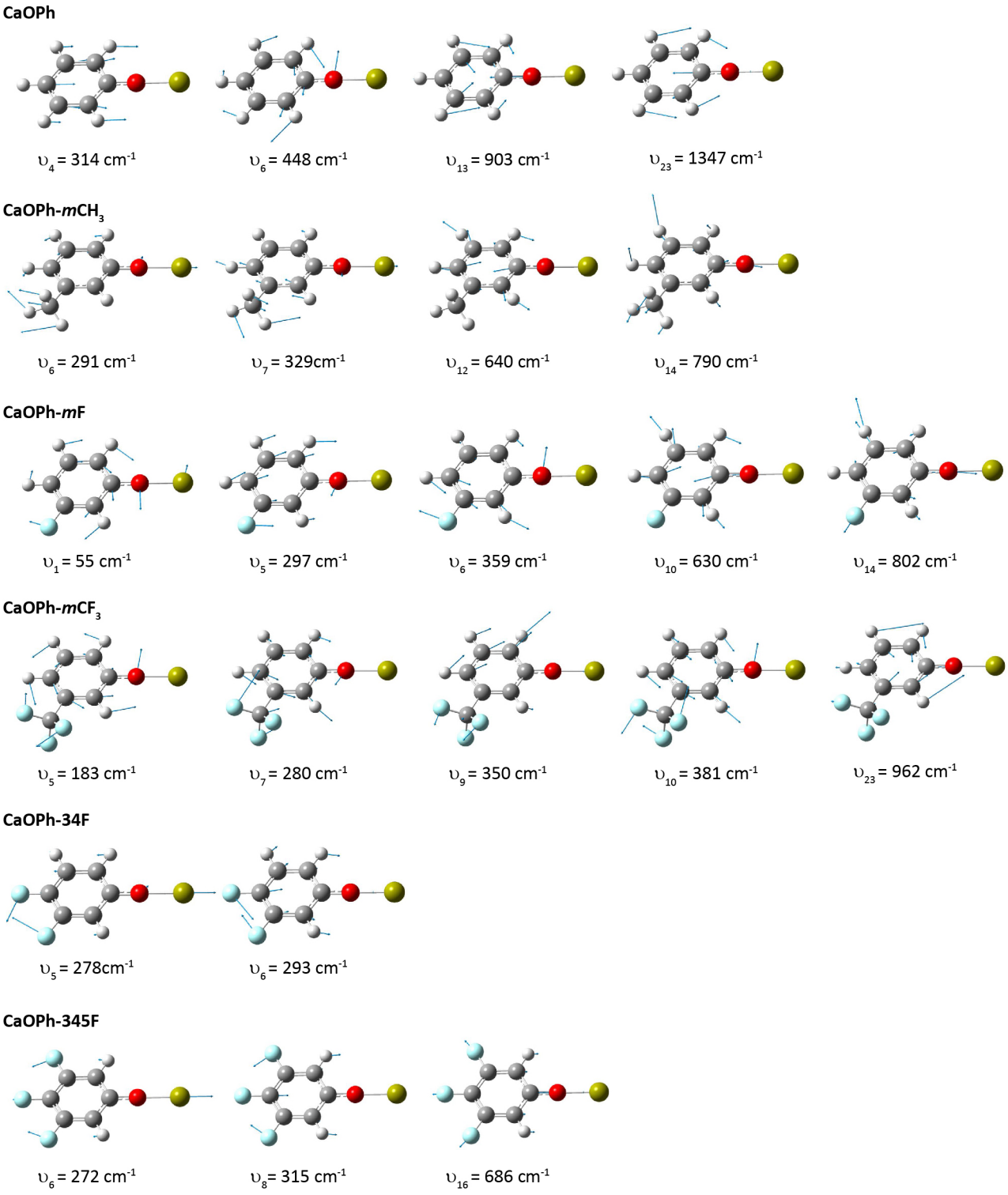

Figure B.2: Schematic illustrations of resolved fundamental normal vibrational modes. The arrows indicate the direction of vibrational displacements. The corresponding theoretical frequencies are also given.

References

[1] M. H. Anderson, J. R. Ensher, M. R. Matthews, C. E. Wieman, and E. A. Cornell , "Observation of bose-einstein condensation in a dilute atomic vapor", science **269**, 198 (1995).

[2] K. B. Davis, M.-O. Mewes, M. R. Andrews, N. J. van Druten, D. S. Durfee, D. Kurn, and W. Ketterle , "Bose-Einstein condensation in a gas of sodium atoms", Phys. Rev. Lett. **75**, 3969 (1995).

[3] I. Bloch, J. Dalibard, and S. Nascimbene , "Quantum simulations with ultracold quantum gases", Nat. Phys. **8**, 267 (2012).

[4] R. Blatt and C. F. Roos , "Quantum simulations with trapped ions", Nat. Phys. **8**, 277 (2012).

[5] A. D. Ludlow, M. M. Boyd, J. Ye, E. Peik, and P. O. Schmidt , "Optical atomic clocks", Rev. Mod. Phys. **87**, 637 (2015).

[6] C. Monroe, W. C. Campbell, L.-M. Duan, Z.-X. Gong, A. V. Gorshkov, P. W. Hess, R. Islam, K. Kim, N. M. Linke, G. Pagano, P. Richerme, C. Senko, and N. Y. Yao , "Programmable quantum simulations of spin systems with trapped ions", Rev. Mod. Phys. **93**, 025001 (2021).

[7] I. Bloch , "Quantum coherence and entanglement with ultracold atoms in optical lattices", Nature **453**, 1016 (2008).

[8] M. Kasevich and S. Chu , "Measurement of the gravitational acceleration of an atom with a light-pulse atom interferometer", Appl. Phys. B **54**, 321 (1992).

[9] J. R. Anglin and W. Ketterle , "Bose-Einstein condensation of atomic gases", Nature **416**, 211 (2002).

[10] O. Carnal and J. Mlynek , "Young's double-slit experiment with atoms: A simple atom interferometer", Phys. Rev. Lett. **66**, 2689 (1991).

[11] P. Cladé, E. De Mirandes, M. Cadoret, S. Guellati-Khélifa, C. Schwob, F. Nez, L. Julien, and F. Biraben , "Determination of the fine structure constant based on bloch oscillations of ultracold atoms in a vertical optical lattice", Phys. Rev. Lett. **96**, 033001 (2006).

[12] L. D. Carr, D. DeMille, R. V. Krems, and J. Ye , "Cold and ultracold molecules: science, technology and applications", New J. Phys. **11**, 055049 (2009).

[13] B. L. Augenbraun, J. M. Doyle, T. Zelevinsky, and I. Kozyryev , "Molecular asymmetry and optical cycling: laser cooling asymmetric top molecules", Phys. Rev. X **10**, 031022 (2020).

[14] E. S. Shuman, J. F. Barry, and D. DeMille , "Laser cooling of a diatomic molecule", Nature **467**, 820 (2010).

[15] M. T. Hummon, M. Yeo, B. K. Stuhl, A. L. Collopy, Y. Xia, and J. Ye , "2d magneto-optical trapping of diatomic molecules", Phys. Rev. Lett. **110**, 143001 (2013).

[16] V. Zhelyazkova, A. Cournol, T. E. Wall, A. Matsushima, J. J. Hudson, E. Hinds, M. Tarbutt, and B. Sauer , "Laser cooling and slowing of caf molecules", Phys. Rev. A **89**, 053416 (2014).

[17] I. Kozyryev, L. Baum, K. Matsuda, B. L. Augenbraun, L. Anderegg, A. P. Sedlack, and J. M. Doyle , "Sisyphus laser cooling of a polyatomic molecule", Phys. Rev. Lett. **118**, 173201 (2017).

[18] D. Mitra, N. B. Vilas, C. Hallas, L. Anderegg, B. L. Augenbraun, L. Baum, C. Miller, S. Raval, and J. M. Doyle , "Direct laser cooling of a symmetric top molecule", Science **369**, 1366 (2020).

[19] R. V. Krems , "Cold controlled chemistry", Phys. Chem. Chem. Phys. **10**, 4079 (2008).

[20] M. T. Bell and T. P. Softley , "Ultracold molecules and ultracold chemistry", Mol. Phys. **107**, 99 (2009).

[21] B. R. Heazlewood , "Cold ion chemistry within coulomb crystals", Mol. Phys. **117**, 1934 (2019).

[22] J. Lim, J. R. Almond, M. A. Trigatzis, J. A. Devlin, N. J. Fitch, B. E. Sauer, M. R. Tarbutt, and E. A. Hinds , "Laser cooled YbF molecules for measuring the electron's electric dipole moment", Phys. Rev. Lett. **120**, 123201 (2018).

[23] V. Andreev, D. G. Ang, D. DeMille, J. M. Doyle, G. Gabrielse, J. Haefner, N. Hutzler, L. Z., C. Meisenhelder, B. R. O'Leary, C. D. Panda, A. D. West, E. West, and X. Wu , "Improved limit on the electric dipole moment of the electron", Nature **562**, 355 (2018).

[24] B. L. Augenbraun, Z. D. Lasner, A. Frenett, H. Sawaoka, C. Miller, T. C. Steimle, and J. M. Doyle , "Laser-cooled polyatomic molecules for improved electron electric dipole moment searches", New J. Phys. **22**, 022003 (2020).

[25] D. DeMille , "Quantum computation with trapped polar molecules", Phys. Rev. Lett. **88**, 067901 (2002).

[26] P. Yu, L. W. Cheuk, I. Kozyryev, and J. M. Doyle , "A scalable quantum computing platform using symmetric-top molecules", New J. Phys. **21**, 093049 (2019).

[27] J. T. Hougen , "Double group considerations, Jahn-Teller induced rovibronic effects, and the nuclear spin-electron spin hyperfine hamiltonian for a molecule of symmetry C_{3v} in an electronic ^{2}E state", J. Mol. Spectrosc. **81**, 73 (1980).

[28] I. B. Bersuker , "Modern aspects of the Jahn-Teller effect theory and applications to molecular problems", Chem. Rev. **101**, 1067 (2001).

[29] A. Amrein, H. Hollenstein, M. Quack, R. Zenobi, J. Segall, and R. Zare , "Fermi

resonance structure in the ch vibrational overtones of cd3cho", J. Chem. Phys. **90**, 3944 (1989).

[30] T. Uzer and W. Miller , "Theories of intramolecular vibrational energy transfer", Phys. Rep. **199**, 73 (1991).

[31] J. M. Brown and A. Carrington, *Rotational spectroscopy of diatomic molecules* (Cambridge University Press, 2003).

[32] Di Rosa, M. D. , "Laser-cooling molecules - concept, candidates, and supporting hyperfine-resolved measurements of rotational lines in the $A - X(0, 0)$ band of CaH", Eur. Phys. J. D **31**, 395 (2004).

[33] C. E. Dickerson, H. Guo, A. J. Shin, B. L. Augenbraun, J. R. Caram, W. C. Campbell, and A. N. Alexandrova , "Franck-Condon tuning of optical cycling centers by organic functionalization", Phys. Rev. Lett. **126**, 123002 (2021).

[34] H. Lefebvre-Brion and R. W. Field, *The spectra and dynamics of diatomic molecules* (Elsevier Acad. Press, Amsterdam, 2004).

[35] J. Liu , "Rotational and fine structure of open-shell molecules in nearly degenerate electronic states", J. Chem. Phys. **148** (2018).

[36] J. Brown , "The effective Hamiltonian for the Renner-Teller effect", J. Mol. Spectrosc. **68**, 412 (1977).

[37] G.-Z. Zhu, D. Mitra, B. L. Augenbraun, C. E. Dickerson, M. J. Frim, G. Lao, Z. D. Lasner, A. N. Alexandrova, W. C. Campbell, J. R. Caram, J. M. Doyle, and E. R. Hudson , "Functionalizing aromatic compounds with optical cycling centers", Nat. Chem. **14**, 995 (2022).

[38] G. Lao, G.-Z. Zhu, C. E. Dickerson, B. L. Augenbraun, A. N. Alexandrova, J. R. Caram, E. R. Hudson, and W. C. Campbell , "Laser spectroscopy of aromatic

molecules with optical cycling centers: strontium (i) phenoxides", J. Phys. Chem. Lett. **13**, 11029 (2022).

[39] P. M. Morse , "Diatomic molecules according to the wave mechanics. II. vibrational levels", Phys. Rev. **34**, 57 (1929).

[40] J. Vázquez and J. F. Stanton , "Treatment of Fermi resonance effects on transition moments in vibrational perturbation theory", Mol. Phys. **105**, 101 (2007).

[41] J. Autschbach and T. Ziegler , "Nuclear spin–spin coupling constants from regular approximate relativistic density functional calculations. II. spin–orbit coupling effects and anisotropies", J. Chem. Phys. **113**, 9410 (2000).

[42] C. M. Marian, "Spin-orbit coupling in molecules", in *Reviews in computational chemistry*, Vol. 17 (Wiley, 2001) pp. 99–204.

[43] I. Broser, H. Maier, and H.-J. Schulz , "Fine structure of the infrared absorption and emission spectra of Cu^{2+} in ZnS and CdS crystals", Phys. Rev. **140**, A2135 (1965).

[44] A. C. Stanton and C. E. Kolb , "Direct absorption measurement of the spin-orbit splitting and $^2p_{1/2}$ radiative lifetime in atomic fluorine $(2p^5)$", J. Chem. Phys. **72**, 6637 (1980).

[45] M. Kepenekian, R. Robles, C. Katan, D. Sapori, L. Pedesseau, and J. Even , "Rashba and Dresselhaus effects in hybrid organic–inorganic perovskites: From basics to devices", ACS Nano **9**, 11557 (2015).

[46] G. Dresselhaus , "Spin-orbit coupling effects in zinc blende structures", Phys. Rev. **100**, 580 (1955).

[47] D. West, Y. Y. Sun, H. Wang, J. Bang, and S. B. Zhang , "Native defects in second-generation topological insulators: effect of spin-orbit interaction on Bi_2Se_3", Phys. Rev. B **86**, 121201 (2012).

[48] I. Aguilera, C. Friedrich, and S. Blügel , "Spin-orbit coupling in quasiparticle studies of topological insulators", Phys. Rev. B **88**, 165136 (2013).

[49] I. V. Khudyakov, Y. A. Serebrennikov, and N. J. Turro , "Spin-orbit coupling in free-radical reactions: on the way to heavy elements", Chem. Rev. **93**, 537 (1993).

[50] J. Brown and T. Sears , "A reduced form of the spin-rotation Hamiltonian for asymmetric-top molecules, with applications to HO_2 and NH_2", J. Mol. Spectrosc. **75**, 111 (1979).

[51] J. H. Van Vleck , "The coupling of angular momentum vectors in molecules", Rev. Mod. Phys. **23**, 213 (1951).

[52] C. J. Whitham and C. Jungen , "Laser-induced fluorescence spectroscopy of the B–X and A–X transitions of $CaNH_2$", J. Chem. Phys. **93**, 1001 (1990).

[53] E. Arimondo, M. Inguscio, and P. Violino , "Experimental determinations of the hyperfine structure in the alkali atoms", Rev. Mod. Phys. **49**, 31 (1977).

[54] A. Bohr and V. F. Weisskopf , "The influence of nuclear structure on the hyperfine structure of heavy elements", Phys. Rev. **77**, 94 (1950).

[55] A. Weber , "Ro-vibronic species, overall allowed species, and nuclear spin statistical weights for symmetric top molecules belonging to the Dnd and D_{nh} (n6) point-groups", J. Chem. Phys. **73**, 3952 (2008).

[56] A. Weber , "Rovibronic species, overall allowed species, and nuclear spin statistical weights for symmetric top molecules. II. Point groups C_{n_v} and C_{n_h}(n6)", J. Chem. Phys. **76**, 3694 (1982).

[57] J. H. Van Vleck , "The Jahn-Teller Effect and Crystalline Stark Splitting for Clusters of the Form XY_6", J. Chem. Phys. **7**, 72 (1939).

[58] T. A. Barckholtz and T. A. Miller , "Quantitative insights about molecules exhibiting jahn-teller and related effects", Int. Rev. Phys. Chem. **17**, 435 (1998).

[59] A. F. Wells, *Structural inorganic chemistry* (Oxford, 2012).

[60] J. Chaboy, A. Muñoz Páez, F. Carrera, P. Merkling, and E. S. Marcos , "Ab initio X-ray absorption study of copper K-edge XANES spectra in Cu(II) compounds", Phys. Rev. B **71**, 134208 (2005).

[61] H. Köppel, L. S. Cederbaum, and W. Domcke , "Interplay of Jahn–Teller and pseudo-Jahn–Teller vibronic dynamics in the benzene cation", J. Chem. Phys. **89**, 2023 (1988).

[62] A. C. Paul, K. Sharma, M. A. Reza, H. Telfah, T. A. Miller, and J. Liu , "Laser-induced fluorescence and dispersed-fluorescence spectroscopy of the $\tilde{A}^2E$ - $\tilde{X}^2A_1$ transition of jet-cooled calcium methoxide ($CaOCH_3$) radicals", J. Chem. Phys. **151**, 134303 (2019).

[63] J.-i. Adachi, N. Kosugi, E. Shigemasa, and A. Yagishita , "Renner–Teller splitting in the C 1s $\rightarrow \pi^*$ excited states of CS_2, OCS, and CO_2", J. Chem. Phys. **107**, 4919 (1997).

[64] M. Li and J. A. Coxon , "High-resolution analysis of the fundamental bending vibrations in the $A^2\Pi$ and $X^2\Sigma^+$ states of CaOH and CaOD: Deperturbation of Renner–Teller, spin–orbit and K-type resonance interactions", J. Chem. Phys. **102**, 2663 (1995).

[65] C. N. Jarman and P. F. Bernath , "High resolution laser spectroscopy of the $C^2\Delta - X^2\Sigma^+$ transition of CaOH and CaOD: Vibronic coupling and the Renner–Teller effect", J. Chem. Phys. **97**, 1711 (1992).

[66] S. Ding, Y. Wu, I. A. Finneran, J. J. Burau, and J. Ye , "Sub-doppler cooling and compressed trapping of YO molecules at μK temperatures", Phys. Rev. X **10**, 021049 (2020).

[67] D. Mitra, N. B. Vilas, C. Hallas, L. Anderegg, B. L. Augenbraun, L. Baum, C. Miller, S. Raval, and J. M. Doyle , "Direct laser cooling of a symmetric top molecule", Science **369**, 1366 (2020).

[68] A. N. Petrov, L. V. Skripnikov, A. V. Titov, and V. V. Flambaum , "Evaluation of *CP* violation in HfF^+", Phys. Rev. A **98**, 042502 (2018).

[69] J. J. Hudson, B. E. Sauer, M. R. Tarbutt, and E. A. Hinds , "Measurement of the electron electric dipole moment using ybf molecules", Phys. Rev. Lett. **89**, 023003 (2002).

[70] T. A. Collaboration, J. Baron, W. C. Campbell, D. DeMille, J. M. Doyle, G. Gabrielse, Y. V. Gurevich, P. W. Hess, N. R. Hutzler, E. Kirilov, I. Kozyryev, B. R. O'Leary, C. D. Panda, M. F. Parsons, E. S. Petrik, B. Spaun, A. C. Vutha, and A. D. West , "Order of magnitude smaller limit on the electric dipole moment of the electron", Science **343**, 269 (2014).

[71] M. Saffman, T. G. Walker, and K. Mølmer , "Quantum information with Rydberg atoms", Rev. Mod. Phys. **82**, 2313 (2010).

[72] N. Hinkley, J. A. Sherman, N. B. Phillips, M. Schioppo, N. D. Lemke, K. Beloy, M. Pizzocaro, C. W. Oates, and A. D. Ludlow , "An atomic clock with 10^{-18} instability", Science **341**, 1215 (2013).

[73] D. McCarron , "Laser cooling and trapping molecules", J. Phys. B: At. Mol. Opt. Phys. **51**, 212001 (2018).

[74] M. R. Tarbutt , "Laser cooling of molecules", Contemp. Phys. (2019).

[75] J. A. Blackmore, L. Caldwell, P. D. Gregory, E. M. Bridge, R. Sawant, J. Aldegunde, J. Mur-Petit, D. Jaksch, J. M. Hutson, B. E. Sauer, M. R. Tarbutt, and S. L. Cornish , "Ultracold molecules for quantum simulation: rotational coherences in CaF and RbCs", Quantum Sci. Technol. **4**, 014010 (2018).

[76] N. R. Hutzler , "Polyatomic molecules as quantum sensors for fundamental physics", Quantum Sci. Technol. **5**, 044011 (2020).

[77] N. Balakrishnan , "Perspective: Ultracold molecules and the dawn of cold controlled chemistry", J. Chem. Phys. **145**, 150901 (2016).

[78] Y. Liu, M.-G. Hu, M. A. Nichols, D. Yang, D. Xie, H. Guo, and K.-K. Ni , "Precision test of statistical dynamics with state-to-state ultracold chemistry", Nature **593**, 379 (2021).

[79] M. D. Di Rosa , "Laser-cooling molecules", Eur. Phys. J. D **31**, 395 (2004).

[80] S. Truppe, H. J. Williams, M. Hambach, L. Caldwell, N. J. Fitch, E. A. Hinds, B. E. Sauer, and M. R. Tarbutt , "Molecules cooled below the doppler limit", Nat. Phys. **13**, 1173 (2017).

[81] L. Anderegg, B. L. Augenbraun, E. Chae, B. Hemmerling, N. R. Hutzler, A. Ravi, A. Collopy, J. Ye, W. Ketterle, and J. M. Doyle , "Radio frequency magneto-optical trapping of CaF with high density", Phys. Rev. Lett. **119**, 103201 (2017).

[82] A. L. Collopy, S. Ding, Y. Wu, I. A. Finneran, L. Anderegg, B. L. Augenbraun, J. M. Doyle, and J. Ye , "3D magneto-optical trap of yttrium monoxide", Phys. Rev. Lett. **121**, 213201 (2018).

[83] L. Baum, N. B. Vilas, C. Hallas, B. L. Augenbraun, S. Raval, D. Mitra, and J. M. Doyle , "1D magneto-optical trap of polyatomic molecules", Phys. Rev. Lett. **124**, 133201 (2020).

[84] J. Nguyen and B. Odom , "Prospects for doppler cooling of three-electronic-level molecules", Phys. Rev. A **83**, 053404 (2011).

[85] R. Li, X. Yuan, G. Liang, Y. Wu, J. Wang, and B. Yan , "Laser cooling of the SiO^+ molecular ion: A theoretical contribution", Chem. Phys. **525**, 110412 (2019).

[86] J. H. V. Nguyen, C. R. Viteri, E. G. Hohenstein, C. D. Sherrill, K. R. Brown, and B. Odom , "Challenges of laser-cooling molecular ions", New J. Phys. **13**, 063023 (2011).

[87] Q.-Q. Zhang, C.-L. Yang, M.-S. Wang, X.-G. Ma, and W.-W. Liu , "The low-lying electronic states and optical schemes for the laser cooling of the BH^+ and BH^- ions", Spectrochim. Acta A **182**, 130 (2017).

[88] C.-Y. Lien, C. M. Seck, Y.-W. Lin, J. H. V. Nguyen, D. A. Tabor, and B. C. Odom , "Broadband optical cooling of molecular rotors from room temperature to the ground state", Nat. commun. **5**, 1 (2014).

[89] S.-Y. Kang, F.-G. Kuang, G. Jiang, D.-B. Li, Y. Luo, P. Feng-Hui, W. Li-Ping, W.-Q. Hu, and Y.-C. Shao , "Ab initio study of laser cooling of AlF^+ and $AlCl^+$ molecular ions", J. Phys. B: At. Mol. Opt. Phys. **50**, 105103 (2017).

[90] M. V. Ivanov, T.-C. Jagau, G.-Z. Zhu, E. R. Hudson, and A. I. Krylov , "In search of molecular ions for optical cycling: a difficult road", Phys. Chem. Chem. Phys. **22**, 17075 (2020).

[91] P. R. Stollenwerk, B. C. Odom, D. L. Kokkin, and T. Steimle , "Electronic spectroscopy of a cold SiO^+ sample: Implications for optical pumping", J. Mol. Spectrosc. **332**, 26 (2017).

[92] P. R. Stollenwerk, I. O. Antonov, S. Venkataramanababu, Y.-W. Lin, and B. C. Odom , "Cooling of a zero-nuclear-spin molecular ion to a selected rotational state", Phys. Rev. Lett. **125**, 113201 (2020).

[93] R. C. Pankhurst , "A complex band-spectrum associated with an oxide of silicon", Proc. Phys. Soc. **52**, 707 (1940).

[94] L. H. Woods , "On the silicon oxide bands", Phys. Rev. **63**, 426 (1943).

[95] S. N. Ghosh, J. Van der Linde, and R. D. Verma , "Confirmation of the SiO^+ spectrum", J. Mol. Spectrosc. **75**, 169 (1979).

[96] E. A. Colbourn, J. M. Dyke, E. P. F. Lee, A. Morris, and I. R. Trickle , "The vacuum

ultra-violet photoelectron spectrum of the SiO ($X^1\Sigma^+$) molecule", Mol. Phys. **35**, 873 (1978).

[97] L. Zhang, R. Cameron, R. A. Holt, T. J. Scholl, and S. D. Rosner , "New observations of the optical spectrum of SiO^+ and the prediction of its rotational spectrum", Astrophys. J. **418**, 307 (1993).

[98] R. Cameron, T. J. Scholl, L. Zhang, R. A. Holt, and S. D. Rosner , "Fast-ion-beam laser spectroscopy of the $B^2\Sigma^+ - X^2\Sigma^+$ and $B^2\Sigma^+ - A^2\Pi$ systems of SiO^+: Experiment", J. Mol. Spectrosc. **169**, 352 (1995).

[99] R. Cameron, T. J. Scholl, L. Zhang, R. A. Holt, and S. D. Rosner , "Fast-ion-beam laser spectroscopy of the $B^2\Sigma^+ - X^2\Sigma^+$ and $B^2\Sigma^+ - A^2\Pi$ systems of SiO^+: Deperturbation analysis", J. Mol. Spectrosc. **169**, 364 (1995).

[100] S. D. Rosner, R. Cameron, T. J. Scholl, and R. A. Holt , "A study of the $X^2\Sigma^+$ and $A^2\Pi$ states of SiO^+ using fast-ion-beam laser spectroscopy", J. Mol. Spectrosc. **189**, 83 (1998).

[101] D. P. Chong and Y. Takahata , "Vibrational structure in diatomic photoelectron spectra: application to CS, PN, SiO and P_2", J. Electron Spectrosc. Relat. Phenom. **10**, 137 (1977).

[102] H.-J. Werner, P. Rosmus, and M. Grimm , "Ab initio calculations of radiative transition probabilities in the $X^1\Sigma^+$ state of SiO and the $X^2\Sigma^+$ and $A^2\Pi$ states of SiO^+", Chem. Phys. **73**, 169 (1982).

[103] Z.-L. Cai and J. P. François , "Ab initio study of the electronic spectrum of the SiO^+ cation", J. Mol. Spectrosc. **197**, 12 (1999).

[104] Z.-L. Cai and J. P. François , "An internally contracted multireference configuration interaction analysis of the SiO^+ $B^2\Sigma^+ - X^2\Sigma^+$ transition moment", Chem. Phys. Lett. **282**, 29 (1998).

[105] Z.-L. Cai and J. P. François , "Ab initio study of the $X^2\Sigma^+$ and $A^2\Pi$ states of the SiO^+ cation including the effect of core correlation", Chem. Phys. **234**, 59 (1998).

[106] S. Chattopadhyaya, A. Chattopadhyay, and K. Das , "Electronic spectrum of SiO^+: a theoretical study", J. Mol. Struct.-Theochem. **639**, 177 (2003).

[107] D. Shi, W. Li, W. Xing, J. Sun, Z. Zhu, and Y. Liu , "Mrci study on electronic spectrum of several low-lying electronic states of the SiO^+ cation", Comput. Theor. Chem. **980**, 73 (2012).

[108] R. Li, G.-Y. Liang, X.-H. Lin, Y.-H. Zhu, S.-T. Zhao, and Y. Wu , "Explicitly correlated configuration interaction investigation on low-lying states of SiO^+ and SiO", Chin. Phys. B **28**, 043102 (2019).

[109] Z. Qin, T. Bai, J. Zhao, and L. Liu , "Transition properties between low-lying electronic states of SiO^+", J. Mol. Spectrosc. **370**, 111298 (2020).

[110] E. R. Hudson and W. C. Campbell , "Dipolar quantum logic for freely rotating trapped molecular ions", Phys. Rev. A **98**, 040302 (2018).

[111] T. Ruster, C. T. Schmiegelow, H. Kaufmann, C. Warschburger, F. Schmidt-Kaler, and U. G. Poschinger , "A long-lived Zeeman trapped-ion qubit", Appl. Phys. B **122**, 1 (2016).

[112] J. E. Christensen, D. Hucul, W. C. Campbell, and E. R. Hudson , "High-fidelity manipulation of a qubit enabled by a manufactured nucleus", npj Quantum Inf. **6**, 1 (2020).

[113] C. Roman, A. Ransford, M. Ip, and W. C. Campbell , "Coherent control for qubit state readout", New J. Phys. **22**, 073038 (2020).

[114] G. Cowan, *Statistical data analysis* (Oxford university press, 1998).

[115] L. B. Knight Jr, A. Ligon, R. W. Woodward, D. Feller, and E. R. Davidson , "The generation and trapping of the high-temperature oxosilyliumyl cation radicals ($^{28}SiO^+$

and $^{29}SiO^+$) in neon matrixes at 4 K; an ESR and *ab* initio CI theoretical investigation", J. Am. Chem. Soc. **107**, 2857 (1985).

[116] J. Aldegunde and J. M. Hutson , "Hyperfine structure of $^2\Sigma$ molecules containing alkaline-earth-metal atoms", Phys. Rev. A **97**, 042505 (2018).

[117] T. J. Scholl, R. Cameron, S. D. Rosner, and R. A. Holt , "Beam-laser measurements of lifetimes in SiO and N_2^+", Phys. Rev. A **51**, 2014 (1995).

[118] C. Marian, M. Larsson, B. Olsson, and P. Sigray , "Theoretical and experimental studies of radiative lifetimes of excited electronic states in CO^+", Chem. Phys. **130**, 361 (1989).

[119] E. R. Hudson and W. C. Campbell , "Laserless quantum gates for electric dipoles in thermal motion", Phys. Rev. A **104**, 042605 (2021).

[120] A. Sørensen and K. Mølmer , "Quantum computation with ions in thermal motion", Phys. Rev. Lett. **82**, 1971 (1999).

[121] N. V. Vitanov, A. A. Rangelov, B. W. Shore, and K. Bergmann , "Stimulated raman adiabatic passage in physics, chemistry, and beyond", Rev. Mod. Phys. **89**, 015006 (2017).

[122] J. M. Pino, J. M. Dreiling, C. Figgatt, J. P. Gaebler, S. A. Moses, M. Allman, C. Baldwin, M. Foss-Feig, D. Hayes, K. Mayer, *et al.* , "Demonstration of the trapped-ion quantum ccd computer architecture", Nature **592**, 209 (2021).

[123] S. Debnath, N. M. Linke, C. Figgatt, K. A. Landsman, K. Wright, and C. Monroe , "Demonstration of a small programmable quantum computer with atomic qubits", Nature **536**, 63 (2016).

[124] S. M. Brewer, J.-S. Chen, A. M. Hankin, E. R. Clements, C. W. Chou, D. J. Wineland, D. B. Hume, and D. R. Leibrandt , "$^{27}Al^+$ quantum-logic clock with a systematic uncertainty below 10^{-18}", Phys. Rev. Lett. **123**, 033201 (2019).

[125] F. Schäfer, T. Fukuhara, S. Sugawa, Y. Takasu, and Y. Takahashi , "Tools for quantum simulation with ultracold atoms in optical lattices", Nat. Rev. Phys. **2**, 411 (2020).

[126] B. K. Stuhl, B. C. Sawyer, D. Wang, and J. Ye , "Magneto-optical trap for polar molecules", Phys. Rev. Lett. **101**, 243002 (2008).

[127] T. A. Isaev and R. Berger , "Polyatomic candidates for cooling of molecules with lasers from simple theoretical concepts", Phys. Rev. Lett. **116**, 063006 (2016).

[128] I. Kozyryev, L. Baum, K. Matsuda, and J. M. Doyle , "Proposal for laser cooling of complex polyatomic molecules", ChemPhysChem **17**, 3641 (2016).

[129] R. Albrecht, M. Scharwaechter, T. Sixt, L. Hofer, and T. Langen , "Buffer-gas cooling, high-resolution spectroscopy, and optical cycling of barium monofluoride molecules", Phys. Rev. A **101**, 013413 (2020).

[130] Y. Zhang, Z. Zeng, Q. Liang, W. Bu, and B. Yan , "Doppler cooling of buffer-gas-cooled barium monofluoride molecules", Phys. Rev. A **105**, 033307 (2022).

[131] R. Gu, K. Yan, D. Wu, J. Wei, Y. Xia, and J. Yin , "Radiative force from optical cycling on magnesium monofluoride", Phys. Rev. A **105**, 042806 (2022).

[132] S. Hofsäss, M. Doppelbauer, S. Wright, S. Kray, B. Sartakov, J. Pérez-Ríos, G. Meijer, and S. Truppe , "Optical cycling of alf molecules", New J. Phys. **23**, 075001 (2021).

[133] P. W. Graham and S. Rajendran , "Axion dark matter detection with cold molecules", Phys. Rev. D **84**, 055013 (2011).

[134] K. Van Tilburg, N. Leefer, L. Bougas, and D. Budker , "Search for ultralight scalar dark matter with atomic spectroscopy", Phys. Rev. Lett. **115**, 011802 (2015).

[135] J. J. Hudson, D. M. Kara, I. Smallman, B. E. Sauer, M. R. Tarbutt, and E. A. Hinds , "Improved measurement of the shape of the electron", Nature **473**, 493 (2011).

[136] S. K. Tokunaga, C. Stoeffler, F. Auguste, A. Shelkovnikov, C. Daussy, A. Amy-Klein, C. Chardonnet, and B. Darquié , "Probing weak force-induced parity violation by high-resolution mid-infrared molecular spectroscopy", Mol. Phys. **111**, 2363 (2013).

[137] C. Daussy, T. Marrel, A. Amy-Klein, C. Nguyen, C. J. Bordé, and C. Chardonnet , "Limit on the parity nonconserving energy difference between the enantiomers of a chiral molecule by laser spectroscopy", Phys. Rev. Lett. **83**, 1554 (1999).

[138] A. Shelkovnikov, R. J. Butcher, C. Chardonnet, and A. Amy-Klein , "Stability of the proton-to-electron mass ratio", Phys. Rev. Lett. **100**, 150801 (2008).

[139] S. Truppe, R. Hendricks, S. Tokunaga, H. Lewandowski, M. Kozlov, C. Henkel, E. Hinds, and M. Tarbutt , "A search for varying fundamental constants using hertz-level frequency measurements of cold ch molecules", Nat. Commun. **4**, 1 (2013).

[140] M. V. Ivanov, S. Gulania, and A. I. Krylov , "Two cycling centers in one molecule: Communication by through-bond interactions and entanglement of the unpaired electrons", J. Phys. Chem. Lett. **11**, 1297 (2020).

[141] J. Kłos and S. Kotochigova , "Prospects for laser cooling of polyatomic molecules with increasing complexity", Phys. Rev. Res. **2**, 013384 (2020).

[142] N. R. Hutzler, H.-I. Lu, and J. M. Doyle , "The buffer gas beam: An intense, cold, and slow source for atoms and molecules", Chem. Rev. **112**, 4803 (2012).

[143] N. J. Reilly, T. W. Schmidt, and S. H. Kable , "Two-dimensional fluorescence (excitation/emission) spectroscopy as a probe of complex chemical environments", J. Phys. Chem. A **110**, 12355 (2006).

[144] J. R. Gascooke, U. N. Alexander, and W. D. Lawrance , "Two dimensional laser induced fluorescence spectroscopy: A powerful technique for elucidating rovibronic structure in electronic transitions of polyatomic molecules", J. Chem. Phys. **134**, 184301 (2011).

[145] D. L. Kokkin, T. C. Steimle, and D. DeMille , "Branching ratios and radiative lifetimes of the U, L, and I states of thorium oxide", Phys. Rev. A **90**, 062503 (2014).

[146] B. L. Augenbraun, Z. D. Lasner, A. Frenett, H. Sawaoka, A. T. Le, J. M. Doyle, and T. C. Steimle , "Observation and laser spectroscopy of ytterbium monomethoxide, yboch3", Phys. Rev. A **103**, 022814 (2021).

[147] A. Acharya, S. Chaudhuri, and V. S. Batista , "Can TDDFT describe excited electronic states of naphthol photoacids? A closer look with EOM-CCSD", J. Chem. Theory Comput. **14**, 867 (2018).

[148] W. Domcke, L. Cederbaum, H. Köppel, and W. Von Niessen , "A comparison of different approaches to the calculation of Franck-Condon factors for polyatomic molecules", Mol. Phys. **34**, 1759 (1977).

[149] G. Fischer, *Vibronic Coupling: The Interaction between the Electronic and Nuclear Motions* (Academic Press, 1984).

[150] P. J. Dagdigian , "State-resolved collision-induced electronic transitions", Annu. Rev. Phys. Chem. **48**, 95 (1997).

[151] A. Kramida, Y. Ralchenko, J. Reader, and NIST ASD Team (2021) , "NIST Atomic Spectra Database (ver. 5.9), [online]. available: https://physics.nist.gov/asd", National Institute of Standards and Technology, Gaithersburg, MD .

[152] D. Mitra, Z. D. Lasner, G.-Z. Zhu, C. E. Dickerson, B. L. Augenbraun, A. D. Bailey, A. N. Alexandrova, W. C. Campbell, J. R. Caram, E. R. Hudson, and J. M. Doyle , "Pathway towards optical cycling and laser cooling of functionalized arenes", J. Phys. Chem. Lett. **13**, 7029 (2022).

[153] C. M. Western , "Pgopher: A program for simulating rotational, vibrational and electronic spectra", J. Quant. Spectrosc. Radiat. Transf. **186**, 221 (2017).

[154] Y. Endo, S. Saito, and E. Hirota , "The microwave spectrum of the methoxy radical CH_3O", J. Chem. Phys. **81**, 122 (1984).

[155] I. Bowater, J. Brown, and A. Carrington , "Microwave spectroscopy of nonlinear free radicals-I. general theory and application to the Zeeman effect in HCO", Proc. R. Soc. A **333**, 265 (1973).

[156] J. Brown and T. Sears , "A reduced form of the spin-rotation Hamiltonian for asymmetric-top molecules, with applications to HO_2 and NH_2", J. Mol. Spectrosc. **75**, 111 (1979).

[157] K. Balasubramanian , "A method for nuclear spin statistics in molecular spectroscopy", J. Chem. Phys. **74**, 6824 (1981).

[158] I. Guseinov, B. Mamedov, and E. Çopuroğlu , "Use of binomial coefficients in fast and accurate calculation of Clebsch–Gordan and Gaunt coefficients, and Wigner n-j symbols", J. Theor. Comput. Chem. **8**, 251 (2009).

[159] J. Konečnỳ, J. Liu, P. Richtárik, and M. Takáč , "Mini-batch semi-stochastic gradient descent in the proximal setting", IEEE J. Sel. Top. Signal Process. **10**, 242 (2015).

[160] W. L. Meerts, M. Schmitt, and G. C. Groenenboom , "New applications of the genetic algorithm for the interpretation of high-resolution spectra", Can. J. Chem. **82**, 804 (2004).

[161] J. H. Van Vleck , "The coupling of angular momentum vectors in molecules", Rev. Mod. Phys. **23**, 213 (1951).

[162] Z. Morbi, C. Zhao, and P. F. Bernath , "A high-resolution analysis of the $\widetilde{C}\ ^2A_1 - \widetilde{X}\ ^2A_1$ transition of $CaNH_2$: Pure precession in polyatomic molecules", J. Chem. Phys. **106**, 4860 (1997).

[163] P. I. Presunka and J. A. Coxon , "Laser excitation and dispersed fluorescence investigations of the $A^2\Pi - X^2\Sigma^+$ system of SrOH", Chem. Phys. **190**, 97 (1995).

[164] M. V. Ivanov, F. H. Bangerter, and A. I. Krylov , "Towards a rational design of laser-coolable molecules: Insights from equation-of-motion coupled-cluster calculations", Phys. Chem. Chem. Phys. **21**, 19447 (2019).

[165] M. V. Ivanov, F. H. Bangerter, P. Wójcik, and A. I. Krylov , "Toward ultracold organic chemistry: Prospects of laser cooling large organic molecules", J. Phys. Chem. Lett. **11**, 6670 (2020).

[166] C. E. Dickerson, H. Guo, G.-Z. Zhu, E. R. Hudson, J. R. Caram, W. C. Campbell, and A. N. Alexandrova , "Optical cycling functionalization of arenes", J. Phys. Chem. Lett. **12**, 3989 (2021).

[167] A. C. Paul, K. Sharma, H. Telfah, T. A. Miller, and J. Liu , "Electronic spectroscopy of the $\widetilde{A}_1\ ^2A''/\widetilde{A}_2\ ^2A' - \widetilde{X}\ ^2A'$ transitions of jet-cooled calcium ethoxide radicals: Vibronic structure of alkaline earth monoalkoxide radicals of C_s symmetry", J. Chem. Phys. **155**, 024301 (2021).

[168] H. Telfah, K. Sharma, A. C. Paul, S. S. Riyadh, T. A. Miller, and J. Liu , "A combined experimental and computational study on the transition of the calcium isopropoxide radical as a candidate for direct laser cooling", Phys. Chem. Chem. Phys. **24**, 8749 (2022).

[169] C. E. Dickerson, C. Chang, H. Guo, and A. N. Alexandrova , "Fully saturated hydrocarbons as hosts of optical cycling centers", J. Phys. Chem. A **126**, 9644 (2022).

[170] P. Yu, A. Lopez, W. A. Goddard, and N. R. Hutzler , "Multivalent optical cycling centers: Towards control of polyatomics with multi-electron degrees of freedom", Phys. Chem. Chem. Phys. **25**, 154 (2023).

[171] H. Sinenka, Y. Bruyakin, A. Zaitsevskii, T. Isaev, and A. V. Bochenkova , "Zwitterions functionalized by optical cycling centers: Toward laser-coolable polyatomic molecular cations", J.Phys. Chem. Lett. **14**, 5784 (2023).

[172] P. B. Changala, N. Genossar-Dan, E. Brudner, T. Gur, J. H. Baraban, and M. C. McCarthy , "Structural and electronic trends of optical cycling centers in polyatomic molecules revealed by microwave spectroscopy of MgCCH, CaCCH, and SrCCH", Proc. Natl. Acad. Sci. U.S.A. **120**, e2303586120 (2023).

[173] H. Guo, C. E. Dickerson, A. J. Shin, C. Zhao, T. L. Atallah, J. R. Caram, W. C. Campbell, and A. N. Alexandrova , "Surface chemical trapping of optical cycling centers", Phys. Chem. Chem. Phys. **23**, 211 (2021).

[174] D. J. Nesbitt and R. W. Field , "Vibrational energy flow in highly excited molecules: Role of intramolecular vibrational redistribution", J. Phys. Chem. **100**, 12735 (1996).

[175] J. C. Keske and B. H. Pate , "Decoding the dynamical information embedded in highly mixed quantum states", Annu. Rev. Phys. Chem. **51**, 323 (2000).

[176] N. Fitch and M. Tarbutt (Academic Press, 2021) pp. 157–262.

[177] B. L. Augenbraun, L. Anderegg, C. Hallas, Z. D. Lasner, N. B. Vilas, and J. M. Doyle (Academic Press, 2023) pp. 89–182.

[178] B. L. Augenbraun, S. Burchesky, A. Winnicki, and J. M. Doyle , "High-resolution laser spectroscopy of a functionalized aromatic molecule", J. Phys. Chem. Lett. **13**, 10771 (2022).

[179] E. Fermi , "Über den ramaneffekt des kohlendioxyds", Z. Phys. **71**, 250 (1931).

[180] H.-R. Dübal and M. Quack , "Tridiagonal Fermi resonance structure in the IR spectrum of the excited CH chromophore in CF_3H", J. Chem. Phys. **81**, 3779 (1984).

[181] C. Zhang, B. L. Augenbraun, Z. D. Lasner, N. B. Vilas, J. M. Doyle, and L. Cheng , "Accurate prediction and measurement of vibronic branching ratios for laser cooling linear polyatomic molecules", J. Chem. Phys. **155**, 091101 (2021).

[182] C. Zhang, N. R. Hutzler, and L. Cheng , "Intensity-borrowing mechanisms pertinent to laser cooling of linear polyatomic molecules", J. Chem. Theory Comput. **19**, 4136 (2023).

[183] P. W. Atkins and R. S. Friedman, *Molecular Quantum Mechanics* (Oxford University Press, 2011).

[184] H. Lefebvre-Brion and R. W. Field, *The Spectra and Dynamics of Diatomic Molecules* (Elsevier, 2004).

[185] J. P. Perdew, M. Ernzerhof, and K. Burke , "Rationale for mixing exact exchange with density functional approximations", J. Chem. Phys. **105**, 9982 (1996).

[186] F. Weigend and R. Ahlrichs , "Balanced basis sets of split valence, triple zeta valence and quadruple zeta valence quality for H to Rn: Design and assessment of accuracy", Phys. Chem. Chem. Phys. **7**, 3297 (2005).

[187] S. Grimme, J. Antony, S. Ehrlich, and H. Krieg , "A consistent and accurate ab initio parametrization of density functional dispersion correction (DFT-D) for the 94 elements H-Pu", J. Chem. Phys. **132**, 154104 (2010).

[188] D. Rappoport and F. Furche , "Property-optimized gaussian basis sets for molecular response calculations", J. Chem. Phys. **133**, 134105 (2010).

[189] M. J. Frisch, G. W. Trucks, H. B. Schlegel, G. E. Scuseria, M. A. Robb, J. R. Cheeseman, G. Scalmani, V. Barone, G. A. Petersson, H. Nakatsuji, X. Li, M. Caricato, A. V. Marenich, J. Bloino, B. G. Janesko, R. Gomperts, B. Mennucci, H. P. Hratchian, J. V. Ortiz, A. F. Izmaylov, J. L. Sonnenberg, D. Williams-Young, F. Ding, F. Lipparini, F. Egidi, J. Goings, B. Peng, A. Petrone, T. Henderson, D. Ranasinghe, V. G. Zakrzewski, J. Gao, N. Rega, G. Zheng, W. Liang, M. Hada, M. Ehara, K. Toyota, R. Fukuda, J. Hasegawa, M. Ishida, T. Nakajima, Y. Honda, O. Kitao, H. Nakai, T. Vreven, K. Throssell, J. A. Montgomery, Jr., J. E. Peralta, F. Ogliaro, M. J. Bearpark, J. J. Heyd, E. N. Brothers, K. N. Kudin, V. N. Staroverov, T. A. Keith,

R. Kobayashi, J. Normand, K. Raghavachari, A. P. Rendell, J. C. Burant, S. S. Iyengar, J. Tomasi, M. Cossi, J. M. Millam, M. Klene, C. Adamo, R. Cammi, J. W. Ochterski, R. L. Martin, K. Morokuma, O. Farkas, J. B. Foresman, and D. J. Fox, "Gaussian 16 Revision C.01" (2016), gaussian Inc. Wallingford CT.

[190] T. Lu and F. Chen , "Multiwfn: a multifunctional wavefunction analyzer", J. Comput. Chem. **33**, 580 (2012).

[191] S. Gozem and A. I. Krylov , "The ezspectra suite: An easy-to-use toolkit for spectroscopy modeling", WIREs Comput. Mol. Sci. **12**, e1546 (2022).

[192] H. H. Nielsen , "The vibration-rotation energies of molecules", Rev. Mod. Phys. **23**, 90 (1951).

[193] V. Barone , "Anharmonic vibrational properties by a fully automated second-order perturbative approach", J. Chem. Phys. **122**, 014108 (2005).

[194] M. A. Boyer and A. B. McCoy , "Pyvibptn, a general package for vibrational perturbation theory", Zenodo **5563091** (2021).

[195] M. A. Boyer and A. B. McCoy , "A flexible approach to vibrational perturbation theory using sparse matrix methods", J. Chem. Phys. **156**, 054107 (2022).

[196] M. A. Boyer and A. B. McCoy , "A wave function correction-based approach to the identification of resonances for vibrational perturbation theory", J. Chem. Phys. **157**, 164113 (2022).

[197] S. J. Stropoli, T. Khuu, M. A. Boyer, N. V. Karimova, C. F. Gavin-Hanner, S. Mitra, A. L. Lachowicz, N. Yang, R. B. Gerber, A. B. McCoy, *et al.* , "Electronic and mechanical anharmonicities in the vibrational spectra of the h-bonded, cryogenically cooled X-HOCl (X= Cl, Br, I) complexes: Characterization of the strong anionic H-bond to an acidic OH group", J. Chem. Phys. **156** (2022).

[198] J. A. Lau, M. DeWitt, M. A. Boyer, M. C. Babin, T. Solomis, M. Grellmann, K. R. Asmis, A. B. McCoy, and D. M. Neumark , "High-resolution photoelectron spectroscopy of vibrationally excited vinoxide anions", J. Phys. Chem. A **127**, 3133 (2023).

[199] P. Krantz, M. Kjaergaard, F. Yan, T. P. Orlando, S. Gustavsson, and W. D. Oliver , "A quantum engineer's guide to superconducting qubits", Appl. Phys. Rev. **6**, 021318 (2019).

[200] F. A. Zwanenburg, A. S. Dzurak, A. Morello, M. Y. Simmons, L. C. Hollenberg, G. Klimeck, S. Rogge, S. N. Coppersmith, and M. A. Eriksson , "Silicon quantum electronics", Rev. Mod. Phys. **85**, 961 (2013).

[201] A. M. Kaufman and K.-K. Ni , "Quantum science with optical tweezer arrays of ultracold atoms and molecules", Nat. Phys. **17**, 1324 (2021).

[202] C. D. Bruzewicz, J. Chiaverini, R. McConnell, and J. M. Sage , "Trapped-ion quantum computing: Progress and challenges", Appl. Phys. Rev. **6**, 021314 (2019).

[203] N. B. Vilas, C. Hallas, L. Anderegg, P. Robichaud, A. Winnicki, D. Mitra, and J. M. Doyle , "Magneto-optical trapping and sub-doppler cooling of a polyatomic molecule", Nature **606**, 70 (2022).

[204] L. W. Cheuk, L. Anderegg, B. L. Augenbraun, Y. Bao, S. Burchesky, W. Ketterle, and J. M. Doyle , "Λ-enhanced imaging of molecules in an optical trap", Phys. Rev. Lett. **121**, 083201 (2018).

[205] J. Shaw, J. Schnaubelt, and D. McCarron , "Resonance raman optical cycling for high-fidelity fluorescence detection of molecules", Phys. Rev. Res. **3**, L042041 (2021).

[206] N. Schlosser, G. Reymond, I. Protsenko, and P. Grangier , "Sub-poissonian loading of single atoms in a microscopic dipole trap", Nature **411**, 1024 (2001).

[207] H. Bernien, S. Schwartz, A. Keesling, H. Levine, A. Omran, H. Pichler, S. Choi, A. S.

Zibrov, M. Endres, M. Greiner, *et al.* , "Probing many-body dynamics on a 51-atom quantum simulator", Nature **551**, 579 (2017).

[208] T. Graham, Y. Song, J. Scott, C. Poole, L. Phuttitarn, K. Jooya, P. Eichler, X. Jiang, A. Marra, B. Grinkemeyer, *et al.* , "Multi-qubit entanglement and algorithms on a neutral-atom quantum computer", Nature **604**, 457 (2022).

[209] L. Anderegg, L. W. Cheuk, Y. Bao, S. Burchesky, W. Ketterle, K.-K. Ni, and J. M. Doyle , "An optical tweezer array of ultracold molecules", Science **365**, 1156 (2019).

[210] C. M. Holland, Y. Lu, and L. W. Cheuk , "Bichromatic imaging of single molecules in an optical tweezer array", Phys. Rev. Lett. **131**, 053202 (2023).

[211] E. T. Campbell, B. M. Terhal, and C. Vuillot , "Roads towards fault-tolerant universal quantum computation", Nature **549**, 172 (2017).

[212] G.-Z. Zhu, G. Lao, C. E. Dickerson, J. R. Caram, W. C. Campbell, A. N. Alexandrova, and E. R. Hudson , "Extending the large molecule limit: The role of fermi resonance in developing a quantum functional group", J. Phys. Chem. Lett. **15**, 590 (2024).

[213] P. F. Bernath and C. R. Brazier , "Spectroscopy of CaOH", Astrophys. J. **288**, 373 (1985).

[214] P. Crozet, F. Martin, A. Ross, C. Linton, M. Dick, and A. Adam , "The $A^2E--X^2A_1$ system of $CaOCH_3$", J. Mol. Spectrosc. **213**, 28 (2002).

[215] C. R. Brazier, L. C. Ellingboe, S. Kinsey-Nielsen, and P. F. Bernath , "Laser spectroscopy of alkaline earth monoalkoxide free radicals", J. Am. Chem. Soc. **108**, 2126 (1986).

[216] J. Mooney and P. Kambhampati , "Get the basics right: Jacobian conversion of wavelength and energy scales for quantitative analysis of emission spectra", J. Phys. Chem. Lett. **4**, 3316 (2013).

[217] S. P. Jain, E. R. Hudson, W. C. Campbell, and V. V. Albert , "\ae\codes", arXiv preprint arXiv:2311.12324 (2023).

[218] P. Hanoian, P. A. Sigala, D. Herschlag, and S. Hammes-Schiffer , "Hydrogen bonding in the active site of ketosteroid isomerase: Electronic inductive effects and hydrogen bond coupling", Biochem. **49**, 10339 (2010).

[219] L. P. Hammett , "The effect of structure upon the reactions of organic compounds. Benzene derivatives", J. Am. Chem. Soc. **59**, 96 (1937).